A new algorithm to retrieve the sea ice concentration using weather-corrected 85 GHz SSM/I measurements

Dissertation
zur
Erlangung des Grades eines
Doktors der Naturwissenschaften
- Dr. rer. nat. -

dem Fachbereich Physik
der Universität Bremen
vorgelegt von

Stefan Kern
im Januar 2001

Datum der Promotion: 22. Februar 2001

Institute of Environmental Physics, Bremen, Germany

Contents

Acknowledgements

This work was funded by the European Union, Bruessel, Belgium, under contract ENV4-CT97-0415. I would like to gratefully acknowledge the following institutions for providing me with the data required: EOS Distributed Active Archive Center (DAAC) at the National Snow and Ice Data Center (NSIDC), University of Colorado, Boulder, CO, U.S.A., for DMSP daily gridded SSM/I data; Marshall Space Flight Center (MSFC), NASA, Huntsville, AL, U.S.A., and Danish Centre for Remote Sensing (DCRS) at the Danish Technical University (DTU), Lyngby, Danmark, for DMSP SSM/I swath data; National Geographic Data Center (NGDC), NOAA, Boulder, CO, U.S.A. for OLS data; European Centre for Medium-Range Weather Forecast (ECMWF), Reading, U.K., and Deutsches Klimarechenzentrum (DKRZ), Hamburg, Germany, as well as the Danish Meteorological Institute (DMI), Copenhagen, Danmark, for data of the operational ECMWF weather-forecast model and of the Danish weather-forecast model, respectively; Antarctic Meteorology Research Center (AMRC) at the Space Science Engineering Center (SSEC), University of Wisconsin, Madison, WI, U.S.A., for ship observations.

In this context I would like to address special thanks to Prof. Dr. W. Alpers of the Institute for Marine Research, University of Hamburg, Hamburg, Germany, and to the GAF mbH, Munich, Germany, for providing 9 RADARSAT-1 SAR scenes in the Greenland Sea. Also, I would like to give my thanks to C. Haas, Alfred Wegener Institute for Polar and Marine Research (AWI), Bremerhaven, Germany, for *in situ* observations of Antarctic snow and ice properties.

Also, it's time to draw a resume about the last three years at the Institute of Environmental Physics (IUP). First of all, I would like to thank Prof. Dr. K. Künzi and G. Heygster for choosing and hosting me. For helpful discussions with my colleagues I'm indebted to G. Heygster, K.-P. Johnsen, L. Kaleschke, J. Miao and C. Thomas. Cracking jokes, having a brain-reset is also very important – many thanks to J. Dannenberg, O. Funke, B. Klocke, H. Laue, H. Rohr, N. Schlüter, R. Schmidt, N. Selbach and S. Voss. Thanks also to H. Schellhorn and B. Teuchert. They kept the hardware, the software and the administrative things going.
All you people of the SEA LION project – it was a pleasure to collaborate with you. Also, I would like to express my gratitude to G. Hoffmann and M. Lautenschlager. They enabled easy access to the ECMWF data and proved their patience when responding to my questions about handling these data. C. Haas and J. Kolatschek – thank you for participating in your knowledge about sea ice and snow.

Three people provided the most important contribution: a sincere interest in my work. In this context honour is due to S. Andersen with whom I had four weeks of a splendid collaboration during my stay as a visiting scientist at the DMI in spring 1999. Thanks a lot for this time – I'll never forget the evening with Chinese food, Whisky and Ummagumma – and for your support concerning the model data. Moreover, honour is due to C. Garrity and R. Ramseier. They became kind of "Doctor parents" to me. While being critical they always encouraged me by letting me know: "You're on the right way", showed a deep interest in my results and hosted me during my stay at a conference in Ottawa. Thank you very much!

This work would not have been possible without my parents and parents in law, always keeping an eye on me, and, of course, without my beloved wife Sybille. She maintained my creativity and health, and kept an unquestionable confidence in me and my abilities.

ABSTRACT – Sea ice is a very important component of the climate system. While the sea ice extent has retreated in the Arctic during the past 20 years, it has remained constant in the Antarctic. In order to better understand the role of sea ice within the climate system in the context of global warming state-of-the-art coupled Atmosphere-Ocean Global Circulation Models have to be improved. This requires to know the sea ice concentration C for a long period for both hemispheres and at the best possible spatial resolution. Currently used methods to calculate C like the NASA Team algorithm are based on data aquired by the Special Sensor Microwave/Imager (SSM/I) at 19 and 37 GHz. The SEA LION algorithm presented here allows to calculate C with the polarization P at 85 GHz taking advantage of the higher spatial resolution associated with this frequency. However, the decrease of the polarization caused by the weather influence leads to an overestimation of C. Therefore, the polarization is corrected using a radiative transfer model and atmospheric data taken from Numerical Weather Prediction models and/or derived from SSM/I measurements. The various sea ice and snow properties have been considered calculating monthly sea ice tie points. The average standard deviation of the sea ice concentration derived with the SEA LION algorithm is about $12\,\%$ for $C \leq 50\,\%$ and less than $5\,\%$ for $C > 90\,\%$. The sea ice edge obtained with the SEA LION algorithm agrees within 10 km with the ice edge evident in VIS/IR images. The gradient of the SEA LION ice concentration across the marginal ice zone (MIZ) agrees much better with the one inferred from RADARSAT-1 SAR scenes in the Greenland Sea if compared to results of the NASA Team algorithm. The SEA LION algorithm suggests a faster and earlier retreat of the sea ice cover during Austral spring/summer in comparison to former sea ice extent data sets. This can be explained with the higher spatial resolution at 85 GHz allowing to detect smaller areas of open water than the other SSM/I channels. Averaging C over the investigated period 1992-1999, the SEA LION algorithm provides higher values than the NASA Team algorithm (difference $\approx 5\,\%$) and lower values than the Bootstrap algorithm (difference $\approx 3\,\%$). A major limitation for using the SEA LION algorithm arises from the quality of atmospheric data needed for the weather correction. A spatial resolution of atmospheric data lower than the 85 GHz SSM/I channels and/or a time lag larger than half an hour between both data sets can cause relative errors above $100\,\%$, particulary in the cloud-covered parts of the MIZ.

ZUSAMMENFASSUNG – Meereis spielt ein Schlüsselrolle im Klimasystem. Die arktische Meereisbedeckung hat über die letzten zwei Jahrzehnte signifikant abgenommen, die antarktische jedoch nicht. Um dies vor dem Hintergrund einer globalen Klimaänderung zu untersuchen, müssen bestehende gekoppelte Atmosphäre-Ozean Globale Zirkulationsmodelle verbessert werden. Dafür benötigt man die prozentuale Meereisbedeckung C beider Hemisphären über einen möglichst langen Zeitraum und mit einer möglichst guten räumlichen Auflösung. Zur Zeit verwenden die Methoden zur Berechnung von C, z. B. der NASA Team-Algorithmus, Daten der 19 und 37 GHz Kanäle des *Special Sensor Microwave/Imager* (SSM/I). Der hier vorgestellte SEA LION-Algorithmus bestimmt C auf Basis der Polarisation P der räumlich besser aufgelösten 85 GHz SSM/I-Daten. Jedoch verringert der Wettereinfluss P und verursacht eine Überschätzung von C. Dieser Fehler wird mittels eines Strahlungstransportmodells korrigiert. Dafür benötigte atmosphärische Parameter stammen entweder aus Wettervorhersagemodellen oder werden aus Daten der übrigen SSM/I-Kanäle berechnet. Veränderungen der Schnee- und Eisbedingungen werden durch monatliche Meereiseichpunkte berücksichtigt. Die mittlere Standardabweichung der SEA LION-Eiskonzentration liegt bei $12\,\%$ für $C \leq 50\,\%$ und ist kleiner als $5\,\%$ für $C > 90\,\%$. Der Verlauf der Meereiskante wurde mit dem SEA LION-Algorithmus berechnet und mit Bildern im sichtbaren und infraroten Frequenzbereich validiert. Beide Verläufe stimmen auf etwa 10 km genau überein. Das neue Verfahren liefert, im Vergleich zum NASA Team-Algorithmus, einen realistischeren Gradienten von C quer zur Eisrandzone, wie RADARSAT-1 SAR Szenen aus der Grönlandsee belegen. Verglichen mit herkömmlichen Datensätzen nimmt die mit dem SEA LION-Algorithmus bestimmte antarktische Meereisbedeckung im Südfrühling schneller und früher ab. Das enspricht den Erwartungen, denn die 85 GHz SSM/I-Kanäle erfassen dank der besseren räumlichen Auflösung kleinere offene Wasserflächen als die übrigen SSM/I-Kanäle. SEA LION-Eiskonzentrationen, gemittelt über die Periode 1992-1999, übertreffen entsprechende NASA Team-Eiskonzentrationen um $\approx 5\,\%$, liegen jedoch um $\approx 3\,\%$ unterhalb den entsprechenden Bootstrap-Eiskonzentrationen. Die Verwendbarkeit des SEA LION Algorithmus wird durch die Qualität der für die Wetterkorrektur benötigten Daten eingeschränkt. Relative Fehler von über $100\,\%$ sind in wolkenbedeckten Gebieten der Eisrandzone dann möglich, wenn die Auflösung der atmosphärischen Daten deutlich unter derjenigen der 85 GHz Daten liegt bzw. wenn beide Datensätze einen Zeitversatz von mehr als einer halben Stunde aufweisen.

Chapter 1

Introduction

1.1 Sea Ice in the Climate System

Sea ice covers about $7\,\%$ of the Earth's surface all the year round [Cavalieri and St. Germain, 1995] affecting the interaction between the ocean and the atmosphere. The sea ice extends over $2 \times 10^6\,\mathrm{km}^2$ and $19 \times 10^6\,\mathrm{km}^2$ in the Southern and over $6 \times 10^6\,\mathrm{km}^2$ and $16 \times 10^6\,\mathrm{km}^2$ in the Northern Hemisphere in summer and winter of the considered hemisphere, respectively [Cavalieri et al., 1997]. Sea ice can be devided into three categories: thin or young ice, first-year (FY) ice and old ice, which is second-year (SY) ice or multiyear (MY) ice. A sea ice cover can reduce the vertical fluxes of latent and sensible heat from the ocean into the atmosphere by up to two orders of magnitude at high latitudes [Maykut, 1978], [Smith et al., 1990], [Launiainen and Vihma, 1994]. Even a small fraction, for instance $5\,\%$, of water or thin ice (10 cm) within an area covered by thicker ice (100 cm) has a considerable influence on the surface heat budget of this area. The exchange of momentum is also different above sea ice if compared to open water and depends on the aerodynamic surface roughness of both surfaces. While the aerodynamic surface roughness of undeformed sea ice is smaller than that of open water, which is usually roughened by the surface wind, deformed or broken sea ice exhibits a larger surface roughness. The quasi-permanent snow cover often smoothes out the higher-frequency surface roughness [Andreas, 1987], [Sturm et al., 1998].

The albedo of sea ice ($0.45 \ldots 0.98$) is much larger than that of open water ($0.03 \ldots 0.1$). Consequently, sea ice reflects much more solar radiation, the surface radiation budget is negative almost all the time and strong surface air tem-

perature inversions can develop. During summer, when the sea ice/snow is at its freezing point, all available solar energy is used to melt the sea ice and the snow. Surface air temperatures exceed 0°C only during periods of advection of warmer air from lower latitudes [Massom et al., 1997], [Drinkwater and Liu, 2000]. These low surface air temperatures cause only a small maximum amount of water vapor to be captured by the air. Thus, in terms of its absolute water vapor content air is much drier in polar regions, particularly over sea ice. As a result, the sea ice cover maintains the horizontal gradients of air temperature and water vapor content between polar and temperate latitudes and is a key element in the general atmospheric circulation. However, the relative humidity is sufficiently high to cause a high-percentage of cloud cover in polar regions.

During its growth and aging sea ice rejects large quantities of salt into the ocean. A cold, highly saline and therefore very dense water mass forms and sinks by vertical convection into the deep ocean becoming so-called *Deep Bottom Water*. This water mass is of crucial importance for the global conveyor belt in the World's Oceans [Johannessen et al., 1994], [Harder et al., 1998]. Major areas of Deep Bottom Water formation are the Greenland and Labrador Seas and all polynyas in the Southern Ocean, which surrounds Antarctica as part of the Pacific, Indic and Atlantic Oceans. Conversely, during sea ice melt a less dense freshwater layer forms on top of the ocean, stratifying its upper 100 meters. This is more pronounced in the Arctic where the land masses of the adjacent continents not only prevent a water exchange with the surrounding oceans but also force the sea ice, on average, to become thicker and older and therefore less saline than in the Southern Ocean.

Ocean currents such as the East Greenland Current or the Weddell Gyre and local wind phenomena such as katabatic winds often carry the sea ice away from its formation area. This makes the sea ice a very effective medium for freshwater transport as can be seen in the Fram Strait where the freshwater transport due to sea ice drift is the second largest in the world compared to river runoffs [Harder et al., 1998], [Martin and Augstein, 2000].

Finally, sea ice and the water underneath contain various biological species. Some species of phytoplankton have not only adopted to the polar environment but may serve as indicator for changes in sea ice extent and/or thickness. The latter was shown, for instance, for the interaction between the biogenic *Particulate Organic Carbon* (POC) content and the sea ice extent in the Greenland Sea [Ramseier et al., 1999].

Several feedback mechanisms exist between sea ice, the ocean and the atmosphere, making regions covered by sea ice of particular interest for climate

research. It is widely accepted that the shortening of the Arctic sea ice season and probably also of the sea ice thickness over the past 25 years is linked to the observed air temperature increase at high northern latitudes [Parkinson, 1992], [Smith, 1998]. Simultaneously, the Antarctic sea ice cover reveals a slight positive trend [Stammerjohn and Smith, 1997], [Thomas, 1998]. However, the considerably larger typical time scale of the ocean to react on a change in the atmosphere and/or the sea ice cover causes problems when explaining the decreasing sea ice cover and thickness in the Northern Hemisphere. Time-series of the observed ocean and sea ice properties are certainly too short to understand all details of their natural variability. Modelling the interaction between the ocean and the atmosphere in polar regions, for instance with a *Global Circulation Model* (GCM), is an alternative – provided that a sophisticated sea ice model is implemented [Lemke et al., 1997]. The development of such a sea ice model and the implementation into a GCM requires to know the physical sea ice properties and to have time-series of the observed sea ice area and extent for comparison with the model output. These time-series can be obtained from remote sensing data.

1.2 Remote Sensing of Sea Ice

Much is known about physical sea ice properties from tank experiments such as performed at the *Cold Regions Research Engineering Laboratory* (CRREL), Hanover, New Hampshire, and from field experiments, *e. g.* the *Marginal Ice Zone EXperiment* (MIZEX) which lasted several years or the *Winter Weddell Sea Project* (WWSP). For details and results look into [The NORSEX Group, 1983], [Onstott et al., 1987], [Comiso et al., 1989], [Ackley and Weeks, 1990], [TuckerIII et al., 1992], [Eppler et al., 1992]. These experiments have provided very detailed information about the sea ice such as its percentage coverage, thickness or snow-cover properties on a very small spatial scale. However, when using a GCM a reasonable intercomparison of modelled with observed sea ice parameters requires the above-mentioned parameters to be available on a hemispherical scale for several years. This demand can be fulfilled using spaceborne remote sensing data.

One can distinguish between *actice* and *passive* remote sensing instruments. Active sensors such as a RADAR emit electromagnetic energy and receive the power reflected and/or scattered at the surface or in the atmosphere. The received power can be related to the surface backscatter coefficient and thus allows to gain information about the surface roughness. Among others, the *Active Microwave In-*

strument (AMI) aboard the polar orbiting *European Space Agency* (ESA) satellites ERS-1 (1991-1996) and ERS-2 (1995-present) and the Canadian RADARSAT-1 SAR (1995-present) belong to this sensor type. Both sensors acquire data at C-band (5.3 GHz) and are therefore able to look through clouds. In the SAR mode the spatial resolution is 25 m within a 100 km wide swath (ERS-1/2) and 50 m within a 460 km wide swath (RADARSAT-1). In the EScat mode (AMI only), the spatial resolution is about 20 km within a 500 km wide swath [Raney et al., 1991], [Long et al., 1993], [Drinkwater, 1998]. Many studies have illustrated the potential of SAR data in gaining information about the sea ice type and its surface state on a scale of a few tens of meters [Onstott, 1992], [Winebrenner et al., 1994], [Drinkwater and Lytle, 1997], [Drinkwater, 1998], [Tsatsoulis and Kwok, 1998]. EScat data have widely been used to estimate the ocean surface wind vector [Bentamy et al., 1999] and, more recently, to map the sea ice extent as well as its roughness, *e. g.* [Gohin, 1995], [Drinkwater and Lytle, 1997], [Drinkwater, 1998], [Drinkwater and Liu, 2000], [Haas, 2001].

Passive remote sensing instruments receive electromagnetic energy emitted by the surface and/or the atmosphere or depend on scattered solar radiation. Sensors of this type are, for instance, the *Operational Linescan System* (OLS) in the visible (0.4 μm - 0.7 μm) and infrared (0.7 μm - 300 μm) range and the *Special Sensor Microwave/Imager* (SSM/I) in the microwave frequency range, both aboard the polar orbiting spacecraft of the *Defense Meteorological Satellite Program* (DMSP). In the visible/infrared (VIS/IR) range, spaceborne sensors allow to acquire data of the shortwave albedo and the IR temperature with a spatial resolution of approximately 1 km within a 3000 km wide swath. Almost all clouds are opaque in the VIS/IR range and sea ice can only be observed in cloud-free areas. The large average cloud cover in polar regions ($> 70\,\%$) in the Southern Ocean according to the *International Satellite Cloud Climatology Project* (ISCCP, see [Schiffer and Rossow, 1983]) reduces the amount of useful VIS/IR data drastically. In the VIS range, the amount of data to be used for sea ice monitoring is further reduced since daylight is required. Nevertheless, data collected by the *Advanced Very High Resolution Radiometer* (AVHRR) aboard the NOAA spacecraft are used to estimate the sea ice and/or snow surface temperature in clear-sky areas [Key and Haefliger, 1992], [Comiso, 1994] and the thickness of thin sea ice [Yu and Rothrock, 1996]. These data are also very helpful to validate sea ice products derived from other spaceborne remote sensing data, *e. g.* [Cavalieri, 1994], [St. Germain and Cavalieri, 1997], [Agnew et al., 1999].

The need for daylight and clear-sky conditions can largely be avoided using microwave radiometers. These sensors measure the so-called *brightness tempe-*

rature of almost the complete sea ice cover in both polar areas at least once each day. The launch of the first imaging microwave radiometer, the *Electrically Scanning Microwave Radiometer* (ESMR) aboard the NASA Nimbus 5 satellite in 1973 [Gloersen et al., 1974] was followed in 1978 by the *Scanning Multichannel Microwave Radiometer* (SMMR, see [Gloersen and Barath, 1977]) aboard the NASA Nimbus 7 satellite. In 1987, the first sensor of a new generation, the SSM/I [Hollinger et al., 1987], was launched as part of the DMSP. Since then identical sensors have been launched aboard successive DMSP spacecraft, providing an almost continuous time-series of passive microwave data lasting from 1973 to present. Although these sensors provide data with a spatial resolution between 10 and 100 km which is coarse compared to data collected by the earlier-mentioned active and VIS/IR sensors, the large emissivity difference between open water and sea ice as well as land and snow has been exploited to estimate the sea ice concentration and the amount of snow, *e. g.* [Comiso and Zwally, 1982], [Künzi et al., 1982], [Cavalieri et al., 1984], [Cavalieri et al., 1991], [Comiso and Sullivan, 1986], [Comiso et al., 1992]. Besides this, over the radiometrically cold open ocean, SMMR and SSM/I data have been used to retrieve atmospheric parameters such as the surface wind speed V, the integrated water vapor content W and the integrated cloud liquid water content L, *e. g.* [Swift, 1980], [Gloersen et al., 1984], [Bauer and Schlüssel, 1993].

Well known sea ice concentration algorithms are, among others, the *Bootstrap* (BS) algorithm [Comiso, 1986] and the *NASA Team* (NT) algorithm [Cavalieri et al., 1984]. These algorithms have originally been developed for SMMR data and have been adopted to SSM/I data [Cavalieri et al., 1991], [Comiso et al., 1992]. The actual versions of both algorithms use the 19 and 37 GHz channels of the SSM/I. While the BS algorithm allows to obtain the total sea ice concentration C only, the NT algorithm provides areal fractions of FY and MY ice in addition. The quality of the derived sea ice products depends on an appropriate choice of so-called *tie points* – brightness temperatures typical for the surface types involved. During the past years, several improvements have been made to overcome difficulties arising from ambiguous surface signals or from the atmospheric influence. The *thin ice* algorithm [Cavalieri, 1994] considers the similarity of brightness temperatures measured above thin ice and a broken FY ice cover using a new set of tie points. Wensnahan et al. [1993] suggest to use a principal components analysis to solve this problem. The atmospheric influence on the retrieval of sea ice parameters from microwave radiances has been reported by Gloersen and Cavalieri [1986] for the first time. Since then several approaches have been made to correct either the microwave radiances or the derived sea ice parameters, *e. g.* [Walters et

al., 1987], [Cavalieri et al., 1995], [Thomas, 1998].

In the revised NT algorithm the influence of ice layers within the snow on the retrieval of the sea ice concentration is considered [Markus and Cavalieri, 2000]. However, products of the BS and NT algorithms suffer from the coarse spatial resolution of the selected SSM/I channels. Using the 85 GHz SSM/I channels would allow for a resolution improvement by at least a factor of four which, for instance, is of great interest when observing polynyas. Moreover, due to the smaller wavelength at 85 GHz the penetration depth is considerably smaller compared to the other SSM/I channels. Therefore, the 85 GHz channels are more sensitive to thin ice and to the physical properties of the upper few centimeters of snow on sea ice. Consequently, using these channels a better estimation of the sea ice concentration can be expected, particularly in areas covered by thin ice. In case of snow-covered sea ice, the obtained sea ice concentration would be less influenced by snow inhomogenities, for instance icy snow layers deeply buried in the snow [Markus and Cavalieri, 2000].

1.3 Outline of the Work

One aim of the *European Union*- (EU) funded project *SEa ice in the Antarctic – LInked with OceaN-atmosphere forcing* (SEA LION, see *http://www-iup.physik.uni-bremen.de/iuppage/sealion_ed1.html*) is to develop a new sea ice concentration algorithm, called SEA LION (SL) algorithm, and takes advantage of the higher spatial resolution of the 85 GHz SSM/I channels. The products of this new algorithm will be used for intercomparison with results of a numerical sea ice model and of GCMs with different representations of sea ice [Lemke et al., 1997], [Lemke et al., 2000].

The spatial resolution of geophysical parameters obtained from SSM/I data such as C or V is determined by the effective field-of-view (FOV) of the SSM/I and by the sampling distance of the measurements. At 19 GHz, the FOV is $69 \times 43\,\mathrm{km}^2$ and the distance between two samplings is 25 km. Consequently, adjacent FOVs have a considerable overlap. Projecting 19 GHz SSM/I data into a $25 \times 25\,\mathrm{km}^2$ grid, as done at the *National Snow and Ice Data Centre* (NSIDC), means to distribute the information contained in each single FOV over an area of almost five grid cells. Therefore, even for one SSM/I overpass the brigthness temperature within one grid cell is an average over at least five FOVs. The 85 GHz SSM/I channels have a FOV of $15 \times 13\,\mathrm{km}^2$ and are sampled each 12.5 km. Adjacent FOVs overlap only slightly and each FOV covers the area of almost just

one grid cell when projecting these data into the NSIDC $12.5 \times 12.5\,\mathrm{km}^2$ grid [NSIDC, 1996]. Using 85 GHz SSM/I data in combination with data acquired by other SSM/I channels improves the quality of the derived product by including, in terms of the other SSM/I channels, subpixel-scale information as has been shown by Markus and Burns [1995] and Hunewinkel et al. [1998]. In this thesis, 85 GHz SSM/I data have been used to derive the total sea ice concentration C in the Southern Ocean as well as in the Greenland Sea. To the best knowledge of the author, studies reporting the estimation of C from 85 GHz SSM/I data [Lomax et al., 1995], [Lubin et al., 1997] or higher-frequency data [Svendsen et al., 1987] deal only with Arctic conditions and will be described in Chapter 4.

The surface brightness temperature polarization difference ΔT is the key parameter for retrieving C from higher-frequency microwave radiances [Svendsen et al., 1987]. In order to reduce the impact of the physical temperature of the radiating sea ice and/or snow layer, ΔT has been normalized to use this quantity in the SL algorithm presented in this thesis. The basic equation of this algorithm is a simple relationship between C, the normalized ΔT at 85 GHz and tie points of open water and sea ice, and is described in Section 5.1.

The small penetration depth associated with the small wavelength at 85 GHz suggests a higher sensitivity to the sea ice surface properties when compared to the other SSM/I channels. Especially snow is an important factor since Antarctic sea ice is covered by snow almost all the year round due to the small number of melt-days in Austral summer [Drinkwater and Liu, 2000]. Once snow has been deposited on the sea ice it undergoes a pronounced metamorphism. It can be compacted and redistributed by the surface wind. Rain or melt water percolating the snow can cause single snow grains to coagulate. Melt-freeze cycles or freezing rain can cause a coarse-grained, icy crust on top of the snow, which may be buried by fresh snow after the next snow fall. This buried crust considerably affects the melt water drainage and/or conductive heat flux through the snow. As a consequence depth hoar may form below this crust while the above-mentioned metamorphism takes places above this crust – until the next snow fall. Therefore, the Antarctic snow cover on sea ice is highly stratified and can exhibit very different surface properties [Sturm et al., 1998]. In order to consider both, the interannual variability of sea ice and/or snow properties as well as the higher sensitivity of the 85 GHz SSM/I channels to changing surface conditions, new tie points of sea ice and open water have been derived from SSM/I data for each month. *In situ* measurements of the emissivity of sea ice and open water have been used for comparison (Section 5.2).

Compared to the other SSM/I channels the atmospheric influence on the

85 GHz SSM/I brightness temperatures is much larger and requires a correction. The radiative transfer model *MicroWave MODel* (MWMOD, see [Simmer, 1994], [Fuhrhop et al., 1998]) has been used to estimate the weather influence induced by the atmospheric parameters V, W and L in terms of a brightness temperature change over a wide emissivity range. When these parameters are known, the corresponding effect on the 85 GHZ SSM/I measurements can be estimated and corrected for as will be explained in Section 5.3. The required atmospheric parameters have been calculated from SSM/I data and/or taken from *Numerical Weather Prediction* (NWP) models as will be described in Chapter 3.

The SL algorithm allows to calculate C with the above-mentioned basic equation from daily gridded 85 GHz SSM/I data provided by the NSIDC on a $12.5 \times 12.5\,\mathrm{km}^2$ grid for the entire Southern Ocean. For this purpose, the weather-influenced 85 GHz SSM/I brightness temperatures are used to calculate a first guess of C. In the next step, MWMOD is used to model the 85 GHz brightness temperatures which would be measured by the SSM/I according to the first guess of C and according to the weather influence given by V, W and L. The result is compared to the real 85 GHz SSM/I measurement in terms of the normalized ΔT value. As long as the difference between the modeled and measured value of the normalized ΔT exceeds a certain threshold, the first guess of C is not accepted, the 85 GHz SSM/I measurements are corrected for the weather influence and a new guess of C is calculated. This iteration and some more details of the SL algorithm will be described in Section 5.4.

The SL algorithm is used to calculate C for the entire Southern Ocean for the period 1992-1999. These results are compared with OLS VIS/IR imagery, *in situ* ship observations of the sea ice cover and – in terms of area, extent and distribution of sea ice concentration anomalies – with the results of the BS and NT algorithms. This is presented in Section 6.1. Also, the SL algorithm is tested using SSM/I swath data obtained in the Arctic in April 1999. Results of this test which includes an intercomparison between C obtained with the SL and NT algorithms and RADARSAT-1 SAR images are shown in Section 6.2.

Chapter 2

Theoretical Basis

In this chapter, at first some fundamentals of microwave remote sensing are given in Section 2.1. Monitoring the Earth's surface from space requires the knowledge of 1.) the electromagnetic properties of the surface, of 2.) the interaction of the surface radiation with the atmosphere, and of 3.) the atmospheric radiation. Physical properties determining the microwave radiation of open water, sea ice and snow are discussed in Sections 2.2 and 2.3. The latter section includes a few aspects of sea ice growth and decay, and of snow metamorphism. This is followed by the radiation properties of the surface in Section 2.3.4. Section 2.4 focusses on atmospheric radiation and the interaction of the surface radiation with the atmosphere. Section 2.5 describes the microwave radiative transfer and the tool used to model the atmospheric influence on the SSM/I brightness temperature.

2.1 Thermal Emission

Each substance with a finite physical temperature T_a, *i. e.* with a continuous random motion of its atoms and molecules, radiates electromagnetic energy. Atomic gases emit electromagnetic energy at *discrete* frequencies and, therefore, normally exhibit line spectra. According to quantum theory, each spectral line corresponds to a transition between two atomic energy levels. The probability of these transitions and thus the emitted electromagnetic energy is proportional to the kinetic energy of the random motion and the density of the atomic gas. The kinetic energy of a substance is defined in terms of its physical temperature T_a. Accordingly, the emitted electromagnetic energy of a substance increases with T_a. Gases with molecules consisting of two or more atoms exhibit more complicated electromag-

netic spectra. Associated with a molecule is a set of additional modes describing the motion of the atoms relative to one another (*vibrational energy*) and the rotation of the whole molecule according to its degrees of freedom (*rotational energy*). The spectra associated with molecular gases often show bands rather than lines due to the much smaller frequency difference of vibrational and particularly rotational energy levels. These bands are separated by so-called *transmission windows*. Liquids and solids can be regarded as very large molecules. Therefore, they have much more degrees of freedom and a large number of adjacent spectral lines. Their radiation spectrum becomes almost continuous.

Electromagnetic energy can be absorbed by a substance if the frequency of the incident electromagnetic wave allows the transition of an electron from its actual energy level to another higher energy level. The capability of a substance to absorb and/or emit electromagnetic energy increases with the number of energy levels and allowed transitions. A *blackbody* is defined as an idealized, perfectly opaque material that absorbs electromagnetic energy at all frequencies while reflecting none. Therefore, a blackbody is also a perfect emitter. The spectral brightness of a blackbody B_f radiated uniformly in all directions is given by Planck's radiation law

$$B_f = \frac{2hf^3}{c^2}\left(\frac{1}{e^{\frac{hf}{kT_a}} - 1}\right), \tag{2.1}$$

where
B_f = Blackbody spectral brightness [$\mathrm{W\,m^{-2}\,sr^{-1}\,Hz^{-1}}$],
h = Planck's constant = 6.63×10^{-34} J,
f = Frequency [Hz],
k = Boltzmann's constant = $1.38 \times 10^{-23}\,\mathrm{J\,K^{-1}}$,
T_a = Physical temperature [K],
c = Velocity of light $\approx 3 \times 10^8\,\mathrm{m\,s^{-1}}$.

Figure 2.1 shows B_f as obtained when applying Planck's radiation law for a typical terrestric physical temperature $T_a = 300\,\mathrm{K}$ (solid line) in comparison with B_f as obtained with two possible approximations of Planck's law (dashed lines). These approximations are $\frac{hf}{kT_a} \gg 1$ (Wien's Law) at high frequencies and $\frac{hf}{kT_a} \ll 1$ (Rayleigh-Jeans' Law) at low frequencies. The wavelength associated with the maximum of B_f increases with T_a according to Wien's displacement law

$$\lambda_{max} = aT_a \tag{2.2}$$

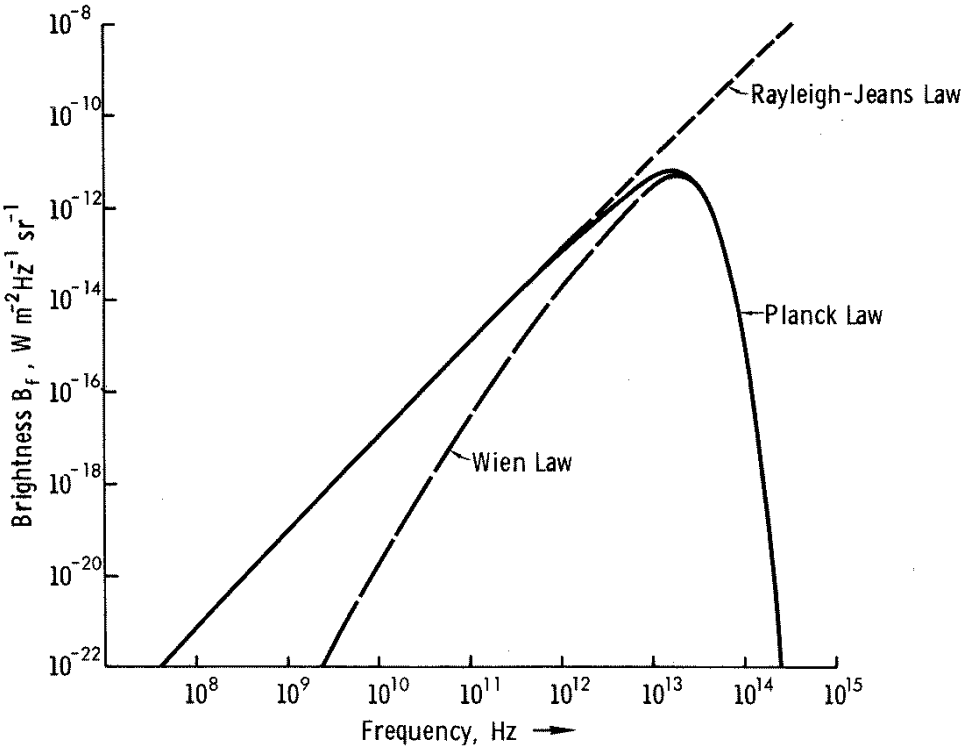

Figure 2.1: *Comparison of Planck's law with its low-frequency (Rayleigh-Jeans law) and high-frequency (Wien's law) approximations at 300 K (from [Ulaby et al., 1981].*

with the constant $a = 2.879 \times 10^{-3}\,\mathrm{m\,K^{-1}}$ and the wavelength at maximum spectral brightness λ_{max}. Thus, for the terrestrial spectral brightness, the maximum occurs at a wavelength $\lambda \approx 10\,\mu\mathrm{m}$ ($f \approx 30\,\mathrm{THz}$) in the so-called *atmospheric window* in the IR range. The Rayleigh-Jeans approximation yields

$$B_f = \frac{2f^2kT_a}{c^2} = \frac{2kT_a}{\lambda^2}, \tag{2.3}$$

and can be applied for terrestrial temperatures in the microwave (MW) range *i. e.* for $1\,\mathrm{GHz} < f < 300\,\mathrm{GHz}$ ($0.001\,\mathrm{m} < \lambda < 0.3\,\mathrm{m}$).

The brightness temperature T of a blackbody equals its physical temperature T_a. In the MW range, one can therefore write

$$T = \frac{\lambda^2}{2k} B_f. \tag{2.4}$$

Real substances are so-called *grey bodies* and emit and absorb less electromagnetic energy than a blackbody. The spectral brightness of a grey body may be direction dependent as given in spherical coordinates by the angles Θ and Φ, for instance, if some portion of the incident electromagnetic energy is reflected into a preferred direction. Furthermore, the spectral brightness may become polarized since, as soon as reflection and scattering takes place, the vector of the electric field may oscillate in a preferred plane relative to the propagation direction of the incident electromagnetic wave. This leads to the brightness temperature of a grey body at polarization p observed at direction Θ, Φ

$$T(\Theta, \Phi, p) = \frac{\lambda^2}{2k} B_f(\Theta, \Phi, p). \tag{2.5}$$

The ratio of the brightness temperatures of a grey body and of a blackbody is called the emissivity

$$\epsilon_f(\Theta, \Phi, p) = \frac{B_f(\Theta, \Phi, p)}{B_f} = \frac{T(\Theta, \Phi, p)}{T}. \tag{2.6}$$

The emissivity of a blackbody is 1, regardless of frequency, observation angle and polarization. Grey bodies emit or absorb less electromagnetic energy than a blackbody, *i. e.* $B_f(\Theta, \Phi, p) \leq B_f$, and their emissivity $\epsilon_f(\Theta, \Phi, p)$ is always less than 1. However, for grey bodies, emission and absorption depend on the frequency. Therefore, they may behave like a blackbody over a certain frequency range. For instance, the emissivity of water is 0.95 in the IR range but less than 0.1 in the VIS range (see Table 2.1).

The main quantity describing the interaction of electromagnetic radiation with a substance is the *relative complex dielectric constant* ε:

$$\varepsilon = \varepsilon' - i\varepsilon''. \tag{2.7}$$

The real part of ε is the so-called *permittivity* ε' which is related to the refraction index n by

$$n = \sqrt{\varepsilon'}. \tag{2.8}$$

The imaginery part of ε, ε'', is proportional to the dielectric loss γ given by

$$\gamma \propto \frac{f}{n} \varepsilon''. \tag{2.9}$$

Considering these two relations, the relative complex dielectric constant ϵ is a measure of the frequency dependend electric conductivity, which is a function

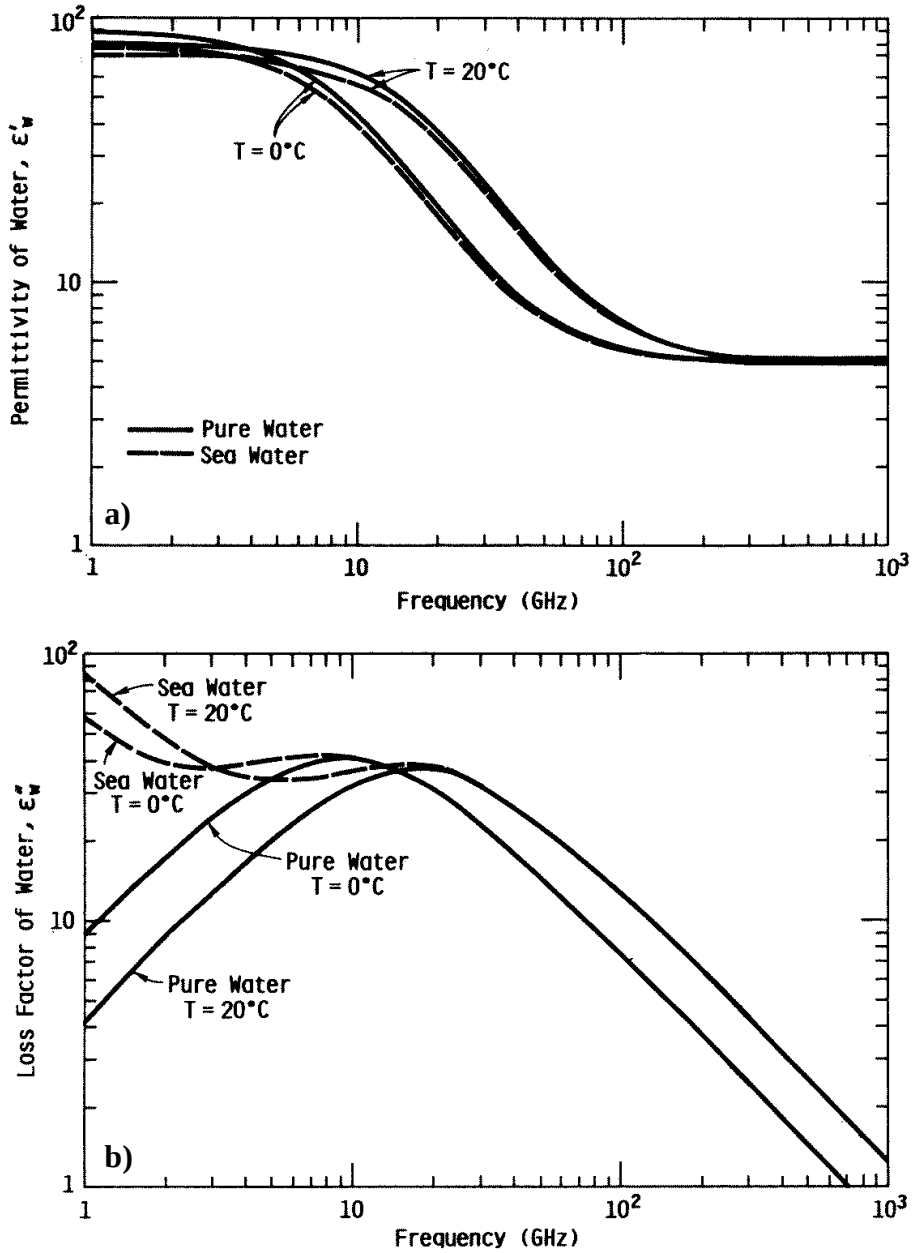

Figure 2.2: *Complex dielectric constant of pure water and sea water versus frequency for 0 °C and 20 °C and a salinity of sea water of 32.54 ‰:* **a)** *real part,* **b)** *imaginery part (from [Ulaby et al., 1986]).*

of temperature and degree of polarity of the molecules. In the MW range, for a polar molecule such as of water, ε typically ranges between 5 and 200 and is significantly influenced by its salinity and its physical temperature. Figure 2.2 shows ε' and ε'' as a function of frequency and temperature for pure and saline water.

In case of a substance with a *specular* surface, emission and reflection can be described by the Fresnel reflection coefficients $\Gamma(\theta, v)$ and $\Gamma(\theta, h)$ at vertical (v) and horizontal (h) polarization. These coefficients relate the electromagnetic properties of the substance, which are given by ε and the relative permeability μ, to the local incidence angle θ (= angle between the surface normal and the viewing direction):

$$\Gamma(\theta, h) = \left| \frac{\mu \cos\theta - (\mu\varepsilon - \sin^2\theta)^{\frac{1}{2}}}{\mu \cos\theta + (\mu\varepsilon - \sin^2\theta)^{\frac{1}{2}}} \right|^2 \tag{2.10}$$

$$\Gamma(\theta, v) = \left| \frac{\varepsilon \cos\theta - (\mu\varepsilon - \sin^2\theta)^{\frac{1}{2}}}{\varepsilon \cos\theta + (\mu\varepsilon - \sin^2\theta)^{\frac{1}{2}}} \right|^2 . \tag{2.11}$$

Equations 2.10 and 2.11 yield the emissivities via $\epsilon_v(\theta) = 1 - \Gamma(\theta, v)$ and $\epsilon_h(\theta) = 1 - \Gamma(\theta, h)$ according to Kirchhoff's energy conservation law.

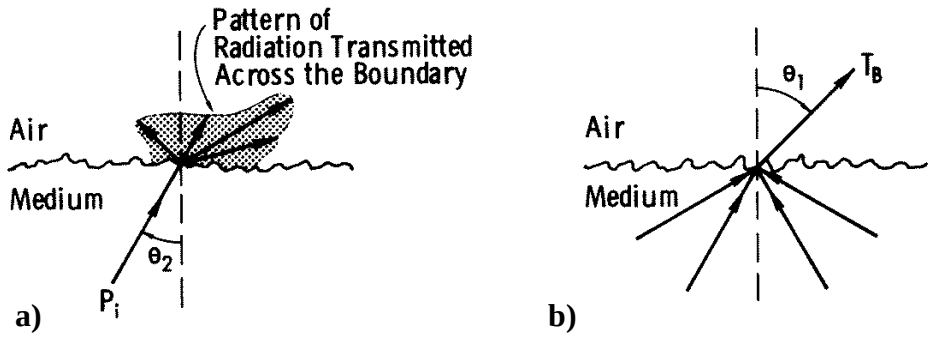

Figure 2.3: *Emission of a substance with a surface roughness scale which is similar to the wavelength at the frequency of observation:* **a)** *diffuse emission,* **b)** *contributions to the brightness temperature* T_B *observed under the angle* Θ_1 *(from [Ulaby et al., 1981]). In* **a)**, P_i *is the power incident on the surface under the angle* Θ_2 *from the underlying medium.*

Emission and reflection of electromagnetic radiation at a *rough* surface is much more complex. Figure 2.3 shows that **a)** a substance with a rough surface may emit electromagnetic energy into many different directions and that **b)** the observed brightness temperature may consist of many contributions incident at the surface from inside the substance under different angles. The emissivity of such a substance can be described using the bistatic scattering cross-section per unit area (surface scattering coefficient) $\sigma^o(\theta_i, \theta_s, p_i, p_s)$. This coefficient relates the power incident under the direction θ_i at polarization p_i to the power scattered into the direction θ_s at polarization p_s. According to Peake [1959], the corresponding emissivity can be expressed by

$$\begin{aligned} \epsilon(\theta_i, h) &= 1 - \frac{1}{4\pi \cos\theta_i} \int [\sigma^o(\theta_i, \theta_s, h, h) \\ &+ \sigma^o(\theta_i, \theta_s, h, v)] d\Omega_s \end{aligned} \tag{2.12}$$

$$\begin{aligned} \epsilon(\theta_i, v) &= 1 - \frac{1}{4\pi \cos\theta_i} \int [\sigma^o(\theta_i, \theta_s, v, v) \\ &+ \sigma^o(\theta_i, \theta_s, v, h)] d\Omega_s. \end{aligned} \tag{2.13}$$

The integration is carried out over the upper half space. The second term of Equations 2.12 and 2.13, respectively, denotes the contribution from incoherent scattering.

2.2 Open Water

In the MW range, mainly three parameters influence emission, absorption and reflection of electromagnetic radiation over open water:

- the sea surface salinity S,
- the sea surface temperature (SST),
- the sea surface roughness and its coverage with foam and whitecaps.

The surface salinity and the SST are distributed homogeneously when concerning the FOV of the SSM/I (Section 3.1.2). In the Southern Ocean, values of $33.5\,‰ < S < 34.5\,‰$ and $-2°\mathrm{C} < T < +2°\mathrm{C}$ [Olbers et al., 1992] are common. The

sea surface roughness and foam coverage is caused by the ocean swell and the local influence of the surface wind which can vary on scales of a few meters within some seconds. However, the SSM/I integrates over FOV areas between $\approx$ 200 km^2 at 85 GHz and $\approx$ 3000 km^2 at 19 GHz (Section 3.1.2). Hence, its measurements reflect the average surface roughness of a local- to mesoscale area.

2.2.1 Radiative Properties of Open Water

The SST and the salinity S are sufficient to describe the interaction of microwave radiation with open water. Ulaby et al. [1986] (Figures 18.4 a,b) show that for saline sea water the penetration depth, *i. e.* the depth where the intensity of the incident electromagnetic energy has decreased to I_0/e (I_0 = incident intensity), is always less than 1 cm in the MW range and, in particular, less than 1 mm at the SSM/I frequencies (see Section 3.1.2).

Dissolved salts increase the ionic conductivity and alter the relative complex dielectric constant ε of water, which decreases with frequency above 10 GHz as is shown in Figure 2.2. The permittivity ε' is almost independent of S for values typical of sea water. The imaginary part ε'' is dominated by the ionic conductivity and, therefore, depends on S at frequencies below 3 GHz. At frequencies above 10 GHz, the Debye relaxation becomes the dominating process and ε'' is independent of S (see Figure 2.2). In conclusion, at the SSM/I frequencies the sea surface emissivities are nearly independent of S. But the sea surface emissivities increase with frequency due to the decrease of ε' and ε''.

The penetration depth approaches zero with increasing frequency [Ulaby et al., 1986]. Therefore, one can expect an increase of the sensitivity of the brightness temperature T_p at polarization p to the SST; that is $Q_{SST} = \frac{\partial T_p}{\partial T}$, p refers to vertical or horizontal polarization. Between 19 and 37 GHz Q_{SST} decreases from 0.25 to 0.11 at vertical and from 0.08 to -0.06 at horizontal polarization, respectively [Ulaby et al., 1986]. Extrapolating these trends towards higher frequencies, one can conclude that at 85 GHz Q_{SST} decreases to zero at vertical polarization and approaches -0.2 at horizontal polarization. This would lead to a decrease of the horizontally polarized 85 GHz SSM/I brightness temperature by 1 K for an increase of the SST by 5 K (compare Figure 18.13 b, [Ulaby et al., 1986]). Taking into account the sensor noise at 85 GHz (see Table 3.2) and the small variability of the SST of the polar Southern Ocean, this brightness temperature decrease can be neglected.

A water surface is highly polarizing. Therefore, the Fresnel reflection coefficients (Equations 2.10 and 2.11) show considerable differences at both polariza-

tions for incidence angles $\theta < 90\,^{\circ}$. Over a calm sea surface, for instance, $\Gamma(\theta, h)$ increases monotonically over the entire range of θ while $\Gamma(\theta, v)$ first decreases monotonically until θ equals the Brewster angle and then increases rapidly with θ [Schanda, 1986]. The Brewster angle α_B is related to the refraction index n (see Equation 2.8) by

$$\tan \alpha_B = n \tag{2.14}$$

and varies between 66.5 ° at 100 GHz and 83.5 ° at 1 GHz for sea water with a SST of 0°C. Therefore, the SSM/I viewing angle of approximately 53° ensures quite a large reflectivity polarization difference and thus emissivity polarization difference $\Delta\epsilon = \epsilon_v - \epsilon_h$ with values between 0.2 and 0.25 at the SSM/I frequencies over a smooth water surface [Comiso et al., 1992]. However, in contrast to the VIS/IR range, at the microwave frequencies the wind-induced sea surface roughness influences the emissivity of the sea surface strongly.

Without foam, two roughness scales can be identified on a wind-roughened sea surface. The first and larger scale is described by large-scale gravity waves with radii of curvature larger than the wavelength of observation. The second scale is associated with very short-scale gravity waves or capillary waves with radii of curvature comparable to that wavelength. This scale is particularly important in regions, where a limited fetch hampers the development of large-scale gravity waves as, for instance, in leads and polynyas. The emissivity of such a perturbed surface can be computed with a facet-model and modified Fresnel reflection coefficients together with a sea surface spectrum which gives the probabilities of the occurences of the sea surface slope as a function of the wind speed [Ulaby et al., 1986]. The modified Fresnel reflection coefficients explain the energy transfer from the large-scale to the small-scale surface roughness. By using the slope variance relations given by Cox and Munk [1954], Ulaby et al. [1986] have found that at 19 GHz, vertical polarization, and the SSM/I viewing angle the emissivity is almost independent of the wind-induced roughness of a foam-free sea surface. At 19 GHz and horizontal polarization, however, the emissivity is most sensitive to this roughness. This fact has been exploited to infer the surface wind speed V from SMMR and SSM/I data ([Swift, 1980], [Goodberlet et al., 1989], [Chang and Li, 1998], see also Section 3.2.1).

With foam, a third scale comes into play. Foam can appear in form of streaks and patches aligned along the surface wind direction and as whitecaps forming on the wave crests. According to Ross and Cardone [1974], both forms may together cover one third of the open ocean at wind speeds over 20 m s^{-1}. Foam can be

considered as a water layer with entrapped air bubbles, thus as a mixture of air and saline water with its associated dielectrical properties. Bursting air bubbles adjacent to the water surface increase the small-scale surface roughness. The reflectivity of an open water facet with a whitecap fraction C_{wc} and a foam streak fraction C_{fs} ($C_{wc} + C_{fs} \leq 1$) is given by

$$\begin{aligned} \Gamma(\theta, p) &= \Gamma_{ff}(\theta, p)(1 - C_{wc} - C_{fs}) \\ &+ \Gamma_{wc}(\theta, p)C_{wc} \\ &+ \Gamma_{fs}(\theta, p)C_{fs}. \end{aligned} \tag{2.15}$$

At the viewing angle θ and at vertical v or horizontal h polarization p, the reflection coefficients of foam-free water, whitecaps and foam streaks are denoted by $\Gamma_{ff}(\theta_1, p)$, $\Gamma_{wc}(\theta_1, p)$ and $\Gamma_{fs}(\theta_1, p)$, respectively. Above a foam layer, incoherent reflection dominates [Ulaby et al., 1986] resulting in an asymptotically increase of the emissivity of foam-free water to that of completely foam-covered water.

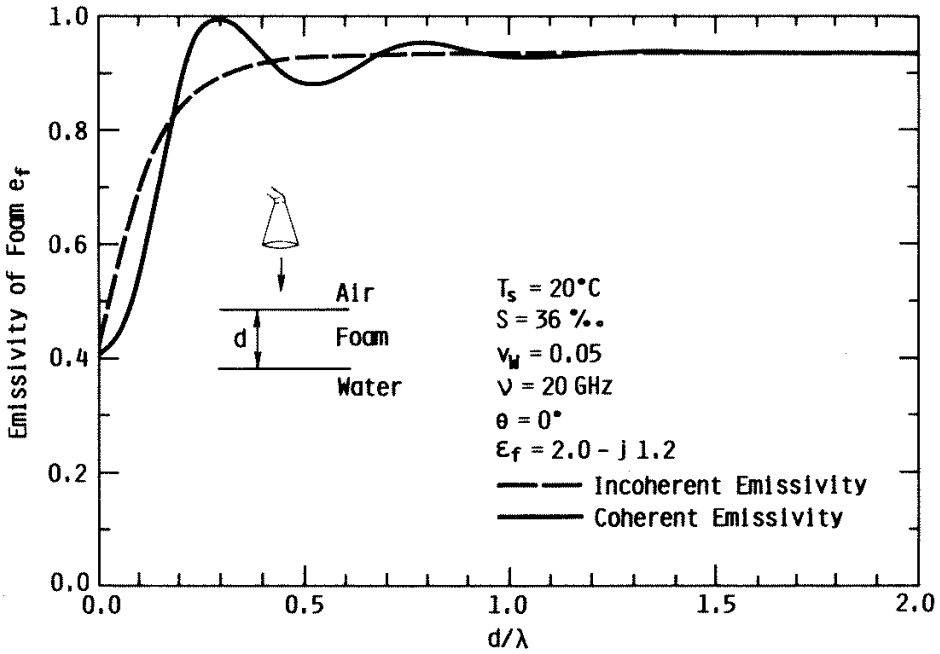

Figure 2.4: *Variation of the emissivity of foam over open water as a function of the foam-layer thickness d in units of λ (from [Ulaby et al., 1986]).*

Figure 2.4 shows the emissivity increase due to foam at a frequency of 20 GHz as a function of the foam-layer thickness. At this frequency, the emissivity increases from ≈ 0.42 over foam-free open water to ≈ 0.92 over a foam layer with a thickness $\geq \lambda$. This was confirmed by airborne brightness temperature measurements taken nadir-looking at 19 GHz by Ross et al. [1970] and Nordberg et al. [1971].

In contrast to a calm sea surface, brightness temperatures measured over a foam cover decrease with the viewing angle at *both* polarizations. Consequently, the brightness temperature polarization difference is significantly smaller over a foam-covered than over a foam-free sea surface [Stogryn, 1972]. Moreover, the smaller wavelength at 85 GHz suggests a higher sensitivity to the foam cover compared to the other SSM/I channels. Above a partly foam-covered sea surface, the 85 GHz brightness temperatures increase with surface wind speed by an amount similar to that at 37 GHz and larger than that at 19 GHz ([Fuhrhop et al., 1998] and Section 5.3.1).

The radiative transfer model used in this thesis (Section 2.5.1) considers all three surface roughness scales and can therefore be expected to model the brightness temperatures above open water realistically.

2.3 Sea Ice and Snow

Unlike the open ocean, which – if neglecting surface wind effects – exhibits only two surface properties relevant to microwave remote sensing, sea ice has a few more properties that determine its interaction with and the emission of microwave radiation. This section starts with an overview over mechanisms of sea ice growth and decay as well as snow cover metamorphism before concentrating on the physical sea ice and snow properties relevant for microwave remote sensing of the sea ice.

2.3.1 Sea Ice Types and Initial Ice Growth

The structural and physical properties of sea ice have been investigated by many authors [Lange and Eicken, 1991], [Jeffries and Weeks, 1992], [TuckerIII et al., 1992], [Eicken et al., 1994], [Jeffries et al., 1994], [Worby et al., 1998], [Eicken, 1998]. In contrast to other constituents of the cryosphere, sea ice is saline. The structure of sea ice can be regarded as a mixture of ice crystals, brine and air,

and is determined by the conditions during the sea ice growth as well as by the interaction of the sea ice with the ocean, the atmosphere and its snow cover.

Important for the understanding of the freezing process of sea water are two facts:

- Salt depresses the freezing point of water [Neumann and Pierson, Jr., 1966].
- Pure water $S = 0\,‰$ has its highest density at $+4°\mathrm{C}$. For salinities $0 < S \leq 24.7\,‰$, highest density occurs between $+4°\mathrm{C}$ and the freezing point according to the actual salinity. For salinities larger than $24.7\,‰$, the highest density is formed at the freezing point.

In polar regions, sea water exhibits a freezing point of $-1.8°\mathrm{C}$ at a typical salinity of $\approx 34\,‰$. At this salinity, cooling results in an unstable vertical density distribution over the first ten meters of the sea water column. This leads to convective overturning of the water until the entire water column involved is at its freezing point. Continued cooling results in the formation of saline ice platelets and needles (*frazil ice*). A layer comprising a mixture of frazil ice and sea water (*grease ice*) develops. Under quiet conditions, *i. e.* at low wind speeds and in the absence of ocean swell, continued cooling increases the frazil ice fraction until the ice crystals coalesce to a smooth, elastically behaving, saline sea ice cover of up to 3 cm thickness (*nilas*). This sea ice cover becomes thicker under favourable cold and quiet conditions to form the young ice types *grey ice* (4 to 6 cm) and *grey-white ice* ($\geq$ 10 cm), and finally reaches the state of *first-year ice* (FY ice) at a thickness above 30 cm – according to the sea ice type nomenclature of the World Meteorological Organization (WMO) [1989]. Under the action of wind and ocean swell, semi-consolidated masses of frazil ice are formed to so-called *pancake ice*. These pancake ice floes can have diameters between 0.3 and 3 m, can be several centimeters thick, and often exhibit higher rims at their margins caused by continuous collisions of single floes under the wave action. Pancake ice can either consolidate together with the grease ice between the floes to build an ice sheet continuing to grow like the above-mentioned young ice types. Or it becomes thicker due to rafting of the floes under on-going wave action and without consolidation.

The main process for sea ice to gain thickness under quiet conditions is *congelation growth* underneath the sea ice as has been discussed by several authors [Lange and Eicken, 1991], [Jeffries and Weeks, 1992], [Jeffries et al., 1994]. Frazil ice crystals become attached at the bottom of the sea ice, which then starts to grow vertically into the water until equilibrium between heat loss and gain is

achieved. The equilibrium and the growth rate depend on the heat supply by the ocean and on the heat loss to the atmosphere at the sea ice surface, which in turn depends on the air temperature, the wind speed, and the thickness and composition of a snow cover.

During the freezing process, saline water is entrapped in the sea ice in so-called *brine pockets* forming between the vertically aligned frazil ice crystals. The brine salinity depends on the phase equilibrium of brine, thus on its temperature. At a given temperature only a certain amount of brine can coexist with ice. Decreasing temperatures will disturb the phase equilibrium and cause freezing on the pocket walls which is accompanied by salt rejection into the brine. Therefore, a salinity increase will result until the phase equilibrium is reached again [TuckerIII et al., 1992]. This process is associated with a pocket volume decrease and a pressure increase inside the brine pockets eventually forcing brine to be expelled out of the pockets through fine cracks in the sea ice – one mechanism for the desalination of sea ice. The opposite is true for rising temperatures. The major mechanism for desalination is the drainage of colder, thus denser brine from the upper sea ice layers through brine channels into warmer sea ice layers where the brine is less dense – the so-called *gravity drainage*. Consequently, the bulk salinity of sea ice

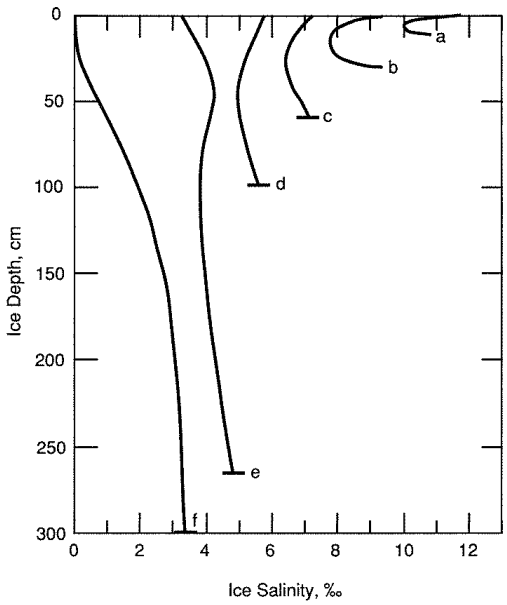

Figure 2.5: *Idealized sea ice salinity profiles: a) to d) FY ice, e) and f) MY ice (from [TuckerIII et al., 1992]).*

depends on its temperature, which in turn is a function of the oceanic heat supply, of the thickness of both the sea ice and the snow cover. Thin ice is often covered by a layer of highly saline brine that has been expelled up onto the surface by capillary effects.Figure 2.5 shows some idealized vertical salinity profiles of different sea ice types. All FY ice profiles outline the typical C-shape.

The vertical temperature profile in sea ice depends strongly on the snow-cover thickness and the season. A negative temperature gradient with temperatures around $-1.8°C$ at the bottom of the sea ice and considerably lower temperatures at its surface is observed during winter. During summer, the sea ice may be isothermal at a temperature of $-1.8°C$ or may exhibit a slightly positive temperature gradient, with a temperature of $-1.8°C$ at the bottom of the sea ice and approximately $0°C$ at its surface [TuckerIII et al., 1992], [Perovich et al., 1998].

2.3.2 Hemispherical Differences and further Ice Growth

Antarctica and the Arctic show a very different geography. While the Arctic Ocean is surrounded by land masses, the Southern Ocean is part of the world oceans as is shown in Figure 2.6. The water exchange of the Arctic Ocean with the oceans at lower latitudes is much more limited than that of the Southern Ocean. As a consequence, the Arctic ocean is much more stratified than the Southern Ocean, hampering the heat exchange between the surface mixed layer and the wa-

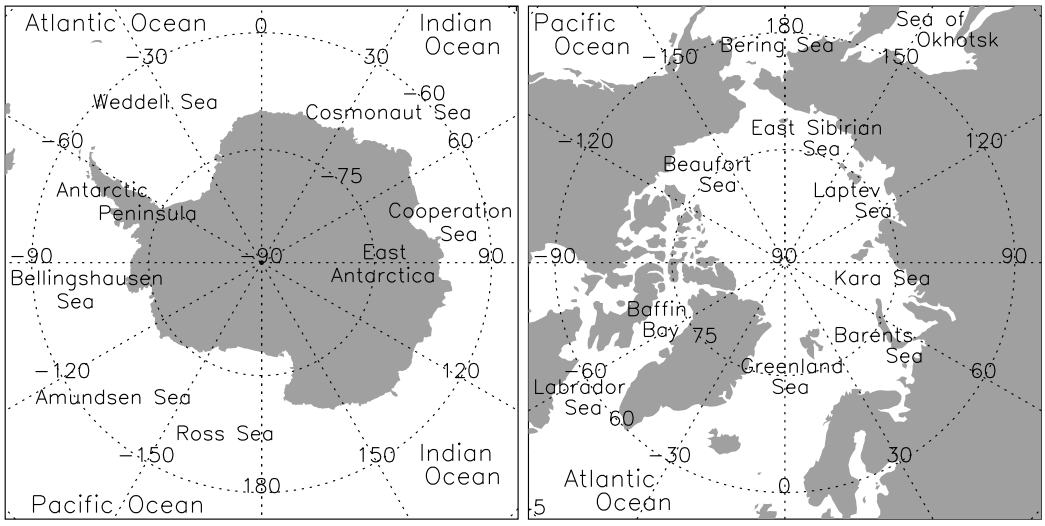

Figure 2.6: *Maps of* **a)** *the Antarctic and* **b)** *the Arctic.*

ter masses below the thermocline. Furthermore, ocean swell can penetrate into the sea ice as far as 600 km [Squire et al., 1986], [Worby et al., 1998] along the entire Antarctic sea ice edge. In the Arctic, only the sea ice in the marginal seas, which are the Bering, Labrador, Barents and Greenland Seas as well as the Sea of Okhotsk (see Figure 2.6), is influenced by ocean swell once the Arctic Ocean is frozen.

The continents surrounding the Arctic Ocean shield this area almost completely from storms during winter. Only the marginal seas are more often overpassed by cyclones. In contrast, cyclones move frequently over polar Southern Ocean during the entire year and may penetrate into the sea ice covered area as far as 1000 km [Andreas, 1984], [Massom et al., 1997]. Due to the large moisture supply by the surrounding open water of the Southern Ocean and the large air temperature gradient across the sea ice edge, cyclones are more vigorous and yield more precipitation in Antarctica than in the Arctic [King and Turner, 1997]. Finally, the underwater topography of the Southern Ocean together with the ocean currents can cause up-welling of warmer water masses and sea ice melt even in Austral winter, for instance, in the region of Maud-Rise [Zwally et al., 1985].

In the light of these conditions, one can easily explain the main differences of growth and characteristics of Arctic and Antarctic sea ice. Periods without ocean swell and with low wind speeds are seldom in the Antarctic. Consequently, in the Antarctic sea ice formation takes place in the so-called *pancake cycle* as proposed by Lange et al. [1989]. According to their work and the investigations of Wadhams et al. [1987], frazil and pancake ice forms as soon as air temperatures fall below $-1.8°$C. Once the sea surface is covered by a frazil/pancake ice mixture, sea ice formation ceases or remains at equilibrium because the lack of open water and the usually large vertical heat flux between the ocean and the atmosphere inhibits further sea ice growth. Open water generated by redistribution and rafting of the pancake ice floes is covered soon by a frazil/pancake ice mixture again. Congelation growth at the bottom of the floes is almost negligible [Lange and Eicken, 1991]. This process lasts until either ocean swell cannot penetrate far enough into the sea ice or if the wave energy is too small to generate new open water areas. At this point, the floes have gained a thickness of 40 to 60 cm and may consist of several frazil and granular ice layers [Wadhams et al., 1987]. This is followed by consolidation of the pancake ice floes to a solid sea ice cover and further growth at its bottom.

In the Arctic, sea ice grows under quieter conditions in terms of ocean swell and surface wind speed, resulting in a larger fraction of thin ice types such as nilas and grey ice at the beginning of ice formation. Moreover, the marked strat-

ification of the Arctic Ocean between 50 and 150 m results in very low vertical diffusion rates in the upper water column and prevents winter convection and surface mixed layer deepening greater than ≈ 50 m. The underlying warmer layer of Atlantic water masses are effectively insulated [Aagaard and Carmack, 1994]. This environment limits the mean oceanic heat flux to values around $5\,\mathrm{W\,m^{-2}}$ [Mellor and Häkkinen, 1994] and allows thick sea ice to grow. In the Antarctic, the mean oceanic heat flux is comparably larger (up to $\approx 40\,\mathrm{W\,m^{-2}}$ [McPhee and Martinson, 1994]), thus limits the sea ice thickness.

A snow cover can influence the sea ice thickness in a twofold manner. On the one hand, a thick snow cover insulates sea ice from both cold and warm air, decreasing the growth or melt rate [Eicken et al., 1995], [Massom et al., 1998]. On the other hand, snow can increase the sea ice thickness by flooding of the snow-ice interface followed by the formation of *snow ice*, or by melt water percolating the snow and refreezing at the snow-ice interface to form *meteoric ice*. Snow and meteoric ice contribute between 13 and 40 % to the sea ice mass of the Southern Ocean [Eicken et al., 1994], [Worby et al., 1996], [Worby et al., 1998]. Major reasons for flooding are hydrostatic imbalance [Adolphs, 1998] and the break-up of a consolidated sea ice cover because of ocean swell. Both processes are less frequent in the Arctic due to the different geography preventing ocean swell to penetrate deeply into the sea ice, and due to the smaller precipitation amounts combined with thicker sea ice making flooding a seldom event.

The sea ice thickness can also change in areas or periods of convergent and divergent sea ice motion. The strong and persistent cold katabatic winds, which join the easterly winds south of the Antarctic divergence [King and Turner, 1997], generate polynyas along almost the entire Antarctic coast. Frazil and grease ice forming in these polynyas during Austral winter is continuously advected to their leeward side, where it consolidates quickly to nilas and thicker ice types. This sea ice is slowly carried away from the coast by the coriolis deflection associated with the prevailing easterly winds. The sea ice formed in these coastal polynyas contributes a large fraction to the Antarctic sea ice cover. For this reason, coastal polynyas are often referred to as “ice factories”. Along the Antarctic coast, divergent sea ice motion dominates with only a few exceptions. The western Weddell Sea, for instance, is known as an area where sea ice is continuously pushed towards the coast of the Antarctic Peninsula. This convergent motion results in an increasing internal ice stress that causes rafting and ridging of the sea ice. Consequently, largest Antarctic sea ice thicknesses are reported from this area [Massom et al., 1997].

Sea ice areas that are frequently overpassed by cyclones exhibit alternating

convergent and divergent conditions associated with warm, northerly winds at the front side and cold, southerly winds at the back side of the cyclones, respectively. During convergent conditions, a consolidated sea ice cover may breakup due to the enhanced internal ice stress. Rafting and ridging may occur. Higher temperatures can cause a weakening of the physical strength of the sea ice due to larger brine volumes. The sea ice edge may retreat considerably depending on sea ice type and concentration, while the marginal ice zone (MIZ) becomes more compact. During divergent conditions, new open water areas are generated and covered with new ice according to the pancake cycle. The sea ice edge advances and becomes diffuse. The physical strength of the sea ice increases due to smaller brine volumes caused by the lower temperatures. Figure 2.7 summarizes some of the above-mentioned processes.

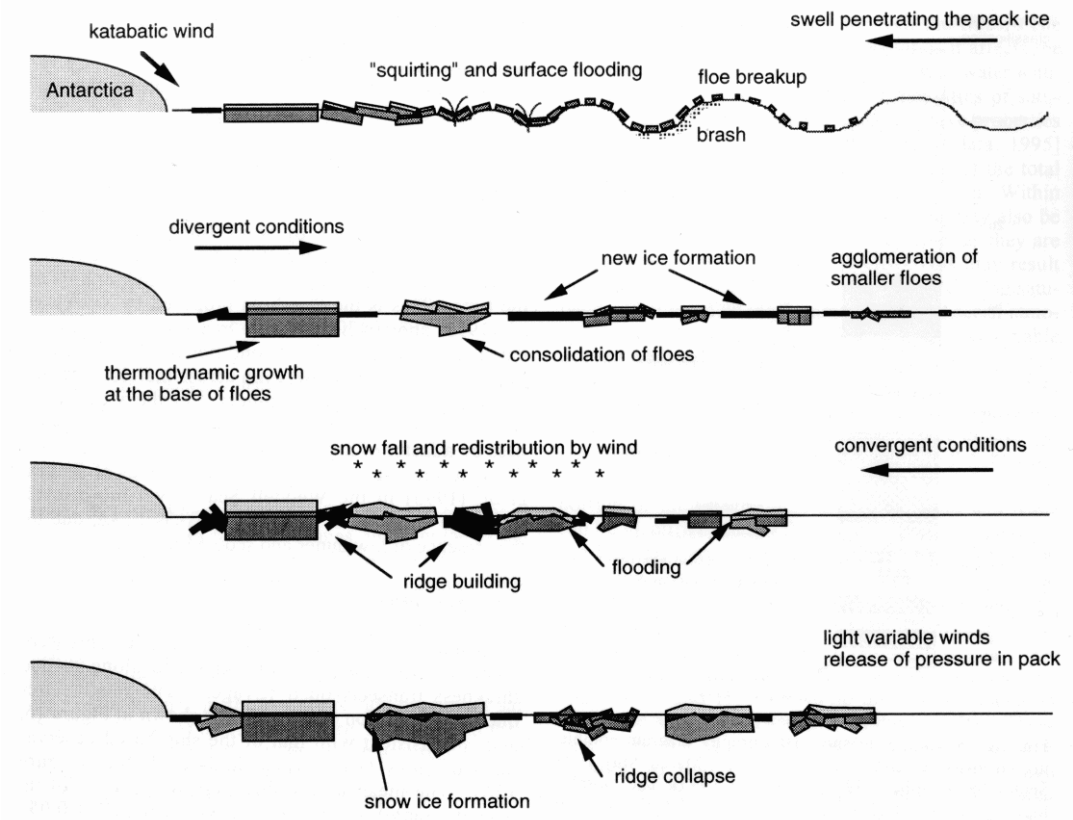

Figure 2.7: *Schematic sketch of possible interactions and processes of Antarctic sea ice (from [Worby et al., 1998]).*

Therefore, Antarctic environmental conditions force maximum thicknesses of FY ice of approximately 70 cm in the central and eastern Weddell Sea ([Wadhams et al., 1987], [Lange and Eicken, 1991] as well as in the Pacific Sector [Adolphs, 1998] and slightly less in the East Antarctic region [Worby et al., 1998]. In the Arctic, environmental conditions favour undisturbed sea ice growth leading to FY ice thicknesses up to 200 cm [TuckerIII et al., 1992], [Perovich et al., 1998] and to quite a high fraction of *columnar* or *congelation* ice. Investigations of Antarctic sea ice cores by Eicken et al. [1994], Jeffries [1998] and Worby et al. [1998] have revealed a fraction of congelation ice of approximately one third. The rest is of *granular* type, *i. e.* originates from the pancake cycle and other ice growth mechanisms. Between 13 and 40 % of the cores investigated show granular textures typical for snow ice and/or meteoric ice. Figure 2.8 shows one example of each, columnar and granular ice.

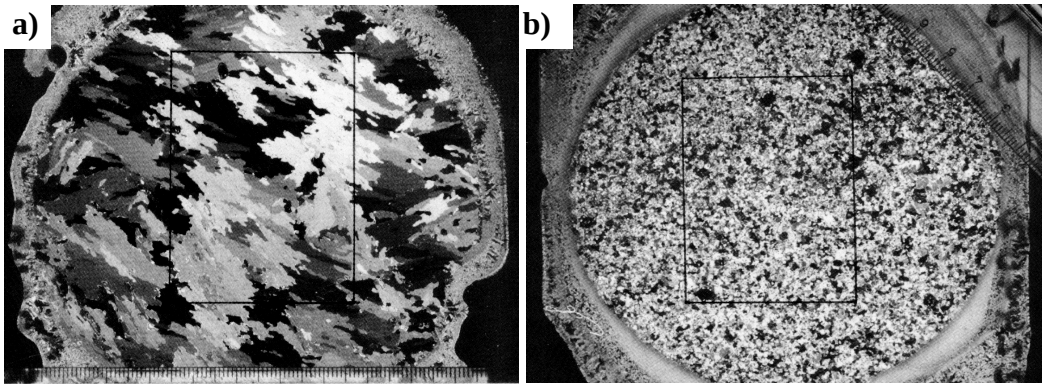

Figure 2.8: *Horizontal thin sections of* **a)** *columnar ice and* **b)** *granular ice. The photographs have been taken between cross polarizers; the scale bar (***a)***: bottom edge,* **b)***: upper right corner) is in millimeters (from [Eicken et al., 1990]).*

A snow cover effectively insulates sea ice from melting from the top. In the Arctic, however, the snow cover disappears rapidly within a few weeks in May/June [TuckerIII et al., 1992] while Antarctic sea ice remains snow-covered during summer due to a significantly smaller number of melt-days [Drinkwater and Liu, 2000]. This is again caused by the different geography. During spring/summer land and consequently the air heats up quickly once the snow cover has disappeared. In contrast, air heats up very slowly over water because of the much larger heat capacity of water. Therefore, air masses advected into the Arctic in late spring/early summer are considerably warmer than in the Antarctic and lead to enhanced melting of the snow cover and the sea ice from the top. Melt ponds

form and can cover more than $50\,\%$ of the sea ice. Brine pockets widen due to the higher temperatures and weaken the sea ice cover until it breaks up under physical stress along its weakest parts. These are usually cracks and leads formed during the last winter. Melt water drains quickly from the floes, exposing a porous sea ice surface. Most brine pockets above the freeboard level become now air pockets. At the beginning of the following freeze-up these air pockets remain trapped in the sea ice, which becomes *second-year* (SY) ice. If this sea ice survives the next summer it becomes *multiyear* (MY) ice. Both, SY and MY ice will be called *old* ice, henceforth. Due to the larger number of air pockets, the average density of old ice ($\approx 0.87\,\mathrm{g\,cm^{-3}}$) is smaller than that of FY ice ($\approx 0.92\,\mathrm{g\,cm^{-3}}$). Old ice can exhibit densities as low as $0.7\,\mathrm{g\,cm^{-3}}$ in its upper part.

However, a snow cover cannot insulate sea ice from melting from the bottom, which is common in the Antarctic becoming increasingly effective when air temperatures are too high to allow the formation of snow ice and meteoric ice. As a result, the Antarctic sea ice cover starts to decay rapidly in November/December in almost the entire Southern Ocean although average air temperatures remain below $0°\mathrm{C}$ [Drinkwater and Liu, 2000] and although the sea ice is still snow-covered. Only in areas with an above-average sea ice thicknesses, the sea ice survives Austral summer and becomes old ice. Large sea ice thicknesses occur in

- the western Weddell Sea because of ridging and rafting,
- the Pacific Sector due to enhanced snow/meteoric ice growth caused by a large snow accumulation,
- coastal embayments or regions where the westbound coastal current bends away from the coast because of grounded ice bergs or glacier ice tongues (*e. g.* near Syowa Station (70°S, 40°E) and the Drygalski Ice Tongue (75°S, 165°E)), where the sea ice can grow more undisturbed.

The Weddell Sea is known to be the site of the largest amount of old ice in the Southern Ocean. However, this sea ice seldomly becomes older than two or three years since it is continuously advected by the Weddell Gyre along the Antarctic Peninsula northwards into warmer waters where it melts. Therefore, in the Antarctic old ice is on average younger than in the Arctic and can be expected to have larger salinities. According to Eicken [1998] the desalination process during summer rather than the sea ice age determines the salinity of old ice. He has found average salinities of FY ice to be quite similar in both hemispheres. However, considerably larger salinities are observed for old ice in the Antarctic compared to

the Arctic. This can be explained by the different melt conditions forcing Arctic sea ice to melt from the top while Antarctic sea ice melts from the sides and from below. Consequently, much more melt water percolates Arctic sea ice flushing out the salt. Therefore, the salinity profiles given in Figure 2.5 for MY ice are less valid for Antarctic conditions.

2.3.3 Snow Properties

The snow cover on sea ice is not only important because of its influence on the sea ice itself, but because it considerably affects the microwave radiances obtained at frequencies above 85 GHz. Antarctic sea ice is frequently overpassed by cyclones giving rise to precipitation, usually snow, allowing quite a large amount of snow to be accumulated on the sea ice during the entire year. Average Antarctic snow depths vary between 7 and 40 cm [Markus and Cavalieri, 1998], [Sturm et al., 1998], [Worby et al., 1998]. The largest snow amount is found on old ice. In the Arctic, precipitation and, therefore, snow accumulation on sea ice is almost negligible between November and May, except in the marginal seas. However, during freeze-up in September/October quite a high amount of snow may be deposited on Arctic sea ice. Snow depths range from 5 to 15 cm in the central Arctic to up to 40 cm on old ice east of Greenland [TuckerIII et al., 1992]. Despite the smaller precipitation amount, Arctic snow depths are quite similar to Antarctic snow depths. This can be explained by a larger snow portion being transformed into snow ice or meteoric ice due to the larger probability of flooding in the Antarctic.

Besides the depth, a snow cover is characterized by its *salinity*, *liquid water fraction*, *density*, and *grain size and shape plus orientation*. Typical ranges for these properties and the physical processes associated with snow metamorphism have been published by numerous authors [Akitaya, 1974], [Marbouty, 1980], [Massom et al., 1997], [Sturm et al., 1998]. Figure 2.9 shows typical vertical distributions of selected snow properties of snow on sea ice in the Pacific Sector. The snow salinity is mainly determined by the properties of the sea ice and the snow-cover thickness. Generally, larger salinities are found at the basal snow layers (see Figure 2.9 **b.**). On thin ice, this is caused by brine expulsion into the snow-ice interface during cold air temperatures. In case of a broken sea ice cover such as pancake ice, large salinities are caused by the infiltration of sea water at the floe margins. Thick sea ice such as Antarctic old ice may exhibit a highly saline, slushy basal snow layer which is often covered by dry snow [Drinkwater and Lytle, 1997]. The slushy layer can be caused by both flooding of the snow-ice

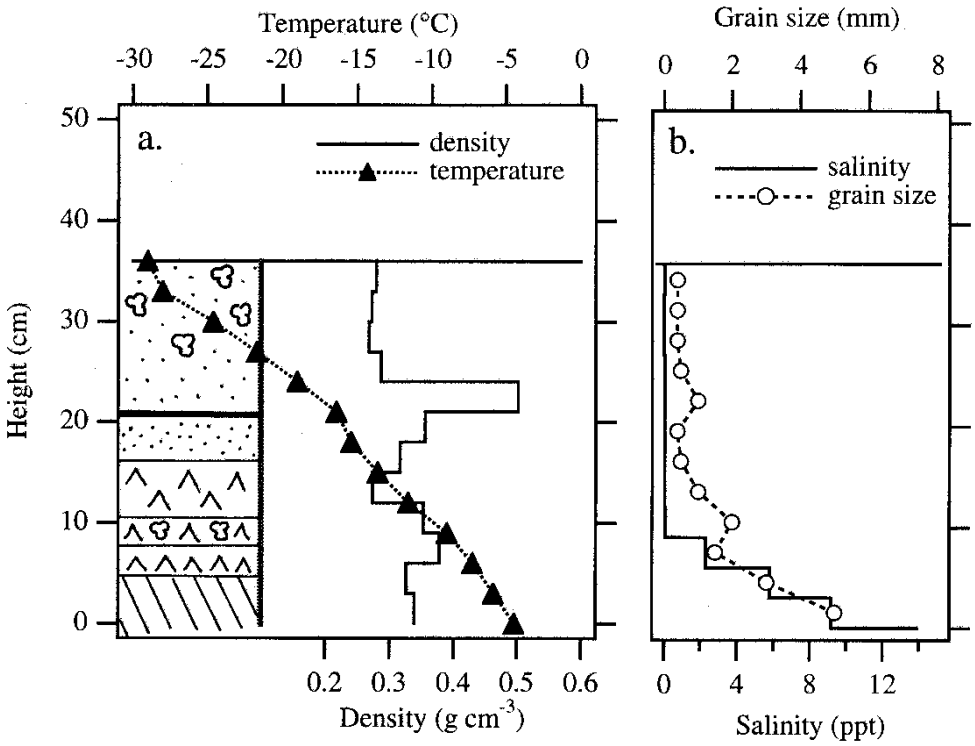

Figure 2.9: *A typical snow-pit diagram for a snow cover on sea ice in the Pacific Sector:* **a.** *snow stratigraphy, density and temperature,* **b.** *salinity and grain size (from [Sturm et al., 1998]).*

interface and by wicking-up of sea water through enlarged brine channels into this layer.

The snow liquid water content is determined by the temperature and the moisture supply from both underneath (sea water) and above (air humidity and precipitation). The snow liquid water content remains small, *i. e.* below 1 %, for temperatures below $-5\,^{\circ}$C and increases with temperature [Garrity, 1992]. Rain percolating the snow cover can also increase the snow liquid water content if the snow temperature is close to $0\,^{\circ}$C. However, due to the stratigraphy of a snow cover, large snow liquid water contents may be limited to the basal and/or the uppermost snow layer, particulary if icy snow layers are embedded in the snow [Garrity, 1992].

Snow density and grain size are closely related to each other in terms of the physical processes determining their magnitude: the vertical gradients of tempe-

rature and water vapor, the wind stress at the snow surface and the time elapsed since the last snow fall. Freshly fallen snow exhibits either very low densities ($< 0.15\,\mathrm{g\,cm^{-3}}$) and consists of single needles and crystals if fallen during low wind speeds, or moderate densities ($\approx 0.35\,\mathrm{g\,cm^{-3}}$) and consists of rounded grains (*soft/moderate wind slab*) if fallen during high wind speeds [Massom et al., 1997], [Sturm et al., 1993], [Sturm et al., 1998]. Figure 2.10 gives an overview about typical grain sizes and forms of snow on sea ice in the Pacific Sector with the snow types mentioned above shown in the images at the top. Redistribution and compaction of the snow results in snow drifts or a *hard wind slab* without considerably changing the grain size and with slightly increasing the density to $\approx 0.45\,\mathrm{g\,cm^{-3}}$ [Sturm et al., 1998]. The density maximum in Figure 2.9 **a.** may be due to such a layer.

Thermodynamic snow metamorphism can occur in two major forms and can lead to the average vertical grain size profile shown in Figure 2.9 **b.** (see also [Perovich et al., 1998]). A large negative vertical temperature gradient in the snow of $-0.25\,\mathrm{K\,cm^{-1}}$ or less, as measured for instance by Massom et al. [1997] and Sturm et al. [1998], can cause faceted growth of *depth hoar* at the expense of rounded grains [Akitaya, 1974], [Colbeck, 1982]. Depth hoar crystals can be

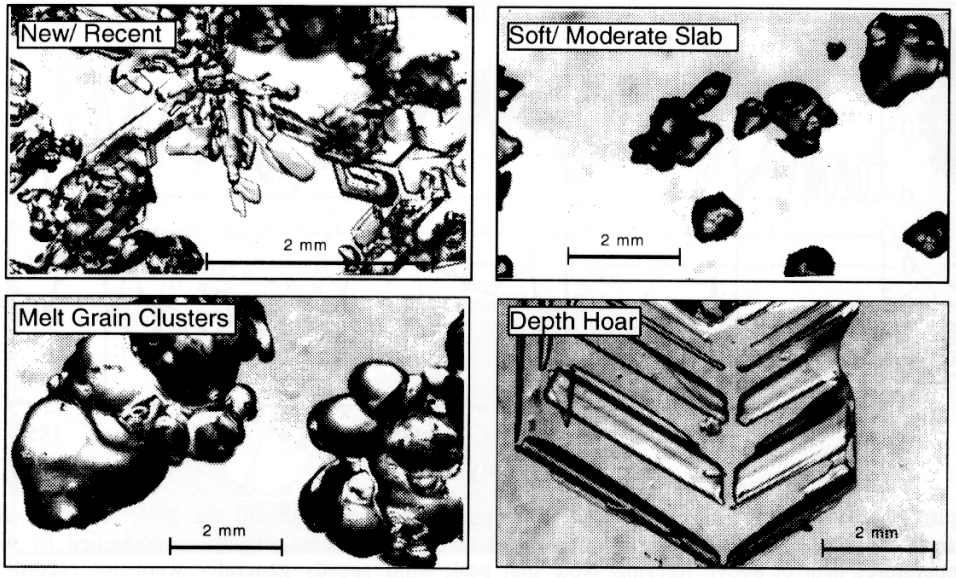

Figure 2.10: *Photo-micrographs of the four primary snow-grain types of the snow cover on sea ice in the Pacific Sector (from [Sturm et al., 1998]). Note the larger scale bar in the upper left image.*

quite large, *i. e.* > 5 mm ([Massom et al., 1997], see also Figure 2.10, bottom right) and lead to a density decrease to values between 0.2 and 0.3 g cm^{-3}. These crystals are often oriented anisotropically since their growth is determined by the vertical water vapor pressure gradient. Depth hoar layers play an important role in the heat budget of snow because of their poor thermal conductivity [Sturm, 1991]. For a given heat flow, the growth of depth hoar crystals decreases the average thermal conductivity of that particular snow layer, maintains the higher temperatures underneath while increasing the vertical temperature gradient and, therefore, enhancing the depth hoar formation.

Air temperatures close to or above 0°C lead to snow melt at the surface. Melt water drains into the snow forcing the snow grains to coagulate to so-called *melt grain clusters*, which are usually much more rounded and isotropically oriented than depth hoar crystals (Figure 2.10, bottom left). The same happens during a rain event. If a warm and maybe rainy episode is followed by a colder period, the wet snow surface refreezes to form an icy, coarse-grained surface crust. Grain sizes may then exceed 5 mm [Massom et al., 1997]. The change between above and below freezing point temperatures which is quite frequent during Austral summer, causes also a coarse-grained snow structure.

Summary:

- **Salinity**: Average snow bulk salinities are 4 ‰ [Eicken et al., 1994] and 8.6 ‰ [Massom et al., 1997] in the Weddell Sea and 8.5 ‰ on East Antarctic sea ice [Worby et al., 1998]. Snow salinities vary between < 0.01 ‰ in the upper parts of a thick snow cover on thick undeformed sea ice and > 66 ‰ in a wet and slushy basal snow layer adjacent to the snow-ice interface [Massom et al., 1997], [Worby et al., 1998].

- **Liquid water content**: Average spring and summer snow liquid water contents amount between 0.8 % and 1.2 % in the Arctic and 1.0 % in the Weddell Sea [Garrity, 1992]. Extreme values of more than 10 % are reported by Garrity [1992] and Grenfell [1992].

- **Density**: Values for average snow densities are 0.37 g cm^{-3}, 0.36 g cm^{-3} and 0.31 g cm^{-3} in the Pacific Sector [Sturm et al., 1998], on East Antarctic sea ice [Worby et al., 1998] and in the Weddell Sea [Eicken et al., 1994], [Massom et al., 1997], respectively. However, the density of adjacent snow layers is highly variable and ranges typically between 0.11 g cm^{-3} for fresh snow and 0.85 g cm^{-3} for icy snow layers [Massom et al., 1998].

- **Grain size**: Average snow grain sizes are difficult to obtain and to interpret due to the high degree of snow stratigraphy. Typical values are 1.6 mm on East Antarctic sea ice [Worby et al., 1998], 1.5 mm in the Pacific Sector [Sturm et al., 1998] and 2.7 mm in the Weddell Sea [Massom et al., 1997]. Modal values are generally 0.5 mm larger, standard deviations range between 1 and 3 mm, indicating the large variability. Grain sizes range from 0.1 mm for fresh snow crystals to 10 mm or more for well-developed depth hoar in both East Antarctica and the Weddell Sea.

2.3.4 Radiative Properties of Sea Ice and Snow

Sea Ice:

Sea ice is a mixture of ice crystals, liquid brine and air pockets. At the SSM/I frequencies (see Section 3.1.2), the emissivity of sea water is independent of the salinity S. The salinity S of liquid brine increases with decreasing temperature and exceeds 200 ‰ at $-18°$C, a value that may occur in the upper layers of bare sea ice [Ulaby et al., 1986], [Hallikainen and Winebrenner, 1992]. However, empirical results obtained by Stogryn and Desargeant [1985] for temperatures between $-2.8°$C and $-25.0°$C reveal no significant difference of the decrease of ε' and ε'' with frequency if compared to sea water. In the SSM/I frequency range, ε' of sea ice is almost constant and approximately of the same order of magnitude than ε' of saline water (see Figure 2.2). But ε'' of sea ice is about three orders of magnitude smaller than that of sea water due to the lack of free charge carriers [Hallikainen and Winebrenner, 1992] and increases slightly with frequency. Consequently, according to Equation 2.7, at the same frequency and polarization the emissivity of sea ice is usually larger than that of open water [Grenfell et al., 1994]. Figure 2.11 shows the emissivities of open water and FY ice at both polarizations and illustrates quite well the large emissivity difference. However, this difference becomes smaller for old ice due to the larger number of air pockets. They force volume scattering and thus decrease the surface emissivity with increasing frequency. The emissivity of old ice may fall below 0.6 at 90 GHz ([Hallikainen and Winebrenner, 1992] and [Grenfell, 1992]) a value which is smaller than the emissivity of open water at 85 GHz and vertical polarization.

The bubbly uppermost sea ice layer increases also the average penetration depth which, in sea ice, generally decreases with increasing frequency (decreasing wavelength λ). At 20 GHz, the penetration depth in old ice is ≈ 10 cm while that in FY ice is a few centimeters [Ulaby et al., 1986]. Radiometric measurements taken by Grenfell et al. [1998] at the outdoor pond at the CRREL reveal that at

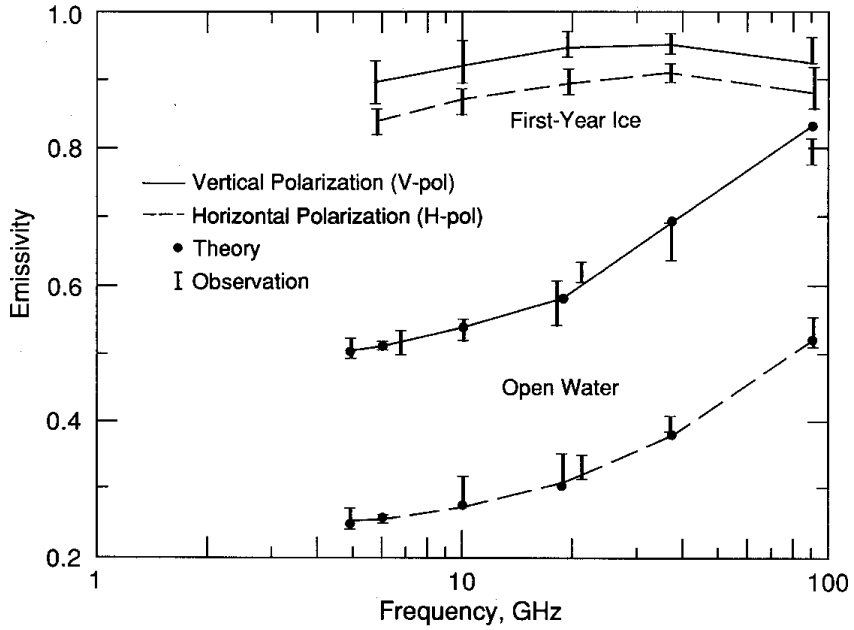

Figure 2.11: *Emissivities of saline water and FY ice as obtained using the results of Stogryn and Desargeant [1985] (Theory) and from field measurements during the* NORvegian remote Sensing EXperiment *NORSEX, the various* Marginal Ice Zone EXperiments *MIZEX' 83, MIZEX' 84, MIZEX' 87 and some other experiments (from [Hallikainen and Winebrenner, 1992]).*

90 GHz nilas becomes opaque for a thickness of 2 to 3 mm. However, field measurements, *e. g.* during the *NORvegian remote Sensing EXperiment* [The NORSEX Group, 1983], reveal emissivities of 0.84 and 0.88 for nilas [Hallikainen and Winebrenner, 1992] at 90 GHz, suggesting a thickness of one centimeter rather than a few millimeters to be required to unambiguously distinguish thin ice from open water at this frequency. The penetration depth in old ice decreases to a few centimeters at 90 GHz.

Snow:

Since the wavelength at 85 GHz is only 3.5 mm the surface emissivity is affected by snow almost as soon as it starts covering the sea ice. This is illustrated in Figure 2.12 (a) and (b), showing *in situ* brightness temperature measurements as a function of snow depth and frequency. Dry snow can be regarded as a mixture of snow or ice crystals and air. Wet snow additionally includes liquid water

which may be saline, particularly in the basal snow layers. This mixture is quite similar to that of sea ice. Therefore, in the SSM/I frequency range, the dielectric properties of snow are similar to those of sea ice and in case of dry snow are mainly determined by the snow density. For snow, the ε' value equals that of sea ice whereas ε'' is one order of magnitude smaller than that of sea ice and increases with frequency. Following Equation 2.7 and Equations 2.10 and 2.11, the emissivity of snow-covered sea ice is larger than that of bare sea ice. This can be identified in Figure 2.12 (a) and (b) by the brightness temperature increase with snow depth at all frequencies shown except at 90 GHz. However, volume scattering in the snow decreases the emissivity. This is illustrated in Figure 2.12. The snow-depth increase from < 3 mm to $3 \ldots 50$ mm has almost no effect on the 90 GHz brightness temperatures (images (a) and (b)) and these temperatures decrease by more than 10 K for snow depths above 50 mm (image (c)).

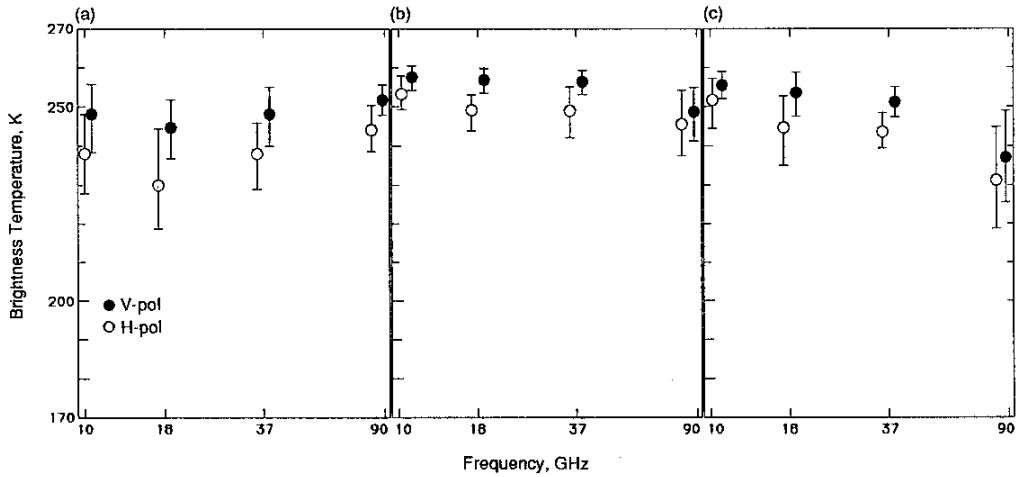

Figure 2.12: *In situ brightness temperature measurements over sea ice of 10 to 40 cm thickness with dry snow layers of different depth:* **(a)** < 3 *mm,* **(b)** $3 \ldots 50$ *mm,* **(c)** > 50 *mm. (from [Grenfell and Comiso, 1986]).*

From theoretical calculations of the microwave signature over dry snow using the *Mie* theory and assuming independent scatterers, *i. e.* describing dry snow as ice crystals being embedded in air, Ulaby et al. [1986] have found that volume scattering dominates for frequencies above 15 GHz. Measurements of the extinction properties of dry snow reveal an increase of the extinction coefficient κ_e with frequency. At 90 GHz, κ_e increases from 50 dB m^{-1} at a mean snow grain size of 0.4 mm to 500 dB m^{-1} at a mean snow grain size of 1.4 mm, suggesting a scattering coefficient $\kappa_s = \kappa_e - \kappa_a$ that is much larger than the absorption coefficient κ_a

[Hallikainen et al., 1987]. Recent *in situ* emissivity measurements conducted in the Arctic by Barber et al. [1998] and Perovich et al. [1998] confirm this. They have reported a decrease of the emissivity at 90 GHz over dry snow of ≈ 0.1 at vertical and between 0 and 0.05 at horizontal polarization. The larger emissivity change at vertical polarization can be explained by the snow-crystal orientation in the basal snow layer (Section 2.3.3), which is often anisotropic, thus favouring scattering at vertical polarization ([Barber and Nghiem, 1999] and Barber (2000), personal communication). The emissivity decrease may be larger if the mean snow grain size matches the wavelength of observation, which is most likely the case in summer when coarse-grained snow occurs. Surface emissivities modeled at 90 GHz for a refrozen snow cover over land are about 0.5 at both polarizations [Bauer and Grody, 1995]. Radiometric *in situ* measurements taken during the *Marginal Ice Zone EXperiment*s in 1983/84 show, at 90 GHz and both polarizations, a decrease of the emissivity from values above 0.9 over melting sea ice to ≈ 0.6 over a coarse-grained, icy snow layer of 6 cm thickness [Grenfell, 1992].

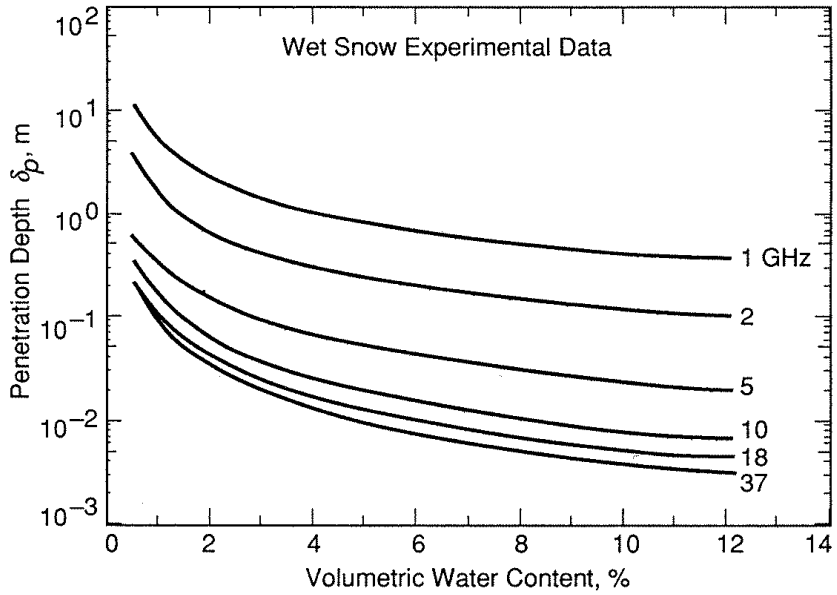

Figure 2.13: *Penetration depth of microwave radiation in snow as modeled using a modified Debye-like model for different frequencies and snow wetness (from [Hallikainen and Winebrenner, 1992]).*

The measurements of Grenfell [1992] also illustrate the influence of the third important snow parameter, its wetness or volumetric snow liquid water content m_v. Snow liquid water occurs in two regimes: the *pendular* and the *funicular*

regime [Colbeck, 1982]. The former regime is characterized by snow containing liquid water as isolated inclusions while air is continuous throughout the pore space. In the latter regime, the snow is almost saturated with liquid water, *i. e.* liquid water is continuous throughout the snow while air occurs in distinct bubbles. The transition between both regimes takes place at $m_v \approx 3\,\% \ldots 6\,\%$ [Ulaby et al., 1986], [Hallikainen and Winebrenner, 1992]. Taking these two regimes into account when modeling the dielectric properties of wet snow, ε' and ε'' increase with m_v and, more importantly, ε'' increases by a factor of 1000 compared to dry snow [Hallikainen et al., 1987]. Consequently, the emissivity ϵ and the absorption coefficient κ_a increase with m_v. The penetration depth in snow decreases with both increasing wetness and frequency to about one centimeter or less at $m_v = 5\,\%$ and 90 GHz [Eppler et al., 1992]. Figure 2.13 shows penetration depths in snow as function of frequency and snow wetness. These values have been obtained with a modified Debye-like model as described by Hallikainen et al. [1986] assuming that the spectral behaviour of wet snow is dominated by the dispersion behaviour of water because of the much higher permittivity of water, and including empirical results from experiments. However, there is evidence that at 90 GHz in the pendular regime, volume scattering can be regarded as the dominant process, particularly during the metamorphism of fresh snow. In this latter case, an emissivity increase with m_v may be compensated by an emissivity decrease due to volume scattering caused by an increasing mean snow grain size [Barber et al., 1998], [Perovich et al., 1998].

Summary:

- Antarctic sea ice consists primarily of FY ice. Only a minor fraction, mainly limited to the Weddell Sea, is old ice and on average younger than three years. Sea ice formation in the Antarctic can be divided into three categories: the pancake ice cycle at the MIZ, ice growth in coastal polynyas ("ice factories"), and the formation of snow ice and meteoric ice. Once formed, Antarctic sea ice is almost continuously covered by snow.

- At 85 GHz, sea ice can be unambiguously distinguished from open water at a thickness above $\approx$ 1 cm. The emissivity of bare young and FY ice is always considerably larger than that of open water at 85 GHz for both polarizations except for old ice, which exhibits a smaller emissivity than open water at vertical polarization. At 85 GHz, emissivities are independent of the sea ice salinity.

- Snow affects the emissivity at 85 GHz as soon as it starts covering the sea ice because of the small penetration depth associated with a wavelength of 3.5 mm. Snow on sea ice is usually stratified and heterogeneous. Snow-property changes can be caused by air temperature changes and/or precipitation. Related processes affect the snow on a spatial scale of at least a few SSM/I 85 GHz channel FOVs and a temporal scale of a few hours to a few weeks and, therefore, have an impact on the 85 GHz SSM/I measurements.

- The 85 GHz emissivity increases strongly with the snow liquid water content at both polarizations. As a result, $T_p(85)$ values increase significantly while $P(85)$ remains constant or decreases slightly.

- An increasing grain size enhances volume scattering and thus causes an emissivity decrease at 85 GHz. Consequently, $T_p(85)$ values decrease depending on the polarization and $P(85)$ values may both decrease or increase.

- The interaction between snow liquid water, density and grain size is complex. The first parameter certainly dominates the radiometric signal at $m_v > 3\,\%$. Particularly at lower m_v values volume scattering may compensate the absorption due to the snow liquid water. In dry snow, the effect of volume scattering dominates and may lead to a decrease of both $T_h(85)$ and $T_v(85)$ at a grain size above 2 mm. Large grain sizes as associated for instance with an icy snow surface crust and a depth hoar layer can depress the 85 GHz emissivities to values below 0.5.

- There is evidence for a strong polarization dependency of the emissivity change due to snow if slush is present at the snow-ice interface – at least at 37 GHz – when brightness temperatures decrease significantly at horizontal polarization and remain almost constant at vertical polarization [Garrity, 1992].

2.4 The Atmosphere

This section, following a brief description of the atmospheric composition, concentrates on the radiometric properties of the atmosphere and their impact on the surface radiation.

2.4.1 Atmospheric Constituents

The relative composition of the atmosphere remains essentially constant up to an altitude of $\approx$ 90 km. The main *dry* atmosphere gaseous constituents exhibiting constant volume fractions are $78.1\,\%$ per volume of molecular Nitrogen (N_2), $20.9\,\%$ per volume of molecular Oxygen (O_2) and $0.9\,\%$ per volume of molecular Argon (Ar_2). Another important and variable atmospheric gas is Carbondioxide (CO_2) with an average volume fraction of $0.035\,\%$. Depending on atmospheric activity, geographical latitude and season, the *humid* atmosphere can contain up to $4\,\%$ per volume of water (H_2O) in form of water vapor, which is mainly confined to the troposphere. The height of the troposphere is determined by the vertical convective heat transfer which depends mainly on the surface air temperature [Barry and Chorley, 1989] and, therefore, is significantly smaller ($\approx$ 8 km) at high latitudes than at low latitudes ($\approx$ 16 km). Integration of the water vapor contained in a vertical column of the atmosphere yields the integrated water vapor content W which, on average, is below $5\,\mathrm{kg\,m^{-2}}$ at polar latitudes and can be as high as $50\,\mathrm{kg\,m^{-2}}$ at tropical latitudes [Raschke, 1996].

In the troposphere, pressure and density decrease almost exponentially with height while the air temperature has a mean vertical lapse rate of $-6.5\,\mathrm{K\,km^{-1}}$. The maximum amount of water vapor that can be carried by the air without condensation is governed by the Clausius-Clapeyron equation [Holton, 1992]

$$\frac{de_s}{dT_a} = \frac{m_{mol} L_c e_s}{R^* T_a^2} \tag{2.16}$$

where T_a is the air temperature, m_{mol} the molecular weight of water, R^* the universal gas constant, L_c the latent heat of condensation and e_s the water vapor pressure at saturation. Obviously, e_s increases exponentially with T_a, suggesting that at low temperatures considerably smaller absolute amounts of water vapor are sufficient to cause condensation. If air raises, either due to orographic features or due to free convection, it cools adiabatically until condensation (sublimation) will form cloud droplets (ice crystals) and eventually clouds. Water clouds are typically confined to the troposphere and can be divided into *low*-, *middle*- and *high*-level clouds [World Meteorological Organization (WMO), 1956]. At high latitudes, these levels extend between 0 and 2 km, 2 and 4 km and above 3 km, respectively [Barry and Chorley, 1989]. While the lowest (highest) cloud level contains mostly liquid water (ice) clouds, the middle level is the site of mixed clouds with both liquid water and ice. Clouds can further be divided into *cumuliform* (Cumulus, Strato-, Alto- and Cirrocumulus) and *stratiform* (Stratus, Nimbo-, Alto-

and Cirrostratus) clouds [World Meteorological Organization (WMO), 1956].

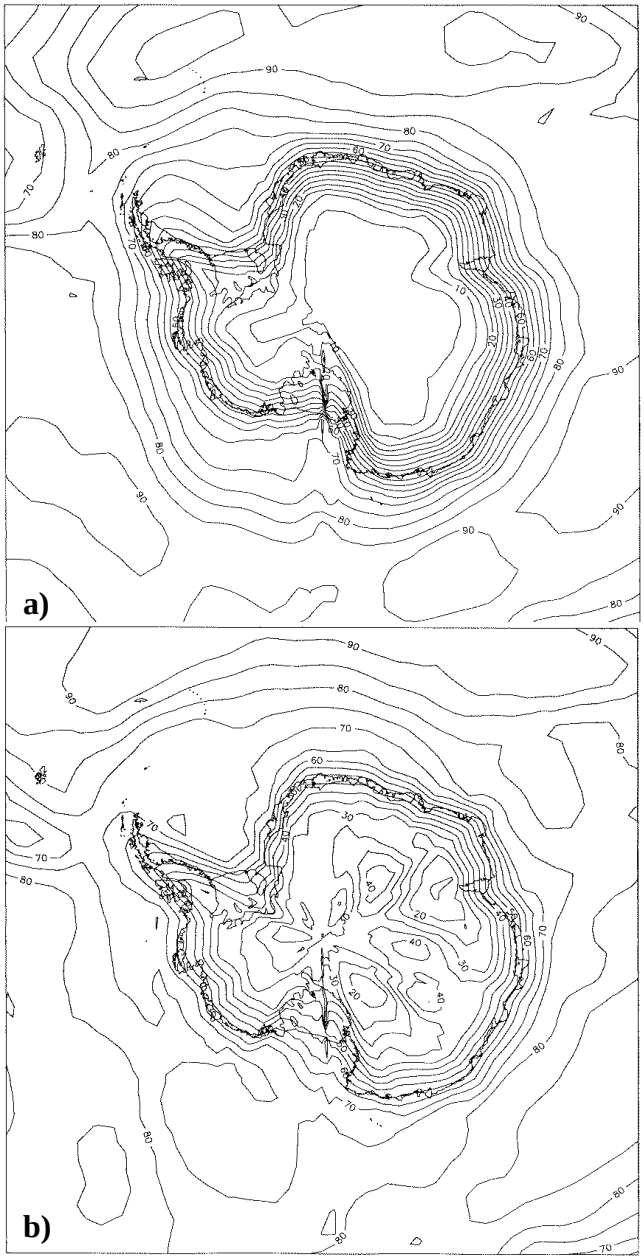

Figure 2.14: *Average cloud cover in the Antarctic taken from ISCCP data:* **a)** *for summer and* **b)** *for winter (from [King and Turner, 1997]).*

The cloud liquid water content (LWC) expressed in $\mathrm{g\,m^{-3}}$ can be estimated by integrating the water contained in all cloud droplets (the water equivalent of all ice crystals) of a cloud volume using an appropriate drop (particle) size distribution [Deirmendjian, 1969]. The liquid water path or integrated cloud liquid water content L can be obtained integrating the LWC over the vertical cloud column, yielding a few $\mathrm{g\,m^{-2}}$ for ice clouds (LWC $\approx 0.01\,\mathrm{g\,m^{-3}}$) and up to $1000\,\mathrm{g\,m^{-2}}$ for cumuliform clouds (LWC $\approx 1\,\mathrm{g\,m^{-3}}$). In polar regions, clouds exhibit smaller maximum values of L, particularly due to the smaller absolute water content of the troposphere associated with lower temperatures.

The average seasonal cloud cover exceeds $70\,\%$ over large areas of the Southern Ocean according to the *International Satellite Cloud Climatology Project* (ISCCP, [Schiffer and Rossow, 1983]). This is shown in Figure 2.14 for Austral summer and winter. The low temperatures typical for high latitudes favour the formation of stratiform rather than cumuliform clouds, which are usually shallow anyway [King and Turner, 1997]. Consequently, Stratus, Stratocumulus and Altostratus dominate the cloud cover of the Southern Ocean between $55°\mathrm{S}$ and $70°\mathrm{S}$, followed by ice clouds and Nimbostratus [King and Turner, 1997].

At high latitudes, the formation of precipiation always includes the ice phase requiring cloud levels with subfreezing temperatures and can be described by the Bergeron-Findeisen theory [Bergeron, 1960]. However, in the Southern Ocean, weaker vertical motions, shallower clouds and lower temperatures force low precipitation intensities and small precipitation particle sizes [King and Turner, 1997], [Lachlan-Cope and Turner, 1997]. Snow is observed in most cases, though rain may appear throughout the entire year [Turner et al., 1995]

2.4.2 Radiative Properties of the Atmosphere

Some comparisons between sea ice concentration maps and images taken in the VIS/IR range will be shown in Chapter 6. Therefore, the first part of Section 2.4.2 concentrates on this frequency range. The second part focusses on the interaction between the atmosphere and microwave radiation.

Visible/Infrared Frequency Range:

In the VIS range ($0.4\,\mu\mathrm{m} < \lambda < 0.7\,\mu\mathrm{m}$) as well as in the atmospheric window between 8 and 11 μm in the IR range ($0.7\,\mu\mathrm{m} < \lambda < 100\,\mu\mathrm{m}$), the atmosphere is almost transparent. This is illustrated by the absorbtivity of some atmospheric constituents shown in Figure 2.15. Both frequency ranges include the wavelengths associated with the maximum radiation intensity according to Wien's displace-

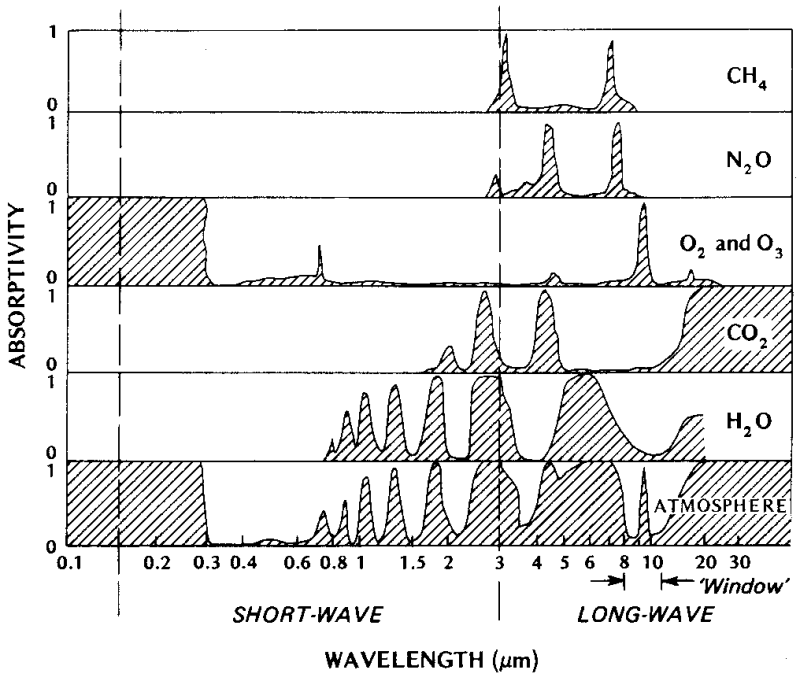

Figure 2.15: *Absorption by atmospheric constituents and by the atmosphere as a whole at various wavelengths (from [Fleagle and Businger, 1963]).*

ment law (Equation 2.2), which is 0.48 μm in the VIS range and 10 μm in the IR range for blackbodies with a temperature of $\approx$ 6000 K and of $\approx$ 270 K, respectively. Using spaceborne measurements in the VIS/IR range, for instance of the AVHRR, allows to discriminate sea ice from open water. Moreover, the sea ice surface temperature can be obtained [Key and Haefliger, 1992], [Yu and Rothrock, 1996], [St. Germain and Cavalieri, 1997]. This requires clear-sky conditions since the albedo α and IR emissivity ϵ_{IR} of clouds is similar to the corresponding value of α or ϵ_{IR} of sea ice and snow – except fresh snow. Some values of α and ϵ_{IR} are listed in Table 2.1. Using measurements in the VIS range additionally requires daylight.

Although there is no emissivity difference between sea water and sea ice in the IR range, different surface temperatures allow to distinguish between these two surfaces, at least during winter. The same is true to a smaller degree when distinguishing clouds from sea ice or snow. Cloud tops are often located at the semi-permanent surface inversion [King and Turner, 1997] and appear warmer than the surface. Nevertheless, sea ice and/or its snow cover can have the same

Table 2.1: *Albedo α and IR emissivity ϵ_{IR} for sea water [Oke, 1981], sea ice and snow [Grenfell et al., 1998], and clouds [Paltridge and Platt, 1984], [Barry and Chorley, 1989]. The letter d denotes the thickness of the sea ice. In the lower part of the table, α is the average albedo integrated over wavelengths $0.3\,\mu m \ldots 4.0\,\mu m$. Values of ϵ_{IR} depend strongly on particle density and cloud thickness and are omitted therefore.*

surface type	α	ϵ_{IR}
Old (melting) snow	0.4 – 0.6	0.82
Fresh snow	0.9 – 1.0	0.99
bare sea ice ($d \leq 15\,\text{cm}$)	0.1 – 0.4	0.98 – 1.0
bare sea ice ($d > 15\,\text{cm}$)	0.4 – 0.55	0.99
snow-covered sea ice (winter)	0.8 – 0.92	0.995
Sea water	0.03 – 0.1	0.92 – 0.97
Clouds	0.4 – 0.9	

temperature than the cloud tops. Moreover, both cloud albedo and IR emissivity depend strongly on the solar zenith angle, the cloud particle size distribution and the cloud thickness. This means that within one AVHRR or OLS image in one particular region sea ice might be discriminated from clouds quite well, *e. g.* sea ice covered by melting snow from a thick cloud cover such as Nimbostratus, whereas in another part of the image this discrimination is impossible, *e. g.* sea ice covered by melting snow from a thin, low-level Stratus layer. This limits the usage of these sensors for sea ice monitoring. A comparison of the structure or texture of sea ice and clouds evident in these images can provide additional information helping to identify cloud-covered regions over sea ice [Schlüter, 2000].

Microwave Frequency Range:

In the MW range, absorption and emission by all atmospheric gases except oxygen and water vapor are less pronounced or cause only a weak background absorption due to their small volumetric fractions [Ulaby et al., 1981]. The SSM/I frequency range (Section 3.1.2) covers the water vapor absorption line at 22.235 GHz and the so-called 60 GHz oxygen complex at frequencies between 51.5and 67.9 GHz [Ulaby et al., 1981]. Pressure broadening causes the oxygen absorption lines to overlap and to form an absorption band. The so-called *wings* of these bands extend into other frequency ranges and so do the wings of the oxygen

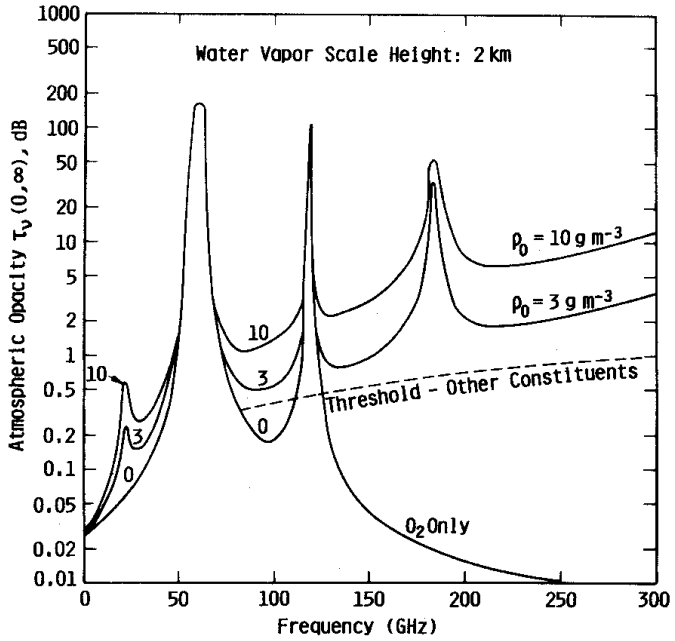

Figure 2.16: *Zenith opacity of the U.S. Standard Atmosphere for a surface temperature of 288 K and surface pressures of 1020.5 hPa (humid atmosphere) and 1013 hPa (oxygen only) (from [Smith, 1982]).*

and water vapor absorption bands that lie outside of the SSM/I frequency range: O_2 at 118.75 GHz, water vapor at 183.3 GHz. The distribution of these bands in the MW range is illustrated in Figure 2.16 for frequencies up to 300 GHz for a dry atmosphere and a humid atmosphere with two different water vapor contents.

Compared to mid-latitudes (Figure 2.16), a polar atmosphere exhibit a smaller water vapor content and thus a smaller atmospheric opacity τ at 90 GHz and in the microwave window at 35 GHz where the wings of the absorption lines contribute less to τ. Spaceborne data obtained at 22.235 GHz with the SSM/I and at 183.3 GHz with the *Water vapor profiler Special Sensor Microwave/Temperature2* (SSM/T2) have been used to retrieve the integrated water vapor content W over open water [Gloersen et al., 1984], [Bauer and Schlüssel, 1993], [Simmer, 1994], [Rossow, 1996] and over sea ice [Miao, 1998], [Miao et al., 2001].

The atmosphere contains also water as liquid and frozen particles (*hydrometeors*) which appear as clouds and precipitation. Particle radii range between $\approx$ 0.1 μm and 100 μm for cloud droplets and between 50 μm and a few millimeters for drizzle/rain drops and snow crystals. Non-precipitating cumuli- and

stratiform clouds usually exhibit particle radii around 5 μm [Mason, 1972] and absorb a lot but scatter little microwave radiation [Gasiewski, 1993]. Scattering by drizzle and rain particles and by most frozen hydrometeors becomes increasingly important with increasing frequency f (decreasing wavelength λ) – particularly at $f > 30$ GHz ($\lambda < 10$ mm) [Gasiewski, 1993]. This behaviour can be expressed by the Mie parameter χ as follows [Simmer, 1996]

$$\chi = \frac{2\pi r}{\lambda}, \tag{2.17}$$

where r is the particle radius. The *Rayleigh* approximation holds for $\chi < 0.1$ at the SSM/I frequencies and scattering is almost negligible [Gasiewski, 1993]. At $\chi \geq 0.1$, however, the Mie approximation holds and scattering has to be considered. For a typical cloud particle ($r = 5$ μm), χ increases from ≈ 0.002 at 19 GHz to ≈ 0.009 at 85 GHz while for a typical rain drop or ice crystal ($r = 1$ mm) one can expect an increase of χ from ≈ 0.4 at 19 GHz to ≈ 1.8 at 85 GHz. Therefore, scattering by liquid hydrometeors of non-precipitating clouds can be neglected at SSM/I frequencies, also at 85 GHz where brightness temperatures increase significantly with the cloud liquid water content [Fuhrhop et al., 1997]. Frozen hydrometeors and almost all precipitation particles scatter microwave radiation at 85 GHz. Simmer [1996] has shown that at 85 GHz the volume absorption coefficient is significantly larger for liquid precipitation particles than for frozen ones, and is similar to the volume scattering coefficients for precipitation particles of both phases. Volume scattering coefficients are similar for typical maximum Antarctic precipitation rates of up to 10 mm h^{-1}. Consequently, one can expect a large brightness temperature decrease due to scattering over rain and snow clouds at 85 GHz (see [Fuhrhop et al., 1997]). Furthermore, this decrease may depend on the polarization since falling rain drops are oblate and snow flakes are aspherical. Both effects are not accounted for in the radiative transfer model of Fuhrhop et al. [1998] which is briefly described in Section 2.5.1. The interaction of microwave radiation with ice particles of cirrus clouds can be neglected at SSM/I frequencies [Simmer, 1996].

Measurements of the SMMR and the SSM/I have been widely used to retrieve L and/or the rain rate over open water [Curry et al., 1990], [Bauer and Schlüssel, 1993], [Greenwald et al., 1993], [Karstens et al., 1994]. These approaches are mainly based on the lower SSM/I frequencies 19 GHz, 22 GHz and 37 GHz and, where possible, omit the horizontal polarized SSM/I channels in order to avoid a bias by scattering at the wind-roughened sea surface. In this study, the algorithm of Karstens et al. [1994] which is briefly described in Section 3.2.3 is used to cal-

culate L. The retrieval of L remains difficult over land or sea ice. Although some attempts have been made towards this issue over land [Jones and Vonder Haar, 1990], [Greenwald et al., 1997], a quantitative approach to retrieve L over sea ice is still missing. However, Miao et al. [2000] developed a method to qualitatively identify sea ice regions covered by clouds with SSM/I data. This method is used in this thesis also (Section 3.2.4). The rain rate is not retrieved here since average precipitation rates are small ($< 0.5\,\mathrm{mm\,h^{-1}}$) in polar regions, particulary over sea ice [Szeto et al., 1997], [King and Turner, 1997], [Lachlan-Cope and Turner, 1997]. However, even low precipitation rates may considerably affect the 85 GHz brightness temperatures becasue the mass absorption and extinction coefficients of precipitating clouds are larger for light ($1\,\mathrm{mm\,h^{-1}}$) than for heavy precipitation ($50\,\mathrm{mm\,h^{-1}}$) at 85 GHz [Simmer, 1996].

Summary:

The atmospheric water content, which is the integrated water vapor content W and the integrated cloud liquid water content L, increases the 85 GHz SSM/I brightness temperatures considerably. This increase is small over a surface with a high emissivity and becomes larger with decreasing emissivity. Therefore, the normalized brightness temperature polarization difference (Section 5.1) decreases at 85 GHz due to the influence of W and L. Scattering by precipitation particles decreases the 85 GHz brightness temperatures. This decrease depends probably also on the polarization to a degree which is unknown so far.

2.5 Radiative Transfer

In the MW range, the Rayleigh-Jeans approximation can be applied (see Section 2.1). Assuming a horizontally homogeneous, non-scattering and stratified atmosphere over a specularly reflecting surface the microwave brightness temperature $T_p(f)$ measured at polarization p and frequency f from space can be written as [Swift and Cavalieri, 1985]

$$\begin{aligned} T_p(f) &= \epsilon_p(f) T e^{-\tau(f)} + \int_0^{z_{TOA}} T(z) e^{-\tau(f)+\tau(z,f)} dz \\ &+ (1-\epsilon_p(f)) e^{-\tau(f)} \int_0^{z_{TOA}} T(z) e^{-\tau(z,f)} dz \\ &+ (1-\epsilon_p(f)) T_{p,space}(f) e^{-2\tau(f)}. \end{aligned} \tag{2.18}$$

where
$\epsilon_p(f)$ = Emissivity of the radiating layer,
$\tau(f)$ = Total atmospheric opacity at zenith angle $\Theta = 53.1\,^\circ$ [m^{-1}],
$\tau(z, f)$ = Atmospheric opacity at height z and $\Theta = 53.1\,^\circ$ [m^{-1}],
z_{TOA} = Height of the atmosphere [m],
T = Physical temperature of the radiating layer [K],
$T(z)$ = Air temperature at height z [K],
$T_{p,space}(f)$ = Cosmic background brightness temperature [K].

TOA stands for *Top Of Atmosphere*. The signal received by a spaceborne microwave radiometer has four contributions: a) surface radiation, attenuated by the entire atmosphere; b) atmospheric radiation towards the radiometer, attenuated only by the part of the atmosphere between the radiating layer of the atmosphere and the radiometer; c) atmospheric radiation towards the surface, attenuated by the part of the atmosphere between the radiating layer of the atmosphere and the surface, reflected at the surface and attenuated by the entire atmosphere; d) cosmic radiation, reflected at the surface and attenuated twice by the entire atmosphere. The last contribution can be neglected at $f > 5\,\mathrm{GHz}$ [Ulaby et al., 1981]. Over sea ice, $\epsilon_p(f)$ is usually close to 1 and the first term of Equation 2.18 dominates. However, as soon as changing sea ice and/or snow properties, or an increasing open water fraction cause a significant decrease of $\epsilon_p(f)$ in the FOV, the second contribution becomes larger in absolute terms and the third contribution grows in relative terms, when considering a transparent atmosphere, *i. e.* at frequencies outside the absorption bands of oxygen and water vapor.

Of particular importance is the physical temperature T of the radiating layer, called *emission temperature* in the following. Sea ice concentration algorithms using the low-frequency SSM/I channels perform best with the emission temperature set to the snow-ice interface temperature. However, this temperature is difficult to obtain and depends strongly on the stratigraphy of a snow cover [Sturm et al., 1993], [Sturm et al., 1998]. With increasing frequency, one can assume that the main radiating layer becomes more and more the surface itself due to the decreasing penetration depth [Ulaby et al., 1986], [Vander Veen and Jezek, 1993]. Therefore, over snow-covered sea ice the 85 GHz brightness temperature can be expected to depend less on the snow-ice interface temperature but more on the temperature of the uppermost snow layers if compared to the other SSM/I frequencies. Also, over bare sea ice the main radiating layer can be expected to be closer to the surface at 85 GHz compared to the other SSM/I frequencies.

Consequently, the difference between the emission temperature and the surface temperature of bare of snow-covered sea ice is smaller at 85 GHz than at lower frequencies. Fuhrhop et al. [1997] have investigated the sensitivities of modeled brightness temperatures to the emission temperature of different ice types. In doing this, the emission temperature of snow-covered FY ice was set to the snow-ice interface temperature and that of bare FY ice was set to the average physical temperature of the sea ice layer between 1 and 9 cm. For snow-covered FY ice, the modeled brightness temperatures turned out to be independent of the emission temperature at all SSM/I frequencies. For bare FY ice, the modeled brightness temperatures are found to exhibit a decreasing emission temperature dependency with increasing frequency. Consequently, the error caused by setting the emission temperature equal to the surface temperature is smaller at 85 GHz compared to the low-frequency SSM/I channels.

2.5.1 MWMOD

The radiative transfer model MicroWave MODel (MWMOD) has been developed by Simmer [1994], Fuhrhop and Simmer [1997] and can be used to model both the downward and upward microwave radiation over open water and sea ice [Fuhrhop et al., 1997], [Fuhrhop et al., 1998], [Miao, 1998], [Miao et al., 2000]. The modular outline of MWMOD allows a separate description of the properties of sea ice, open water and the atmosphere, as well as computation of their radiative characteristics. The interaction between atmosphere, sea ice and open ocean, *i. e.* the radiative transfer, can be calculated for different frequencies and viewing angles, for instance those of the SSM/I. In the following, the modules and the most important parameters used in this thesis are described briefly. See Fuhrhop et al. [1997], Fuhrhop et al. [1998] and the *User Manual* [Fuhrhop and Simmer, 1998] for more details.

In MWMOD, open water can be characterized by its salinity, its SST and the roughening of the surface according to the surface wind speed V. In this thesis, these parameters are set to 34 ‰, 272 K and $0\,\mathrm{m\,s^{-1}} < V < 30\,\mathrm{ms^{-1}}$, respectively. In order to consider scattering by the wind-roughened and foam-covered sea surface (Section 2.2.1), MWMOD utilizes a three-scale model. This is a facet model, where the Fresnel reflection coefficients calculated for the first scale (large-scale gravity waves) are modified by scattering on the second scale (small-scale gravity and capillary waves) (Section 2.2.1) and by multiple scattering on to the third scale (see [Guissard and Sobieski, 1987]), the foam cover. Alternatively, MWMOD can be provided with surface reflectivities at both polarizations instead of

calculating them. The reflectivities are used together with the modules specifying the atmospheric conditions and the radiative transfer in the atmosphere to model brightness temperatures over open water.

For sea ice, MWMOD provides two possibilities to model brightness temperatures. The first is to divide the sea ice into horizontal layers of specified thickness and to describe these layers in detail with the sea ice parameters: density, temperature, salinity, brine pocket orientation and aspect ratio, grain size, air bubble diameter and liquid water content. The same is done for the snow cover. MWMOD allows to calculate the radiative transfer within the sea ice/snow and to obtain the surface reflectivity of the radiating layer selected for a given physical temperature of these layer (emission temperature). This temperature has to be choosen carefully for the frequency used because of the dependency of the emission temperature on sea ice and snow properties. As for the open ocean, these reflectivities and the emission temperatures are used together with the modules specifying the atmospheric conditions and the radiative transfer in the atmosphere to model brightness temperatures over sea ice. In case of a sea ice concentration C below $100\,\%$, one can provide MWMOD with the values of C and the brightness temperatures modeled separately for open water and sea ice are combined according to C. The second possibility is to provide MWMOD with reflectivities and emission temperatures typical for the sea ice conditions to be investigated. This approach is choosen in this thesis since, to the author's knowledge, reflectivities and brightness temperatures obtained with MWMOD at frequencies above 40 GHz over sea ice have not yet been validated for the large number of parameters to specify in the sea ice module and, also, have been questioned at 37 GHz [Fuhrhop et al., 1998]. Furthermore, the main goal using MWMOD in this thesis is to estimate the weather influence on the 85 GHz brightness temperatures over a surface with known reflectivities. Therefore, the second approach is used here.

The gaseous absorption of oxygen and water vapor is treated in MWMOD according to the *Liebe* model [Liebe et al., 1993]. Absorption, emission and scattering by non-precipitating clouds is modelled with the Rayleigh theory. MWMOD provides several possibilities to specify the atmospheric properties [Fuhrhop et al., 1998]. Simulations used in this thesis are based on pre-defined profiles of air pressure and air temperature typical for a polar atmosphere. The profiles are interpolated onto a user-defined grid with a finer vertical resolution, particularly near the surface. The atmospheric humidity is specified by W and a typical vertical water vapor distribution. In order to consider the effect of L on the brightness temperatures, low-level clouds are included at an altitude level of 500 m with a cloud thickness of 500 m. Both values remain fixed. Within MWMOD, L can be

calculated using typical drop-size distributions of various cloud types. Stratus and Stratocumulus clouds usually provide the largest contribution to L because they are low-level clouds. Altostratus is a dominant cloud type in frontal cloud bands [Barry and Chorley, 1989] and exhibits a typical drop-size distribution similar to that of Stratocumulus [Paltridge and Platt, 1984]. Therefore, in order to consider simultaneously Altostratus and typical Antarctic low-level clouds, the drop-size distribution of Stratocumulus is used in this thesis. Only non-precipitating clouds are used to model the brightness temperatures, since precipitating clouds are masked out using the R-factor method described in Section 3.2.4.

Chapter 3

Data Basis

This chapter describes the data sets used in this thesis. They can be divided into four categories:

- remote sensing data *e. g.* the brightness temperature,
- quantities derived from remote sensing data such as the integrated water vapor content,
- quantities obtained from models,
- data measured or observed *in situ*, for instance, sea ice observations aboard a ship.

3.1 Remote Sensing Data

Remote sensing data collected by polar orbiting satellites are the backbone of this thesis. A brief description of the visible (VIS) and infrared (IR) data used is given in Section 3.1.1 and is followed by a discussion of the microwave (MW) data used in Section 3.1.2.

3.1.1 Visible/Infrared Range

In polar regions, using data obtained in the VIS and IR range to gain information about the surface is restricted to clear-sky conditions and additionally requires daylight in the VIS range. Data taken the VIS range are a measure of the reflectivity and can be transformed into the shortwave *albedo*. Data taken in the thermal

IR range can be used to estimate the surface temperature of both clouds and the Earth's surface. Since sea ice reduces the heat flux from the ocean into the atmosphere, one can expect lower surface temperatures over sea ice than over open water, at least during winter. Therefore, surface temperatures derived from IR data (see [Key and Haefliger, 1992]) can be used to discriminate sea ice from open water and, more importantly, to estimate the thickness of thin ice [St. Germain and Cavalieri, 1997]. In this thesis, data of the *Operational Linescan System* (OLS) are used. This sensor is equipped with two broadband channels, one in the VIS and one in the IR range (see Table 3.1). The OLS scans the Earth across-track with a swath width of $\approx$ 3000 km. The spatial resolution is about 2.7 km. The OLS and the *Special Sensor Microwave/Imager* (SSM/I) are both part of the U.S. *Defense Meteorological Satellite Program* (DMSP) payload.

Table 3.1: *Bandwidths of the OLS sensor.*

Channel	VIS	IR
Wavelength [μm]	0.4 – 1.1	10.5 – 12.6

3.1.2 Microwave Range

In the MW range, one has to distinguish between active and passive sensors. Passive microwave data collected by the SSM/I are used extensively in this thesis and will be discussed at first. The SSM/I is a multi-channel total-power passive microwave radiometer which has been flown continuously on different DMSP spacecraft since 1987. These spacecraft have sun-synchronous polar orbits with an inclination angle of 98.8 ° and an orbit period of 102 minutes, and fly at an average altitude of 833 km [Hollinger et al., 1987].

The SSM/I is equipped with seven channels. Frequencies f, polarizations p, wavelengths λ, noise and effective *field-of-view* (FOV) are listed in Table 3.2. The FOV is approximately the 3 dB width of the antenna pattern projected onto the Earth's surface. The SSM/I scans the Earth's surface conically across-track with a constant ground incidence zenith angle of 53.1° while looking backwards. The swath width is about 1394 km. The low-frequency SSM/I channels (19 GHz to 37 GHz) are sampled every 25 km, the 85 GHz channels every 12.5 km. This yields 64 and 128 pixels per scan, respectively. Figure 3.1 illustrates the SSM/I orbit and swath geometry. About 14 SSM/I overflights per day provide a complete

coverage of the entire polar regions with the exception of a small area centered at the poles remaining uncovered because of the SSM/I orbit geometry (see Fig. 1.2, [Hollinger et al., 1987]).

Table 3.2: *SSM/I sensor characteristics (from [Hollinger et al., 1987]).*

f [GHz]	p	λ [mm]	noise [K]	FOV [km$\times$km]
19.35	h, v	15.5	0.8	69×43
22.235	v	13.5	0.8	50×40
37.0	h, v	8.1	0.6	37×29
85.5	h, v	3.5	1.1	15×13

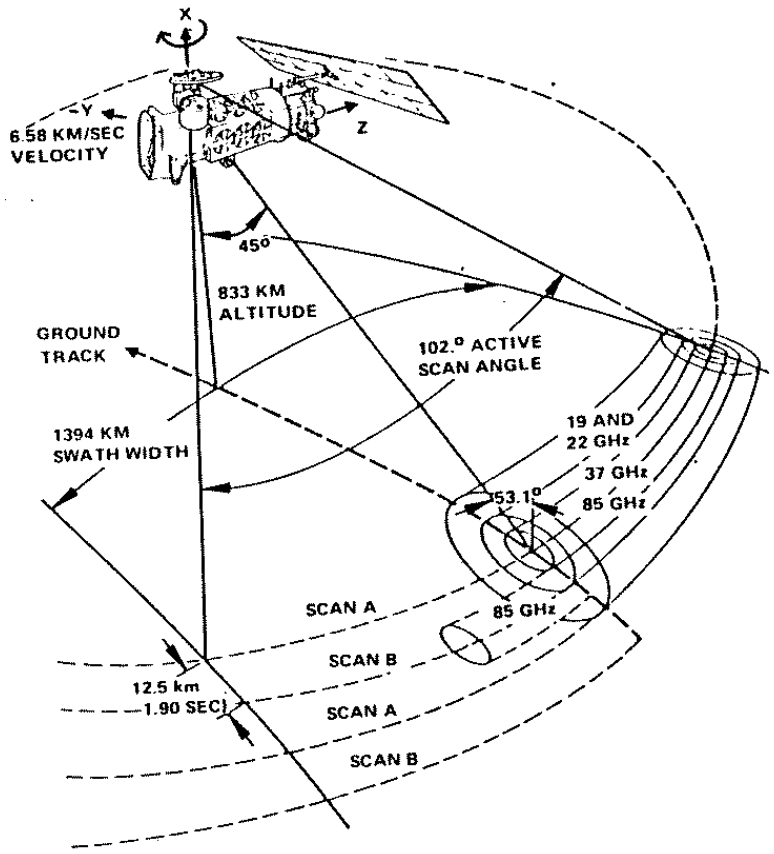

Figure 3.1: *Orbit and swath geometry of the SSM/I (from [Hollinger et al., 1987]).*

The *National Snow and Ice Data Centre* (NSIDC), Boulder, Colorado, distributes daily average brightness temperatures interpolated into a stereographic grid with cell sizes at 19 to 37 GHz of $25 \times 25\,\mathrm{km}^2$ and at 85 GHz of $12.5 \times 12.5\,\mathrm{km}^2$ [NSIDC, 1996]. Each cell contains the average of all brightness temperatures that fall into the considered cell within one day ("Drop into the bucket"). To minimize the distortion, the projection is true at 70 °S (N). The used ellipsoid and details of the gridding routine are compiled in NSIDC [1996]. Although the first SSM/I sensor was launched in 1987, only data that have been provided by the NSIDC for the period December 1991 to December 1999 are used in this thesis because a failure of the 85 GHz sensor causes measurements to be unreliable between May 1988 and December 1991 at vertical polarization and between February and December 1991 at horizontal polarization [NSIDC, 1990].

Due to its orbit geometry, the SSM/I passes more often over high latitudes than over middle or low latitudes within one day. Consequently, the "Drop into the bucket"-method can cause artefacts arising from the different number of overflights used to generate maps of the daily gridded brightness temperature. Usually between four and seven SSM/I overflights cover one pixel of the NSIDC grids poleward of 60° S (N) as is evident in Fig. 1.2 in Hollinger et al. [1987] (not shown here). However, equatorwards of 60° S (N) the number of artefacts increases and has to be taken into account, particularly when using these data to retrieve the atmospheric parameters V, W and L. The latter parameter is highly variable on both spatial and temporal scales. Therefore, averaging over three instead of two overflights can cause a relative change in L of more than 100 %.

3.2 Remotely Sensed Meteorological Data

Two kinds of meteorological data are used in this thesis for the correction of the brightness temperatures for the atmospheric influence. This section describes briefly the data obtained from remote sensing data.

3.2.1 Surface Wind

In the SSM/I frequency range, the sea surface emissivity depends mainly on the surface wind speed V (see Section 2.2.1). Therefore, over open water, SSM/I brightness temperatures can be used to retrieve V, for instance, with the so-called *D-matrix* algorithm [Lo, 1983]. This algorithm is based on the following Equation:

$$\begin{aligned} V &= A_0(j) \\ &+ A_1(j)T(19h) + A_2(j)T(22v) \\ &+ A_3(j)T(37v) + A_4(j)T(37h). \end{aligned} \tag{3.1}$$

The *D-matrix* coefficients $A_i(j)$ are listed in Table 3.3. These coefficients can be taken from a climate-code table containing appropriate values for latitude and season selected. The index j denotes the so-called *climate-code index* (after [Lo, 1983]). The algorithm has been validated by Goodberlet et al. [1989]. They found an accuracy between $2\,\mathrm{m\,s^{-1}}$ and $5\,\mathrm{m\,s^{-1}}$ for wind speeds between $5\,\mathrm{m\,s^{-1}}$ and $30\,\mathrm{m\,s^{-1}}$.

Table 3.3: *Coefficients to retrieve the parameters surface wind speed V, integrated water vapor content W and integrated cloud liquid water content L from SSM/I data.*

i	0	1	2	3	4
V: A_i, summer	109.93	0.8695	-0.4710	-0.6008	0.1158
V: A_i, winter	137.72	0.7330	-0.4208	-0.7533	0.1804
W: B_i	260.82	48.128	0.15718		
L: $E_i \times 10^{-3}$	3232.16	2.285	492.984	-1850.55	433.686

3.2.2 Water Vapor

The SSM/I measures brightness temperatures at 22.235 GHz, which is at the center of a water vapor absorption line and at 37 GHz, which is near the MW absorption window at 35 GHz (see Figure 2.16). These brightness temperatures are least influenced by the wind-induced sea surface roughness at vertical polarization and, therefore, can be used to retrieve the integrated water vapor content W over open water [Simmer, 1994]. The Equation

$$W = B_0 - B_1(\log 290 - T(22v)) - B_2T(37v) \tag{3.2}$$

provides W in $\mathrm{kg\,m^{-2}}$ with the given brightness temperatures and the coefficients B_i compiled in Table 3.3. The accuracy of this retrieval is about $2\,\mathrm{kg\,m^{-2}}$ according to Simmer [1994].

Miao [1998] (see also [Miao et al., 2001]) has developed a method to retrieve W up to values of 6 kg m^{-2} over open water *and* sea ice using data of the humidity sounder *Special Sensor Microwave/Temperature 2* (SSM/T2). However, using this method over Antarctic sea ice the limitation to values of $W \leq 6\,\mathrm{kg\,m^2}$ would lead to large data gaps in the maps of W, since W often exceeds this limit as is shown in Figures 3.2 and 3.3 and in Table 5.1.

3.2.3 Cloud Liquid Water

The absorption and emission of microwave radiation by cloud droplets at the SSM/I frequencies can be exploited to estimate the integrated cloud liquid water content L from SSM/I data. Several algorithms have been developed to calculate L over open water. In polar regions, the method of Karstens et al. [1994] has been found to provide quite reliable results. It is based on the following Equation

$$\begin{aligned} L &= E_0 + E_1 T(19v) + E_2 \ln(280 - T(22v)) \\ &+ E_3 \ln(280 - T(37v)) + E_4 \ln(280 - T(37h)), \end{aligned} \tag{3.3}$$

and yields L in kg m^{-2} with an accuracy of about 0.030 kg m^{-2}. The coefficients E_i are compiled in Table 3.3. In polar regions, precipitation was observed to occur at $L > 0.35\,\mathrm{kg\,m^{-2}}$ [Curry et al., 1990]. Due to scattering at precipitation particles, L is most likely biased towards too high values at L above 0.35 kg m^{-2}. Also, one can expect an overestimation of W since the decrease of the brightness temperatures due to scattering by precipiation particles causes a smaller amount to be subtracted from B_0 (see Equation 3.2). Figures 3.2 and 3.3 show maps of V, W and L calculated from SSM/I data (plates **a)** to **c)**) and of W inferred from data of the *European Medium-range Weather Forecasting Center* (ECMWF) model (image **d)** for Austral summer and winter. See Section 3.3 for details of the model data. Both examples show typical values of V, W and L in the Southern Ocean. Note the good agreement of the main patterns in the water vapor fields taken from both data sets. Triangular shaped regions with sudden changes in W (see Figures 3.2 and 3.3 **b)**) are due to the averaging process discussed in Section 3.1.2. These discontinuities are evident in the maps of V and L as well. Figure 3.3, images **b)** and **d)**, illustrates that air with a water vapor content of $\approx 10\,\mathrm{kg\,m^{-2}}$ or more can penetrate well into the sea ice covered area, for instance at 30 °E and in the Ross Sea between 150 °W and 180 °W, where a tongue of moist air reaches even the continent.

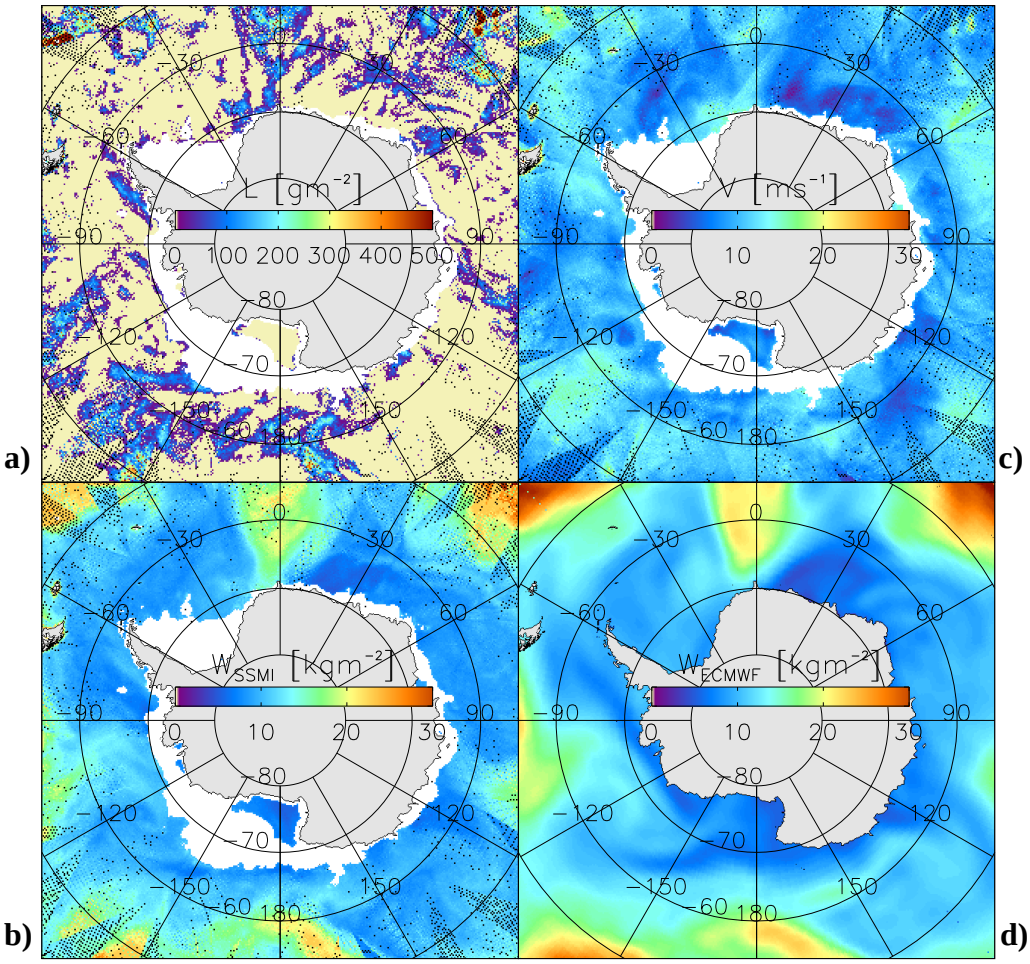

Figure 3.2: *Atmospheric parameters of January 18, 1999.* **a)***: L,* **b)***: W,* **c)***: V (all from SSM/I data) and* **d)***: W from ECMWF data (Section 3.3). The area covered by sea ice [Heygster et al., 1996] is masked white in plates* **a)** *to* **c)**.

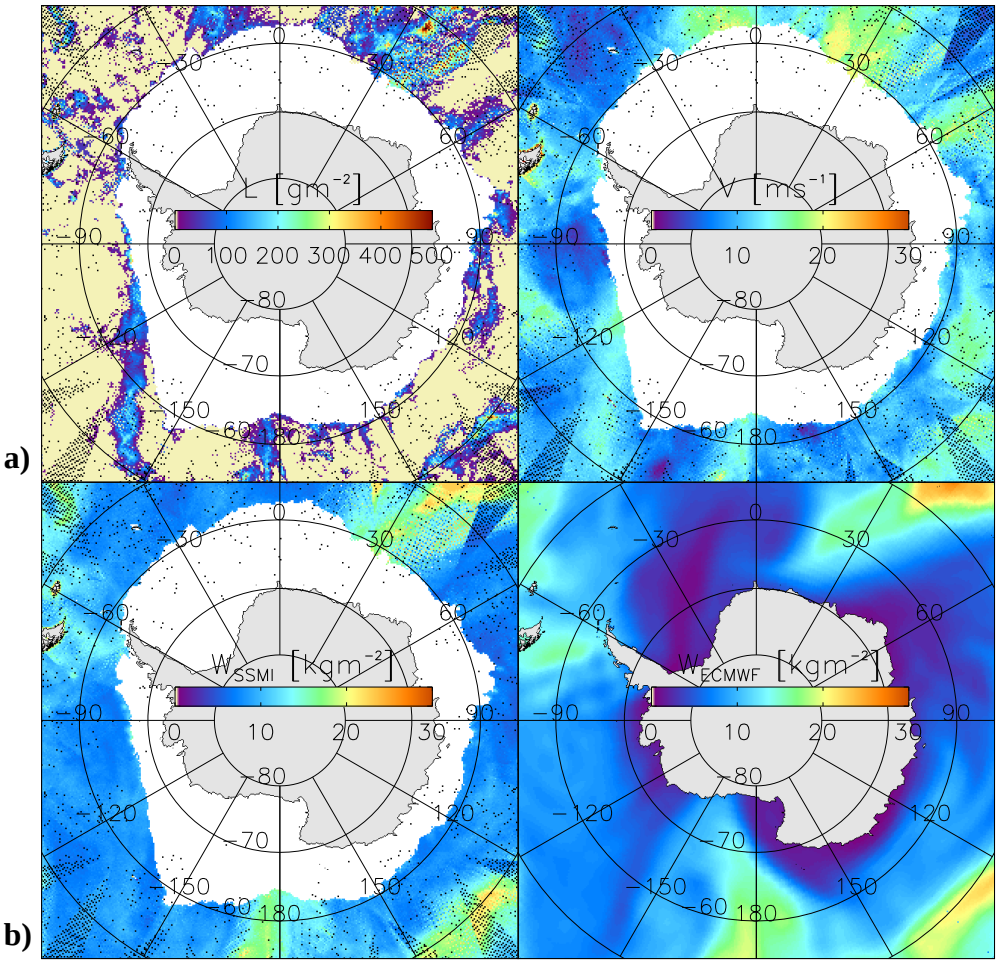

Figure 3.3: *Same as Figure 3.2 for July 22, 1999.*

3.2.4 R-factor

The lack of reliable data of L over the Southern Ocean is mitigated using the R-factor method developed by Miao et al. [2000]. The R-factor is given by

$$R(f_1, f_2) = \ln \frac{T_v(f_1) - T_h(f_1)}{T_v(f_2) - T_h(f_2)}, \tag{3.4}$$

where f_1 and f_2 denote the frequencies 37 GHz and 85 GHz, respectively. For a dry polar atmosphere, the R-factor is the sum of two terms, one describing the

ground surface signal R_s and the other representing the contribution of L and, to a smaller amount, of W:

$$R = R_s + \beta(L + \alpha_{WL} W). \tag{3.5}$$

The quantities α_{WL} and β are constants and given by

$$\alpha_{WL} = \frac{\Delta\kappa_W}{\Delta\kappa_L} = 1.038 \times 10^{-2} \quad \text{and} \quad \beta = 2 \sec\theta \Delta\kappa_L = 2.208\,\mathrm{m^2 kg},$$

where $\Delta\kappa_W$ ($\Delta\kappa_L$) is the frequency difference of the water vapor (liquid water) mass absorption coefficient at f_1 and f_2, and θ is the SSM/I viewing angle. In order to avoid the unwanted influence of R_s, which is the logarithm of the ratio of the surface emissivity polarization differences at f_1 and f_2, a background term R_b is defined, which is a measure of the surface emissivity variability (large R_b = large variability). For this purpose, on calculates a time-series of the R-factor for a period which is sufficiently long to account for the high average cloud cover around Antarctica (see Figure 2.14) and which is sufficiently short to keep the influence of the temporal variability of the surface signal low. For each pixel, R_b is the median of all R-factor values that lie between the minimum and the average R-factor of the time-series considered. The so-called *cloud signature* L', which is L plus a small contribution of W depending on the difference between the actual W value and the W value averaged over the period considered, can be estimated using the difference between the actual R-factor and R_b. Miao et al. [2000] have shown that this method allows to unambiguously identify clouds with $L' > 50\,\mathrm{g\,m^{-2}}$ over Antarctic sea ice during Austral summer melt conditions.

Miao et al. [2000] have used SSM/I swath data and have shown that a ten-day period is sufficient for the time-series analysis required to derive R_b and to obtain maps of L' for each swath (about 4 to 5 per day) of this period. Using daily gridded SSM/I brightness temperatures [NSIDC, 1996] to estimate L', requires more days to obtain a sufficiently long R-factor time-series. Therefore, in a first step, the R-factor is calculated for each day of the period December 16, 1991 to January 15, 2000. In the next step, a 31-day window is applied to this R-factor time-series – similar to a running 31-day average. This defines a time-series of 31-day subsets centered around each day of the period 1992-1999. These subsets are used to calculate R_b and to estimate L' for each day, which is different to the method of Miao et al. [2000]. Moreover, in this thesis R_b is the median of all R-factor values between the *maximum* and the average R-factor of the subset selected. Taking the maximum instead of the minimum R-factor (compare [Miao

et al., 2000]) becomes necessary because using the minimum far too few clouds would be identified.

With this approach each R_b value reflects the temporal variability of the surface conditions of a significantly longer period (31 days) if compared to the original method [Miao et al., 2000] (10 days). However, the temporal variability inherent in the basic data used here (daily gridded data) is much smaller compared to the data used in the original method (swath data). This can be explaind by the diurnal melt-freeze cycle causing a diurnal surface emissivity change which can be identified in the R-factor time-series derived from swath data but does not occur in the one derived from daily gridded brightness temperatures. As a consequence, the temporal variability contained in each R_b value stems from a day-to-day rather than from a diurnal change in the surface emissivity over the period used. An overestimation of R_b caused by changing sea ice concentrations cannot be excluded in general. For this reason, re-calculating R_b for each day seems to be quite reasonable when using a 31-day period and daily gridded brightness temperatures as done in this thesis, particularly in regions and/or during periods of variable sea ice concentrations.

For each day, all pixels where the R-factor exceeds R_b are set to 1 in a binary cloud mask. All pixels with a smaller R-factor remain at 0. These masks are compared with maps of L for each day of 1997. About $75\,\%$ of all pixels with $L \geq 50\,\mathrm{g\,m^{-2}}$ are identified to be cloud-covered with this method. Cloud masks are derived for each day of the period 1992-1999 and are used as a reliable tool to exclude most pixels with $L > 50\,\mathrm{g\,m^{-2}}$ from the sea ice concentration retrieval. Figure 3.4 shows, as an example, the capability of the R-factor method to identify regions with $L \geq 50\,\mathrm{g\,m^{-2}}$. The map of R_b given in Figure 3.4 **a)** indicates that, for the 31-day period selected, large variabilities in the surface emissivity occur over sea ice in the Weddell Sea (west of $20\,^{\circ}$W, north of $70\,^{\circ}$S), in almost the entire Pacific Sector except the southern Ross Sea and, less pronounced, in the MIZ. Regions are identified to be cloud-covered, where the R-factor of the selected day (see Figure 3.4 **b)**) is larger than R_b. Almost all patches with $L > 50\,\mathrm{g\,m^{-2}}$ shown in Figure 3.4 **d)** can be identified in the cloud mask shown in Figure 3.4 **c)**. More importantly, the smooth continuation of areas identified as being cloud-covered across the ice edge seems to be reasonable, since these areas correspond to regions where a considerable gradient of W indicates a front between two air masses of different humidity (see Figure 3.3 **d)**). However, the cloud-covered area might be overestimated over the sea ice in those regions, where sea ice surface properties cause an R-factor which is larger than R_b. Therefore, the area identified to be cloud-covered in the northwestern Weddell Sea is more likely caused by a highly

variable surface emissivity rather than high L values. These areas probably exhibit non-average surface properties, such as an icy snow surface crust after freezing rain, and are excluded from the sea ice concentration retrieval as well.

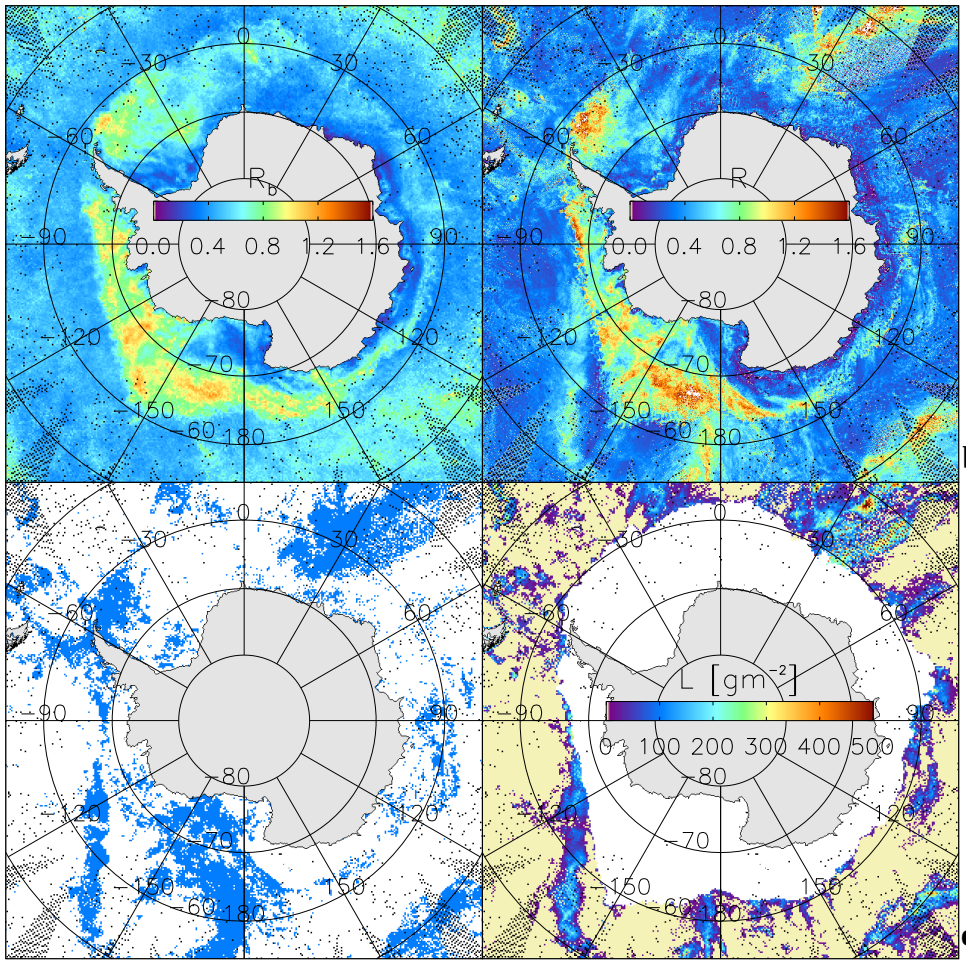

Figure 3.4: *Parameters involved in the development of the cloud mask for July 22, 1999.* **a)***: background term R_b obtained from the period July 7 to August 5,* **b)***: R-factor for July 22,* **c)***: cloud mask (clouds = blue) and* **d)***: L obtained from SSM/I data. The white area in the last image denote the sea ice covered area [Heygster et al., 1996].*

3.3 Modeled Meteorological Data

Originally, it was planned to quantify and correct the atmospheric influence with data from numerical models alone. During this study, however, it became evident that data of L are either not available from models or are not sufficiently reliable – partly due to the coarse spatial resolution of these models. This is particularly true for data of the ECMWF model in the Southern Ocean where only few observations enter the model. Therefore, in a first step, areas exhibiting clouds with high L values are excluded in advance to any retrieval using the cloud mask derived with the R-factor method. In the next step, over open water, L is calculated from daily gridded brightness temperatures as is described in Section 3.2.3. Over sea ice, L is set to its averaged monthly value computed over open water adjacent to the sea ice edge (see Section 5.2.1).

The influence of V on the SSM/I brightness temperatures can be expected to decrease rapidly with an increasing sea ice fraction in the FOV – particulary due to the influence of the limited wind fetch in areas enclosed by sea ice or land. For this reason, over open water, V is calculated from daily gridded brightness temperatures as described in Section 3.2.1. Over sea ice, V is set to its averaged monthly value computed over open water adjacent to the sea ice edge (see Section 5.2.1).

The integrated water vapor content W is derived from ECMWF data over both open water and sea ice for the period 1992-1999. For this purpose, air temperatures and humidities on the main pressure levels (1000, 850, 700, 500, 400 and 300 hPa) and of the synoptic times (00, 06, 12, and 18 GMT) are taken from the operational NWP model of the ECMWF [Persson, 2000] for each day of the period 1992-1999. The ECMWF Reanalysis data set ends in February 1994 and, therefore, is not used here. The first step is to calculate the daily averages of air temperature and humidity for each pressure level. These average humidities are integrated over all levels mentioned above to obtain W. In doing this, it is assumed that the contribution to W from levels above the 300 hPa level ($\approx$ 9 km) can be neglected. The average air temperatures and W are on the T106-grid with a spatial resolution of $1.125\,^\circ \times 2.25\,^\circ$ (*i. e.* approximately $63 \times 250\,\mathrm{km}^2$ at 60 °S and $42 \times 250\,\mathrm{km}^2$ at 70 °S) and are mapped into the NSIDC $12.5 \times 12.5\,\mathrm{km}^2$ grid using cubic spline interpolation (see image **d)** in Figures 3.2 and 3.3). The T106-grid provides the best spatial resolution when considering the entire Southern Ocean.

The available ECMWF data did not include the surface temperature required to estimate the sea ice and/or snow emissivity with Equation 5.8. Brightness temperatures obtained with the SSM/I 19 GHz channels at vertical polarization would allow to estimate the snow-ice interface temperature. However, this would require

to know the corresponding emissivity which is unkown. From the ECMWF data one can calculate the monthly average air temperature at 1000 hPa: $T_{a,1000}$. Due to an average surface pressure of (1000 ± 10) hPa in the Southern Ocean [King and Turner, 1997], $T_{a,1000}$ is quite similar to the average surface air temperature, which is usually measured at a height of 2 m above ground level: $T_{a,2m}$. However, the average $T_{a,2m}$ value is usually larger than the average surface temperature because of the quasi-permanent surface inversion evident over snow and/or sea ice, at least during winter. King and Turner [1997] found a temperature decrease of ≈ 2 K over the last 1.5 m above the ground over the Antarctic Plateau. Oke [1981] reported a temperature decrease of ≈ 3 K over the last 2 m above the ground over lake ice with a melting snow cover in spring and of 20 K over the lowermost 20 m above the ground over a fresh snow cover. In the latter case, the temperature difference between $T_{a,2m}$ and the surface temperature T_s may be 5 K or more since the air temperature increases exponentially with height due to radiative cooling from below. This is most pronounced during darkness and clear-sky conditions. Therefore, cold and thus dense air masses form near the surface particularly during winter, leading to a stronger stratification of the air and to larger air temperature lapse rates during winter than during summer. Moreover, the advection of warm air masses of oceanic origin associated with overpassing cyclones can lead to larger temperature changes during winter than during summer [Massom et al., 1997] because the temperature difference between the oceanic air mass and the air mass actually present over the sea ice is larger in winter than in summer. Consequently, one can expect a larger variability of $T_{a,2m}$ during winter than during summer as is evident in Figure 3.5.

From these findings and since T_s was not available from the ECMWF data used, average monthly values of $T_{a,1000} \approx T_{a,2m}$ minus one standard deviation obtained from the areas selected to calculate the sea ice tie points (see Section 5.2), are assumed to reflect the surface temperature T_s (see solid line in Figure 3.5). As one can identify from Figure 3.5 the standard deviation ranges between 1 K in summer and about 4 K in winter, matching the above-mentioned temperature difference. A comparison of the average surface temperature of September estimated with this approach for the period 1992-1999 with the climatological surface temperature distribution of September of the SMMR period [Gloersen et al., 1992] yields a good agreement – although the temperatures of the more recent period tend to be larger than those of the SMMR period. Using Equation 5.8 the relative error in the 85 GHz emissivity would be less than 2 % for an over- or underestimation of T_s by 5 K in both winter and summer.

However, strictly speaking, T_s is still too large to calculate the 85 GHz emis-

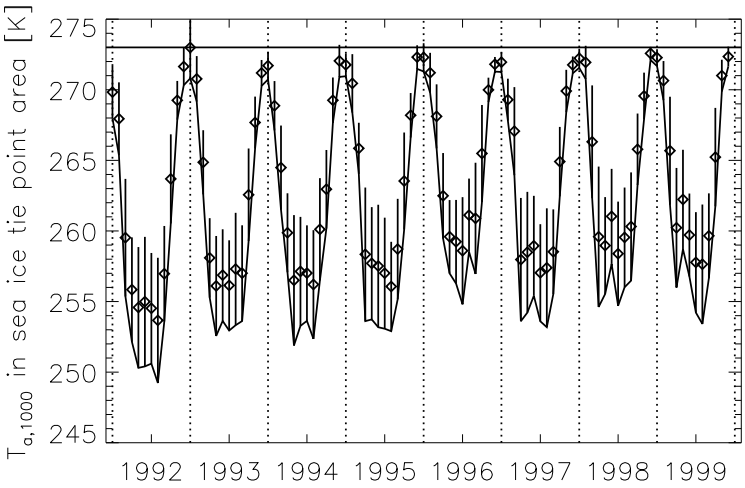

Figure 3.5: *Time-series of the monthly average ECMWF air temperature at the 1000 hPa level $T_{a,1000}$ of all pixels belonging to the area selected to calculate the sea ice tie point of the considered month for the period 1992-1999. The error bars denote $\pm$ one standard deviation. The solid line denotes the temperature assumed as monthly mean surface temperature T_s of the area and month selected.*

sivity with Equation 5.8 since at 85 GHz, despite the small penetration depth, the radiating layer is below the surface. Therefore, when considering snow and its often very strong negative vertical temperature gradient, the physical temperature of the radiating layer is expected to be larger than the snow surface temperature. For this reason, when overestimating T_s with the approach mentioned above, then T_s would be closer to the physical temperature of the radiating layer.

3.4 *In situ* Data

Observations of the sea ice cover from the bridge of a ship can be very helpful when judging the reliability of products from sea ice concentration algorithms. However, there are some limitations. At first, these observations reflect the sea ice conditions along the ship's track only. Consequently, they are often biased towards a smaller sea ice concentration and a thin ice type because regions covered by thin ice and/or less sea ice are easier to cross with a ship. Secondly, these observations are determined by the visibility. During bad weather conditions such as fog or snow fall, the ship's field of view (SFOV) can be below 100 m in diameter. Also, the visibility is limited during hours of darkness. When considering one

SSM/I pixel, in addition to the bias caused by navigating the ship through areas with a small average sea ice concentration, one can assume positive and negative deviations of the observed from this pre-defined average sea ice concentration to have the same probability. Furthermore, the observer's skills and experience are of crucial importance. Different observers can yield different results for the same sea ice conditions. These facts have to be taken into account when comparing ship observations with remotely sensed sea ice concentrations.

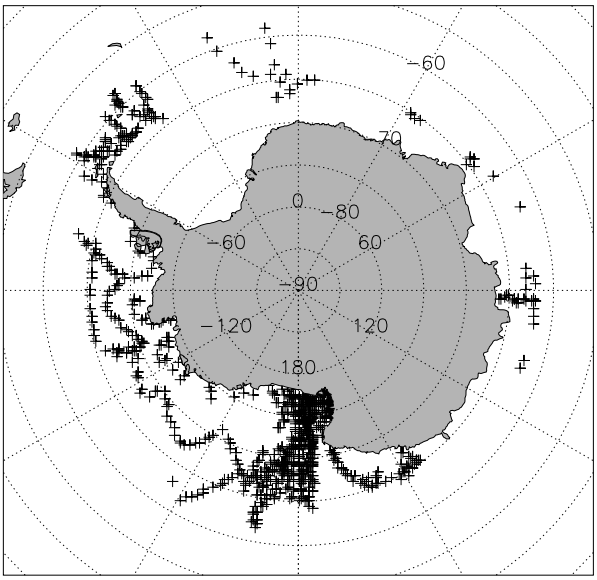

Figure 3.6: *Sample set of positions of the U.S. Research Vessel* NATHANIEL B. PALMER *in the Southern Ocean during 1994-1998. Sea ice observations taken at these positions are used in this thesis.*

In this thesis, sea ice observations are used which were made aboard the U.S. research vessel *Nathaniel B. Palmer* during its trips into the Southern Ocean. This data set was provided by Antarctic Meteorology Research Center (AMRC) [1999] and comprises detailed observations of the sea ice cover taken every six hours (concentration in tenths, snow thickness in centimeter, ice type and corresponding fraction within the SFOV) from 1994-1998. Only those observations are put into a time-series which reveal sea ice concentrations above $15\,\%$. Depending on the velocity of the ship all observations of one day can fall into different cells of the NSIDC $25 \times 25\,\mathrm{km}^2$ grid used for the comparison given in Section 6.1.2. Therefore, daily averages are not calculated in general. Only if more than one observation falls into a grid cell on one day, then the observations are averaged

avoiding cases where, for the day considered, the ship is on station, providing four times the same sea ice concentration, while only one value can be taken from SSM/I data. Therefore, for each pixel, both data sets reveal the same statistics: one value per day. This reduces the total amount of data to be used for the comparison to about 850 observations. The corresponding ship positions are shown in Figure 3.6.

Chapter 4

Sea Ice Concentration Retrieval

This chapter focusses on algorithms that utilize brightness temperatures measured with a spaceborne microwave sensor to compute the sea ice concentration. Common background of these algorithms is the relationship between the sea ice cover fraction in the FOV of the sensor and the brightness temperatures or a variable direved such as the polarization difference or the gradient ratio. In the following two sections, the two most widely used methods to retrieve the sea ice concentration, the NASA Team algorithm (Section 4.1) and the Bootstrap algorithm (Section 4.2) will be described. Attempts using the SSM/I 85 GHz channels for the sea ice concentration retrieval are discussed in Section 4.3.

4.1 NASA Team Algorithm

The NASA Team (NT) algorithm was developed by Cavalieri et al. [1984] to retrieve the total sea ice concentration C and the fractions covered by FY and MY ice from data obtained with the NIMBUS-7 SMMR sensor. This algorithm was adopted for SSM/I data [Cavalieri et al., 1991]. The basis of the NT algorithm is as follows. Neglecting atmospheric effects, the measured brightness temperature can be described by a linear combination of the three dominant surface types: open water, FY and MY ice, each weighted by its fraction within the FOV

$$T_p(f) = C_w T_{p,w}(f) + C_f T_{p,f}(f) + C_m T_{p,m}(f). \tag{4.1}$$

This equation relates the brightness temperature $T_p(f)$ measured by the sensor at frequency f and horizontal (h) or vertical (v) polarization p to the fractions (C_w, C_f and C_m) of a unit area of open water, FY and MY ice, respectively, using

typical brightness temperatures of open water $T_{p,w}(f)$, FY ice $T_{p,f}(f)$ and MY ice $T_{p,m}(f)$. These latter values are henceforth called *tie points*.

The brightness temperature *polarization* difference (*BTPD*) $T_v(f) - T_h(f)$ was found to be significantly smaller over sea ice than over open water at the SMMR and the SSM/I frequencies ([Comiso et al., 1992], [Steffen et al., 1992], see also Figure 5.1 for 85 GHz) and to change almost linearly with the total sea ice concentration $C = C_f + C_m$. Typical brightness temperatures of FY and MY ice differ more at 37 GHz than at 19 GHz – especially at vertical polarization – due to a larger contribution of volume scattering at 37 GHz. Thus, using the brightness temperature *frequency* difference (*BTFD*) $T_v(f_2) - T_v(f_1)$ ($f_2 = 37$ GHz, $f_1 = 19$ GHz), FY and MY ice can be distinguished. In order to eliminate the influence of a changing physical temperature of the radiating sea ice/snow layer, the BTPD and the BTFD are divided by the corresponding brightness temperature sum. This yields the basic parameters of the NT algorithm at frequencies f_1 and f_2: the *normalized* brightness temperature polarization difference (*NBTPD*)

$$P(f_1) = \frac{T_v(f_1) - T_h(f_1)}{T_v(f_1) + T_h(f_1)}, \tag{4.2}$$

and the *normalized* brightness temperature frequency difference (*NBTFD*), the so-called *gradient ratio*

$$G(f_2, f_1) = \frac{T_v(f_2) - T_v(f_1)}{T_v(f_2) + T_v(f_1)}. \tag{4.3}$$

Inserting of Equations 4.2 and 4.3 in Equation 4.1 and solving for C_f and C_m leads to

$$C_f = \frac{F_0 + F_1 P + F_2 G + F_3 PG}{D} \tag{4.4}$$

and

$$C_m = \frac{M_0 + M_1 P + M_2 G + M_3 PG}{D}, \tag{4.5}$$

where

$$D = D_0 + D_1 P + D_2 G + D_3 PG. \tag{4.6}$$

The frequencies are omitted in Equations 4.4 – 4.6 for clarity. The numerical coefficients D_i, F_i and M_i are based on the tie points of the involved surface types.

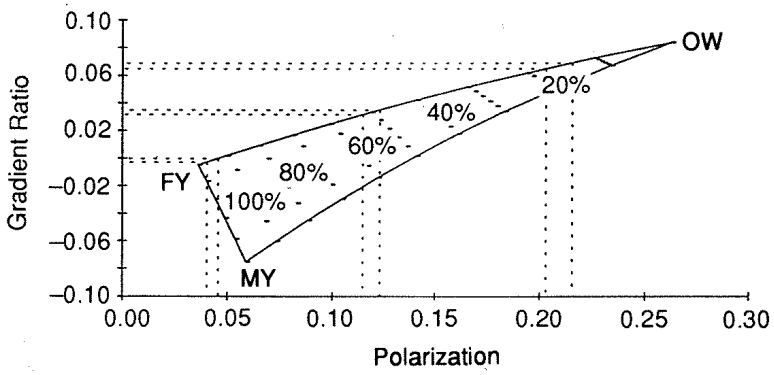

Figure 4.1: *Schematic view of the deformed triangle given by the tie points in the P-G plane (from [Gloersen et al., 1992]).*

Figure 4.1 shows the location of the tie points of open water, FY and MY ice in the P-G plane calculated with Equations 4.2 and 4.3. Clearly, P changes mainly due to C and more at low than at high sea ice concentrations. The change of G is mainly caused by the different properties of FY and MY ice (Section 2.3) and is largest at high sea ice concentrations. For the Arctic, Cavalieri et al. [1984] obtained C and C_m with accuracies of approximately $7\,\%$ and $19\,\%$, respectively. Average standard deviations of C are about $3\,\%$ in the central Arctic. However, brightness temperatures measured at 19 and 37 GHz may be considerably influenced by the atmosphere [Fuhrhop et al., 1997], [Oelke, 1997]. This can lead to an overestimation of C, especially in the marginal sea ice zone (MIZ) [Maslanik, 1992]. In order to avoid this overestimation various weather filters can be implemented. Either C values below $15\,\%$ are excluded from the algorithm product using thresholds of $G(37, 19)$ and $G(22, 19)$ and neglecting the weather influence at higher C values [Gloersen and Cavalieri, 1986], [Steffen et al., 1992]. Or a radiative transfer model is used to quantify the brightness temperature change due to the weather influence and to correct the measured brightness temperatures for the atmospheric influence [Heygster et al., 1996], [Thomas, 1998].

The NT algorithm has been used to produce time-series of C and C_m from both SMMR and SSM/I data by numerous investigators, *e. g.* [Heygster et al., 1996], [Cavalieri et al., 1997], [Johannessen and Miles, 1999]. However, this algorithm has a few shortcomings. As all algorithms based on spaceborne passive microwave radiometry, it suffers from the poor spatial resolution (Section 3.1.2). The contamination of the data by land present in the FOV hampers the possibility to detect coastal polynyas [Markus and Burns, 1995], [Bennartz, 1999]. Thin

ice exhibits emissivities between those of FY ice and open water and can cause – if entirely covering the FOV ($C = 100\,\%$) – the same brightness temperature than a FOV covered by a considerably smaller fraction of FY ice (*e. g.* $50\,°$). However, in this latter case the retrieval of C can be significantly improved in regions covered mainly with thin ice using the *thin-ice* algorithm proposed by Cavalieri [1994] or the method of Wensnahan et al. [1993]. Applying the NT algorithm in the Antarctic requires a modification: old ice is not only less wide-spread in the Southern Ocean but is, on average, younger than in the Arctic and is covered by snow all the year round (see Section 2.3.2). Consequently, a different set of tie points is used in the Southern Ocean and one speaks of sea ice types A and B which compare to FY ice and old ice, respectively [Comiso et al., 1997].

In this study, the NT algorithm is used with tie points given by Comiso et al. [1997] (see Table 4.1) and the extended weather correction proposed by Thomas [1998]. This modified NT algorithm is henceforth called PELICON (PE) algorithm. For the extended weather correction, at first the fields of the surface wind speed V, the integrated water vapor content W and the integrated cloud liquid water content L are calculated with the algorithms described in Section 3.2 over open water. In the next step, in order to model the weather influence on the SSM/I brightness temperatures, these fields are extrapolated into areas covered by less than $50\,\%$ sea ice derived with the NT algorithm. This is followed by modelling the change in the brightness temperature at 19 and 37 GHz for open water and ice concentrations up to $50\,\%$. The results are used to correct the brightness temperatures at 19 and 37 GHz for the atmospheric influence and to calculate more reliable sea ice concentrations in the MIZ. This method allows to account for the wide-spread direct atmospheric influence in the MIZ on a daily basis [Thomas, 1998]. This is an advantage compared to just using a threshold because areas

Table 4.1: *Tie points (brightness temperatures in Kelvin) of open water and sea ice types A and B used to calculate C with the PELICON algorithm in the Southern Ocean [Heygster et al., 1996], [Thomas, 1998]. Letters h and v refer to horizontal and vertical polarization, respectively.*

	19 GHz, h	19 GHz, v	37 GHz, v
Open water	100.3	176.6	200.5
Ice type A	237.8	249.8	243.3
Ice type B	193.7	221.6	190.3

covered with less than 15 % sea ice are not excluded generally and false sea ice concentrations caused by the atmospheric influence can be eliminated according to the actual atmospheric conditions. However, an extrapolation of atmospheric parameters into the area covered by sea ice may be questionable.

4.2 Bootstrap Algorithm

The Bootstrap (BS) algorithm was developed by Comiso and Sullivan [1986] and can be regarded as a multi-dimensional extension of the method applied to ESMR data by Zwally et al. [1983]. The BS algorithm utilizes a linear interpolation between two data point clusters in the plane given by the involved brightness temperatures as is shown in Figure 4.2, **(a)**. Comiso and Sullivan [1986] stated that two modes are necessary to obtain reliable sea ice concentrations: the *polarization mode* which uses the 37 GHz brightness temperatures at both polarizations and the *frequency mode* which uses vertically polarized 19 (SMMR: 18) and 37 GHz brightness temperatures only. The first mode was found to give reliable results in regions covered by old ice such as the central Arctic while in areas with temporal highly variable sea ice conditions the second mode is preferred.

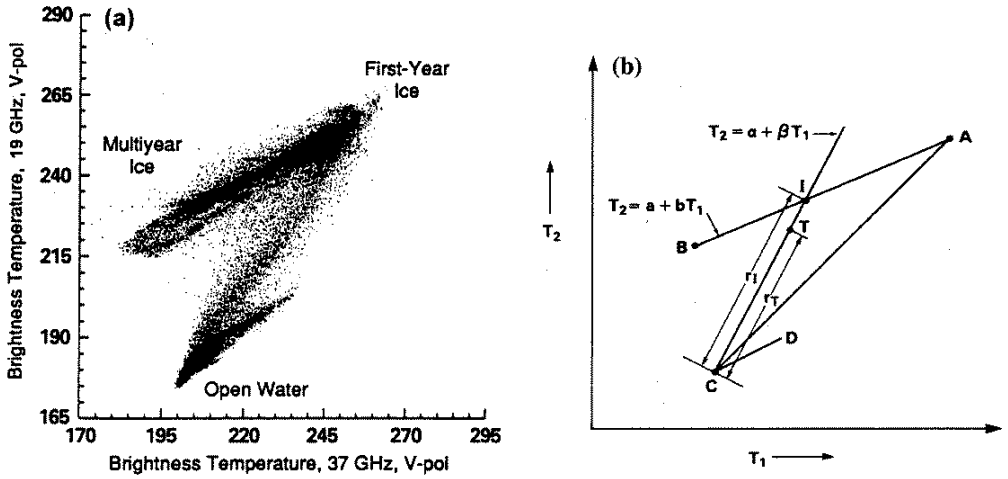

Figure 4.2: **(a)***: SSM/I 19 and 37 GHz brightness temperatures, vertical polarization, measured in the Arctic [Eppler et al., 1992].* **(b)***: Schematic view of the Bootstrap technique to retrieve C [Comiso and Sullivan, 1986]. In the frequency mode (see text),* T_1 (T_2) *is the brightness temperature at 37 GHz (19 GHz) and vertical polarization.*

Figure 4.2 **(b)** illustrates the Bootstrap technique. It is assumed that each point along the line BA represents $100\,\%$ sea ice as a mixture of ice types A and B. The line CD represents open water. Each point T along the line CI can be considered as a mixture of sea ice of types A and B and open water, *i. e.* as the total sea ice concentration C. If point I is the tie point of sea ice $T_{p,ice}(f_2)$ and point C the tie point of open water $T_{p,ow}(f_2)$ at frequency f_2 and polarization p, one can infer the sea ice concentration C from

$$C = \frac{T_p(f_2) - T_{p,ow}(f_2)}{T_{p,ice}(f_2) - T_{p,ow}(f_2)}. \tag{4.7}$$

While $T_{p,ow}(f_2)$ remains fixed, the values of $T_{p,ice}(f_2)$ are estimated from the brightness temperatures measured at the second polarization (polarization mode) or frequency (frequency mode). In the latter case one gets

$$T_{v,ice}(f_2) = a + bT_{v,ice}(f_1), \tag{4.8}$$

where $f_1 = 37\,\mathrm{GHz}$ and $f_2 = 19\,\mathrm{GHz}$. The intersection with the $19\,\mathrm{GHz}$ axis provides a, and b is the slope of the line BA (see Figure 4.2,**(b)**).

For Arctic old ice, accuracies around $4\,\%$ are typically achieved with the BS algorithm [Steffen et al., 1992]. But as soon as the surface properties become more variable, for instance in the MIZ or during melt-onset, the accuracies found are only $10\,\%$ or more. This is probably caused by the influence of varying sea ice/snow properties and changes in the physical temperature leading to a rather large brightness temperature change but quite a small change in the parameters derived such as the NBTPD or the NBTFD (see Section 2.3.4). A comparison of C obtained with the NT and the BS algorithms conducted by Burns [1993] for the Weddell Sea yields generally a good agreement. Large differences are limited to thin ice areas. However, a comparison conducted more recently by Comiso et al. [1997] for the entire Antarctic sea ice cover reveals that C values obtained with the BS algorithm exceed those computed with the NT algorithm by about $10\,\%$ and thus agree much better with C values derived from visible imagery and active microwave radiometry.

In this thesis, the BS algorithm is used in its frequency mode together with seasonal tie points given by Comiso et al. [1997] (see Table 4.2) and without applying a weather filter. Consequently, C is expected to be overestimated in the MIZ during periods of a large weather influence when compared to the NT and PE algorithms (Section 4.1). However, for sea ice concentrations above $50\,\%$, sea ice concentrations computed with the PE and BS algorithms have the same weather

contamination.

Table 4.2: *Tie point of open water and parameters a and b of the linear relationship between $T_{v,ice}(f_1)$ and $T_{v,ice}(f_2)$ ($f_1 = 37$ GHz, $f_2 = 19$ GHz) used to retrieve C with the Bootstrap algorithm in the Southern Ocean [Comiso et al., 1997].*

	summer	winter
$T_{v,ow}(f_2)$ [K]	179.0	
a [K]	102.0	139.0
b	0.620	0.473

4.3 About using 85 GHz Data

The 85 GHz SSM/I channels have already been used in numerous investigations of the sea ice cover, although the weather influence is significantly larger compared to the other SSM/I channels (Section 2.4). Besides the sea ice motion, inferred from 85 GHz SSM/I data in the Arctic [Martin and Augstein, 2000] and in both polar regions [Emery et al., 1997], [Kwok et al., 1998], [Liu and Cavalieri, 1998], these channels can be exploited to retrieve the sea ice concentration C on a medium resolution (Section 4.3.1) and to discriminate different sea ice types. Lomax et al. [1995] made an encouraging attempt to infer the Arctic MY ice concentration C_m from 85 GHz SSM/I data using the so-called *polarization corrected* temperature (PCT). This temperature is originally used to identify precipitating clouds at temperate to tropical latitudes, exploiting the sensitivity of the 85 GHz channels to scattering by precipitation particles (see Section 2.4). However, these particles are significantly smaller at polar latitudes and, therefore, cause a much weaker scattering. Lomax et al. [1995] found no agreement between the distribution of precipitating clouds and the PCT in the Arctic. Instead, they identified the PCT to vary smoothly with the gradient of C_m and exploited this finding to retrieve C_m. Moreover, the higher spatial resolution at 85 GHz compared to the other SSM/I channels was combined with the smaller sensitivity to atmospheric effects at 37 GHz to estimate the area of subpixel-scale coastal polynyas in the Antarctic [Markus and Burns, 1995] and to improve the determination of the sea ice edge [Hunewinkel et al., 1998]. Both approaches illustrate that 85 GHz SSM/I data can be used at least to improve the determination of sea ice extent.

4.3.1 The SVENDSEN algorithm

Svendsen et al. [1987] have been the first to develop an algorithm, henceforth called SVENDSEN (SV) algorithm, using data obtained at frequencies above 37 GHz to retrieve the sea ice concentration. They used the relation given by Equation 4.1. By introducing the brightness temperature polarization difference BTPD at 85 GHz $\Delta T = T_v - T_h$ the following relation is obtained

$$\Delta T = \gamma(aC + \Delta T_{s,ow}), \quad i.e. \quad C = \frac{1}{a}\left(\frac{\Delta T}{\gamma} - \Delta T_{s,ow}\right) \tag{4.9}$$

where C is the total sea ice concentration and $\Delta T_{s,ow}$ the surface BTPD of open water. Assuming similar BTPD values for FY and MY ice, the difference between the surface BTPD of sea ice $\Delta T_{s,ice}$ and $\Delta T_{s,ow}$ is given by a. The parameter γ expresses the atmospheric influence, which depends on the total atmospheric optical depth τ. A few assumptions were made concerning absorption, emission and scattering of the microwave radiation in the atmosphere [Svendsen et al., 1983], [Svendsen et al., 1987]. In order to encompass that τ is unknown, a self-adjusting algorithm was developed. For each sensor overpass, minimum and maximum values of ΔT measured by the sensor are selected as tie points of sea ice ΔT_{ice} and open water ΔT_{ow}, respectively. In doing this, at least some footprints have to be covered by open water or sea ice entirely. These tie points include the actual atmospheric conditions. For 100 % and 0 % sea ice ($C = 1$ and $C = 0$), ΔT can be set to ΔT_{ice} and ΔT_{ow} in Equation 4.9, respectively. The resulting two expressions, one for sea ice and one for open water, can be solved for γ which in turn can be inserted into Equation 4.9 yielding the following two special cases

$$\begin{aligned} C \Rightarrow 1: \quad & C = \left(1 + \frac{\Delta T_{s,ow}}{a}\right)\frac{\Delta T}{\Delta T_{ice}} - \frac{\Delta T_{s,ow}}{a}, \\ C \Rightarrow 0: \quad & C = \left(\frac{\Delta T_{s,ow}}{a}\right)\frac{\Delta T}{\Delta T_{ow}} - \frac{\Delta T_{s,ow}}{a}. \end{aligned} \tag{4.10}$$

These two cases (Equation 4.10) are independent of the atmospheric influence and are used as boundary conditions for a third-order polynomial, assuming that atmospheric effects on the brightness temperatures decrease with increasing surface emissivity and, thus, are a continuous function of C. This polynomial results in a matrix equation which can be solved for the coefficients of the polynomial that are finally used to compute C. An error analysis conducted by Svendsen et al.

[1987] reveals errors of about 5 % for the central Arctic. However, errors may be significantly larger elsewhere and particularly increase with decreasing C.

In the past, the SV algorithm has been used to retrieve the Arctic sea ice concentration with 85 GHz SSM/I data by Lomax et al. [1995] and Lubin et al. [1997]. Recently, Kaleschke (2000) produced daily maps of C of both polar regions with modified version of the SV algorithm (*http://www.seaice.de*). The study of Lomax et al. [1995] focusses on winter sea ice conditions and confirms the results obtained by Svendsen et al. [1987]. Lomax et al. [1995] found that C obtained with the SV algorithm agrees with C derived with the NT algorithm within standard deviations of approximately 3 % and 6 % for clear-sky and overcast Arctic winter conditions, respectively. Lubin et al. [1997] compared ship observations of the sea ice cover with the results of the SV and the NT algorithms for a cruise across the central Arctic in summer 1994. The SV algorithm has been modified slightly: Lubin et al. [1997] used fixed tie point for the entire cruise. They stated that C obtained with the SV algorithm is at least as accurate as C retrieved with the NT algorithm. Also, when compared to the NT algorithm, the SV algorithm provides more accurate information about the sea ice cover in the MIZ and in areas of small- to meso-scale spatial inhomogenities within the pack ice such as leads and polynyas.

4.3.2 Modifications to the SVENDSEN algorithm

The procedure to determine tie points of open water and sea ice using minima and maxima of ΔT of selected FOVs is a possible error source of the SV algorithm. The maximum ΔT certainly represents open water with the smallest weather influence, *i. e.* low surface wind speeds and small atmospheric water contents. However, the minimum ΔT can stem from regions where the weather influence is high (see Section 2.4.2 and Section 5.3) or where a melting sea ice/snow surface is present or both. In this latter case, the sea ice tie point would be significantly smaller than it would be, for instance, under clear-sky conditions. This would cause an underestimation of C in areas where the weather influence is small or the sea ice/snow surface is dry.

Lubin et al. [1997] investigated the error which would be made in C if the weather influence expressed as atmospheric optical depth τ in the area considered, differs from the weather influence included implicitely in the tie points. Generally, C is overestimated for larger and underestimated for smaller values of τ compared to the τ values given by the tie point selection. Figure 4 in Lubin et al. [1997] shows the range of τ where the SV algorithm estimates C with an accuracy of

$\pm 5\,\%$. For typical conditions, *i. e.* larger optical depths over open water than over sea ice, the retrieval of C is almost independent of τ as long as $C \approx 100\,\%$. But it becomes increasingly sensitive to changes in τ for lower sea ice concentrations. An increase of L by $100\,\mathrm{g\,m^{-2}}$, as can be associated with an upcoming frontal cloud band, corresponds to an increase of τ by ≈ 0.1 and might cause errors above $20\,\%$ for $C < 60\,\%$. Figure 4 [Lubin et al., 1997] shows also, that the SV algorithm is sensitive to changes either in the physical temperature or in the average emissivity polarization difference $\Delta\epsilon$, both with regard to the conditions given by the tie point selection. A change in $\Delta\epsilon$ can be caused, for instance, by thin ice present in an area of predominantly thick ice or by polarization-dependent volume scattering (see Sections 2.3.3 and 2.3.4). If the sea ice tie point is 10 K and the BTPD in the considered area is 5 K then, according to Lubin et al. [1997], C would be generally overestimated in areas with $C > 80\,\%$ for typical τ values.

The studies of Lubin et al. [1997] and Lomax et al. [1995] consider only either summer or winter conditions. Therefore, large changes in the atmospheric attenuation can be neglected. In the Arctic, largest changes in the surface properties occur most likely in summer and early fall during the formation and the decay of melt ponds. Moreover, the surface is predominantly wet during Arctic summer melt. The Antarctic is quite different when compared to the Arctic, particularly concerning the typical snow properties, the weather conditions and their impact on the snow (Section 2.3.2). Both, snow properties and weather conditions can vary on a day-to-day scale all the year round in the Antarctic. This causes the errors discussed above to occur more frequently when applying the SV algorithm without modification in the Antarctic.

The high cyclonic activity in the Antarctic cause frequent changes in the air temperature influencing the properties and particularly the temperature of the surface of the sea ice and its snow cover. Due to the small penetration depth at 85 GHz, these brightness temperatures react much faster to changing surface temperatures than those measured at the other SSM/I channels. Assuming typical sea ice emissivities of $\epsilon_v = 0.92$ and $\epsilon_h = 0.88$, and $\Delta T = 10\,\mathrm{K}$, a typical surface temperature increase from $-20\,^\circ\mathrm{C}$ to $0\,^\circ\mathrm{C}$ [Massom et al., 1997] yields a relative increase of ΔT by $10\,\%$. Using average tie points of sea ice (8 K) and open water (35 K) [Lubin et al., 1997], this increase would cause an overestimation of C by approximately $10\,\%$ according to Equation 4.9. This can be avoided using the normalized brightness temperature polarization difference (NBTPD) (see Section 4.1). For the same surface temperature increase the relative change in the NBTPD is below $0.1\,\%$. Furthermore, the SV algorithm assumes the weather-induced brightness temperature change to be always smaller over sea ice than

over open water since τ decreases with decreasing air temperatures which in turn is linked to an increasing sea ice concentration. This assumption is violated particularly in areas covered by frontal cloud bands where τ can be significantly larger over sea ice than over open water.

Taking these facts together, the SV algorithm will undergo the following modifications to become the SEA LION algorithm:

- Usage of the normalized rather than the plain brightness temperature polarization difference to be more independent of the surface temperature of the sea ice and its snow cover.
- Usage of new open water and sea ice tie points of sea ice derived from selected areas separately for each month.
- Quantification of the weather influence on the 85 GHz SSM/I brightness temperatures with MWMOD and correction of these brightness temperatures for this influence [St. Germain, 1993].

Chapter 5

Description of the Algorithm

The first section of this chapter sketches the basic method of the SEA LION (SL) algorithm to calculate the sea ice concentration. The tie point retrieval is described in Section 5.2 while Section 5.3 gives an overview of the atmospheric influence on the 85 GHz SSM/I brightness temperatures. This is followed by the method to correct these SSM/I data for this influence and by the description of the complete SL algorithm. An error estimation is presented in the last section of this chapter.

5.1 Basic Method

The base of the SL algorithm is as follows. Ignoring atmospheric effects, the brightness temperature T_p emitted at frequency f and polarization p ($p = h$ for horizontal and $p = v$ for vertical polarization) from a partly sea ice covered unit area with the fractions of open water C_w, FY ice C_{FY} and MY ice C_{MY} can be written as [Svendsen et al., 1987]

$$T_p(f) = C_w \epsilon_{p,w}(f) T_w + C_{FY} \epsilon_{p,FY}(f) T_{FY} + C_{MY} \epsilon_{p,MY}(f) T_{MY}. \qquad (5.1)$$

The emissivities of open water, FY ice and MY ice at frequency f and polarization p are given by $\epsilon_{p,w}(f)$, $\epsilon_{p,FY}(f)$ and $\epsilon_{p,MY}(f)$, respectively, and T_w, T_{FY} and T_{MY} denote the physical temperature of the sea surface and of the radiating layer of FY ice and MY ice, respectively. Although a sea ice cover of a few millimeters thickness is optically thick at 85 GHz (see Section 2.3) it is difficult to unambiguously discriminate open water from sea ice with 85 GHz brightness temperatures alone. This is mainly caused by snow which can lead to a broad range of surface emissivities at 85 GHz and thus $T_p(85)$ values (see Section 2.3). Moreover, $T_p(85)$

can be influenced largely by the physical temperature of the radiating layer which may approach the SST during melting conditions.

The normalized brightness temperature polarization difference (NBTPD) has already been defined in Equation 4.2 and is used in the SL algorithm at 85 GHz: $P(85)$. At the surface, $P(85)$ is also the ratio of the emissivity polarization difference $\epsilon_v(85) - \epsilon_h(85)$ and the sum of both emissivities $\epsilon_v(85) + \epsilon_h(85)$. The NBTPD is considerably less influenced by snow properties and the physical temperature of the radiating layer than the $T_p(85)$ values (see Sections 2.3 and 4.3). NBTPD values calculated from sea ice emissivities measured *in situ* at 90 GHz in

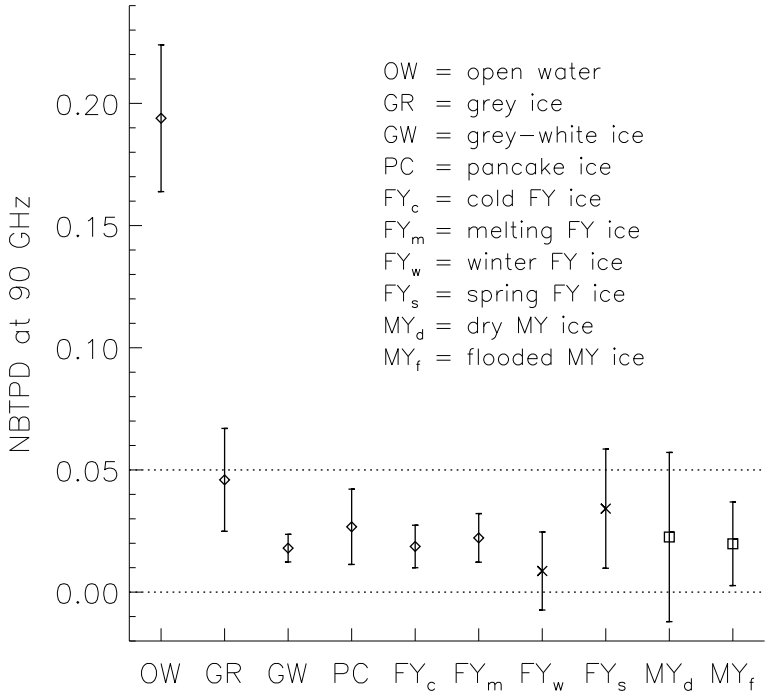

Figure 5.1: *NBTPD of different sea ice types and open water calculated from* in situ *Antarctic [Comiso et al., 1992] and Arctic [Eppler et al., 1992] emissivity measurements at 90 GHz. Diamonds refer to Weddell Sea surface types, squares to Arctic multiyear (MY) ice. The crosses denote the NBTPD calculated from average first-year (FY) ice emissivities taken during cruises of the German research vessel* POLARSTERN *during the Winter Weddell Sea Project (WWSP) in 1986 [Grenfell et al., 1994]. The error bars denote* $\pm\sigma_P$ *calculated with Equation 5.2.*

the Weddell Sea [Comiso et al., 1992] and in the Arctic [Eppler et al., 1992] are given in Figure 5.1. They are small over sea ice and quite large over open water, and allow to discriminate these two surfaces. The error bars given in Figure 5.1 denote the range given by ± one standard deviation of the NBTPD (σ_P) calculated with

$$\sigma_P = \left(\left(\frac{2\epsilon_v \sigma_{\epsilon_h}}{(\epsilon_v + \epsilon_h)^2} \right)^2 + \left(\frac{2\epsilon_h \sigma_{\epsilon_v}}{(\epsilon_v + \epsilon_h)^2} \right)^2 - \frac{8\epsilon_v \epsilon_h r_{\epsilon_v \epsilon_h} \sigma_{\epsilon_v} \sigma_{\epsilon_h}}{(\epsilon_v + \epsilon_h)^4} \right)^{\frac{1}{2}}. \quad (5.2)$$

The first two terms of Equation 5.2 denote the contributions of σ_{ϵ_h} and σ_{ϵ_v}, respectively. The third term of Equation 5.2 is the covariance of ϵ_v and ϵ_h. The correlation coefficient $r_{\epsilon_v \epsilon_h}$ are not provided by Comiso et al. [1992] and/or Eppler et al. [1992] and is assumed to be 0.9. Correlation coefficients calculated from the sea ice emissivities used to derive the NBTPD shown in Figure 5.1 and from 85 GHz SSM/I data of the area selected to estimate the sea ice tie points for the period 1992-1999 (see Section 5.2) are 0.975 and 0.988, respectively. Therefore, the chosen $r_{\epsilon_v \epsilon_h}$ value can be regarded as a lower boundary and standard deviations may be smaller than indicated in Figure 5.1.

The NBTPD values of Figure 5.1 are similar for all sea ice types except grey ice and also nilas (not shown). Antarctic sea ice consists primarily of FY ice (see Section 2.3). Therefore, at $f = 85$ GHz one can simplify Equation 5.1 by setting $C \approx C_{FY} \approx C_{MY}$, $\epsilon_{p,i}(85) \approx \epsilon_{p,FY}(f) \approx \epsilon_{p,MY}(f)$, $T_i \approx T_{FY} \approx T_{MY}$ and $C_w = 1 - C$. This yields

$$T_p(85) = (1 - C)\epsilon_{p,w}(85) T_{s,w} + C\epsilon_{p,i}(85) T_i, \quad (5.3)$$

with the total sea ice concentration C, the physical temperature of the radiating sea ice or snow layer T_i and the emissivity of this layer $\epsilon_{p,i}(85)$ at 85 GHz and polarization p. Inserting of Equation 5.3 into Equation 4.2 and solving for C leads to

$$C = \left(1 + \frac{T_{v,i} + T_{h,i}}{T_{v,w} + T_{h,w}} \frac{P_i - P}{P - P_w} \right)^{-1}, \quad (5.4)$$

where $T_{v,w}$, $T_{h,w}$ and P_w are the tie points of open water and $T_{v,i}$, $T_{h,i}$ and P_i are the tie points of sea ice. The frequency is omitted here for clarity. Knowing the tie points, Equation 5.4 can be used to calculate C from surface brightness temperatures. Equation 5.4 is described in more detail in the Appendix.

5.2 Tie Point Retrieval

Similar to the sea ice concentration algorithms discussed in Chapter 4 the SL algorithm utilizes two sets of tie points, one for sea ice (Section 5.2.1) and one for open water (Section 5.2.2). They are estimated for each month separately in order to consider the highly variable sea ice and snow properties discussed in Section 2.3 and to have open water tie points which are statistically consistent with the sea ice tie points. Accounting for the temporal variability of surface properties relevant for the tie points was proven to have quite a high impact on the quality of the results of sea ice concentration algorithms [Burns, 1993].

5.2.1 Sea Ice

The *in situ* emissivity measurements given by Comiso et al. [1992] are limited to the eastern Weddell Sea and to Austral winter and spring. They are not representative for the entire Antarctic sea ice cover and for all seasons. One goal of the SEA LION project [Lemke et al., 2000] is to calculate C for the entire Southern Ocean for the period from 1992 to present. Therefore, sea ice tie points are derived from NSIDC daily gridded 85 GHz SSM/I brightness temperatures [NSIDC, 1996]. This ensures that sea ice types and snow cover properties of all Antarctic regions and seasons can contribute to the sea ice tie points. At first, maps of the average NBTPD at 85 GHz $< P >$ and of its standard deviation σ_P are calculated on a pixel-by-pixel basis for each month. Examples of both maps are shown in Figures 5.2 and 5.3 for July 1999.

Figure 5.2 shows areas of high (≥ 0.08) and low (≤ 0.035) values of $< P >$ separated by a region with a sharp gradient. These areas certainly belong to open water, sea ice and the MIZ, respectively. Over sea ice, $< P >$ is similar to the NBTPD obtained from *in situ* emissivity measurements at 90 GHz (see Figure 5.1). Over open water, $< P >$ is much larger than the corresponding NBTPD values shown in Figure 5.1. This is caused by the atmospheric water content (integrated contents of water vapor W and cloud liquid water L) and the surface wind speed V which all decrease $P(85)$ (see Sections 2.4 and 5.3). The parameters V, W and L can be calculated from SSM/I data with the methods described in Section 3.2 over open water. Table 5.1 shows monthly averages and corresponding standard deviations of V, W and L calculated within an approximately 100 km wide open water area adjacent to the Antarctic sea ice edge provided by the PE algorithm (see Section 4.1 and [Heygster et al., 1996]) and averaged over the period 1992-1999. The jump in the standard deviations of V between April/May and

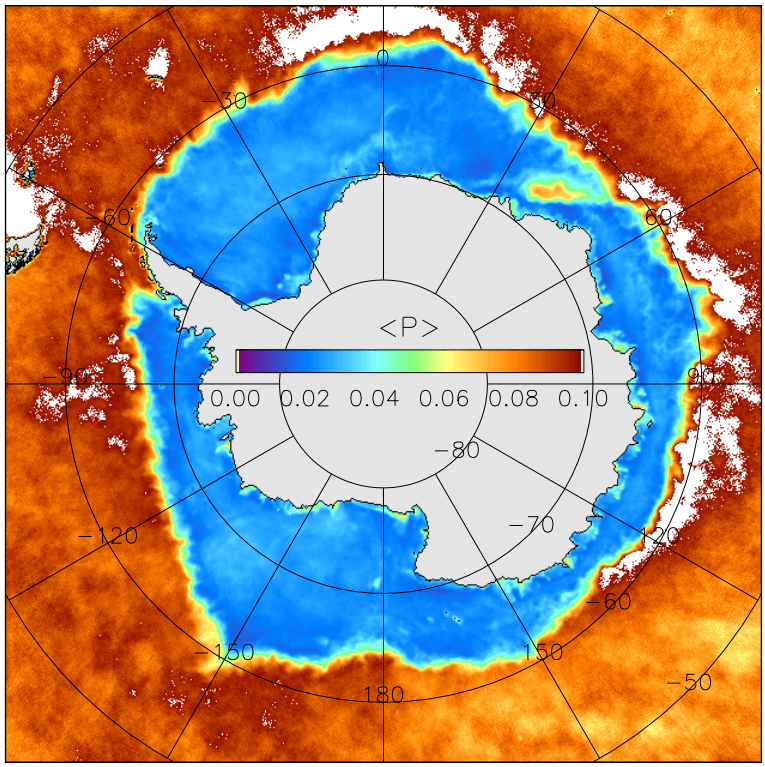

Figure 5.2: *Map of the average NBTPD at 85 GHz:* $< P >$*, for July 1999.*

Table 5.1: *Monthly averages of* V *[*$m\,s^{-1}$*],* W *[*$kg\,m^{-2}$*] and* L *[*$g\,m^{-2}$*]* $\pm$ *the corresponding average standard deviations (top, middle and bottom row of the months considered) calculated over a selected open water area (see text) and averaged over the period 1992-1999.*

Jan.	Feb.	Mar.	Apr.	May	Jun.
7.9 ± 2.8	7.8 ± 2.6	9.3 ± 2.9	9.7 ± 2.8	10.4 ± 3.4	10.0 ± 3.4
9.2 ± 2.7	8.2 ± 2.6	8.5 ± 2.6	8.1 ± 2.6	8.3 ± 2.5	8.0 ± 2.3
36 ± 56	32 ± 53	36 ± 57	35 ± 54	34 ± 51	35 ± 51
Jul.	Aug.	Sep.	Oct.	Nov.	Dec.
11.0 ± 3.5	11.6 ± 3.5	11.3 ± 3.4	11.3 ± 3.4	9.7 ± 2.8	8.9 ± 2.7
8.3 ± 2.4	8.3 ± 2.4	8.2 ± 2.4	8.7 ± 2.5	8.9 ± 2.6	9.5 ± 2.7
34 ± 50	34 ± 51	35 ± 52	39 ± 57	44 ± 60	35 ± 55

in October/November stems from changing climate-code coefficients (see Section 3.2.1). Averages of L include cloud-free areas.

The decrease of $P(85)$ due to the values shown in Table 5.1 would be ≈ 0.11. If one subtracts this amount from the open water NBTPD values of Figure 5.1, the resulting values agree quite well with the those given in Figure 5.2 over open water. The fields of V, W and L causing this decrease extend into the sea ice. Consequently, $< P >$ is negatively biased over sea ice as well (see Figure 5.2), although this bias can be expected to be smaller due to the higher surface emissivity.

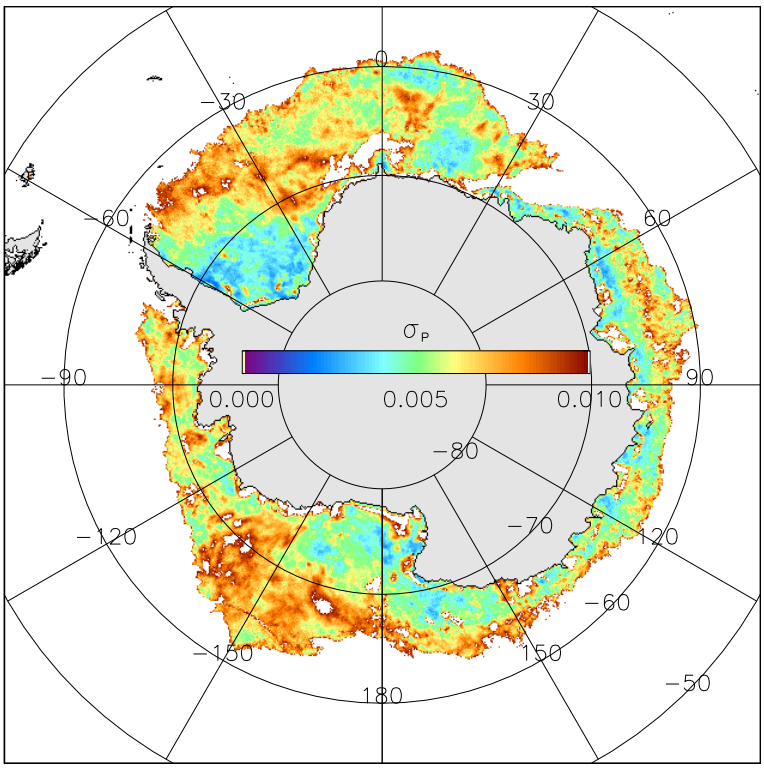

Figure 5.3: *Map of the standard deviation of the NBTPD at 85 GHz: σ_P, for July 1999.*

Figure 5.3 shows a large region with σ_P values above 0.01 (white) surrounding the sea ice. This can be expected over the highly polarizing and radiometrically cold open water where the atmospheric influence causes a larger decrease of $P(85)$ if compared to the less polarizing sea ice (see Sections 2.2.1 and 2.3). Over sea ice, σ_P is significantly smaller than 0.01, except in polynyas (for instance in

the Weddell Sea at 66 °S, 0 °E) and in the MIZ where a highly variable sea ice concentration causes more variable NBTPD values. Andreas [1984] and Oelke [1997] pointed out that clouds, temperature anomalies and precipitation fields associated with cyclones can extend into the sea ice as far as 1000 km. Even in Austral winter, air temperatures may vary between $-30\,^{\circ}$C and $0\,^{\circ}$C in the pack ice within a few days [Massom et al., 1997]. Thus, the temporal variability of $P(85)$ in the MIZ has two additional important contributions, one caused by the direct atmospheric influence such as attenuation by clouds and one related to the indirect atmospheric influence on the sea ice and snow cover as is discussed in Section 2.3. This is illustrated by Figure 5.3. Values of σ_P below 0.005 are widespread in the lee of the Antarctic Peninsula and in the Ross Sea while larger σ_P values are common in the northern and northeastern parts of the Weddell as well as the Ross and Amundsen Seas (see Figure 2.6 for the geography). The latter regions are well-known to be frequently overpassed by cyclones.

The standard deviation σ_P may be partly caused by two additional contributions: a geophysical and a statistical one. The latter one increases towards the North, since the number of SSM/I overflights contributing to each pixel of Figures 5.2 and 5.3 gradually decreases equatorwards as is described in Section 3.1.2. The northern parts of the $< P >$ map contain values which have been averaged over a smaller number of overflights than those in the southern parts. However, neither a general latitudinal increase of σ_P nor a latitudinal preference for high or low σ_P values can be identified in Figure 5.3. This suggests that the statistical contribution to σ_P can be neglected. Secondly, σ_P may be influenced by spatial sea ice inhomogenities in regions with enhanced sea ice drift. In these regions, the sea ice may be completely replaced by the one located up-stream within one to a few days. Regions of a pronounced sea ice drift are the MIZ with the influence of the Circumpolar Current and the eastern margins of the Weddell and Ross Seas where a northbound current displaces the sea ice by about 5 to 10 km per day [Emery et al., 1997], [Toudal and Saldo, 2000]. Much of the variability evident in Figure 5.3 in the MIZ results probably from drifting sea ice and can be taken as a dynamic chance in C rather than a change in sea ice type within the pixel considered. There is no evidence of an enhanced variability of NBTPD values along the eastern margins of the Weddell and Ross Seas in Figure 5.3.

The second step in calculating the sea ice tie points is the generation of monthly masks which contain only pixels with $\approx 100\,\%$ sea ice concentration and which reveal the smallest weather influence. This is achieved by combining $< P >$ and σ_P as follows:

- All pixels with $< P >$ larger than 0.035 are excluded. This threshold can be regarded as an upper limit for $P(85)$ values of Antarctic sea ice (see Figure 5.1) and allows to discriminate the pack ice from the MIZ in Figure 5.2. Thus, the remaining areas probably exhibit average sea ice concentrations near 100 %.

- All pixels with σ_P larger than 0.005 are excluded. This threshold is based on the earlier-discussed σ_P maps (Figure 5.3) as well as on the standard deviations given in Figure 5.1 and ensures that areas being continuously influenced by the atmosphere are not used to calculate the sea ice tie points.

Figure 5.4 **a)** shows the mask obtained by this method for July 1999. Obviously, SSM/I measurements of almost the entire Antarctic sea ice cover (compare Figure 5.2) contribute to the sea ice tie points. The main shortcoming of this method is that regions with highly variable surface properties and a sea ice concentration of 100 % are also excluded and, therefore, are underrepresented in the sea ice tie points. In this particular month, pixels of polynyas and of almost the entire Bellingshausen and Amundsen Seas (60 to 140°W) are excluded from the tie point estimation. Although the two seas mentioned exhibit quite low $< P >$ values (see Figure 5.2), nearly all pixels are masked out due to the high variability of $P(85)$

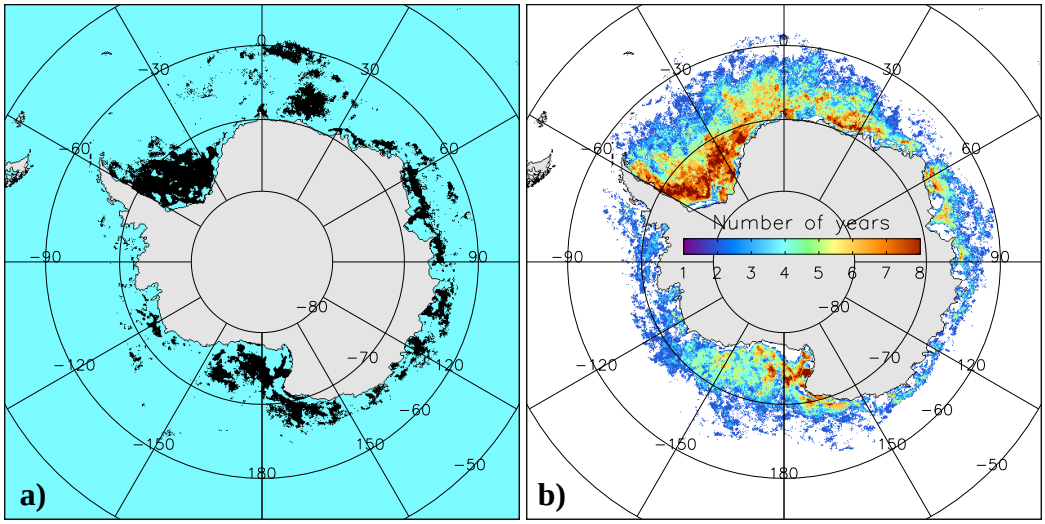

Figure 5.4: **a)***: Map of all pixels that are used to estimate the sea ice tie points for July 1999.* **b)***: Total number of years contributing to an average mask with pixels used to estimate the sea ice tie points for July within the period 1992-1999.*

(see Figure 5.3). This is probably caused by the weather influence since these Seas are overpassed by cyclones in Austral winter more frequently than other regions [Sinclair, 1994]. Figure 5.4 **b)** shows the number of years contributing to an average mask to estimate the sea ice tie point for July of the period 1992-1999. This image illustrates that only pixels belonging to the southern Ross Sea and the southern, central and southeastern Weddell Sea have contributed regularly to the sea ice tie points of July while regions known to be sites of polynyas are excluded in most years.

In the next step, the 85 GHz SSM/I brightness temperatures are averaged separately for each polarization and for each pixel belonging to these monthly masks. These monthly averaged brightness temperatures – called pre-tie points – are still biased by monthly averages of the integrated water vapor content $< W >$ and of the integrated cloud liquid water content $< L >$ typical for the pack ice region. The former parameter is obtained from ECMWF model data (see Section 3.3). Reliable L data are not available over Antarctic sea ice, neither from models nor from remote sensing instruments. Therefore, $< L >$ is set to the average L value calculated from SSM/I data with the method given in Section 3.2.3 within an approximately 100 km wide open water area adjacent to the sea ice edge (see also [Heygster et al., 1996]). Furthermore, it is assumed that over the pack ice region the $< L >$ value amounts only to two thirds of the one over open water [Oelke, 1997], since the latent and sensible heat fluxes from the ocean to the atmosphere are significantly smaller over sea ice than over open water. Both $< W >$ and $< L >$ are used together with the coefficients described in Section 5.3 to correct the pre-tie points for the weather influence, yielding the sea ice tie points $T_{v,i}$ and $T_{h,i}$ and, by using Equation 4.2, P_i at 85 GHz.

Figure 5.5 shows $T_{p,i}$ and P_i values averaged over the period 1992-1999 (images **a)** and **b)**, respectively). Standard deviations of these values are also estimated for each month and averaged over the period 1992-1999 as well, yielding the values given in Figure 5.5. In Figure 5.5 **a)**, freeze-up in March/April coincides well with a sharp increase of the averaged $T_{p,i}$ values. Melt-onset is marked by a decrease of the averaged $T_{p,i}$ values between November and January to remarkably low values around 200 K. These values correspond to an emissivity of ≈ 0.7 and occur in each year of the period investigated as is evident in Figure 5.6 **a)** showing the time-series of $T_{p,i}$ for 1992-1999. This behavior is contrary to passive microwave observations made in the Arctic [Smith, 1998] where a marked brightness temperature increase (decrease) is observed at melt-onset (freeze-up). One possible explanation for this sharp decrease in late spring/early summer could be the presence of old, coarse-grained snow as is described in Section 2.3.4. Also,

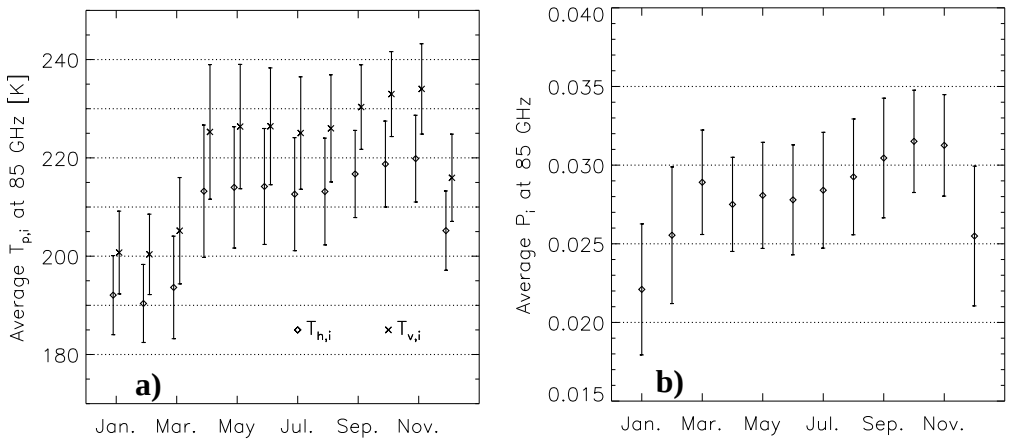

Figure 5.5: *Monthly sea ice tie points averaged over the period 1992-1999.* **a)***: brightness temperatures ($T_{p,i}$),* **b)***: NBTPD values (P_i). The error bars denote $\pm\sigma_{T_{p,i}}$ and $\pm\sigma_{P_i}$, respectively. For clarity, in image* **a)** *data points and error bars at h-polarization are shifted slightly.*

a gradual increase of the averaged $T_{p,i}$ values between August and November can be identified in Figure 5.5 **a)**. It is probably caused by a growing snow liquid water fraction. Table 5.2 lists the $T_{p,i}$ and P_i values averaged over the entire period.

The averages of P_i shown in Figure 5.5 **b)** vary only between 0.022 (January) and 0.032 (October) and almost agree within one standard deviation. However, during one annual cycle extremes of P_i may differ by up to 0.015, for instance in 1992 as is revealed by Figure 5.6 **b)** showing the time-series of P_i for 1992-1999. The interannual variability of $T_{p,i}$ is reflected by this P_i time-series as well. The average of the *in situ* NBTPD values of the different FY ice types shown

Table 5.2: *Open water and sea ice tie points averaged over the period 1992-1999. Standard deviations are given by σ.*

$T_{v,w} \pm \sigma$ [K]	$T_{h,w} \pm \sigma$ [K]	$P_w \pm \sigma$
231.7 ± 0.5	151.6 ± 1.0	0.209 ± 0.002
$T_{v,i} \pm \sigma$ [K]	$T_{h,i} \pm \sigma$ [K]	$P_i \pm \sigma$
220.7 ± 10.3	208.6 ± 10.1	0.028 ± 0.004

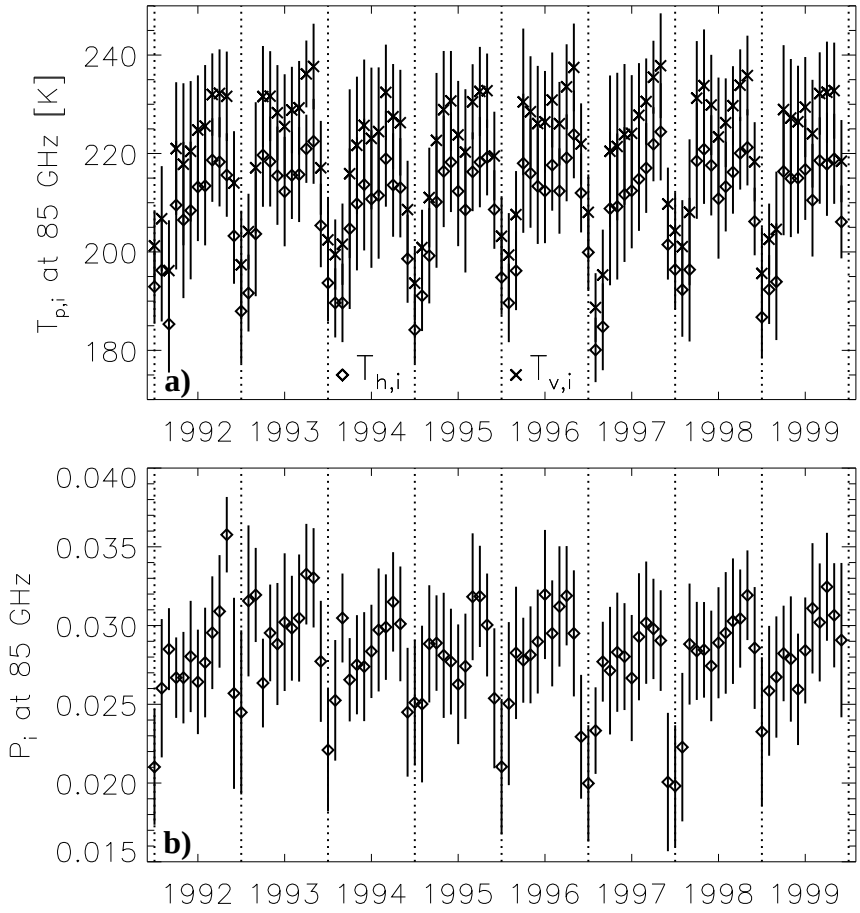

Figure 5.6: *Time-series of the sea ice tie points for each month of the period 1992-1999.* **a)***: brightness temperatures ($T_{p,i}$),* **b)***: NBTPD (P_i). The error bars denote $\pm\sigma_{T_{p,i}}$ and $\pm\sigma_{P_i}$, respectively.*

in Figure 5.1 is about 0.021 and is thus slightly smaller than the average of P_i obtained between 1992 and 1999 (see Table 5.2). It remains unclear at this point whether this is caused by the limitation of the *in situ* data to Austral winter and spring and sea ice and snow types of the Weddell Sea or whether the areas selected to calculate $T_{p,i}$ and P_i exhibit average sea ice concentrations of 95 % rather than 100 %.

5.2.2 Open Water

In order to have the same statistical background than the sea ice tie points, open water tie points are also estimated from NSIDC daily gridded 85 GHz SSM/I brightness temperatures on a monthly basis. For each month, $T_p(85)$ is averaged separately for both polarizations over all pixels which:

- are south of 55°S which is the average position of the Antarctic Circumpolar Current to ensure a SST close to 273 K [White and Peterson, 1996];
- are cloud free, *i. e.* exhibit L values below 10 g m^{-2};
- exhibit V values below 10 m s^{-1} and W values below 10 kg m^{-2}.

The resulting monthly averaged brightness temperatures still include the influence of the corresponding monthly averages of W and V obtained by averaging all values of W and V belonging to the pixels selected. The monthly averaged brightness temperatures are corrected for the influence of the average values of W and V and yield the open water tie points $T_{v,w}$, $T_{h,w}$ and, by using Equation 4.2, P_w at 85 GHz. Their values are very similar for all months of the period 1992-1999. Table 5.2 lists the $T_{v,w}$, $T_{h,w}$ and P_w values averaged over this period. The average P_w value is about 0.015 larger than the one obtained from *in situ* measurements shown in Figure 5.1. However, the surface wind conditions are unclear for these *in situ* measurements. An average wind speed of ≈ 7 m s^{-1} during these measurements, which is quite a typical value when looking at Table 5.1, would be sufficient to explain the mentioned difference of 0.015 with a wind-roughened sea surface.

5.3 Atmospheric Influence

As discussed in Sections 2.2 and 2.4 the atmospheric parameters V, W and L significantly influence $T_p(85)$ and $P(85)$. The radiative transfer model MWMOD described in Section 2.5.1 is used to quantify this weather influence for surface emissivities ϵ_p and atmospheric conditions listed in Table 5.3. Some other settings of MWMOD have already been explained in Section 2.5.1.

5.3.1 Surface Wind

Scattering of microwave radiation at the wind-roughened sea surface has a large depolarizing effect (see Section 2.2) and may bias the sea ice concentration esti-

Table 5.3: *Ranges and step sizes of ϵ_v, ϵ_h, V, W and L used to quantify the atmospheric influence on $T_p(85)$.*

	ϵ_v, ϵ_h	V [m s^{-1}]	W [kg m^{-2}]	L [kg m^{-2}]
Data range	0.44–0.98	0–30	0–30	0.0–0.5
Step size	0.01	1	1	0.02

mate. In order to quantify this effect, 85 GHz brightness temperatures are modeled for dry, clear-sky conditions, wind speeds given in Table 5.3 and a SST of 273.15 K at both polarizations over open water. The results are shown in Figure 5.7 **a)** and reveal a significant decrease of the polarization difference $T_v - T_h$ with increasing V.

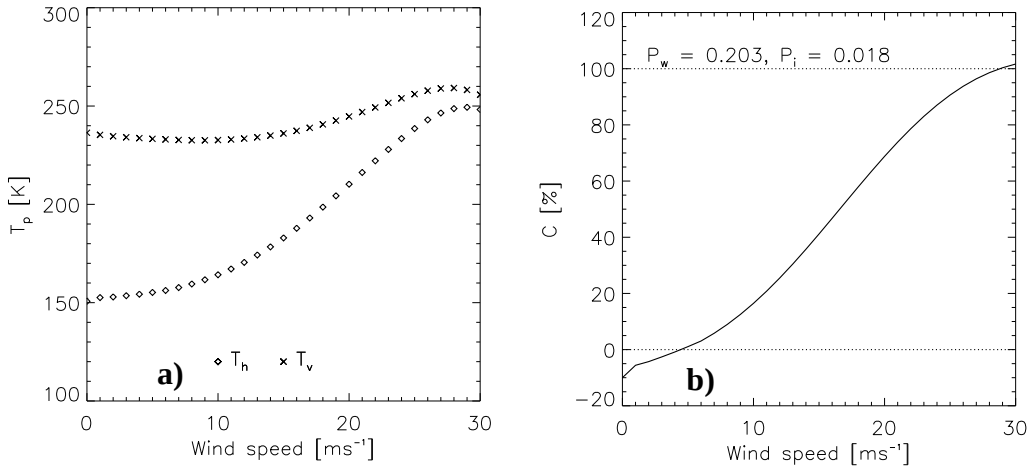

Figure 5.7: **a)** *Influence of the surface wind speed on $T_p(85)$ as modeled with MWMOD for dry, clear-sky conditions and surface wind speeds given in Table 5.3.* **b)** *Sea ice concentration C that would be calculated from uncorrected brightness temperatures over a wind-roughened sea surface for dry, clear-sky conditions.*

The sensitivity $S_V = \frac{\partial T_p}{\partial V}$, *i. e.* the change of $T_p(85)$ due to a change of V of 1 m s^{-1}, is calculated and compared to S_V values obtained by Fuhrhop et al. [1997] in Table 5.4. They are of the same order of magnitude but may differ by up to 1.6 K m^{-1}s. This is probably caused by the fact that the brightness temperatures shown in Figure 5.7 **a)** are modeled for dry, clear-sky conditions, *i. e.* $W = L = 0$ kg m^{-2}, while the results of Fuhrhop et al. [1997] are based on one case study

Table 5.4: *Sensitivities S_V obtained in SEA LION and provided by Fuhrhop et al. (1997) (ATMICE-Project).*

		S_V [K m^{-1}s]	
		V =1 - 6 m s^{-1}	V =6 - 20 m s^{-1}
85 h	SEA LION	0.8	1.4 - 5.8
	ATMICE	1.1	1.4 - 4.2
85 v	SEA LION	-0.4	0.0 - 2.2
	ATMICE	0.0	0.0 - 1.8

with a non-zero atmospheric water content. Since, for the weather correction described in Section 5.3.3, the wind-induced brightness temperature change is subtracted from the $T_p(85)$ values after the correction for the W and L influence, the sensitivities derived here are more suitable. Figure 5.7, **b)** shows C values that would be calculated with the SL algorithm from uncorrected 85 GHz brightness temperatures for dry, clear-sky conditions. Wind speeds below 5 m s^{-1} lead to a slight underestimation of C while an increasing overestimation of C occurs for higher wind speeds. Average daily surface wind speeds range between 5 and 15 m s^{-1}, reaching up to 20 m s^{-1} (see [Heygster et al., 1996] and Figures 3.2 and 3.3). Therefore, on average, the overestimation of C can be as high as 70 %. This demonstrates the necessity to correct $T_p(85)$ for the influence of V if using SSM/I $T_p(85)$ values to calculate C.

The modeled brightness temperatures (see Figure 5.7 **a)**) are fitted with a 4th-order polynomial in order to obtain a relation between V and T_v and T_h. Maximum (average) differences between the modeled brightness temperatures and the fit functions are 0.7 K (< 0.1 K) for T_h and 0.8 K (0.1 K) for T_v. The equation of this fit is

$$T_{p,V\neq 0} = T_{p,V=0} + \sum_{i=1\ldots4} a_i V^i, \tag{5.5}$$

where $T_{p,V=0}$ ($T_{p,V\neq 0}$) denote the 85 GHz brightness temperature above a calm (wind-roughened) sea surface at polarization p, and a_i denote the coefficients of the polynomial. They are listed in Table 5.5. Values of $T_{p,V=0}$ are 150.7 K and 235.3 K at horizontal and vertical polarization, respectively. Equation 5.5 allows to calculate $T_p(85)$ that would be measured by the SSM/I above a sea surface roughened according to V under dry, clear-sky conditions.

Table 5.5: *Coefficients a_i of the polynomial of the modeled brightness temperatures shown in Figure 5.7* **a)**.

a_i [K (m s^{-1})$^{-i}$]	$i=1$	$i=2$	$i=3$	$i=4$
85 h	1.378	-0.198	24.4×10^{-3}	-52.3×10^{-5}
85 v	0.264	-0.194	16.9×10^{-3}	-33.1×10^{-5}

5.3.2 Atmospheric Water Content

Absorption and emission of electromagnetic radiation by the atmospheric water vapor and hydrometeors of non-precipitating clouds increase $T_p(85)$ and decrease $P(85)$. Scattering by precipitation particles decrease $T_p(85)$ and increase $P(85)$, depending on the polarization (Section 2.4). Since areas with high values of L and thus the highest probability of precipiation, are masked out with the R-factor as is described in Section 3.2.4, only the brightness temperature increase due to absorption and emission is discussed here. In order to quantify this increase, 85 GHz brightness temperatures are modeled with MWMOD for values of ϵ_v, ϵ_h, W and L given in Table 5.3. The influences of W and L are considered simultaneously since, at small W values, the brightness temperature increase due to L may be larger than at high W values because the atmosphere is more opaque in the latter case.

Figure 5.8 **a)** and **b)** illustrate the reaction of $T_h(85)$ to an increasing atmospheric water content over open water. For $V = 0\,\mathrm{m\,s^{-1}}$ (Figure 5.8 **a)**), $T_h(85)$ may increase by 70 K for typical extreme values of W and L of $20\,\mathrm{kg\,m^{-2}}$ and $200\,\mathrm{g\,m^{-2}}$, respectively (compare Figures 3.2 and 3.3). Over a wind-roughened sea surface, both the sea surface emissivity and the brightness temperature are considerably larger (see Section 2.2.1 and Figure 5.7 **a)**), at least at horizontal polarization, and the absolute brightness temperature increase can be expected to be smaller. This is illustrated by Figure 5.8 **b)**, showing the brightness temperature increase due to W and L over a rough sea surface at $V = 20\,\mathrm{m\,s^{-1}}$. For the above-mentioned typical extremes this increase is still around 30 K. The absolute brightness temperature increase due to W and L is smaller at vertical polarization due to the higher sea surface emissivity (Section 8.2).

The sensitivities $S_W = \frac{\partial T_p}{\partial W}$ and $S_L = \frac{\partial T_p}{\partial L}$, *i. e.* the changes of $T_p(85)$ due to changes of W and L of $1\,\mathrm{kg\,m^{-2}}$ each, are given in Table 5.6 in comparison to the results of Fuhrhop et al. [1997]. It becomes evident within the SEA LION

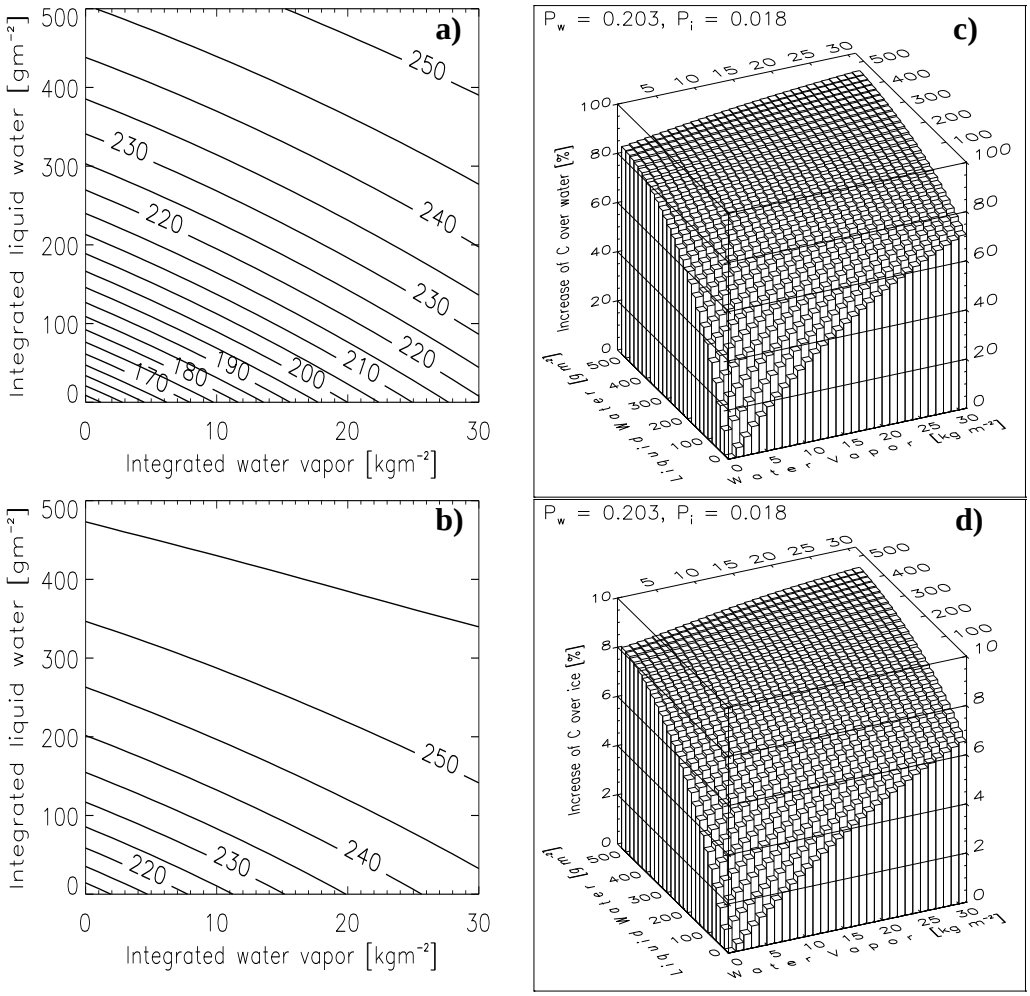

Figure 5.8: *Brightness temperatures at 85 GHz, horizontal polarization, modeled with MWMOD for different atmospheric water contents over open water (salinity: 34 ‰, SST: 272 K):* **a)** $V = 0\,m\,s^{-1}$ *(*$\epsilon_h = 0.49$*),* **b)** $V = 20\,m\,s^{-1}$ *(*$\epsilon_h = 0.73$*). Contour spacing is 5 K. Total sea ice concentrations C that would be calculated from uncorrected brightness temperatures for different atmospheric water contents:* **c)** *over a calm sea surface (*$C = 0\,\%$*,* $V = 0\,m\,s^{-1}$*),* **d)** *over FY ice (*$C = 100\,\%$*).*

project that S_W is larger during clear-sky conditions and decreases with increasing L values. The same is true for S_L which is larger at low W values and decreases with increasing W values. The sensitivities obtained here are quite similar to those of Fuhrhop et al. [1997].

Table 5.6: *Sensitivities S_W and S_L obtained in SEA LION and provided by Fuhrhop et al. [1997] (ATMICE). The two smaller (larger) values of S_W (SEA LION) are for an increase of W from 8 to 20 kg m^{-2} at $L = 0.3$ kg m^{-2} ($L = 0.0$ kg m^{-2}). The two smaller values of S_L (SEA LION) are for an increase of L from 0.3 to 0.4 kg m^{-2} at $W = 20$ kg m^{-2}. The two larger ones are obtained for an increase of L from 0.0 to 0.1 kg m^{-2} at $W = 8$ kg m^{-2}.*

		S_W [K m^{-2}kg]	S_L [K m^{-2}kg]
85 h	SEA LION	0.8 - 2.5	55 - 258
	ATMICE	2.1	85 - 188
85 v	SEA LION	0.1 - 1.1	27 - 135
	ATMICE	0.8	33 - 71

Figure 5.8 **c)** shows C values one would obtain over a calm sea surface with Equation 5.4 and the tie points derived in Section 5.2 without correction of $T_p(85)$ for the influence of W and L. Typical values of W and L (8 kg m^{-2} and 40 g m^{-2}, see Table 5.1 and Sections 3.2.2 and 3.2.3) would cause an overestimation of C over calm open water by $\approx 35\,\%$. At the above-mentioned typical extreme values ($W = 20$ kg m^{-2}, $L = 200$ g m^{-2}), this overestimation would approach $70\,\%$. Both values would further increase for a non-zero surface wind speed, *i. e.* over a rough sea surface. Over sea ice, the overestimation of C would be considerably smaller as is illustrated in Figure 5.8 **d)** for $100\,\%$ of FY ice. Note that the vertical scale in this image is one tenth of that in the previous image. In this case, *i. e.* for emissivities $\epsilon_h = 0.91$ and $\epsilon_v = 0.94$, the overestimation would rarely exceed $5\,\%$. However, sea ice properties vary significantly and may cause emissivities well below these emissivity values and, therefore, considerably larger overestimations of C. As has already been concluded for V, SSM/I 85 GHz brightness temperatures have to be corrected for the influence of W and L to calculate C.

The modeled brightness temperatures shown exemplarily in Figure 5.8 **a)** can be related to W and L by a 2D-polynomial

$$T_{W,L\neq 0} = T_{W=L=0} + \sum_{i,j=0\ldots4} a_{ji}(\epsilon_p(V))W^i L^j. \tag{5.6}$$

Equation 5.6 allows to calculate each $T_p(85)$ value in the W-L-plane using W, L, the 85 GHz brightness temperature of a dry, clear-sky atmosphere $T_{W=L=0}$

and coefficients $a_{ji}(\epsilon_p(V))$ depending on the 85 GHz surface emissivity ϵ_p. A lookup-table of 85 GHz $\epsilon_p(V))$ values modeled with MWMOD for open water (salinity: 34 ‰, SST: 273 K) for a dry, clear-sky atmosphere and V values given in Table 5.3 is compiled in the appendix. Maximum and average differences between the modeled brightness temperatures and the fit functions are less than 0.1 K at both polarizations. Table 5.7 shows a sample set of coefficients for a calm sea surface.

Table 5.7: *A sample set of coefficients a_{ji} [K(kgm^{-2})$^{-2j}$] of the 2D-polynomial of the modeled brightness temperatures at $\epsilon_p(V = 0\,m\,s^{-1}) = 0.49$. The columns denote $j = 0 \ldots 4$, the rows $i = 0 \ldots 4$.*

0.0	8.793	-0.377	11.0×10^{-3}	-16.5×10^{-5}
3.204	-0.295	15.5×10^{-3}	-54.9×10^{-5}	93.2×10^{-7}
-27.5×10^{-3}	37.5×10^{-4}	-28.7×10^{-5}	12.7×10^{-6}	-24.2×10^{-8}
-11.5×10^{-5}	-16.6×10^{-6}	27.9×10^{-7}	-15.8×10^{-8}	34.4×10^{-10}
24.6×10^{-7}	-47.3×10^{-9}	-11.1×10^{-9}	90.6×10^{-11}	-23.5×10^{-12}

5.3.3 Correction for the Atmospheric Influence

Using the SL algorithm the influence of V, W and L on SSM/I 85 GHz brightness temperatures has to be quantified and subtracted from these data separately for open water and sea ice due to the following reasons:

- Each pixel with $C < 100\,\%$ has a certain fraction of open water. In this fraction, $T_p(85)$ values are influenced by W, L and V, whereas in the sea ice fraction the influence of V can be neglected.
- Sea surface emissivities differ from those of sea ice. Consequently, the correction of $T_p(85)$ for the weather influence is different for both surfaces.
- The SL algorithm calculates C for each pixel iteratively (see Section 5.4). At each iteration step, a new C value is obtained, *i. e.* fractions of open water and sea ice change continuously during the retrieval. This alters the surface emissivity distribution and has to be considered in the correction of $T_p(85)$ for the weather influence. As a result, the amount of the weather-induced brightness temperature change subtracted from $T_p(85)$ changes between two iteration steps.

The weather correction is applied to $T_p(85)$ as follows. First of all, the cloud mask derived with the R-factor method is used over both open water and sea ice. Most areas with $L > 0.1\,\mathrm{kg\,m^{-2}}$ (Section 3.2.4) are excluded from the weather correction and sea ice concentration retrieval successfully. The second step is the correction of $T_p(85)$ for the influence of W and L in the remaining areas using the data sets described in Chapter 3 and the coefficients given in Section 5.3.2. This can be achieved over open water by

$$T_{p,W=L=0} = T_p(85) - \sum_{i,j=0\ldots4} a_{ji}(\epsilon_p(V))W^i L^j, \tag{5.7}$$

where $T_{p,W=L=0}$ is $T_p(85)$ measured by the SSM/I and corrected for the influence of W and L, and a_{ji} are the coefficients required for this correction according to $\epsilon_p(V)$. These emissivities are selected using V and the lookup-table given in the appendix. Over sea ice, Equation 5.7 is used together with monthly averages of L as is shown in Table 5.1 and emissivities which are independent of V. They are estimated for each month from the sea ice tie points $T_{p,i}$ given in Section 5.2 and the monthly averaged surface temperature $<T_s>$ derived in Section 3.3:

$$\epsilon_p = \frac{T_{p,i} - \Delta T_{O_2}}{<T_s>}. \tag{5.8}$$

This is the only part of the SL algorithm, where the contribution of the oxygen absorption to $T_p(85)$, denoted by ΔT_{O_2}, is considered explicitely (see Section 2.4). The SSM/I measurements as well as the modeled values of $T_p(85)$ include implicitely the oxygen absorption. Therefore, in order to obtain the sea ice emissivity from the ratio of $T_{p,i}$ and T_a, one has to subtract ΔT_{O_2} from $T_{p,i}$. This is done using Equation 5.8 together with the ΔT_{O_2} values compiled in the appendix. These values are interpolated to match emissivity steps of 0.01. Once a pair of sea ice emissivities is selected it is used for the entire month. The relative error made in the calculation of ϵ_p using an incorrect $<T_s>$ value for the temperature of the radiating sea ice and/or snow layer is smaller than $5\,\%$ for over-/underestimations of $<T_s>$ of 10 K in the range between $-40\,^\circ$C and $0\,^\circ$C.

Over open water, as a third step, the correction for the influence of V has to be applied. This is done using the wind data described in Chapter 3, the coefficients a_i given in Section 5.3.1 and the equation

$$T_{p,W=L=V=0} = T_{p,W=L=0} - \sum_{i=1\ldots4} a_i V^i, \tag{5.9}$$

where $T_{p,W=L=V=0}$ is the 85 GHz SSM/I brightness temperature corrected for the influence of W, L and V and with $T_{p,W=L=0}$ given by Equation 5.7.

5.4 Complete Algorithm

This section gives a detailed description of the SL algorithm. Its flow chart is displayed in Figure 5.9. The SL algorithm allows to calculate the daily total sea ice concentration C. The data used in the SL algorithm have already been described in Chapter 3. Additional requirements are:

- Tie points have to calculated in advance for the retrieval of C for each month.
- Daily cloud masks have to be derived in advance to the retrieval of C (see Section 3.2.4).
- All data have to be mapped into a grid with common resolution, *e. g.* the NSIDC SSM/I grid with $12.5 \times 12.5\,\mathrm{km}^2$ [NSIDC, 1996].

The SL algorithm calculates C iteratively. For each pixel, the first iteration step ($k = 0$) – after applying the cloud mask of the day considered – is to compute a first-guess of the total sea ice concentration $C^{(0)}$ with Equation 5.4, the tie points given in Section 5.2 and $P(85)$ obtained from the uncorrected SSM/I data. The second step is to model 85 GHz brightness temperatures that would be measured by the SSM/I above an area covered with sea ice according to $C^{(0)}$ and for atmospheric conditions given by V, W and L yielding $T_p^{sim,(0)}$. From these values the $P^{sim,(0)}$ value is derived and compared to the SSM/I measurement. If

$$\Delta P = \left| P^{sim,(k)} - P(85) \right| \leq 0.001 \tag{5.10}$$

holds, $C^{(0)}$ is the final sea ice concentration and the iteration is stopped for this pixel (see Figure 5.9). The threshold of 0.001 corresponds to approximately 1 % change in C.

Otherwise, the iteration is continued ($k = k+1$) and the SSM/I measurements are corrected for the weather influence expressed by V, W and L. In doing this, one has to distinguish between the fractions of open water and sea ice within the pixel considered. It is necessary to assume first, that each pixel is covered completely by either open water or sea ice and perform the weather correction separately for both cases since emissivities are known for the pure surface types

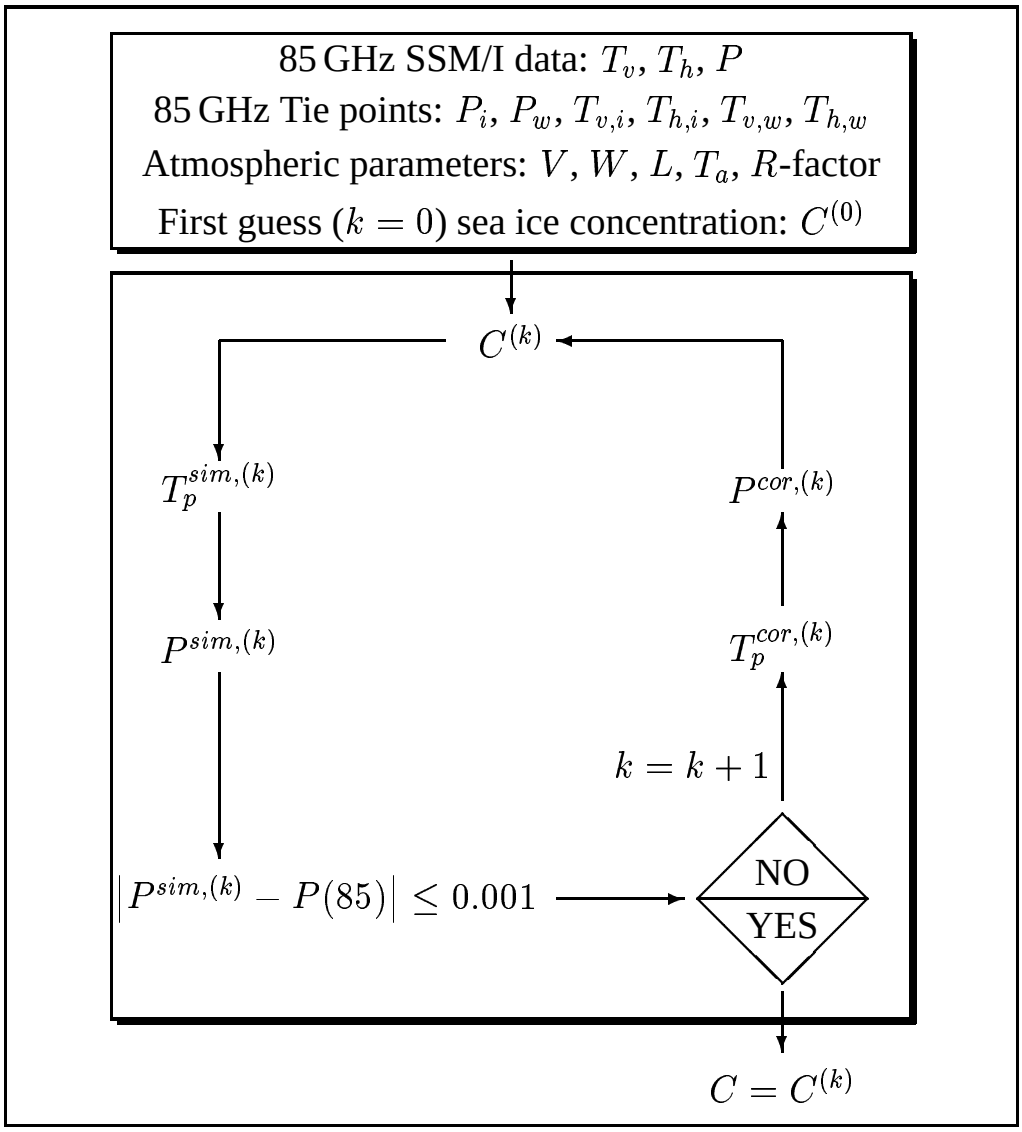

Figure 5.9: *Scheme of the SEA LION algorithm. The quantities $P^{sim,(k)}$ and $T_p^{sim,(k)}$ (k = iteration step) denote modeled values of $P(85)$ and $T_p(85)$. They are obtained at the sea ice concentration $C^{(k)}$ and for given atmospheric conditions (Chapter 3). $P(85)$ is the NBTPD value measured by the SSM/I. The quantities $P^{cor,(k)}$ and $T_p^{cor,(k)}$ are the NBTPD and brightness temperature values measured by the SSM/I and corrected for the weather influence in the kth-order.*

only. For the open water fraction, the lookup-table in the appendix provides the required emissivities $\epsilon_p(V)$. For the sea ice fraction, that pair of emissivities is used which has already been derived for the month considered with Equation 5.8. Knowing these emissivities, $T_p(85)$ can be corrected for the influence of W and L using Equation 5.7 and the coefficients given in Section 5.3.2. Over the open water fraction, this is followed by the correction for the influence of V with Equation 5.9 and the coefficients given in Section 5.3.1. Since the wind-induced sea surface roughening depends on the wind fetch, which is considerably smaller in open water areas surrounded by sea ice than in the open ocean, V is reduced to $\frac{2}{3}V$ in the area covered by sea ice pre-defined with the PE algorithm sea ice concentration data set [Heygster et al., 1996].

Now, one has two 85 GHz brightness temperature pairs for a surface consisting of open water or sea ice only, corrected for the actual weather influence. These pairs, the atmospheric parameters, the emissivities and the measured, uncorrected 85 GHz SSM/I brightness temperatures remain fixed once they are calculated for each pixel. In order to obtain the weather-corrected brightness temperature over a mixed pixel, *i. e.* with $0\,\% < C < 100\,\%$ given by $C^{(k-1)}$, these brightness temperatures are inserted into Equation 5.3. Here, the products $\epsilon_{p,w}(85)T_{s,w}$ and $\epsilon_{p,i}(85)T_i$ correspond to the weather-corrected $T_p(85)$ values over open water and sea ice, respectively. This results in kth-order weather-corrected 85 GHz brightness temperatures at polarization p: $T_p^{cor,(k)}$. Inserting them into Equation 4.2 yields the kth-order weather-corrected 85 GHz NBTPD value: $P^{cor,(k)}$ which is used to calculate a new value of C: $C^{(k)}$. At this point, *i. e.* after one complete cycle, one has two different sea ice concentrations: the first guess $C^{(0)}$ and $C^{(1)}$, one pair of (using $C^{(0)}$) modeled 85 GHz brightness temperatures and the corresponding NBTPD value: $T_v^{sim,(0)}$, $T_h^{sim,(0)}$, $P^{sim,(0)}$, and one pair of weather-corrected 85 GHz SSM/I brightness temperatures and the corresponding NBTPD value used to calculate $C^{(1)}$: $T_v^{cor,(1)}$, $T_h^{cor,(1)}$ and $P^{cor,(1)}$. There are no values for $T_p^{cor,(0)}$ and $P^{cor,(0)}$.

The next step is to check whether the new sea ice concentration $C^{(k)}$ agrees with the SSM/I measurements. Therefore, $T_p^{sim,(k)}$ and $P^{sim,(k)}$ are re-calculated for the same atmospheric conditions, considering the new sea ice distribution given by $C^{(k)}$. It can happen that the new $C^{(k)}$ value leads to a larger ΔP value (see Equation 5.10) than the old one, $C^{(k-1)}$. In this case, depending on the signs of the last two values of ΔP, $C^{(k-1)}$ is set to $0.5(C^{(k-2)}+C^{(k-1)})$ (different signs) or $0.5(C^{(k-3)}+C^{(k-2)})$ (equal signs) and $T_p^{sim,(k)}$ is re-calculated. The iteration is thus forced to alternate around the minimum ΔP value. The new modeled po-

larization $P^{sim,(k)}$ is compared to $P(85)$ (Equation 5.10) and so on. This iteration converges in about $95\,\%$ of all pixels within the first 30 steps, a threshold which is used to stop the iteration in any case. Pixels belonging to the remaining $5\,\%$ are contaminated by values of L and/or W and/or V incompatible to the brightness temperatures observed. This can happen, for instance, due to the coarser spatial resolution of the atmospheric data used. The retrievals of L and the R-factor are certainly influenced by the beamfilling error [Bennartz, 1999], *i. e.* by subpixel-scale clouds within the sensor's FOV. In particular, pixels which are not excluded from the retrieval of C with the cloud mask and exhibit large L values contribute to these remaining $5\,\%$. The iteration may stop at $k = 30$ without ΔP falling below 0.001. In this case it is checked whether ΔP has changed within the last few iterations. If not and if ΔP is additionally below 0.01 the last value of C is accepted. Otherwise, the pixel is flagged as cloud according to the cloud mask.

Once daily maps of C are obtained, linear temporal interpolation is used to replace pixels flagged as clouds. Only pixels flagged as clouds over a maximum of three consecutive days are replaced, assuming that heavy weather conditions last shorter than three days and assuming that C values remain almost constant within three days. Especially the second assumption is often violated in the MIZ and in regions of pronounced sea ice melt during Austral summer. Using the daily gridded 85 GHz SSM/I brightness temperatures the dynamic changes in C associated with rapidly overpassing fronts in the MIZ are smoothed out a bit, causing a smaller influence on the sea ice concentration retrieval. The above-mentioned maximum length of three consecutive days to replace cloud-flagged pixels ensures that the impact of major air mass and thus surface air temperature changes on the sea ice cover are considered. The typical time-scale of such air mass changes is about 4 to 7 days [King and Turner, 1997]. In Section 5.5 as well as in Section 7 the last step of the SL algorithm is discussed: The replacement of SEA LION ice concentrations by PELICON ice concentrations (*i. e.* $0\,\%$) in all pixels supposed to be open water in a distance to the PELICON ice edge greater than 25 km.

5.5 Error Analysis

Numerous data from different data sources are used in the SL algorithm, each with a specific error contribution to the C values obtained. In order to estimate this contribution the concept of statistical error propagation is applied to Equation 5.4

yielding

$$\begin{aligned}\sigma_C^2 &= \left(\frac{\partial C}{\partial T_{v,i}}\right)^2 \sigma_{T_{v,i}}^2 + \left(\frac{\partial C}{\partial T_{h,i}}\right)^2 \sigma_{T_{h,i}}^2 + \left(\frac{\partial C}{\partial T_{v,w}}\right)^2 \sigma_{T_{v,w}}^2 \\ &+ \left(\frac{\partial C}{\partial T_{h,w}}\right)^2 \sigma_{T_{h,w}}^2 + \left(\frac{\partial C}{\partial T_v}\right)^2 \sigma_{T_v}^2 + \left(\frac{\partial C}{\partial T_h}\right)^2 \sigma_{T_h}^2 \\ &- 2\frac{\partial C}{\partial T_{v,i}}\frac{\partial C}{\partial T_{h,i}}\sigma_{T_{v,i},T_{h,i}}^2 - 2\frac{\partial C}{\partial T_{v,w}}\frac{\partial C}{\partial T_{h,w}}\sigma_{T_{v,w},T_{h,w}}^2 - 2\frac{\partial C}{\partial T_v}\frac{\partial C}{\partial T_h}\sigma_{T_v,T_h}^2 \\ &- \text{12 terms with mixed covariances.} \end{aligned} \tag{5.11}$$

with ($p = v$ or h for vertical or horizontal polarization):

$$\begin{aligned}\sigma_{T_p}^2 &= \sigma_V^2 \left(\sum_{i=1\ldots4} a_i i V^{i-1}\right)^2 + \sigma_W^2 \left(\sum_{i,j=0\ldots4} a_{ji}(\epsilon_p(V)) i W^{i-1} L^j\right)^2 \\ &+ \sigma_L^2 \left(\sum_{i,j=0\ldots4} a_{ji}(\epsilon_p(V)) j W^i L^{j-1}\right)^2 + \sigma_{T_{SSMI}}^2, \end{aligned} \tag{5.12}$$

In Equation 5.11, σ_C is the standard deviation of C caused by the errors of the input data: the tie points given in Section 5.2, the atmospheric parameters derived in Section 3.2 and the SSM/I data (Section 3.1.2). These errors are the standard deviations of the sea ice tie points: $\sigma_{T_{v,i}}$, $\sigma_{T_{h,i}}$ (see Figure 5.6), of the open water tie points: $\sigma_{T_{v,w}}$, $\sigma_{T_{h,w}}$ and of the weather-corrected 85 GHz SSM/I brightness temperatures: σ_{T_v}, σ_{T_h}. The former two error pairs as well as the corresponding covariances $\sigma_{T_{v,i},T_{h,i}}^2$, $\sigma_{T_{v,w},T_{h,w}}^2$ result from the tie point retrieval and remain fixed for each day of one month. The latter error pair and the corresponding covariance σ_{T_v,T_h}^2 has to be calculated during the ice concentration retrieval because these quantities vary daily – mainly depending on the atmospheric parameters (W, V and L) used for the weather correction.

Equations 5.7 and 5.9 are the basis for Equation 5.12 which allows to estimate σ_{T_p} ($p = h$ or v) with the knowledge of the sensor noise $\sigma_{T_{SSMI}} = 1.1$ K (see Table 3.2) and the standard deviations of W, V, and L: σ_W, σ_V and σ_L. In order to consider the different basic spatial resolutions of the 85 GHz SSM/I channels, thus $15 \times 13\,\text{km}^2$, and of the other SSM/I channels used to derive W, V and L (Section 3.2), thus $69 \times 45\,\text{km}^2$, these standard deviations are set to twice the retrieval accuracy of W, L and V given in Section 3.2: $\sigma_W = 4\,\text{kg m}^{-2}$, $\sigma_L =$

$0.06\,\mathrm{kg\,m^{-2}}$ and $\sigma_V = 4\,\mathrm{m\,s^{-1}}$. The resulting values of σ_{T_p}, one for open water and one for sea ice at polarization h or v, are combined according to the actual C values as is described in Section 5.4. The covariance $\sigma^2_{T_v,T_h}$ is calculated the same way. All terms with mixed covariances between the sea ice tie points, the open water tie points and the weather-corrected brightness temperatures, for instance $\sigma^2_{T_{v,i},T_{h,w}}$ are neglected, because the crosstalk between these parameters is small.

$$\sigma_C = \left[\frac{A^2}{(A+B)^4}\left(S_1 + S_2 + S_3\right)\right]^{\frac{1}{2}} \tag{5.13}$$

with

$$\begin{aligned}
S_1 &= T_h^2\sigma^2_{T_{v,i}} + T_v^2\sigma^2_{T_{h,i}} - 2T_vT_h\sigma_{T_{v,i},T_{h,i}} \\
S_2 &= \frac{A^2}{B^2}\left(T_h^2\sigma^2_{T_{v,w}} + T_v^2\sigma^2_{T_{h,w}} - 2T_vT_h\sigma^2_{T_{v,w},T_{h,w}}\right) \\
S_3 &= \sigma^2_{T_v}\left(T^2_{h,i} + 2T_{h,i}T_{h,w}\frac{A}{B} + T^2_{h,w}\frac{A^2}{B^2}\right) \\
&+ \sigma^2_{T_h}\left(T^2_{v,i} + 2T_{v,i}T_{v,w}\frac{A}{B} + T^2_{v,w}\frac{A^2}{B^2}\right) \\
&- 2\sigma^2_{T_v,T_h}\left(T_{v,i}T_{h,i} + \frac{A(T_{h,i}T_{v,w} + T_{v,i}T_{h,w})}{B} + T_{h,w}T_{v,w}\frac{A^2}{B^2}\right) \\
A &= T_{v,i}T_h - T_{h,i}T_v \\
B &= T_vT_{h,w} - T_hT_{v,w}
\end{aligned}$$

Equation 5.13 is obtained calculating the derivatives of Equation 5.11 and is used to determine σ_C for each day in 1999. Over the monthly averaged open water fraction, the average σ_C value (not shown) remains almost constant at a value of $19.8\,\% \pm 0.8\,\%$. Relative contributions to this average open water σ_C value are: $0.2\,\%$ from S_1, $0.3\,\%$ from S_2 and $99.5\,\%$ from S_3 (see Equation 5.13). This is reasonable since a) the variability of the sea ice tie points can be expected to be negligible over open water, b) the open water tie points exhibit a very low variability (compare Table 5.2) and c) only the day-to-day variability of the 85 GHz brightness temperatures and of the atmospheric parameters is large. This large average error, however, together with the large overestimation of C even for small L values evident in Figure 5.8 **c)** is the main reason for the last step of the SL

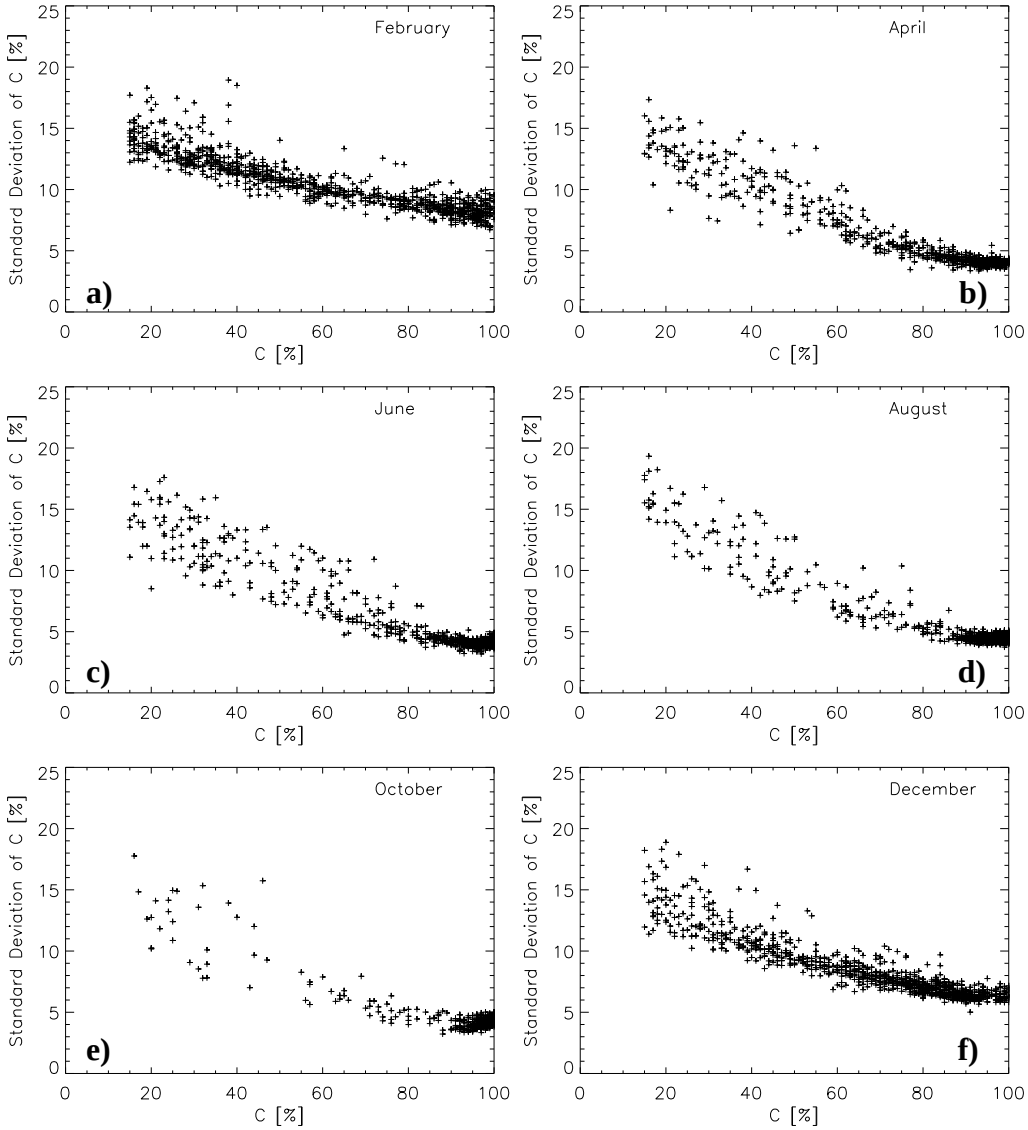

Figure 5.10: *Comparison between the monthly averaged sea ice concentration C and the corresponding standard deviation σ_C obtained with Equation 5.13 for selected months of 1999. Values of C below $15\,\%$ are omitted. In order to reduce the data volume, all plates show only 1000 data pairs.*

algorithm. Spurious sea ice concentrations in the pre-defined open water region are replaced by PELICON ice concentrations [Heygster et al., 1996] in all open

water pixels at a distance greater than 25 km to the PELICON ice edge. This will be discussed in Section 7.

Table 5.8: *Monthly averaged standard deviation σ_C [%] estimated from the errors of the input data with Equation 5.13 for each month of 1999 over the averaged monthly sea ice cover.*

Jan.	Feb.	Mar.	Apr.	May	Jun.
10.6 ± 2.5	10.4 ± 2.2	9.8 ± 3.0	7.0 ± 2.9	5.6 ± 2.6	5.5 ± 2.9
Jul.	Aug.	Sep.	Oct.	Nov.	Dec.
4.8 ± 3.0	5.3 ± 2.4	4.6 ± 2.4	4.8 ± 2.3	5.6 ± 2.4	8.9 ± 2.3

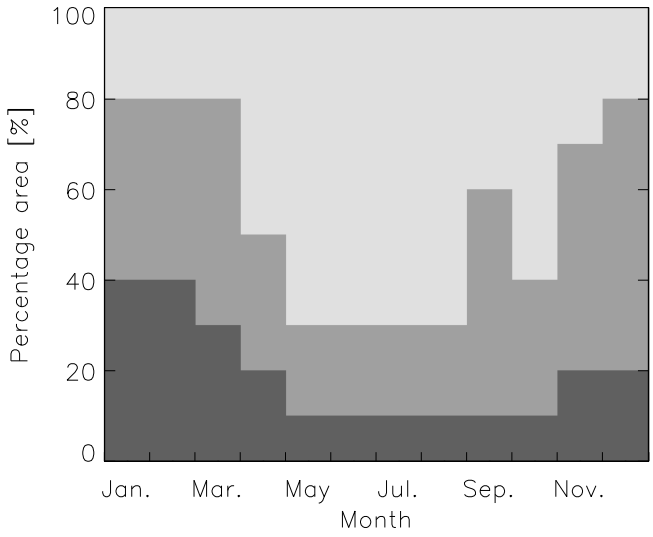

Figure 5.11: *Relative distribution of the sea ice concentration classes within the monthly averaged sea ice extent of 1999:* $15\,\% \leq C \leq 50\,\%$ *(dark grey),* $50\,\% < C \leq 90\,\%$ *(medium grey) and* $C > 90\,\%$ *(light grey).*

Table 5.8 shows σ_C obtained with Equation 5.13 for each month of 1999. Over the sea ice fraction, the average error is anti-correlated with the sea ice extent ($r = -0.88$). This can be explained with the dependence between σ_C and C as is illustrated by Figure 5.10. Small sea ice concentrations are more likely associated with large errors than high sea ice concentrations in absolute as well as in relative terms. On the one hand, this is caused by the larger absolute variability of T_v and T_h, forcing S_3 (see Equation 5.13) to be larger over open water than over sea

ice. On the other hand, the number of pixels exhibiting high C values increases significantly towards Austral winter as is shown in Figure 5.11. Consequently, in Austral winter a larger number of small absolute errors contribute to the monthly averaged value of σ_C forcing it to be small. This is evident in Figure 5.10 indicating that σ_C remains of the order of $5\,\%$ at high sea ice concentrations during Austral winter (see images **b)** to **e)**). However, at low sea ice concentrations, the monthly averaged σ_C value easily approaches $20\,\%$ corresponding to a relative error of $100\,\%$ or more. This is in line with the findings made in Section 5.3. The choosen σ_L value of $0.06\,\mathrm{kg\,m^{-2}}$ can cause spurious sea ice concentrations of $20\,\%$ or more (compare Figure 5.8 **c)**). Therefore, atmospheric parameters used to correct SSM/I 85 GHz data for the weather influence must be selected very carefully.

Table 5.9 reveals that in the low ice concentration class ($15\,\% \leq C \leq 50\,\%$), the average σ_C values agree with each other within one standard deviation ($2.4\,\%$) throughout the year. Therefore, at low sea ice concentrations σ_C is independent of the season. This is different for the high ice concentration class ($C > 90\,\%$), where Figure 5.10 as well as Table 5.9 indicate a significant (standard deviation is here $0.4\,\%$) decrease of the average σ_C values at freeze-up (March/April) and an increase at melt-onset (November/December). These changes coincide with the marked increase/decrease of $T_{v,i}$ and $T_{h,i}$ shown in Figure 5.6. The term S_3 (compare Equation 5.13) has a relative contribution to the monthly averaged σ_C value of about $90\,\%$. A significant change in the sea ice tie points might have a large contribution to S_3. However, the impact of the change in $T_{v,i}$ and $T_{h,i}$

Table 5.9: *Monthly averaged σ_C values binned into three sea ice concentration classes defined in Figure 5.11 and averaged over each of these classes. The values are given in %.*

	Jan.	Feb.	Mar.	Apr.	May	Jun.
$15\,\% \leq C \leq 50\,\%$	$13.3\,\%$	$12.6\,\%$	$13.4\,\%$	$11.5\,\%$	$11.9\,\%$	$12.2\,\%$
$50\,\% < C \leq 90\,\%$	$9.5\,\%$	$9.4\,\%$	$8.7\,\%$	$5.6\,\%$	$6.0\,\%$	$5.9\,\%$
$90\,\% < C$	$8.1\,\%$	$8.2\,\%$	$7.2\,\%$	$4.0\,\%$	$4.6\,\%$	$4.1\,\%$
	Jul.	Aug.	Sep.	Oct.	Nov.	Dec.
$15\,\% \leq C \leq 50\,\%$	$12.2\,\%$	$12.7\,\%$	$11.4\,\%$	$13.0\,\%$	$10.5\,\%$	$11.7\,\%$
$50\,\% < C \leq 90\,\%$	$5.7\,\%$	$5.8\,\%$	$4.0\,\%$	$5.3\,\%$	$5.1\,\%$	$7.4\,\%$
$90\,\% < C$	$3.6\,\%$	$4.4\,\%$	$3.9\,\%$	$4.3\,\%$	$4.2\,\%$	$6.4\,\%$

between March and April (November and December) on S_3 is found to be negligible. Therefore, the change in the monthly averages of σ_C is most likely caused by an increase (decrease) of both pairs T_v, T_h and σ_{T_v}, σ_{T_h} between March and April (November and December). This seems to be reasonable for two reasons. Firstly, the snow can be expected to undergo diurnal melt-freeze cycles and thus to become coarse-grained as soon as the diurnal variation of solar radiation and air temperature has become large enough to force this cycle. This would increase the contribution of volume scattering resulting in a decrease of the surface emissivity and therefore T_v and T_h. Once almost the entire sea ice cover is affected by this cycle, σ_{T_v} and σ_{T_h} would decrease as well. Secondly, during Austral winter, four sea ice types contribute to the sea ice cover: FY ice, old ice, pancake ice and young ice, while during Austral summer pancake ice and young ice have disappeared almost completely. Consequently, σ_{T_v} and σ_{T_h} would decrease because of the fewer different sea ice types. In fall (March/April), pancake ice and young ice re-appear. Moreover, snow properties become highly variable again, depending on the progress of cooling and the spatial distribution of fresh snow. Both processes lead to an increasing variability of surface emissivities and, therefore, to an increase of σ_{T_v} and σ_{T_v}.

Chapter 6

Applications

This chapter is organized in two parts. The first and major part discusses the results obtained with the SEA LION (SL) algorithm for the sea ice cover of the Southern Ocean in comparison with VIS/IR data, ship observations and sea ice products derived with other methods from microwave radiances. The second part gives one case study for the application of the SL algorithm in the Arctic.

6.1 Antarctic

This section focusses first on a few examples of the daily sea ice concentration C obtained with the SL algorithm, C_{SLA}. The ice concentration development during melt-onset is shown in comparison with results of the Bootstrap (BS) algorithm (see Section 4.2) and the PELICON (PE) algorithm (see Section 4.1) in Figure 6.1 for the Amundsen/Ross Sea quadrant. Ice concentrations obtained with these two algorithms are denoted by C_{BSA} and C_{PEA}, respectively. Three days at melt-onset in Austral spring 1996 are selected. The temporal spacing between the days selected is two weeks in order to document the progress of the sea ice decay. Evident in all columns from top to bottom is a retreating sea ice edge and widening coastal polynyas. One can identify, from top to bottom, an increasing number of small regions with lower sea ice concentrations in the pack ice.

However, in the middle column showing C_{SEA} several differences can be identified in comparison to the left and right column:

- the sea ice concentration gradient across the MIZ and in the vicinity of the coastal polynyas is steeper,

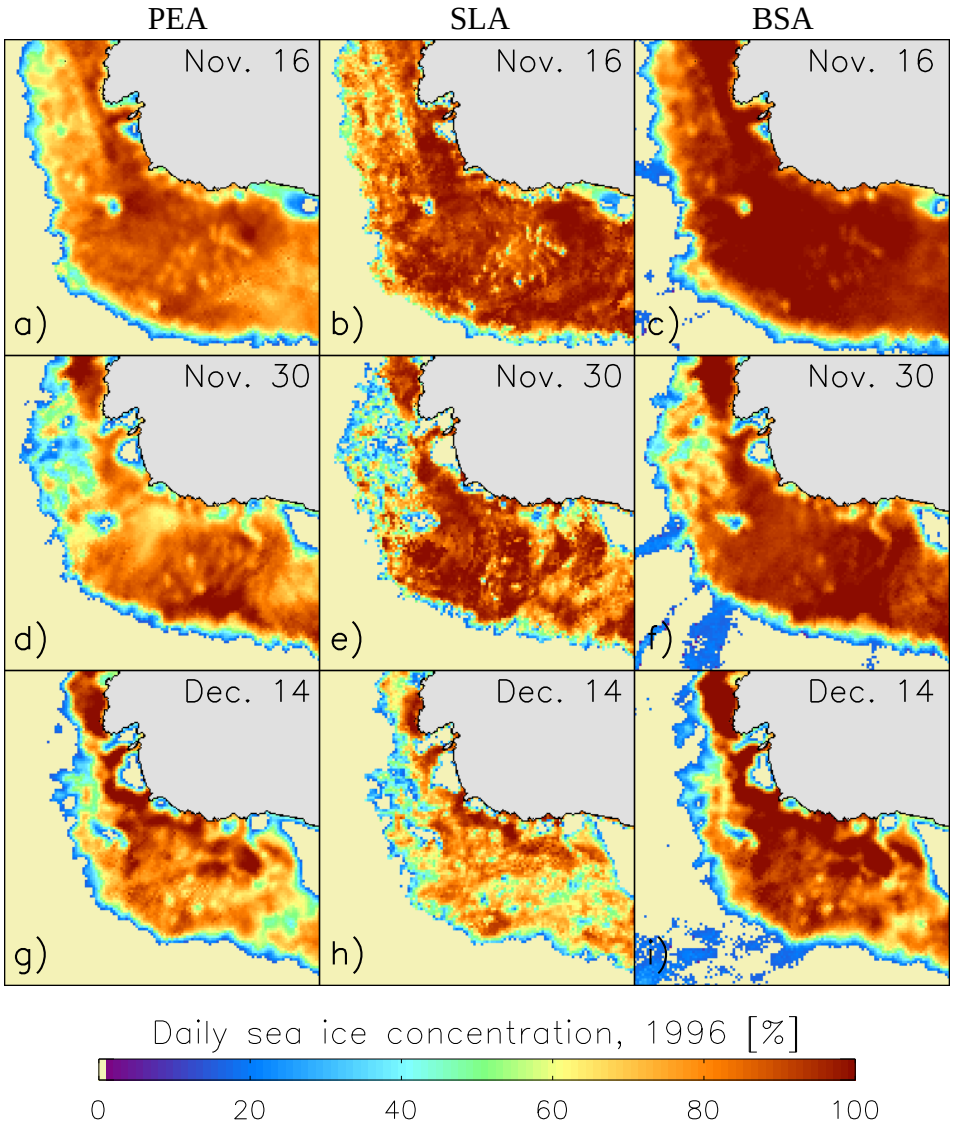

Figure 6.1: *Daily sea ice concentration for selected days at melt-onset in Austral spring 1996; left column: C_{PEA} (PEA=PE algorithm), middle column: C_{SLA} (SLA=SE algorithm), right column: C_{BSA} (BSA=BS algorithm). Values less than* $15\,\%$ *are set to zero in order to exclude remaining spurious ice caused by the weather influence. Each image shows the quadrant between* $90°$ *W and* $180°$ *W with the South Pole at the upper right corner.*

- the coastal polynyas are larger,
- the sea ice concentration in the pack ice is much more variable with frequent drops below $50\,\%$ suggesting subpixel-scale areas of low ice concentration or open water.

Table 6.1: *Average and corresponding standard deviation σ and skewness of the sea ice concentration distribution of the area shown in Figure 6.1. N is the number of pixels with $C \geq 30\,\%$.*

		Average	σ	Skewness	N
C_{PEA}:	Nov. 16	77.6	14.5	-1.23	31445
	Nov. 30	72.9	17.7	-0.66	26391
	Dec. 14	73.0	17.7	-0.52	21058
C_{SEA}:	Nov. 16	84.4	15.5	-1.36	31792
	Nov. 30	78.3	19.4	-0.83	24987
	Dec. 14	67.7	16.3	-0.28	20502
C_{BTA}:	Nov. 16	89.4	16.2	-1.95	33575
	Nov. 30	82.8	18.3	-1.20	28661
	Dec. 14	80.5	19.1	-1.00	22843

These differences become even more striking when considering that the C_{SLA} values shown in Figure 6.1 are averaged over four NSIDC $12.5 \times 12.5\,\mathrm{km}^2$ grid cells in order to match the coarser spatial resolution of the NSIDC grid used to map C_{BSA} and C_{PEA} ($25 \times 25\,\mathrm{km}^2$) and, therefore, to judge whether the larger number of details is just caused by the better spatial resolution. Strictly speaking, this shall be done with the antenna pattern of the SSM/I for the corresponding frequencies, *i. e.* 19 and 37 GHz. By doing this, only a few more details evident in the maps of C_{SLA} would get lost, particularly those of the size of one grid cell. The comparison of the sea ice areas derived from C_{SLA}, C_{BSA} and C_{PEA} given in Section 6.1.3 will allow a few conclusions about any differences in C within the pack ice throughout the year. In order to get a first idea on this, Table 6.1 lists the average, standard deviation and skewness of C obtained with the three algorithms in the area displayed in Figure 6.1. To overcome the weather influence evident in the right column of Figure 6.1 shown by low values of C_{BSA} (blue) in regions indicated as open water by the other two algorithms, only pixels with $C \geq 30\,\%$ are considered in this table. Table 6.1 illustrates the sea ice decay in the

area selected by a decreasing number of pixels with sea ice concentrations above 30 %, a decreasing average sea ice concentration and a decreasing skewness. The latter parameter describes the distribution of C within the sea ice covered area. Therefore, in this particular case, a decreasing skewness indicates that the number of pixels with low values of C increases at the expense of the number of pixels with high values of C. Following the results obtained with the SL algorithm, the sea ice retreats quite fast in the area and the period considered compared to C_{BSA} and C_{PEA}.

In order to specify the locations of the largest differences between the ice concentration maps shown, the maps shown in the middle column of Figure 6.1 (C_{SLA} are subtracted from the corresponding maps of C_{BSA} and C_{PEA}. Maps of the resulting differences are displayed in Figure 6.2. Figure 6.2 **d)** to **f)** reveal a band

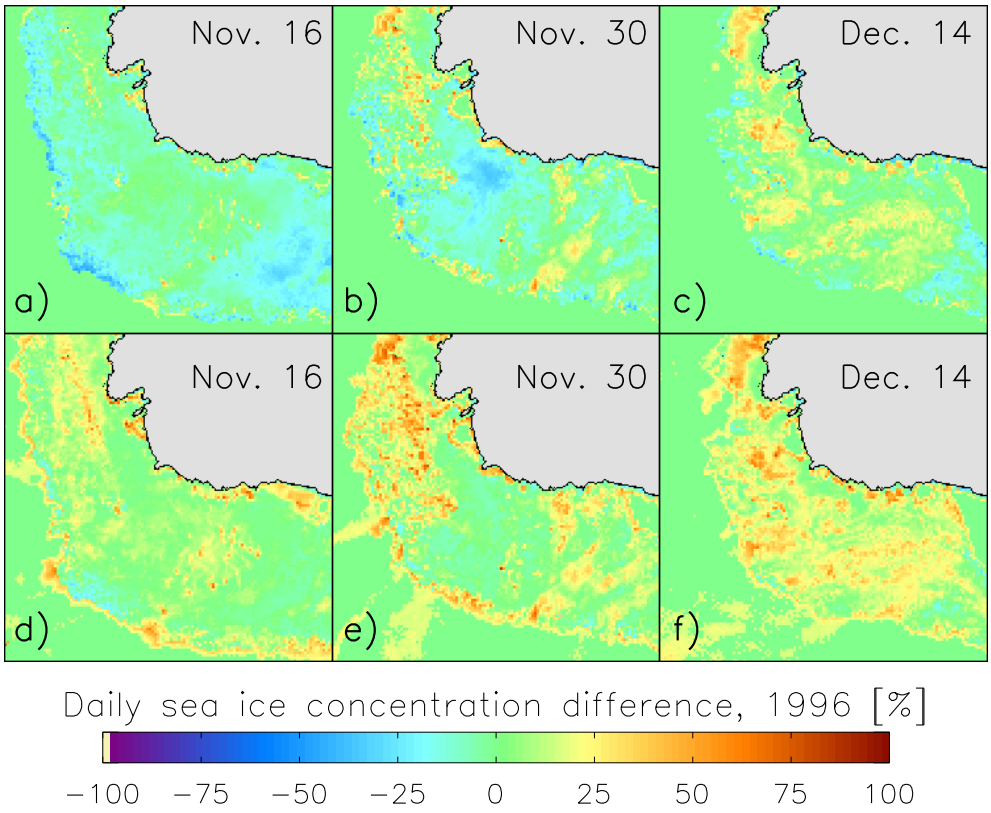

Figure 6.2: *Differences of the sea ice concentrations shown in Figure 6.1 for selected days in spring 1996,* **a)** *to* **c)***:* $C_{PEA} - C_{SLA}$*,* **d)** *to* **f)***:* $C_{BSA} - C_{SLA}$*. The geographical location is the same as in Figure 6.1.*

of positive differences along the MIZ, approximately 1 to 2 pixels wide (≈ 50 km), which cannot be identified in images **a)** to **c)** of Figure 6.2. Positive differences are evident in all images in areas of coastal polynyas. These differences are smaller in images **a)** to **c)**, *i. e.* C_{PEA} seems to give a better estimate of the polynya area than C_{BSA}.

The negative difference evident in Figure 6.2 **a)** along the MIZ and, most pronounced, near the letter "a)" is caused by an insufficient correction of the weather influence yielding an overestimation of C_{SLA}. Maps of the R-factor and the integrated cloud liquid water content L of this particular day and region (not shown) reveal large values for this latter parameter adjacent to the MIZ where L exceeds $120\,\mathrm{g\,m^{-2}}$. The cloud mask that has been obtained with the R-factor method for this day (not shown) misses this area. Consequently, the area is not excluded from the retrieval of C and only the average L value of $\approx 50\,\mathrm{g\,m^{-2}}$ obtained for November 1996 over the open water area along the sea ice edge (see Table 5.1 and its discussion) is used for the weather correction. Therefore, assuming an average sea ice concentration of $50\,\%$ in this part of the MIZ and following the increase of C due to L shown in Figure 5.8 **c)** and **d)** an overestimation of C_{SLA} in the range of $10\,\%$ to $20\,\%$ can be expected – a value which agrees with the observed sea ice concentration difference. Positive differences scattered over the pack ice covered area in all images of Figure 6.2 can be associated with subpixel-scale areas of low ice concentrations or open water which are detected using the 85 GHz SSM/I channels and the SL algorithm but which cannot be resolved with methods depending on the other SSM/I channels.

6.1.1 Comparison with OLS Imagery

This section compares maps of C_{SLA} and C_{PEA} with images collected with the OLS sensor. The focus of this comparison is to highlight the larger number of details evident in the maps of C_{SLA} compared to C_{PEA}. A comparison with VIS/IR imagery requires daylight and clear-sky conditions. Consequently, the following four cases discuss Austral summer conditions only and focus on cloud-free areas. For the comparison, 25 OLS pixels (see Table 3.1 for original spatial resolution) are averaged in order to match the spatial resolution of the NSIDC $12.5 \times 12.5\,\mathrm{km^2}$ grid used for mapping C_{PEA} and C_{SLA}.

The VIS images show the shortwave albedo as greyscale values. Dark (bright) areas denote a low (high) albedo, thus open water can be identified by black areas while the ice and clouds can be associated with grey and white areas. The IR images are converted into infrared temperatures using

$$T_{IR} = 190 + \frac{120}{255}x \tag{6.1}$$

where T_{IR} is the infrared temperature in K and x is the OLS measurement binned to values $0 \ldots 255$ for temperatures between 190 and 310 K [Schlüter, 2000]. Since ϵ_{IR} is very close to unity for most natural surfaces, T_{IR} can be regarded as the surface or cloud-top temperatures. Open water areas exhibit a surface temperature around -1.8°C and appear white in the IR images shown. Superimposed on the VIS images are isolines of C_{SLA} and C_{PEA} at 15 %, 60 % and 90 %, color-coded as indicated in the legend. The IR images are superimposed by the isolines $C_{SLA} = 15\,\%$ (solid red line) and $C_{PEA} = 15\,\%$ (dotted black line). The 15 % isoline can be regarded as the sea ice edge in case of a compact sea ice cover.

Figure 6.3 from mid-November, 1996, shows a typical situation for the melt-onset in the Amundsen/Ross Sea area. While most of this region is still covered by pack ice with $C \geq 90\,\%$ and $T_{IR} < -2$° C, several polynyas can be identified along the coast by a low albedo and values of T_{IR} typical of open water. This seems to be quite realistic because during November the increasing solar radiation accompanied by rising air temperatures stops the sea ice production in the coastal polynyas [Markus et al., 1998]. The decay of the Antarctic sea ice cover starts not only from the MIZ but from the coastal polynyas as well. The reason for this is a positive feedback mechanism. As long as air temperatures are low enough to generate new ice in these polynyas, they remain more or less covered by thin sea ice. Once the air temperature exceed a critical value, the heat loss at the open water surface is to small to form new ice. The open water fraction of the polynya increases and considerably less solar radiation is reflected back. Both air and water heat up slowly, thinning the surrounding sea ice until it disappears. The total area and the open water fraction of the polynya increase. Figure 6.3, top and middle row, reveals quite a good agreement between the coastal polynyas and areas encircled by the 15 % isoline of C_{SLA}, while just one polynya exhibits a small area encircled by the 15 % isoline of C_{PEA}. However, the 60 % isoline of C_{PEA} agrees well with the sea ice edge of all coastal polynyas shown. In the pack ice, also some polynya-like features can be identified by a few dark spots evident in the VIS images shown in the right column of Figure 6.3 revealing a low albedo. The majority of these features are within the 60 % isoline of C_{SLA} and in two cases even within the 15 % isoline of C_{SLA}. At least some of these features are certainly ice-free because they coincide with areas of $T_{IR} \geq -2$ °C in the IR image. However, these polynyas seem to be too small to be detected by the PE algorithm since C_{PEA} remains above 60 %.

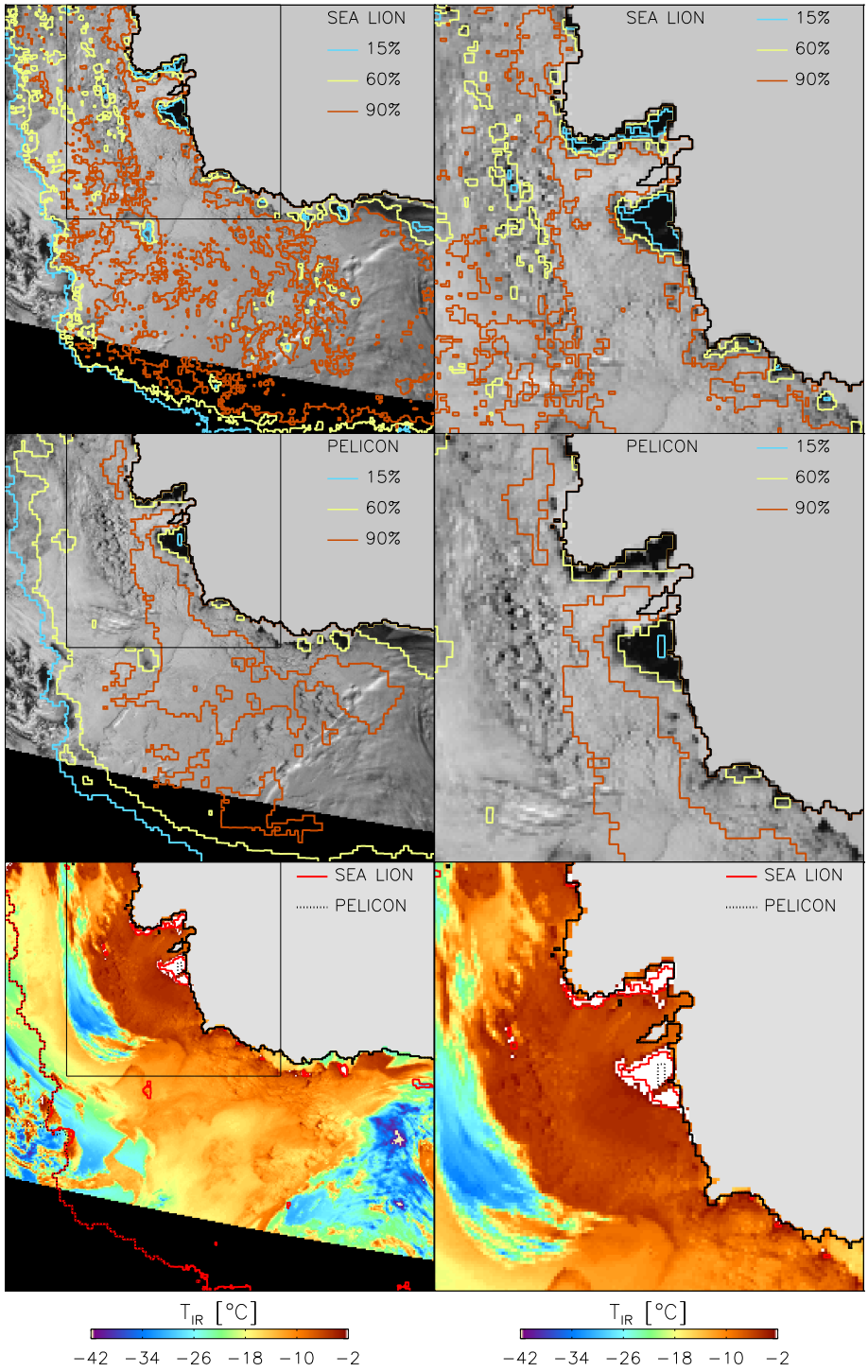

Figure 6.3: *OLS images superimposed with SSM/I sea ice concentration isolines for November 16, 1996. Top and middle: VIS-images and isolines of C_{SLA} and C_{PEA}, respectively. Bottom: IR-temperature and sea ice edge. Left column: area of* $2800 \times 2800\,km^2$ *between 90° W and 180° W (South Pole at the upper right corner). Right column: zoom of the area marked in left column:* $1400 \times 1400\,km^2$.

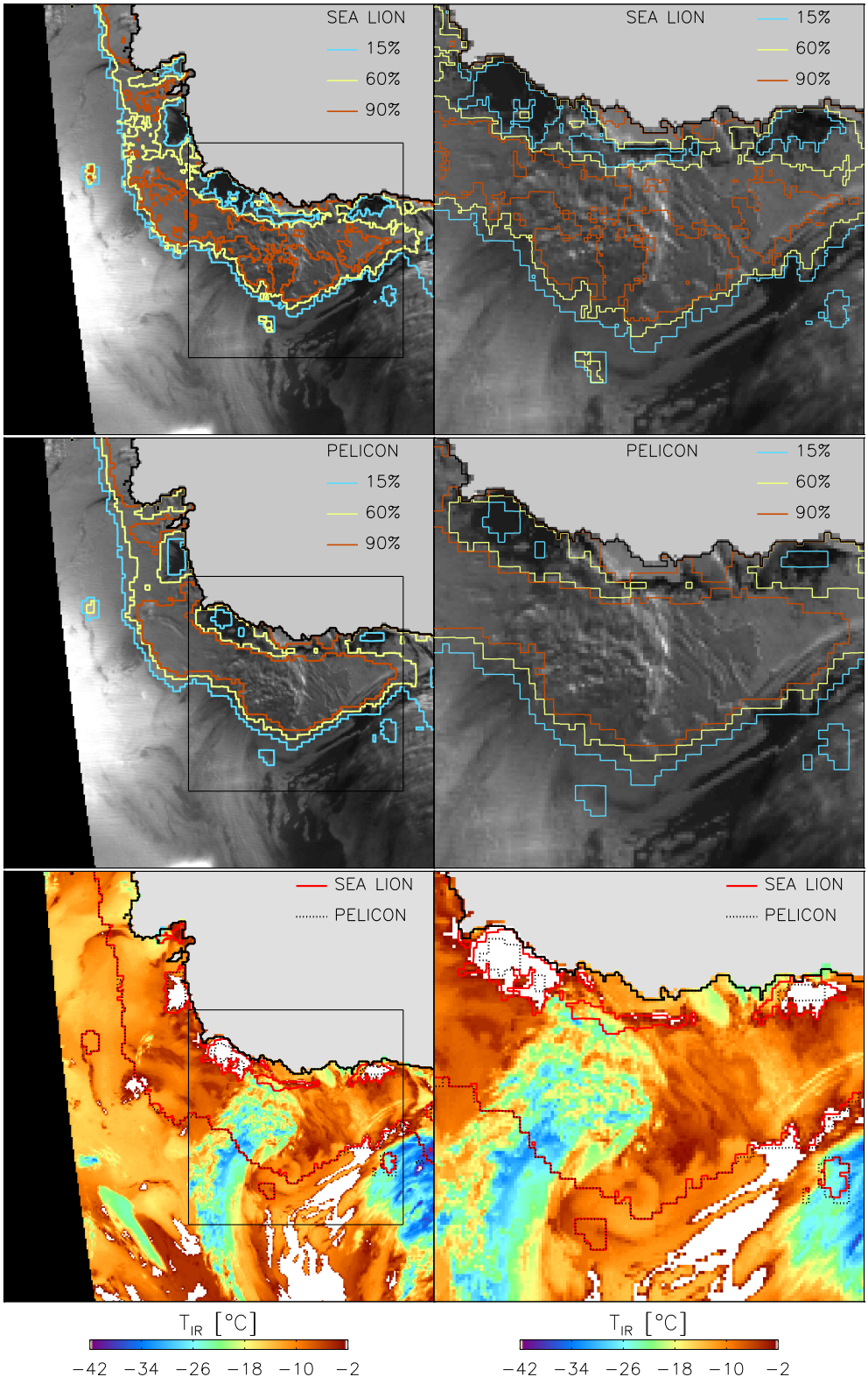

Figure 6.4: *Same as in Figure 6.3 for January 23, 1998.*

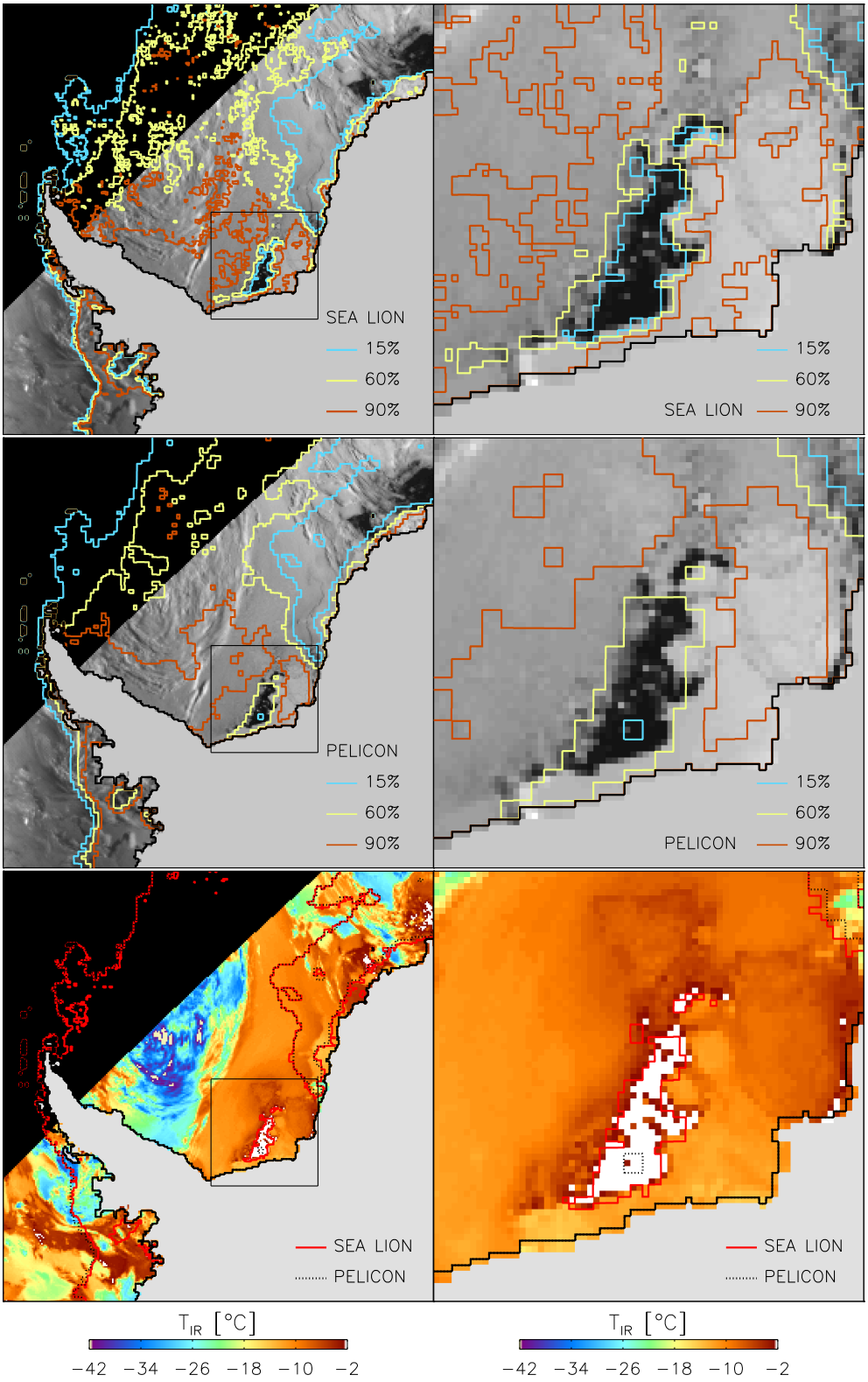

Figure 6.5: *Same as in Figure 6.3 for January 2, 1996. Left column: area of* $2800 \times 2800\,km^2$ *between 0° W and 90° W (South Pole at the lower right corner). Right column: zoom of the area marked in left column:* $700 \times 700\,km^2$.

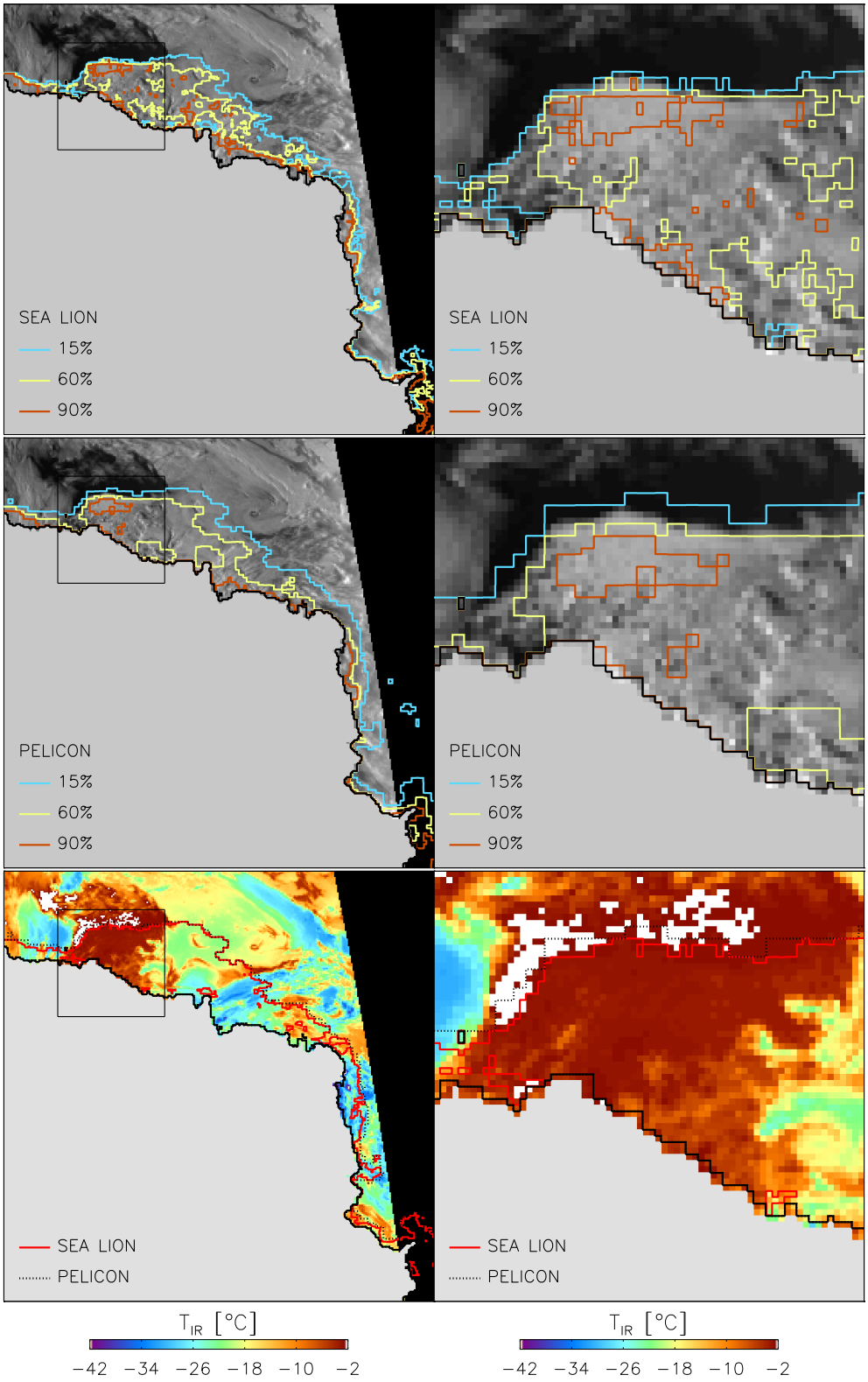

Figure 6.6: *Same as in Figure 6.3 for January 3, 1996. Each image in the left column: area of* $2800 \times 2800\,km^2$ *between* $0°E$ *and* $90°E$ *(South Pole at lower left corner). Right column: zoom of the area marked in the left column:* $700 \times 700\,km^2$.

Figure 6.4 shows the same region later in the melting period of the year 1998. Three large coastal polynyas can be identified in the OLS images of the left column. Almost all details of the sea ice edge of two of these polynyas are evident in the 15 % isolines of C_{SLA} as is demonstrated by the VIS and IR images of the right column. The same holds for the cloud-free part of the outer sea ice edge visible the right half of the images in the right column of Figure 6.4. The 15 % isolines of C_{PEA} show fewer details in both the coastal polynyas as well as the outer ice edge. While both algorithms allow to detect the iceberg B10A evident in the half of the images of the left column of Figure 6.4, only C_{SLA} is above 90 %.

Figure 6.5 displays a flaw polynya *i. e.* a polynya adjacent to shelf ice, in the Weddell Sea. The entire polynya is cloud-free. The sea ice edge of this polynya taken from the VIS and IR images shown agrees within one pixel, *i. e.* within 10 km with the 15 % isoline of C_{SLA} while the agreement of the 15 % isoline of C_{PEA} with this sea ice edge is poor. The 60 % isoline of C_{PEA} agrees much better. The forth case shown in Figure 6.6 is an example of the outer sea ice edge in the eastern Weddell Sea. Most coastal polynyas indicated by the C_{SLA} isolines are obscured by clouds. However, in the cloud-free part, the 15 % isoline of C_{SLA} agrees within 10 km with the sea ice edge identified in the VIS and IR images, thus much better than the 15 % isoline of C_{PEA}.

To summarize these case studies: As can be expected from exploiting the much higher spatial resolution of the 85 GHz SSM/I channels compared to the other SSM/I channels used in the PE algorithm, the sea ice concentration derived with the SL algorithm reveals much more details. It is shown that during Austral summer the sea ice edge indicated by VIS/IR imagery coincides within 10 km with the 15 % isoline of C_{SLA}. This is a substantial improvement compared to the results provided by the PE algorithm.

6.1.2 Comparison with Ship Observations

This section focusses on the comparison between selected *in situ* observations of the sea ice cover aboard the U.S. Research Vessel *Nathaniel B. Palmer*, denoted by C_{SHIP} in the following discussion, and the sea ice concentration calculated from SSM/I data. The latter data set, denoted in summary by C_{SSMI}, consists of C_{BSA}, C_{PEA} and C_{SLA}. Details of the selection are described in Section 3.4.

Figure 6.7 shows the results: the relative occurence of C_{SHIP} in comparison with that of C_{BSA} (C_{PEA}, C_{SLA}) in steps of 10 %, the average difference between C_{BSA} (C_{PEA}, C_{SLA}) and C_{SHIP} and the equation of the linear regression between C_{SHIP} and C_{BSA} (C_{PEA}, C_{SLA}). In terms of the relative occurence, C_{SLA} and C_{BSA}

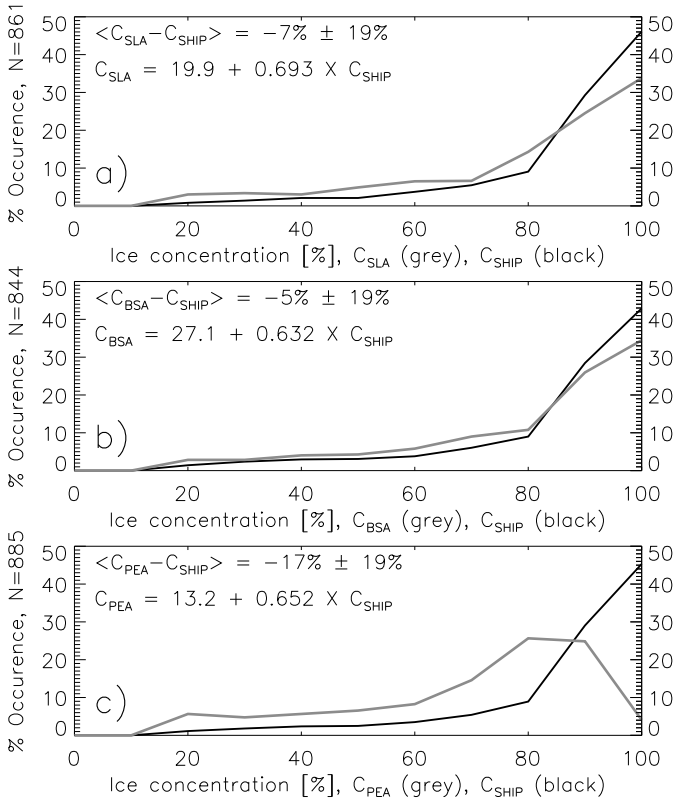

Figure 6.7: *Relative occurences of the total sea ice concentrations observed aboard the U.S. Research vessel* NATHANIEL B. PALMER *(C_{SHIP}) during 1994-1998 in comparison with those obtained from SSM/I data (C_{SSMI}). Images* **a)**, **b)** *and* **c)** *show the comparison with C_{SLA}, C_{BSA} and C_{PEA}, respectively. All values are binned into* $10\,\%$ *intervalls. Average differences between C_{SHIP} and C_{SSMI} (e. g. $< C_{SEA} - C_{SHIP} > \pm$ its standard deviation) and linear regression equations are given in addition in the upper left corners of each image.*

agree quite well with C_{SHIP} (images **a)** and **b)**), whereas C_{PEA} reveals discrepancies particularly at high ice concentrations. The corresponding average differences are also similar for C_{SLA} and C_{BSA} ($-7\,\%$ and $-5\,\%$, respectively), while that between C_{PEA} and C_{SHIP} is considerably larger. The most convincing linear regression between C_{SSMI} and C_{SHIP}, given by the corresponding equation in each image, is obtained with C_{SLA} (see Figure 6.7 **a)**). However, the obtained slope of ≈ 0.7 is considerably smaller than 1. Using C_{BSA} yields the smallest slope and the largest bias and, therefore, the worst fit. In conclusion, the results for all three algorithms are quite similar and certainly not sufficient to judge the quality of

C_{SLA} in comparison to C_{BSA} and C_{PEA}. This is also indicated by quite low linear regression coefficients, ranging between 0.534 for the comparison of C_{SLA} and C_{SHIP} and 0.562 for the comparison of C_{BSA} with C_{SHIP}.

As already mentioned in Section 3.4, ship observations of the sea ice cover are quite difficult to compare with sea ice concentrations obtained from spaceborne remote sensing data, particularly due to the large difference of the area which can be observed by both methods. However, a comparison between ship observations and C obtained from SMMR data with the BS algorithm made by Grenfell et al. [1994] reveals much better results. They obtained a correlation coeffient of 0.849 and a linear regression with a slope of 0.97 and a bias of $2.2\,\%$ which is almost a perfect agreement. The difference between both comparisons can be explained with the different ship observation data sets. Grenfell et al. [1994] have been able to use hourly ship observations. This allows to calculate a weighted average of the sea ice concentration along the ship's track. Moreover, uncertainities in the ship observations can be estimated from the spread of ice concentrations averaged over the particular SMMR pixel. This is a significant advantage compared to the data set used in this thesis, where often only one ship observation falls into one grid cell of $25 \times 25\,\mathrm{km}^2$. This does not allow to estimate the weighted average and spread of C. The agreement between C_{SLA} and C_{SHIP} might be improved comparing C_{SLA} and C_{SHIP} mapped into the $12.5 \times 12.5\,\mathrm{km}^2$ grid. However, in doing so, on the one hand the probability that more than one ship observation falls into one grid cell is significantly reduced. On the other hand, a point observation of the ice cover can be expected to agree more often with the average sea ice conditions of a small than of a large area, since homogeneous sea ice conditions are more probable on smaller spatial scales. This might be a point deserving further studies.

6.1.3 Sea Ice Area

In this and the following section sea ice areas and extents calculated from C_{SLA} are shown in comparison to those calculated from C_{BSA} and C_{PEA}. Sea ice concentrations below $15\,\%$ may be caused by the weather influence (compare Figure 6.1, right column) and are set to zero. In the next step, the sea ice area is calculated by performing the sum of all pixels with $C \geq 15\,\%$, weighted by C. Figure 6.8 (top) illustrates the annual cycle and the interannual variability of the Antarctic sea ice area for the period 1992-1999. All three algorithms yield a similar minimum sea ice area in February of about $2.5 \times 10^6\,\mathrm{km}^2$. The maximum sea ice area occurs in late Austral winter and is found to amount $\approx 15 \times 10^6\,\mathrm{km}^2$ based on C_{PEA} in agreement with the findings of Thomas [1998]. However, C_{SLA} and C_{BSA}

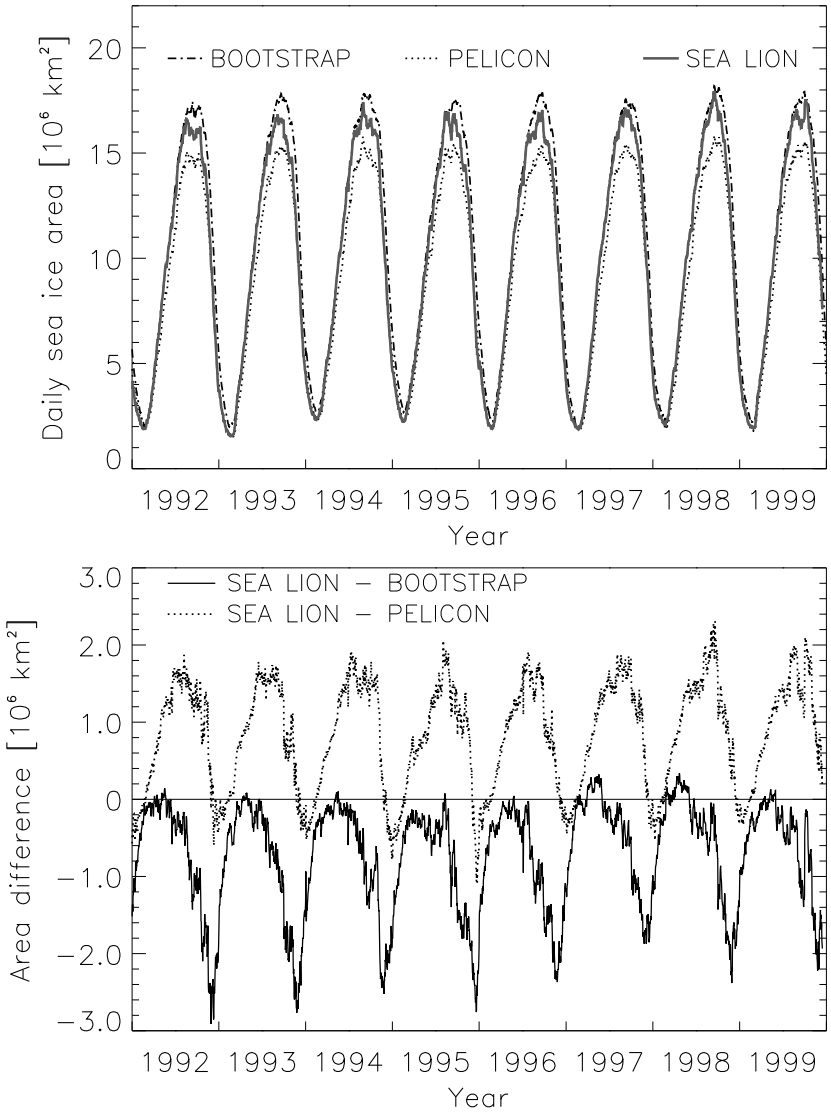

Figure 6.8: *Time-series of the daily Antarctic sea ice area (top) and area difference (bottom) derived from C_{BSA}, C_{PEA} and C_{SLA} for 1992-1999.*

both result in a larger average maximum sea ice area of $\approx 16.5 \times 10^6\,\mathrm{km}^2$ and $\approx 17.5 \times 10^6\,\mathrm{km}^2$, respectively. Figure 6.8 (bottom) reveals more details about the differences between the sea ice areas obtained.

On average, the SEA LION (SL) sea ice area exceeds the one obtained from C_{PEA} (PE sea ice area) during almost the entire year – except in December and

January. The difference between the PE and the SL sea ice areas increases from late Austral summer to Austral winter, remains rather constant throughout this season and decreases rapidly during spring becoming eventually negative. In contrast, the SL sea ice area falls below the one obtained from C_{BSA} (BS sea ice area) for almost the entire period. Starting in mid-winter the difference between the SL and the BS sea ice areas increases rapidly to a maximum in December before decreasing to its minimum during early freeze-up where differences may fall below 0.5×10^6 km^2 and sometimes the SL sea ice area may exceed the BS sea ice area.

Figure 6.9 shows the daily SL sea ice area averaged over the period 1992-1999 (grey) in comparison to correspondingly averaged PE (blue) and BS (red) sea ice areas. From mid-March to mid-November, PE sea ice areas shown in Figure 6.9 are smaller than the mean daily sea ice areas obtained from C_{BSA} and C_{SLA}. This indicates either a smaller average number of pixels covered by sea ice or a lower average sea ice concentration within each pixel. This is discussed in Section 6.1.4. The average BS and SL sea ice areas agree within their standard deviations dur-

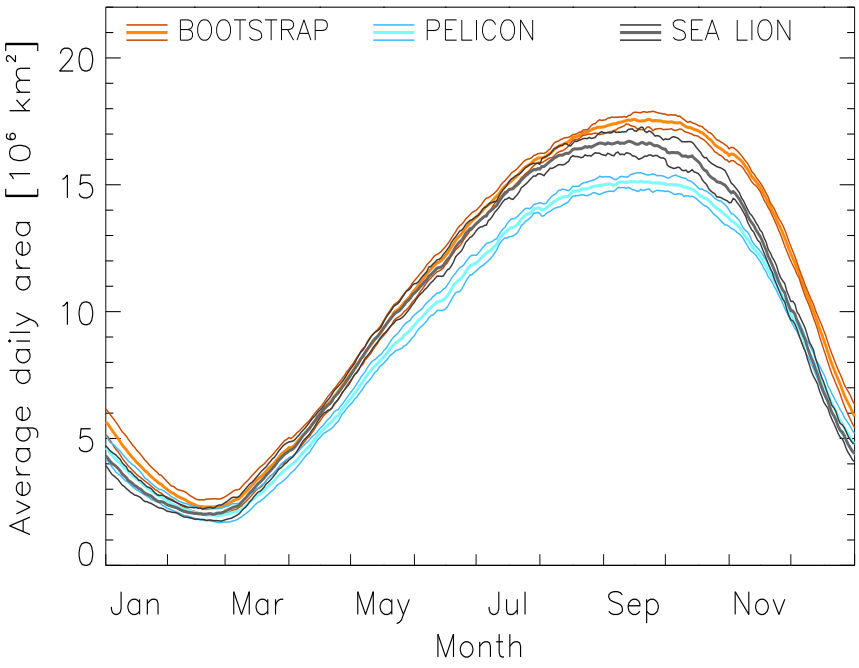

Figure 6.9: *Daily Antarctic sea ice area derived from sea ice concentrations obtained with the three mentioned algorithms and averaged over the period 1992-1999. Thick lines denote the average sea ice area, thin lines denote the range given by* $\pm$ *one standard deviation.*

ing almost the entire freeze-up period. However, starting in mid-September, the average SL sea ice area begins to decrease, at first moderately and after October more rapidly until the minimum sea ice area is reached. During the moderate decrease, the average BS and PE sea ice areas remain constant or decrease slightly by a similar amount. This difference between the results obtained with the PE and BS algorithms and with the SL algorithm must be caused by a different change in the average sea ice concentration because the average daily sea ice extent alters by a similar amount for all three algorithms as is demonstrated in Figure 6.11. In searching for an explanation of this different sea ice concentration change in late winter/early summer at least two reasons seem to be possible:

- The sea ice tie points used to calculate C_{SLA} are too small. In this case, the difference $P_i - P$ (see Equation 5.4) would be too large and C_{SLA} would be underestimated. This seems to be unrealistic since the average sea ice tie points for September/October are quite large and agree with *in situ* measurements (see Figures 5.1 and 5.6).

- The sea ice tie points used by the PE and BS algorithms are inadaequate during these September/October and cause an overestimation of C_{PEA} and C_{BSA}. These algorithms use seasonal (BS) or yearly sea ice tie points (PE). During September/October one can expect the highest snow load on Antarctic sea ice. A high snow load may lead to wide-spread flooding and the formation of slush at the snow-ice interface which causes a polarization-dependent decrease of the 19 and 37 GHz SSM/I brightness temperatures ([Garrity, 1992] and Garrity (2000), personal communication). Consequently, for a $100\,\%$ sea ice cover with slush at the snow-ice interface the SSM/I brightness temperatures are smaller and the corresponding polarization difference is larger than revealed by the sea ice tie points (see Tables 4.1 and 4.2 on page 73). This effect, however, causes an underestimation of the sea ice concentration and, therefore, does not explain the above-mentioned discrepancy in the sea ice concentration change in September/October. An increased snow liquid water fraction would have the opposite effect, causing a brightness temperature increase, a depolarization, thus larger brightness temperatures and a smaller polarization difference than revealed by the sea ice tie points and, finally, an overestimation of the sea ice concentration. This might explain the discrepancy mentioned.

6.1.4 Sea Ice Extent

The sea ice extent is the sum of the area of all ice-covered pixels. Again only sea ice concentrations above 15 % are considered (see beginning of Section 6.1.3). Figure 6.10 illustrates the interannual variability and the annual cycle of the

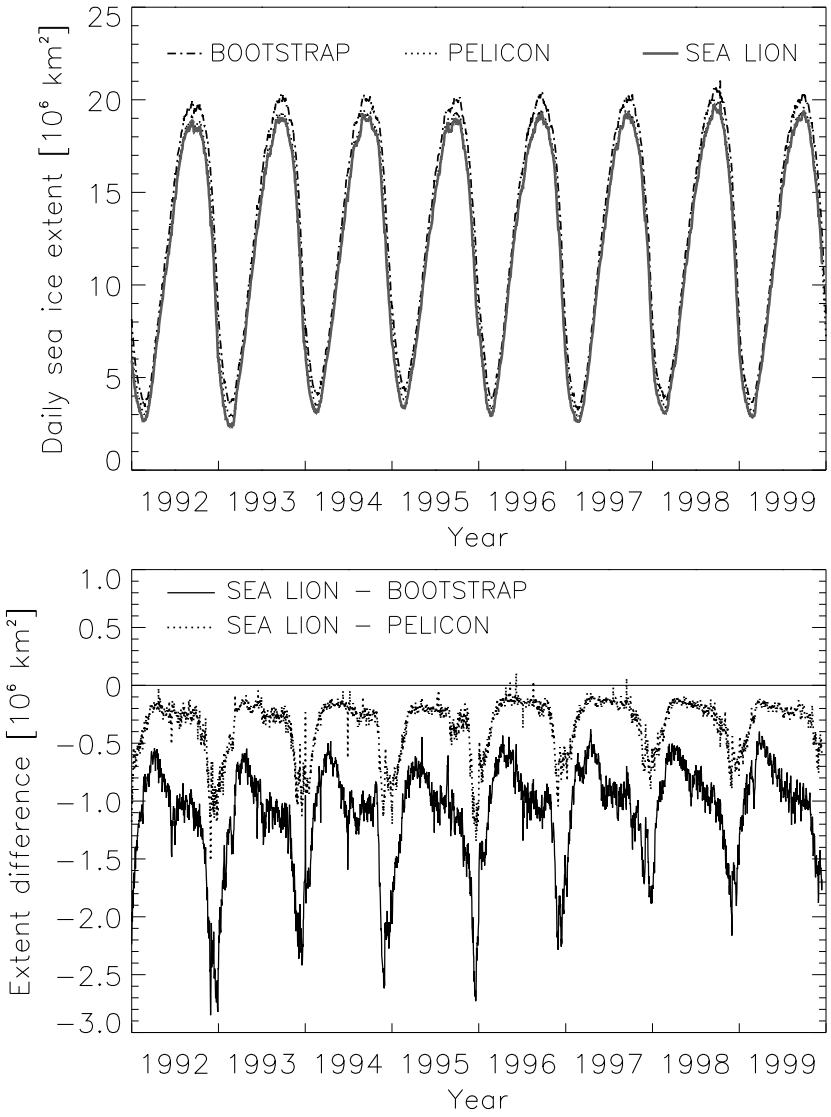

Figure 6.10: *Time-series of the daily Antarctic sea ice extent (top) and extent difference (bottom) derived from C_{BSA}, C_{PEA} and C_{SLA} for the period 1992-1999.*

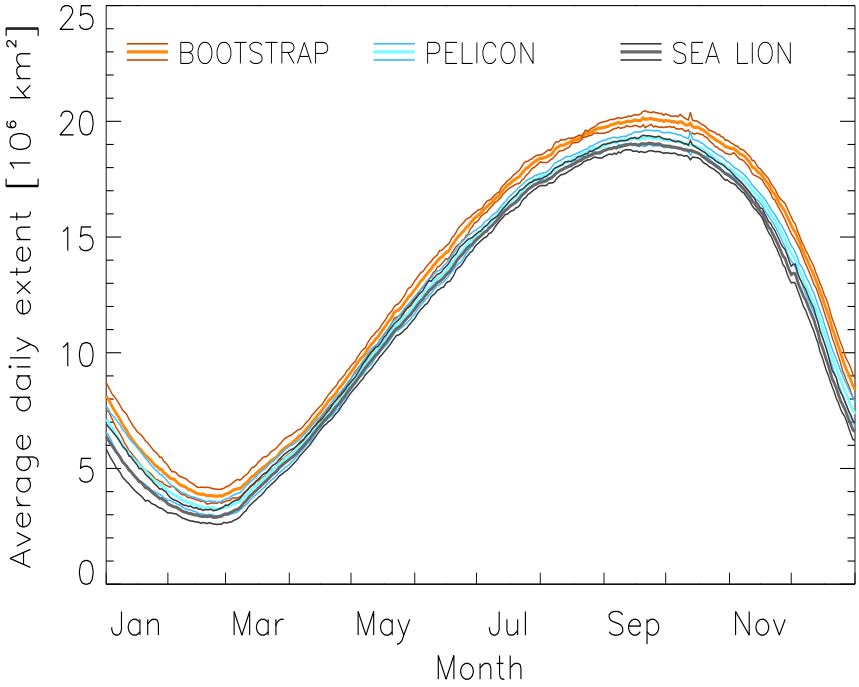

Figure 6.11: *Daily Antarctic sea ice extent derived from sea ice concentrations obtained with the three mentioned algorithms and averaged over the period 1992-1999. Thick lines denote the average sea ice extent, thin lines denote the range given by* $\pm$ *one standard deviation.*

Antarctic sea ice extent varying, on average, between $3.5 \times 10^6\,\mathrm{km}^2$ in Austral summer and $19.5 \times 10^6\,\mathrm{km}^2$ in Austral winter for the period 1992-1999. This agrees with the findings of Comiso et al. [1997] and Thomas [1998]. SEA LION (SL) sea ice extents seem to be smaller than those obtained from C_{BSA} (BS sea ice extent) and C_{PEA} (PE sea ice extent) all year round. This is shown in more detail in Figure 6.10 (bottom) displaying the differences between the SL sea ice extent and the PE and BS sea ice extents. Clearly, SL sea ice extents are systematically smaller than the PE and BS sea ice extents. In comparison to the difference of the SL and PE sea ice extents, the difference between the SL and BS sea ice extents are, on average, twice as large. The few outliers evident in both time-series of the extent difference are caused by data gaps.

Figure 6.11 shows daily SL sea ice extents averaged over the period 1992-1999 (grey) in comparison to correspondingly averaged PE (blue) and BS (red) sea ice extents. Almost throughout the entire year, average BS sea ice extents are larger

than average PE and SL sea ice extents. The average SL and PE sea ice extents agree within their standard deviation between March and September and differ only slightly more in October/November. This indicates that the considerably smaller average PE sea ice area shown in Figure 6.9 is caused by a lower average sea ice concentration. For regions exhibiting high ice concentrations (pack ice) Comiso et al. [1997] have already stated that C_{BSA} agrees much better with sea ice concentrations derived from AVHRR IR imagery than C provided by the NASA Team (NT) algorithm (C_{NTA}). The difference between C_{BSA} and C_{NTA} is found to be $\approx 10\,\%$ (see also Table 6.2). Using C_{PEA} instead of C_{NTA} would make no difference since the extended weather correction used in the PE algorithm is confined to regions with sea ice concentrations below $50\,\%$ [Thomas, 1998].

What should be evident in Figures 6.9 and 6.11 is the earlier detection of the melt-onset due the better spatial resolution of the 85 GHz SSM/I channels as has already been shown in Figures 6.1 and 6.2. In fact, the average SL sea ice extent starts to fall below the average PE sea ice extent in late October/early November and, until March, remains below the average BS and PE sea ice extents.

6.1.5 Sea Ice Anomalies within 1992-1999

In order to gain information about the spatial and temporal variability of the sea ice cover, monthly and yearly averages as well as corresponding anomalies (yearly anomaly = yearly means averaged over the entire period − single yearly mean; monthly anomaly = monthly means averaged over entire period − single monthly mean) and their standard deviations are derived from the time-series of C_{SLA}, C_{BSA} and C_{PEA}. Sea ice concentrations below $15\,\%$ are omitted (see beginning of Section 6.1.3). Averages of C_{SLA}, C_{PEA} and C_{BSA} are very similar for the entire period and are shown in the images of the left column of Figure 6.12.

However, the difference images given in the right column of Figure 6.12 vary considerably. Image **b)** shows that, on average, C_{SLA} exceeds C_{PEA}, particularly along the coast and in the southern Ross Sea. Smallest differences can be identified in the Weddell Sea. In contrast, image **d)** reveals that, on average, C_{SLA} falls below C_{BSA} except along the coast and in the southern Ross Sea. The positive differences evident in images **b)** and **d)** along the coast are most likely due to the smaller contamination of C by land within the FOV when using the 85 GHz SSM/I channels [Bennartz, 1999]. The positive differences located in the southern Ross Sea can be explained by two facts: the smaller sensitivity of the 85 GHz SSM/I channels to thin ice and the better spatial resolution. The smaller sensitivity causes higher ice concentrations in thin ice areas when using the SL algorithm instead of

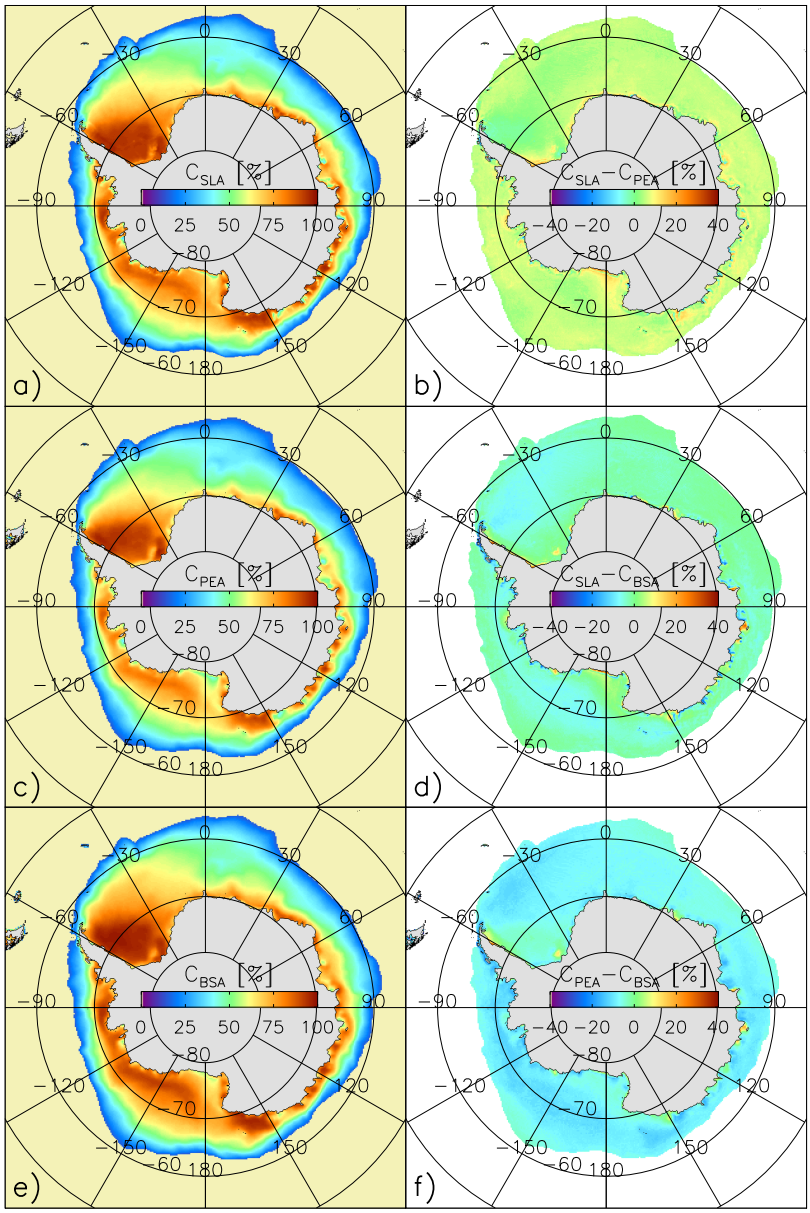

Figure 6.12: *Sea ice concentration averaged over the period 1992-1999 (left column) and differences between these averages (right column). Values below* 15 % *are set to zero in the left images and are not considered when deriving the differences.*

using the BS or the PE algorithms. This, together with the better spatial resolution allows a more realistic estimation of the open water fraction of polynyas which is particularly important during melt-onset. The difference shown in image **f)** is in line with the discussion given in Sections 4.2 and 6.1.4) and with the findings of Comiso et al. [1997] revealing an average value for $C_{PEA} - C_{BSA}$ close to $-10\,\%$ (see Table 6.2). In comparison, the SL algorithm provides average sea ice concentrations which are about $5\,\%$ larger than those obtained with the PE algorithm and which are about $3\,\%$ smaller than those calculated with the BS algorithm as is documented in Table 6.2. Therefore, taking into account the results of Comiso et al. [1997], the SL algorithm provides at least in the pack ice a sea ice concentration which is more realistic than the one given by the PE algorithm.

Table 6.2: *Averages and corresponding standard deviation, σ, of the differences given in the right column of Figure 6.12.*

$(C_{PEA} - C_{BSA}) \pm \sigma$	$(C_{SLA} - C_{PEA}) \pm \sigma$	$(C_{SLA} - C_{BSA}) \pm \sigma$
$(-8.1 \pm 2.7)\,\%$	$(4.6 \pm 2.4)\,\%$	$(-3.5 \pm 3.2)\,\%$

It is well known, that anomalies of the Antarctic sea ice cover are linked to the *Antarctic Circumpolar Wave* (ACW) as stated by White and Peterson [1996]. The ACW is a zonal oceanic wave propagating eastward around Antarctica and acting as a transport medium of atmospheric, oceanic and cryospheric anomalies of, for instance, the average SST, the surface salinity, the surface air pressure and the sea ice extent. One entire loop takes about 8 to 10 years (40° longitude per year). The anomalies usually appear in a bi- or tri-polar structure, *i. e.* reveal two or three minima and maxima, respectively.

Figure 6.13 shows the anomalies of the annual mean sea ice concentration obtained with the SL algorithm for the period 1992-1999. Certainly, this period is too short to observe sea ice concentration anomalies traveling with the ACW for a full cycle. There is only poor evidence for a bi- or tri-polar distribution of the yearly anomalies shown in Figure 6.13. However, when focussing on one area, for instance the Amundsen/Ross Sea sector (-120° to -180°), the change in the sign of the anomaly particularly from 1995 to 1998 ($+,-,+,-$) is quite convincing and seems to indicate a propagating wave.

Figure 6.14 shows the anomalies of the monthly mean sea ice concentration in September for the period 1994-1999. In image **a)** one can clearly identify three waves by alternating positive and negative anomaly values along the MIZ. Forced

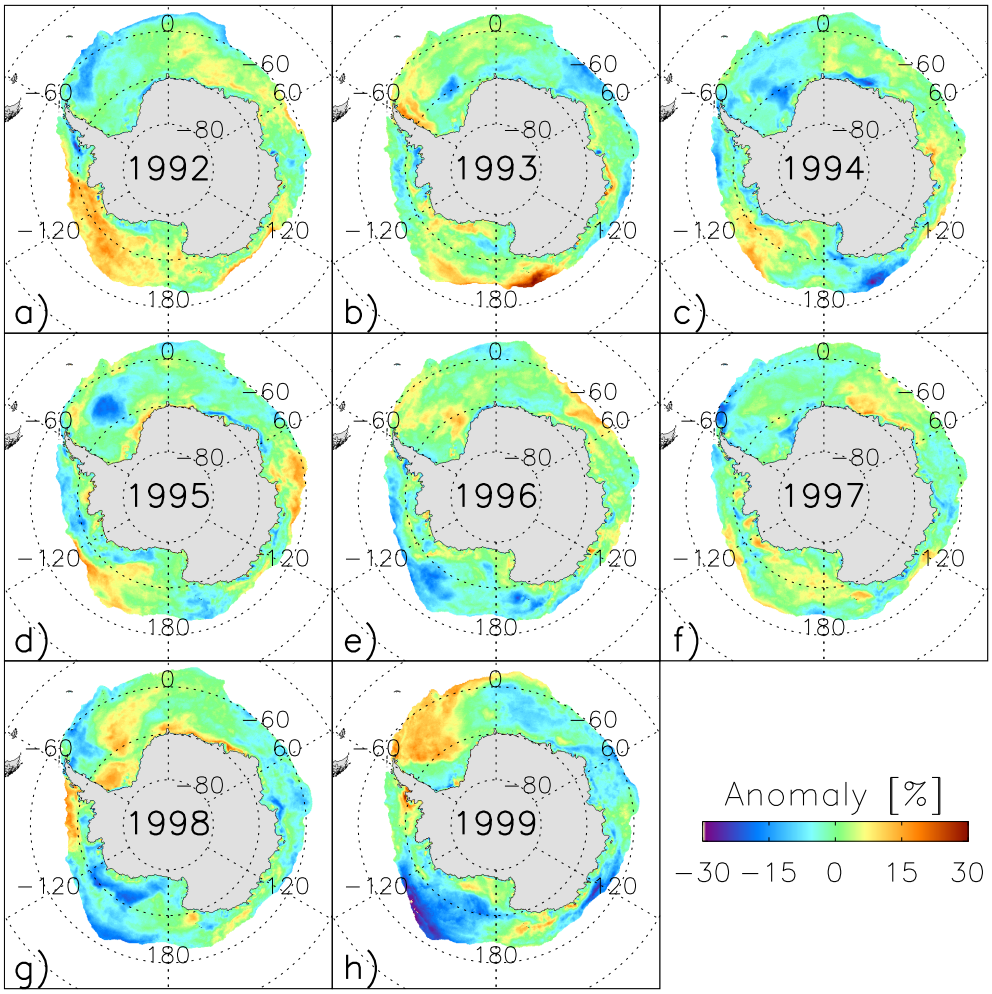

Figure 6.13: *Yearly anomalies of the yearly mean sea ice concentration obtained with the SL algorithm and averaged over the period 1992-1999.*

by the ACW this anomaly distribution propagates eastward. This is illustrated by the next images shown in Figure 6.14 at least partly. The negative anomaly at the Antarctic Peninsula (image **a)**) becomes positive in image **b)**, negative image **c)** and switches back positive values in image **d)**. The same happens at approximately 120°W with reversed signs. In the remaining areas, the anomalies reverse signs at least once during two years.

Averaging the anomalies of the annual mean sea ice concentration obtained with the BS, the PE and the SL algorithms yields the images **a)**, **b)** and **c)** dis-

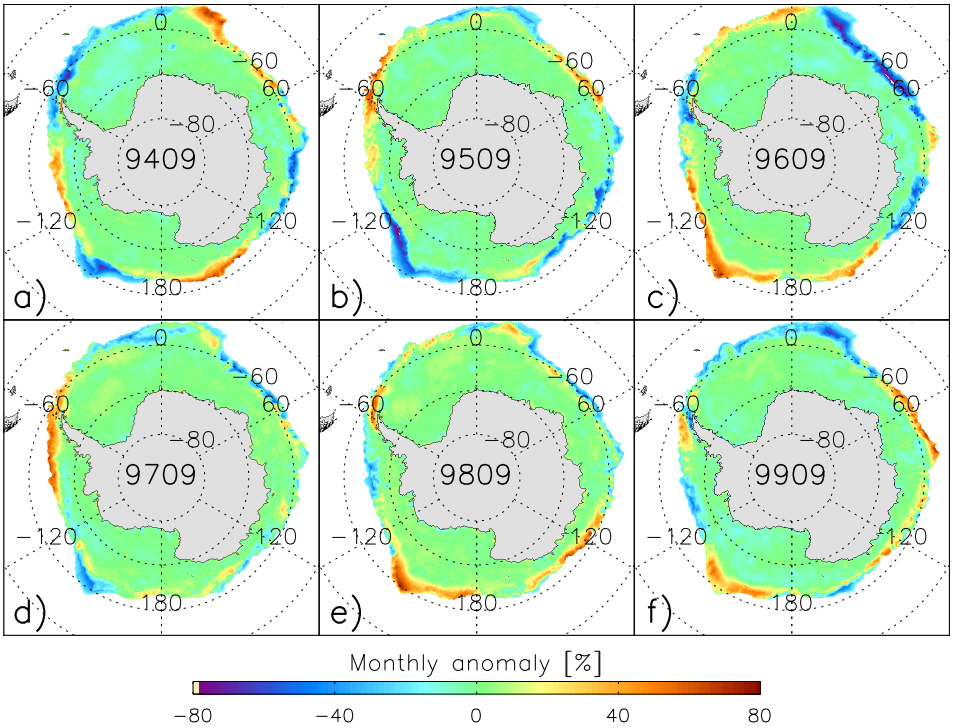

Figure 6.14: *Selected monthly anomalies of the monthly mean sea ice concentration obtained with the SL algorithm and averaged over the period 1992-1999. The digits in the center of each image indicate year and month of the anomaly.*

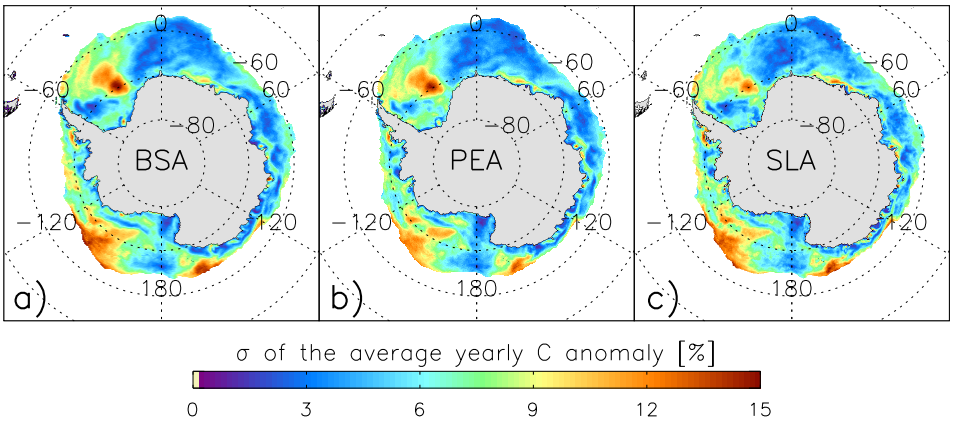

Figure 6.15: *Average yearly sea ice concentration anomaly obtained with* **a)** *the BS algorithm,* **b)** *the PE algorithm and* **c)** *the SL algorithm for 1992-1999.*

played in Figure 6.15, respectively. These images reveal that the yearly anomalies change significantly during 1992-1999 with an interesting spatial distribution which is very similar for the three algorithms used. Following the images of Figure 6.15, the eastern Weddell Sea, almost the entire ice-covered area off East Antarctica and particulary the southern Ross Sea are sites of a low variability of the yearly sea ice concentration anomaly. This agrees with the anomalies shown in Figure 6.13 where, for instance, in the southern Ross Sea, the anomalies are below $5\,\%$ throughout the period. This can be expected since this part of the Ross Sea is not influenced by the ACW and, because of its geography, exhibits very constant weather conditions. This is also valid for the region east of the Antarctic Peninsula where, on average, the largest amount of old ice can be found. In contrast, the central Weddell Sea and large areas of the Amundsen and Ross Seas reveal highly varying anomalies of the annual mean sea ice concentration. These anomalies are most likely caused by the ACW, at least in the latter two areas.

6.2 Arctic

Originally, the SL algorithm has been developed to calculate the sea ice concentration in the Southern Ocean. This section focusses on extending the algorithm in the Northern Hemisphere. In the Arctic, highly resolved data of the integrated cloud liquid water content L are available from the NWP model HIRLAM (see below). They can be used instead of the cloud mask described in Section 3.2.4. The small penetration depth at 85 GHz causing a large influence of the snow cover on sea ice on the SSM/I measurement allows to use the SL algorithm in the Arctic as well – at least over snow-covered areas.

Applying the SL algorithm in the Arctic requires some modifications. At first, one has to calculate a new set of tie points. Secondly, atmospheric quantities such as the integrated water vapor content W, the surface wind speed V and L can be taken from several NWP models. The results shown in Section 6.2.1 are based on investigations of the sea ice cover in the Greenland Sea. Therefore, W, L and V are taken from the Danish NWP model *HIgh Resolution Limited Area Model* (HIRLAM) running operationally at the *Danish Meteorological Institute* (DMI, see [Sass et al., 1999]). In the Greenland Sea, this model provides data with a spatial resolution of $0.15^\circ \times 0.15^\circ$ ($\approx 5 \times 15\,\mathrm{km}^2$ at 75°N), thus similar to that of the SSM/I 85 GHz channels. Moreover, fields of W, V and L are available every hour, keeping the temporal difference between model data and SSM/I data below half an hour. For further details of HIRLAM see Sass et al. [1999].

The spring case study discussed in Section 6.2.1 focusses first on the retrieval of C_{SLA} using HIRLAM data for the weather correction. Then, a comparison between C_{SLA}, C_{NTA} and SAR images taken by the Canadian RADARSAT-1 satellite is given. This satellite, launched in November 1995, allows to acquire the backscatter cross-section σ°_{hh} in the C-band (5.3 GHz) with 50 m spatial resolution in the ScanSAR wide mode with a swathwidth of 460 km [Raney et al., 1991]. These data are operationally used by the Canadian Ice Service and by the DMI to obtain high-resolution operational sea ice maps of the Northern Hemisphere.

6.2.1 Spring Case Study

Figure 6.16 displays the location of the area considered in the Greenland Sea. A total of 12 SSM/I overflights during the period April 10 to 24, 1999, are used to calculate C. All data, SSM/I as well as model data, are interpolated into a $5 \times 5\,\mathrm{km}^2$ grid using *Backus-Gilbert*-Interpolation [Stogryn, 1978], [Poe, 1990]. Sea ice and open water tie points are calculated from SSM/I data of all overflights with the same method used in Antarctica with one exception: the correction of the

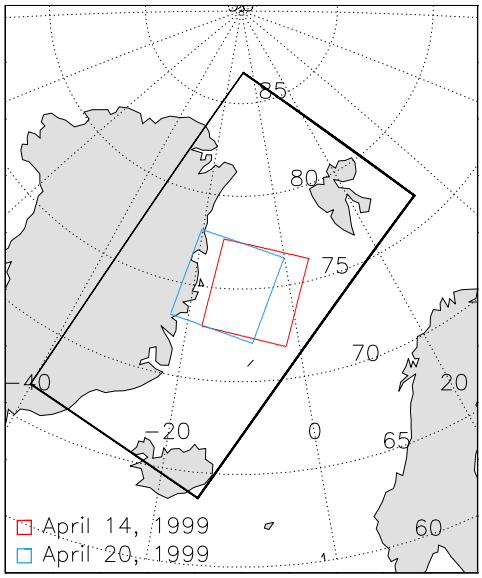

Figure 6.16: *Location of the investigated area in the Greenland Sea. The large rectangle surrounds the region considered to retrieve C. The colored squares denote the location of the RADARSAT-1 SAR frames used for the comparison.*

sea ice tie points for the influence of L is based on HIRLAM data over sea ice. The resulting tie points are listed in Table 6.3.

Table 6.3: *Tie points calculated from SSM/I data of 12 overflights within April 10 to 24, 1999, in the area shown in Figure 6.16.*

$P_i \pm \sigma$	$T_{h,i} \pm \sigma$ [K]	$T_{v,i} \pm \sigma$ [K]
0.028 ± 0.003	212.4 ± 7.8	224.7 ± 8.7
$P_w \pm \sigma$	$T_{h,w} \pm \sigma$ [K]	$T_{v,w} \pm \sigma$ [K]
0.211 ± 0.005	150.6 ± 2.0	231.1 ± 0.9

The HIRLAM data cause problems when correcting the weather influence. Although the temporal difference between the data sets used is small and their spatial resolution is similar, maps of W, V and L derived from SSM/I data over open water with the methods described in Section 3.2 often disagree with the model data. This is evident in (Figures 6.17 and 6.18, images **a)** to **f)**). The best agreement between HIRLAM and SSM/I data can be identified for V. The general distribution of W is similar. However, HIRLAM provides smaller values of W than the SSM/I data, especially in areas where W is small anyway. Adding $2\,\mathrm{kg\,m^{-2}}$ to the modeled W values (Figure 6.17, **a)**) would improve the agreement with image **d)** but this cannot be done for the W data of April 20 shown in Figure 6.18 because the maximum HIRLAM W values in image **a)** are quite similar to the maximum SSM/I W values in image **d)**. Concerning L, the disagreement between HIRLAM and SSM/I data is even more pronounced because L varies on smaller scales. In Figure 6.17, between Iceland and Svalbard, SSM/I L values are always below $100\,\mathrm{g\,m^{-2}}$ (**f)**) while HIRLAM L values exceed $100\,\mathrm{g\,m^{-2}}$ several times (**c)**). This is similar in Figure 6.18. As a result, the weather correction provides too high values for the corrected brightness temperatures in areas where the SSM/I data but not the HIRLAM data show a weather influence. Consequently, in areas where the HIRLAM data do not reflect the actual weather conditions, C will be over- or underestimated – depending on the difference between actual (SSM/I) and modeled (HIRLAM) values of W, L and V.

This can be seen in image **i)** of Figures 6.17 and 6.18. Especially in areas of open water where SSM/I L values exceed those taken from HIRLAM data, the weather influence causes a significant overestimation of C_{SLA}. Over sea ice, if HIRLAM provides too large values of W, L and V, then C_{SLA} is underestimated. The cloud band extending from the East coast of Greenland towards Iceland evi-

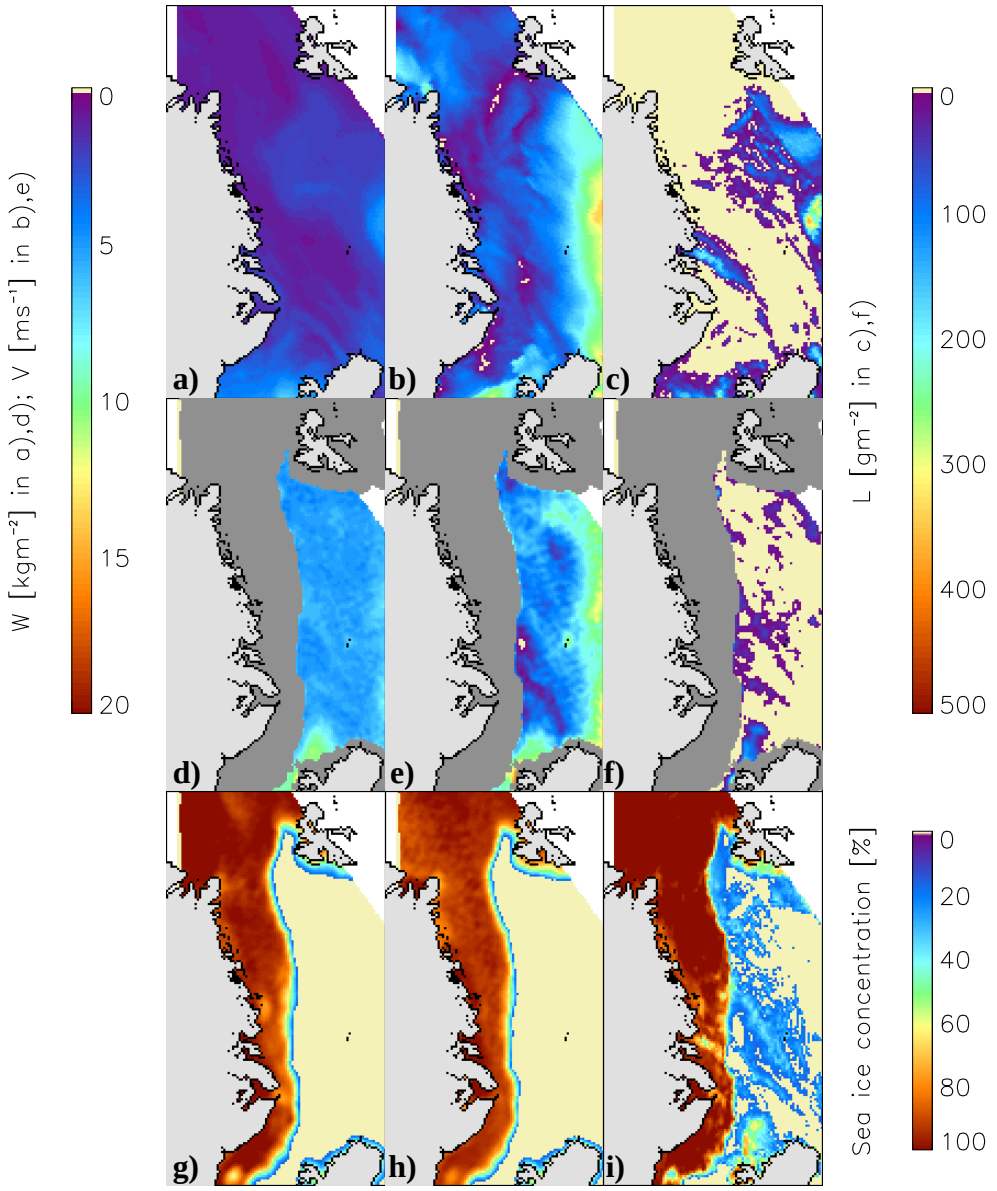

Figure 6.17: *Sea ice retrieval for SSM/I overflight on April 14, 1999, 8 GMT. Images* **a)** *to* **c)**, **d)** *to* **f)**, *and* **g)** *to* **i)** *display (from left to right) W, V and L taken from HIRLAM and SSM/I data, and C_{NTA}, C_{BSA} and C_{SLA}, resepectively. The dark grey area in the middle row is the sea ice extent given by C_{BSA}.*

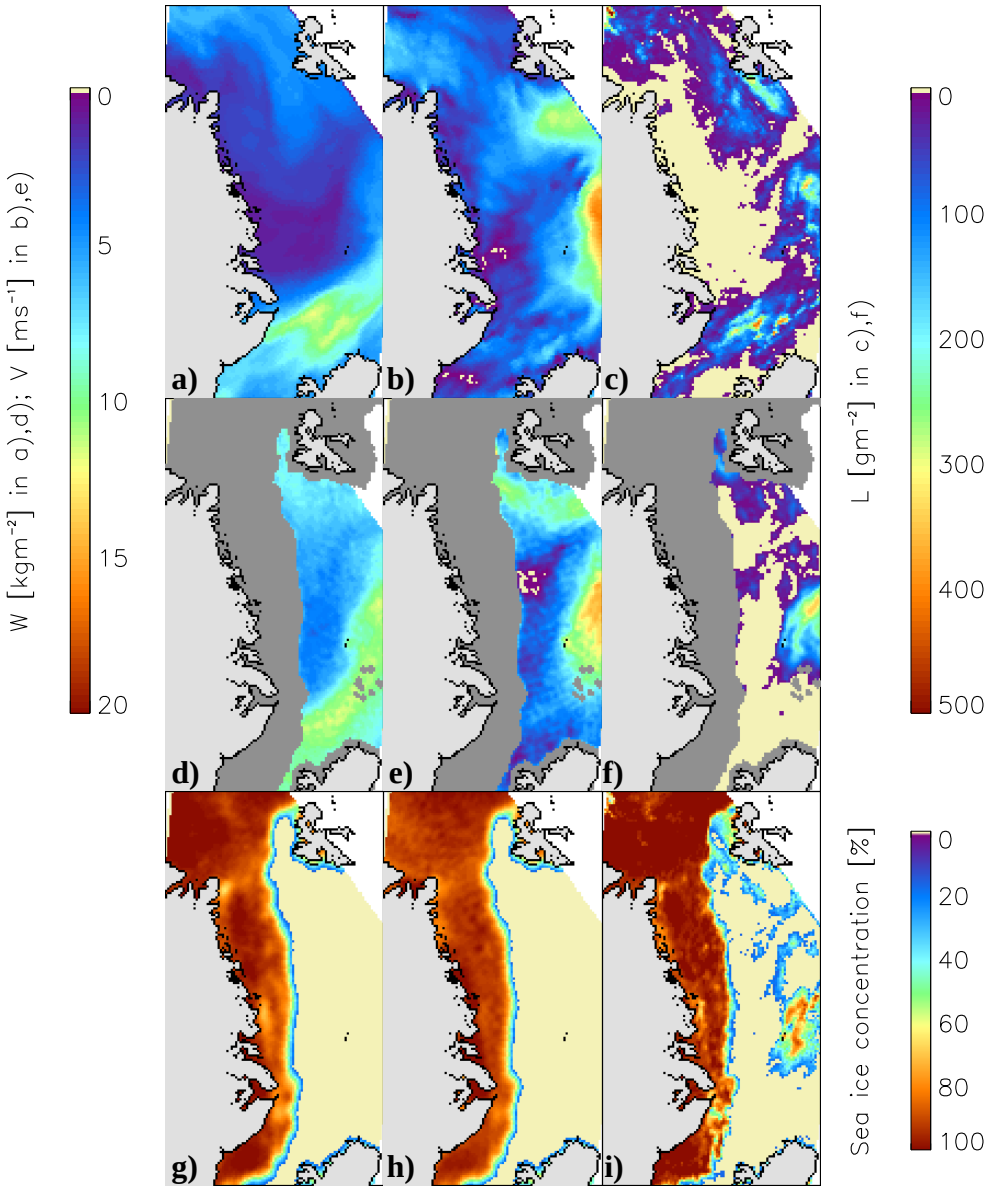

Figure 6.18: *Same as Figure 6.17 for SSM/I overflight on April 20, 1999, 9 GMT.*

dent in the middle of Figure 6.17 **c)** leads to an unrealistic decrease of C_{SLA} in this area as is shown in Figure 6.17 **i)** (compare with images **g)** and **h)**). In comparison, the map showing the SSM/I L data (Figure 6.17 **f)**) shows only poor evidence of

the cloud band mentioned over open water, and it is questionable from this image whether this band continues over sea ice.

In order to perform a more precise weather correction, at least over open water, HIRLAM data are replaced by SSM/I data in all pixels where C_{BSA} is below $15\,\%$. By using this combination of HIRLAM and SSM/I data the overestimation of C_{SLA} is considerably reduced over open water as is illustrated by Figure 6.19 (compare image **i)** of Figures 6.17 and 6.18). Remaining areas with non-zero C_{SLA} values distant from the pack ice can be attributed to the different spatial resolutions of the basic input data which is $12.5 \times 12.5\,\mathrm{km}^2$ for the 85 GHz data and $25 \times 25\,\mathrm{km}^2$ for W, V and L. Also, this spurious ice may be caused by uncertainities in the retrieval of W, V and particularly L from the SSM/I data. Over sea ice, however, this modification cannot decrease the error in C_{SLA}.

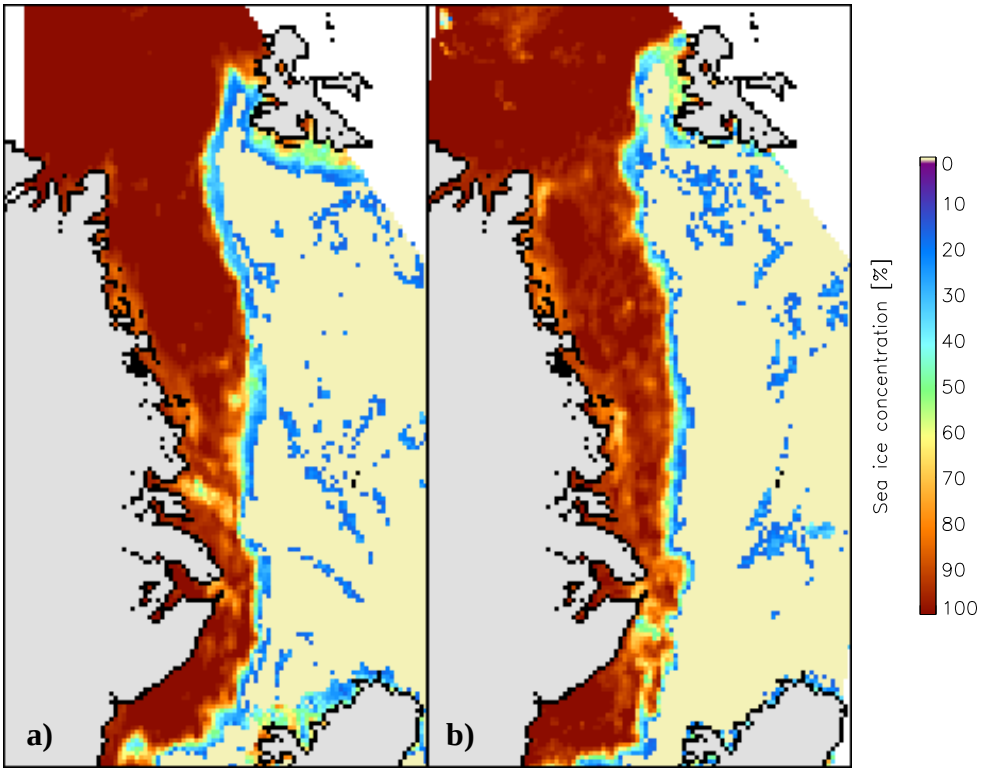

Figure 6.19: *Maps of C_{SLA} obtained for the SSM/I overflights on April 14, 1999, (image* **a)***) and April 20, 1999, (image* **b)***) with a weather correction based on HIRLAM data over sea ice and SSM/I data over open water.*

Figures 6.20 to 6.23 show RADARSAT-1 SAR scenes of April 14 and 20, 1999, respectively, superimposed with isolines of C_{NTA} and C_{SLA}. These scenes (Orbits 17961 and 18047) have been acquired in the descending, ScanSAR wide mode. The original spatial resolution is 50 m. Averaging over 8×8 pixels with this resolution yields the SAR pixels shown in Figures 6.20 to 6.23. In these figures, bright (dark) areas denote a large (small) backscatter coefficient σ°_{hh}. If considering free floating sea ice, *i. e.* no landfast ice, then σ°_{hh} can be expected to increase with sea ice age and/or roughness. Thin ice such as nilas is undeformed and of low porosity. It appears dark, since almost no scattering takes place. Thicker ice such as FY ice and MY ice scatters a significant amount of the microwave radiation – it appears bright. Exceptions are landfast ice appearing dark since it usually grows more undisturbed and remains undeformed, and rough ice such as brash ice and pancake ice appearing bright. Open water exhibits both dark and bright signatures depending on the incidence angle and the sea surface state.

Figures 6.20 and 6.21 show a well developed transition between a compact sea ice edge formed under convergent conditions (top half) and a diffuse sea ice edge with lots of ice streamers formed under divergent conditions (bottom half). These different conditions can be explained by a front, which is supposed to extend from the middle of the bottom edge of these images towards the upper left corner, separating easterly winds on its northern side from northwesterly winds on its southern side. Over open water, these two different wind regimes can hardly be identified on the SAR scenes shown. However, the change in the wind direction is evident by a change in the backscatter pattern across this front in the non-averaged SAR scene (not shown) where south of the front mentioned the backscatter pattern reveals the structure typical for boundary layer rolls aligning parallel to the wind direction. The poorly visible cloud band in image **f)** of Figure 6.17 can also be attributed to this front.

Both C_{SLA} and C_{NTA} depict the compact part of the ice edge quite well. However, the C_{SLA} isolines indicate a much steeper ice concentration gradient in the MIZ in agreement with the SAR scene. While the SAR ice edge corresponds to C_{NTA} values between 50 and 60 %, C_{SLA} takes values between 70 and 80 %. In the diffuse part of the ice edge, the isolines of C_{NTA} as well as those of C_{SLA} extend over a larger area across the MIZ. In the outer parts of the ice edge and in the transition zone between the area covered with ice filaments and the pack ice, the 20 % isoline of C_{SLA} agrees better with the features evident in the SAR scene than C_{NTA}. The 20 % isolines of C_{SLA} evident distant from the ice edge are associated with spurious ice caused by a weather influence.

The sea ice edge shown in Figures 6.22 and 6.23 is also less compact, sug-

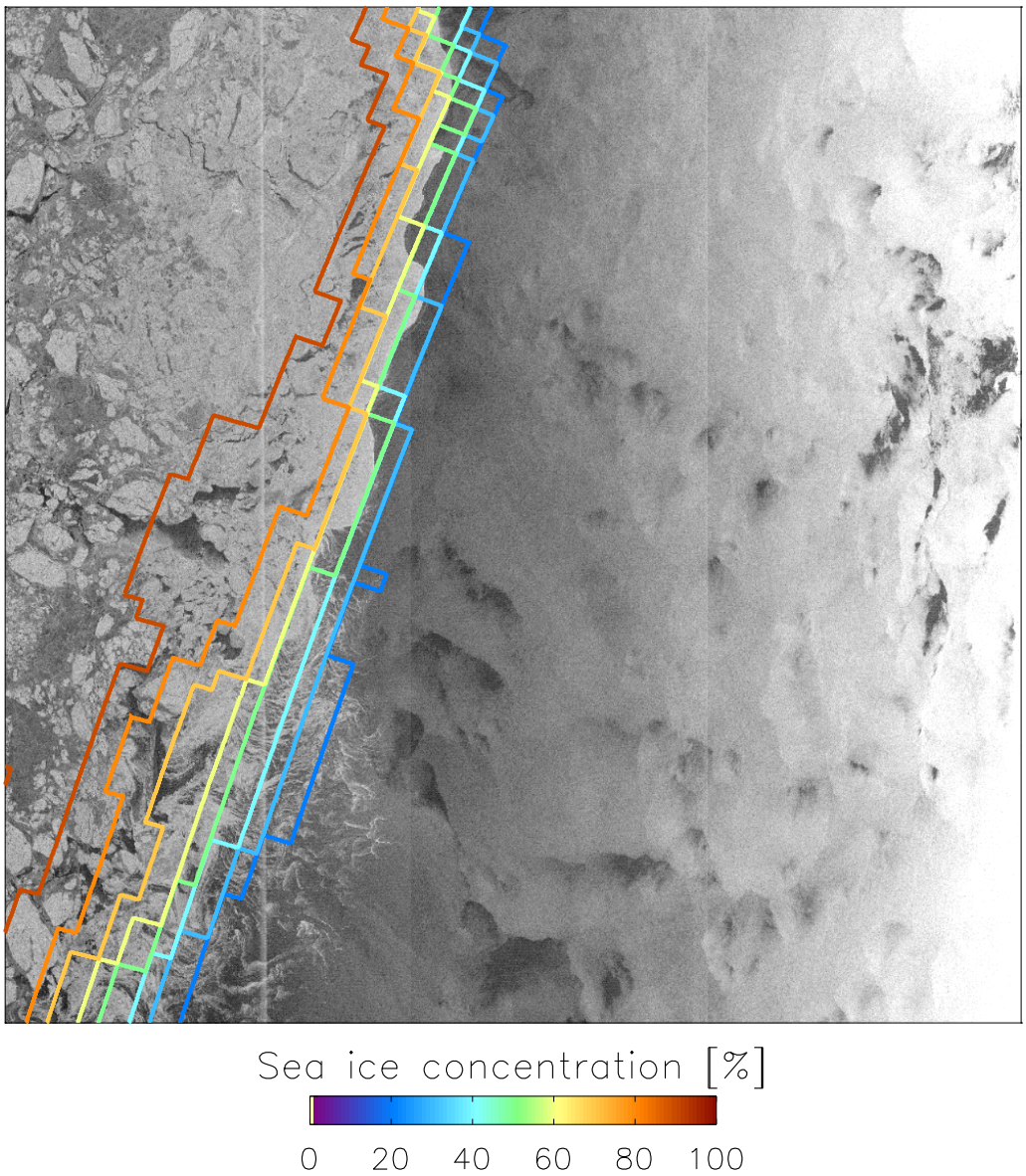

Figure 6.20: *RADARSAT-1 SAR scene from April 14, 1999, 7:26 GMT, superimposed with isolines of C_{NTA} between 20 and 90 %. Isoline spacing is 10 % with colors indicated in the legend.*

gesting a divergent sea ice motion in the MIZ. The 20 % and 30 % isolines of both C_{NTA} and C_{SLA} agree best with the SAR ice edge. The ice concentration gradient

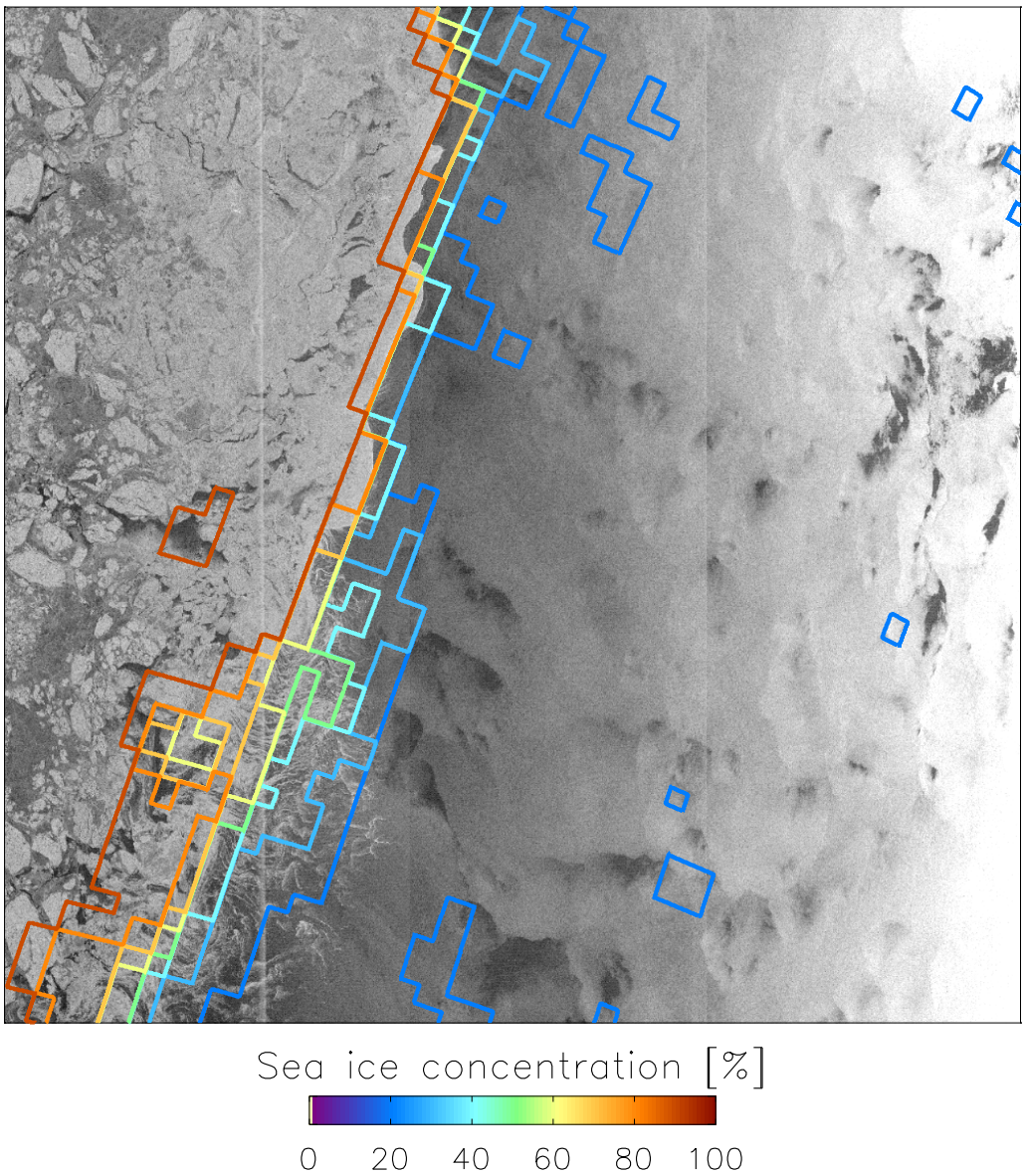

Figure 6.21: *Same as Figure 6.20 with isolines of C_{SLA}.*

given by the separation of the isolines of C_{SLA} is again steeper than the one taken from C_{NTA} isolines. The transition between the outer, diffuse part and the inner, compact part of the SAR ice edge can be identified by an almost uninterrupted band of backscatter values similar to those of the ice filaments. Facing the ice

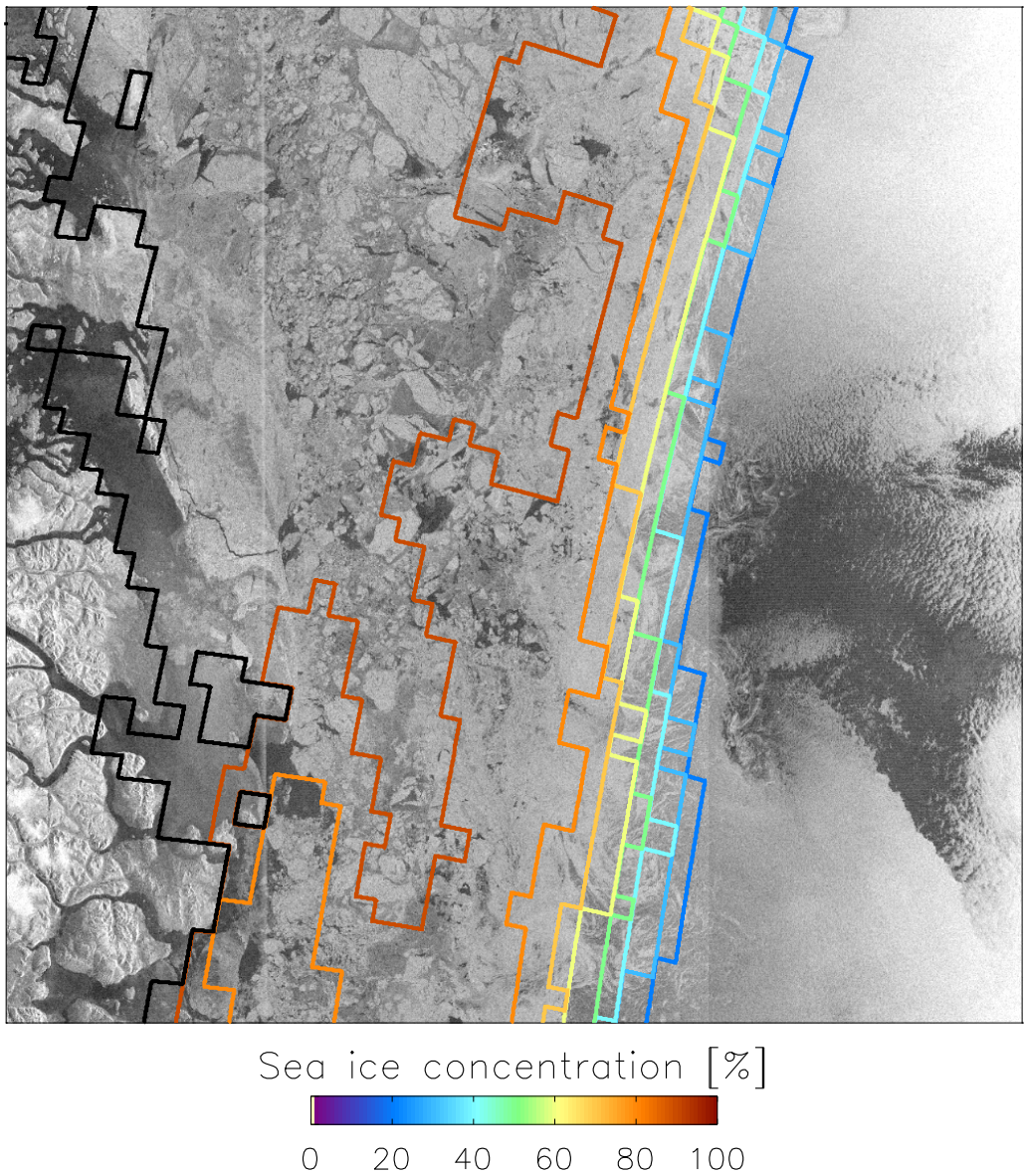

Figure 6.22: *Same as Figure 6.20 using the RADARSAT-1 SAR scene from April 20, 1999, 7:51 GMT. Black lines denote the coastline.*

filaments, this transition corresponds to C_{NTA} values between 60 and 70 % while C_{SLA} takes values between 80 and 90 %.

In the bottom third of Figures 6.22 and 6.23 one can identify two islands. The

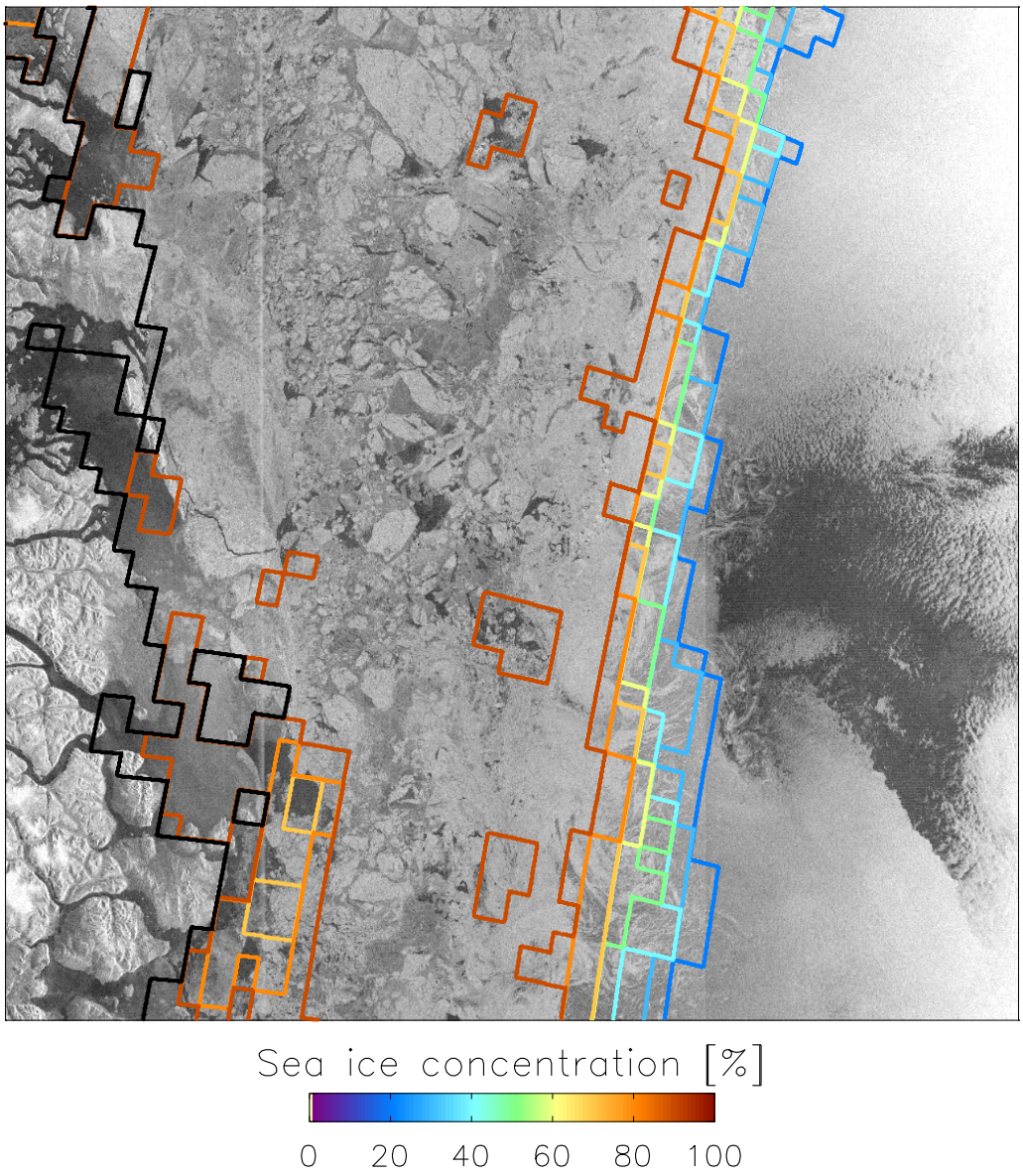

Figure 6.23: *Same as Figure 6.23 with isolines of C_{SEA}.*

area between these islands and the coast is covered by land-fast ice as is indicated by the low backscatter values. The sea ice drifting in the East-Greenland Current (from top to bottom in these images) has to move around the bigger island and piles up north of this island becoming heavily deformed as is shown by larger

backscatter values north of the island compared to further north along the coast. Southeast of this island the SAR images reveal quite low backscatter values which may be attributed to thin ice or land-fast ice. The former ice type seems to be more likely because this region is not sheltered against ocean swell or the sea ice drifting southwards. Therefore, in the case shown in Figures 6.22 and 6.23, some bigger ice floes seem to have prevented the sea ice drift from the north allowing the formation of a polynya during northerly winds on the leeward side of this island. In the shear zone between the thin ice covering the polynya and the sea ice drifting southwards leads and fractures can develop causing a lower sea ice concentration and a mixture of low and high backscatter values. The same happens further south along the coast in the transition zone between land-fast and drifting sea ice. This is evident in Figures 6.22 and 6.23 south of the bigger island mentioned where the shear zone corresponds to C_{NTA} values falling below $80\,\%$ while C_{SLA} takes values below $70\,\%$. In a greater distance to the coast (≈ 30 km) C_{SLA} values quickly exceed $90\,\%$ while C_{NTA} values remain mostly between 80 and $90\,\%$.

More knowledge about the relationship between σ°_{hh} and C is required to judge whether the small areas within the pack ice with C_{SLA} values below $90\,\%$ (see Figure 6.23) are real. It can be expected that over thin ice the SL algorithm provides high ice concentrations at considerably smaller thicknesses than the NT and BS algorithms because the larger penetration depth at 19 and 37 GHz causes a larger contribution of the water underneath the sea ice to the brightness temperatures measured. Therefore, dark areas evident in a SAR scene within the pack ice, *i. e.* thin ice, can less often be attributed to low C_{SLA} values compared to C_{NTA}, and areas of open water or dark nilas can be identified with the SL algorithm with a higher reliability than for instance with the NT algorithm. This is in line with the findings of Lubin et al. [1997].

To sum up the results of this case study, both C_{NTA} and C_{SLA} depict the SAR ice edge quite well. The higher spatial resolution when using the SSM/I 85 GHz channels reveals some advantages, namely a more realistic sea ice concentration gradient across a compact as well as a diffuse sea ice edge, and a better agreement with small-scale features such as ice streamers and local ice concentration minima caused by leads or polynyas. However, the retrieval of C_{SLA} is very sensitive to the quality of the atmospheric parameters used for the weather correction, particularly of L. A difference in the location of about ten kilometers between the modeled L values and those L values which influence the SSM/I measurements can cause absolute errors up to $100\,\%$. These errors can be reduced considerably using atmospheric parameters derived from coincident SSM/I measurements. Therefore,

it is highly desirable to put more effort in the investigation of the R-factor method [Miao et al., 2000], with the goal to obtain L from SSM/I measurements over open water as well as over sea ice.

Chapter 7

Summary and Discussion

The SEA LION (SL) sea ice concentration algorithm allows to calculate the total sea ice concentration C using the 85 GHz SSM/I polarization $P(85)$, which is the 85 GHz brightness temperature polarization difference divided by the sum of the 85 GHz brightness temperatures at horizontal and vertical polarization. With a physical background similar to known sea ice concentration algorithms such as the NASA Team (NT) algorithm [Cavalieri et al., 1991], the NT algorithm with an extended weather correction, called PELICON (PE) algorithm [Heygster et al., 1996], [Thomas, 1998] and the Bootstrap (BS) algorithm [Comiso et al., 1997], the SL algorithm also needs sea ice tie points ($T_{v,i}, T_{h,i}, P_i$) and open water tie points ($T_{v,w}, T_{h,w}, P_w$) – brightness temperatures and polarizations typical for sea ice and open water, respectively. They are discussed in Section 7.1. The large weather influence on SSM/I 85 GHz data requires a correction as is discussed in Section 7.2. Once the tie points are calculated, atmospheric data and correction coefficients needed for the weather correction are processed and the cloud-mask (see Section 3.2.4) is applied, one can start to calculate C. This follows an iteration where, starting with an arbitrarily choosen first-guess C value, the difference (ΔP) between the measured (SSM/I) and eventually weather-corrected $P(85)$ and the modeled $P(85)$ is minimized. A threshold of ΔP of 0.001 ensures a theoretical retrieval accuray of $\approx 1\,\%$ in C. If ΔP obtained from the $P(85)$ values belonging to the current guess of C is too large, the 85 GHz SSM/I measurements are corrected for the weather influence. The resulting weather-corrected $P(85)$ values are used to calculate a new guess of C which, in turn, is used to obtain a new modeled $P(85)$ value. This yields the next combination of modeled and measured, weather-corrected $P(85)$ values which are compared with each other and so on. The iteration is stopped after 30 steps or if ΔP falls below the threshold men-

tioned earlier. Pixels where ΔP is still too large are flagged as bad values. These pixels and those flagged as clouds applying the cloud mask are replaced using a linear temporal interpolation over a maximum of three consecutive days. Sea ice concentrations obtained with the SL algorithm are compared with those obtained with the above-mentioned algorithms and with independent data (see Section 7.3).

7.1 Discussion of Tie Points

The tie points are obtained from NSIDC daily gridded 85 GHz SSM/I brightness temperatures [NSIDC, 1996] of selected areas for each month of the period 1992-1999. The open water tie points are calculated from open water areas of the Southern Ocean which, on a daily basis,

- can be assumed to be almost cloud-free using maps of the integrated cloud liquid water content L,
- exhibit an integrated water vapor content W below $10\,\mathrm{kg\,m^{-2}}$ and a surface wind speed V below $10\,\mathrm{m\,s^{-2}}$,
- have a sea surface temperature close to 273 K.

By this approach the open water tie points have to be corrected only for the influence of W and V within the ranges mentioned above obtained from SSM/I data as described in Section 3.2. Monthly open water tie points remain constant with an average standard deviation of $0.5\,\mathrm{K}$ at vertical and $1.0\,\mathrm{K}$ at horizontal polarization. Consequently, their variability has a negligible influence on the error in C (compare Section 5.5).

The areas to calculate the monthly sea ice tie points from SSM/I data are selected carefully. Requirements for these areas are:

- an almost continuous high-percentage ($\approx 100\,\%$) sea ice cover throughout the month considered,
- a small weather influence within the same month.

These requirements are achieved using maps of monthly averaged $P(85)$ values and of its standard deviation which allow to select an area with low average $P(85)$ values associated with a high average sea ice concentration, and with a low variability of the $P(85)$ values associated with a constant sea ice concentration and

a small weather influence. Using these maps to calculate $T_{v,i}$ and $T_{h,i}$ ensures that the sea ice tie points are almost independent of a change in the sea ice concentration and in the weather influence. The values of $T_{v,i}$ and $T_{h,i}$ obtained for the period considered exhibit a well-defined annual cycle as is illustrated by Figures 5.5 and 5.6, images **a)**). The time-series of $T_{h,i}$ and the one of the surface air temperature estimated from ECMWF data for the areas selected to obtain $T_{v,i}$ and $T_{h,i}$ (see Figure 3.5) show a positive trend. Averages of $T_{h,i}$ and the surface air temperature calculated for the months April to October for 1992-1994 and for 1997-1999 reveal an increase of the surface air temperature from $-15.5°\mathrm{C}$ to $-13.0°\mathrm{C}$ and of $T_{h,i}$ from 213.9 K to 215.2 K. Believing the ECMWF surface air temperatures, the positive trend of $T_{h,i}$ gives some confidence about the sea ice tie points because, assuming that the average surface emissivity has not changed drastically between 1992 and 1999, increasing $T_{h,i}$ values can be expected from increasing surface air temperatures.

In March/April, $T_{v,i}$ and $T_{h,i}$ values averaged over the period 1992-1999 increase by $\approx$ 20 K from Austral summer values (January to March) to Austral winter values (April to August). After August, these averaged sea ice tie points increase further by $\approx$ 10 K, reaching maximum values in November before decreasing rapidly to Austral summer values between November and January. Simultaneously, the average standard deviation of $T_{v,i}$ and $T_{h,i}$ increases in March/April from typical Austral summer values of $\approx$ 9 K to $\approx$ 14 K turning out to be typical for early Austral winter. The average standard deviations gradually decrease throughout the rest of the year reaching their summer values in December.

In order to explain this behaviour, one has to consider the snow metamorphism because snow has a major impact on 85 GHz SSM/I data due to the small penetration depth at this frequency. Starting in January/February, only FY ice and old ice can be found in the Southern Ocean. Moreover, most of the remaining sea ice is covered with old, coarse-grained snow with a snow liquid water content depending on the hour of the day. Freeze-up starts in March/April when a lot of different surface types contribute to the areas selected to estimate $T_{v,i}$ and $T_{h,i}$: young ice, bare or covered by a thin fresh snow layer, FY ice becoming SY ice, covered with fresh snow or old, coarse-grained snow, and old ice, covered with fresh snow or old, coarse-grained snow. This growing number of different surface types between Austral summer and freeze-up causes the increase of the variability of $T_{v,i}$ and $T_{h,i}$. Later in the year, the snow cover becomes more uniform, and the ratio between young ice and FY ice and/or old ice within the areas selected to calculate $T_{v,i}$ and $T_{h,i}$ decreases. Consequently, the spread of the $T_{v,i}$ and $T_{h,i}$ values decreases, particularly in Austral spring when the snow liquid water content starts

to increase.

Moreover, thin ice as well as fresh snow have a larger 85 GHz emissivity than bare old ice or a dry coarse-grained snow cover. Therefore, the marked increase of $T_{v,i}$ and $T_{h,i}$ in March/April might be explained by an increasing areal fraction of a) thin ice and of b) old ice covered with fresh snow. Brightness temperatures increase with the snow liquid water content. Therefore, the increase of $T_{v,i}$ and $T_{h,i}$ values between August and November shown in image **a)** of Figures 5.5 and 5.6 can be attributed to a growing snow liquid water content caused by increasing surface air temperatures. The decreasing sea ice tie point values between November and January are likely associated with an increasing areal fraction of sea ice covered with old, coarse-grained snow and of meteoric ice which is almost freshwater ice and has a considerably larger penetration depth [Ulaby et al., 1986]. It remains unclear at this stage why the large snow liquid water content during Austral summer has no effect on $T_{v,i}$ and $T_{h,i}$. One might assume that the snow consists of icy grains being spaced too widely to hold the water in its pore space.

The annual cycle of the P_i values is less pronounced (see image **b)** of Figures 5.5 and 5.6). However, P_i values averaged over the period 1992-1999 vary between 0.22 (January) and 0.32 (October), increase gradually during Austral spring and decrease rapidly between November and January. The above-mentioned increase of $T_{v,i}$ and $T_{h,i}$ in March/April seems to be shifted in time towards January/March in the P_i values which is difficult to explain. The snow exhibits its largest wetness in January when the surface air temperatures are largest. Correspondingly, in this month the most pronounced depolarization due to the snow wetness can be expected. This is illustrated by the P_i values but not by $T_{v,i}$ and $T_{h,i}$. In February/March, the surface air temperatures have started to decrease causing a smaller snow wetness. This would explain the larger polarization in February compard to January as is shown in Figure 5.5 **b)** and, for most years, also in Figure 5.6 **b)**. However, it turns out that in some years (1994, 1996) the increase of P_i in January/February is caused by a further *decrease* of $T_{v,i}$ and $T_{h,i}$. This cannot be explained by a decreasing snow wetness and may be attributed to polarization-dependend volume scattering [Barber and Nghiem, 1999].

A change of the areas selected to calculate the sea ice tie points, for instance by choosing another P threshold or by choosing areas with surface conditions typical for that particular area in order to obtain regional sea ice tie points, might lead to an improvement in the sea ice concentration retrieval. So far, during Austral summer most brightness temperatures used to obtain $T_{v,i}$ and $T_{h,i}$ are taken from the Weddell Sea although quite a high amount of sea ice remains in the Amundsen and Ross Seas in this season. This is caused by the thresholds choosen for the

monthly averaged $P(85)$ value and its standard deviation, excluding most sea ice pixels of the Amundsen and Ross Seas from the area selected to derive the sea ice tie points.

Certainly, the dependence of microwave radiation at 85 GHz on the snow properties deserves further studies. It would have been quite nice to model the 85 GHz brightness temperatures with a radiative transfer model such as MWMOD (see Section 2.5.1) for the different properties involved, as was done by Fuhrhop et al. [1997]. Unfortunately, the modules specifying the radiative transfer in the sea ice and snow within this model have not yet been validated for frequencies above 40 GHz.

7.2 Discussion of Weather Correction

The error estimation conducted in Section 5.5 reveals quite a small contribution of the variability of the tie points to the standard deviation derived for C_{SLA}. Far larger errors are associated with the weather influence, which is the change in the brightness temperature due to scattering by the ocean surface and due to absorption and attenuation of microwave radiation by the atmospheric water content (integrated contents of the water vapor, W, and of the cloud liquid water, L). The relative contribution of these errors to the standard deviation of C_{SLA} is, on average, larger than $98\,\%$.

The brightness temperature change due to the weather influence has been quantified with the radiative transfer model MWMOD (see Section 2.5.1) over a large range of V, W and L values, and of 85 GHz surface emissivities. In order to avoid a conflict with the questionable results obtained with the sea ice modules of MWMOD for frequencies above 40 GHz (see Section 2.5.1), the sea ice and its snow cover has been simulated using appropriate surface emissivity values as input for MWMOD. This, of course, is one shortcoming of the method proposed since the interaction of microwave radiation at 85 GHz with the sea ice and its snow cover under different atmospheric conditions has not been simulated explicitely in this thesis.

By performing polynomial fits of the modeled 85 GHz brightness temperatures one obtains the coefficients used to correct the 85 GHz SSM/I brightness temperatures for the weather influence. This requires to know the atmospheric parameters V, W and L which are either taken from *Numerical Weather Prediction* (NWP) models of the *European Centre for Medium Range Weather Forecast* (ECMWF) and of the *Danish Meteorological Institute* (DMI), or are calculated

with known algorithms from data of the other SSM/I channels. The often coarser spatial resolution of the atmospheric parameters can cause severe problems, particulary in case of L which, since associated with clouds, exhibits a high temporal and spatial variability. For instance, if using the SSM/I L data set (spatial resolution $= 25 \times 25\,\mathrm{km}^2$) for the weather correction of the 85 GHz SSM/I brightness temperatures (spatial resolution $= 12.5 \times 12.5\,\mathrm{km}^2$), each pixel of the SSM/I L data set covers four 85 GHz pixels. This means that an inhomogenuous distribution of L within one $25 \times 25\,\mathrm{km}^2$ pixel can cause a brightness temperature change in each of these four 85 GHz pixels which may differ from the brightness temperature change associated with the current L value in the $25 \times 25\,\mathrm{km}^2$ pixel. In order to mitigate this error and the lack of reliable, highly resolved L data over the sea ice, the R-factor method ([Miao et al., 2000]) is used to exclude cloud-covered pixels from the sea ice concentration retrieval with the SL algorithm. Although this method successfully masks out about $75\,\%$ of all L values above $50\,\mathrm{g\,m}^2$ over open water as well as over sea ice, the L influence in the remaining $25\,\%$ can lead to a considerable overestimation of C_{SLA}.

It has also turned out that the SSM/I L data set seems to miss areas with low L values as can be concluded from Figure 2.14 in comparison to Figures 3.2 and 3.3. The high average cloud cover revealed by Figure 2.14 is by no means confirmed in the L maps. This is probably only partly caused by the high percentage of ice clouds at high southern latitudes which reveal very small L values. Low-level clouds like Stratus result, on average, in larger L values. Stratus clouds are also very common at these latitudes and, therefore, should be evident in the SSM/I L maps.

For these reasons, the average standard deviation of C_{SLA} of $\approx 20\,\%$ obtained in Section 5.5 over open water cannot be regarded as an upper limit but seems to be quite a common value. Therefore, after C_{SLA} has been calculated spurious ice concentrations are replaced by C_{PEA} values in all open water pixels at a distance greater than 25 km to the PELICON sea ice edge [Heygster et al., 1996].

The inaccuracy in C_{SLA} may become smaller if the L data set used exhibits the same spatial resolution than the 85 GHz data. This is the case for the case study discussed in Section 6.2 where HIRLAM data are used instead of ECMWF data. However, this case study reveals that, despite the much better spatial resolution of the HIRLAM data set, a time lag between HIRLAM and SSM/I data of about half an hour can already cause relative errors in C_{SLA} above $100\,\%$. Moreover, in polar regions, thus in Antarctica as well as in the Arctic, only a few observations are available to validate the modeled data. In conclusion, since the quality of the atmospheric parameters required for the weather correction of the 85 GHz SSM/I

brightness temperatures severely limits the usage of the SL algorithm, it is highly desirable to search for new, more reliable data sets of these parameters.

7.3 Summary of Results

Antarctic sea ice concentrations are calculated with the SL, the PE and the BS algorithms for each day of the period 1992-1999. Visually, sea ice concentrations obtained with the SL algorithm (C_{SLA}) show by far more details than those of the two algorithms, C_{PEA} and C_{BSA}, respectively.

- Coastal polynyas appear as sharp-edged areas of a significantly lower sea ice concentration in daily as well as monthly averaged maps of C_{SLA}.
- Polynyas forced by divergent sea ice motion occur within the pack ice especially in the Amundsen and Ross Seas and can be identified only on daily maps of C_{SLA}.
- The sea ice concentration gradient across the marginal ice zone (MIZ) is much steeper based on daily maps of C_{SLA}.

Moreover, in a time-series showing C_{SLA} in the Pacific Sector one can easily track the huge iceberg B-10A by the polynya forming on its leeward side under favourable surface wind conditions.

Over the period 1992-1999, C_{SLA} takes average values between those of C_{BSA} and C_{PEA} – the latter values being about $8\,\%$ smaller than C_{BSA} values, confirming the difference of $10\,\%$ found by Comiso et al. [1997] in pack ice areas. In detail, C_{SLA} values are about $5\,\%$ *larger* than C_{PEA} values and about $3\,\%$ *smaller* than C_{BSA} values. Therefore, believing the findings of Comiso et al. [1997] average C_{SLA} values are more realistic than those of C_{PEA}. Monthly and yearly sea ice concentration anomalies calculated from all three SSM/I sea ice concentration time-series for the period 1992-1999 yield quite similar results.

The average Antarctic sea ice area obtained from C_{SLA} values for the period 1992-1999 is in best agreement with the Bootstrap (BS) sea ice area, particularly during freeze-up. In contrast, starting in March, the average PELICON (PE) sea ice area becomes increasingly smaller than both the BS and the SEA LION (SL) sea ice area. This difference is most likely caused by a difference in the average sea ice concentration because average Antarctic sea ice extents obtained from the sea ice concentrations of all three algorithms are quite similar or even agree with

each other within one standard deviation between March and September. Particularly during Austral spring and summer, SL sea ice extents are smaller than those of the two other algorithms. This can be explained by the better spatial resolution of the 85 GHz SSM/I data. They allow to detect smaller open water areas within the pack ice and to give a more realistic estimate of coastal polynyas and their open water fraction than the other SSM/I data.

Results of all three sea ice concentration algorithms are compared to about 850 ship observations of the sea ice cover taken every six hours aboard the U.S. research vessel *Nathaniel B. Palmer* in 1994-1998. This comparison shows a poor correlation between the satellite data and the ship observations. The correlation coefficients range between 0.5 and 0.6. Lowest differences between ship observations and the satellite data are found for C_{BSA} (5 %) and C_{SLA} (7 %). SL sea ice concentrations are validated with VIS/IR images of the *Operational Lincescan System* (OLS). Data for 21 days and different areas (MIZ and coastal polynyas) are investigated revealing that the OLS sea ice edge corresponds within 10 km with the 15 % isoline of C_{SLA}. For C_{PEA} values, the OLS sea ice edge is in better agreement with the 60 % isoline. Moreover, the gradient of C_{SLA} values across the MIZ is more realistic than the one inferred from C_{NTA} values. This is illustrated for both a compact and a diffuse sea ice edge in the Greenland Sea for two days in April 1999 by a comparison of C_{SLA} and C_{NTA} maps with RADARSAT-1 SAR scenes.

Chapter 8

Conclusions and Outlook

8.1 Conclusions

A new weather-correcting sea ice concentration algorithm, called SEA LION algorithm, has been develeoped. This algorithm allows to derive the total sea ice concentration from 85 GHz SSM/I data taking full advantage of the better spatial resolution associated with these channels. The SSM/I data used have been corrected for the weather influence using a radiative transfer model and atmospheric parameters taken from models and/or derived from data of the other SSM/I channels. In order to consider the annual cycle of sea ice and snow properties which may change also from year to year, a set of monthly sea ice tie points has been derived and is applied within the SEA LION algorithm. This algorithm is used to calculate a time-series of the daily total sea ice concentration of the Antarctic for the years 1992-1999. Main findings from a comparison of this sea ice concentration time-series with those obtained with known sea ice concentration algorithms (NASA Team and Bootstrap) and independent data sets are outlined below.

- The SEA LION algorithm allows to calculate sea ice concentrations above $90\,\%$ with an accuracy of about $5\,\%$, which is similar to the algorithms mentioned above. However, particularly for sea ice concentrations below $50\,\%$ the average error increases to about $12\,\%$. The error depends strongly on the accuracy of the atmospheric data required for the weather correction and would improve drastically if more accurate atmospheric data could be used.
- The SEA LION algorithm provides, on average, sea ice concentrations that are larger (by $5\,\%$) than the NASA Team sea ice concentration and that are

smaller (by 3 %) than the Bootstrap sea ice concentrations.

- Polynyas in the pack ice as well as along the coast can be identified accurately with the SEA LION algorithm as is shown by comparison with spaceborne visible/infrared imagery. Despite numerous cases of an insufficient weather correction of the SSM/I data used within one month, persistent polynyas remain visible in maps of the monthly averaged sea ice concentration very clearly.

- A comparison with SAR data shows the capability of the SEA LION algorithm to map the sea ice edge under a divergent as well as a convergent sea ice motion. The sea ice concentration gradients across the marginal ice zone (MIZ) are found to be much steeper in sea ice concentration maps obtained with the SEA LION algorithm compared to the NASA Team algorithm. While the transition betwen the MIZ and the pack ice evident in a SAR scene agrees with the 50 % to 60 % isoline of the NASA Team sea ice concentration, the SEA LION algorithm takes values between 80 and 90 %.

- A comparison of Antarctic sea ice areas and extents derived with the three algorithms mentioned demonstrates that, on average, the NASA Team algorithm yields too low sea ice concentrations during Austral winter. The SEA LION and Bootstrap sea ice areas agree quite well and are at least 1×10^6 km^2 larger than the NASA Team sea ice area. Moreover, the SEA LION algorithm allows an earlier detection of the sea ice retreat at the beginning of melt-onset since the SEA LION sea ice extent starts to decrease earlier compared to the other algorithms.

8.2 Outlook

The coming *Advanced Microwave Scanning Radiometer* (AMSR) operates at frequencies close to those of the SSM/I and is additionally equipped with channels at 6 GHz. Its data will allow an improvement of known sea ice concentration products, mainly due to the smaller effective field-of-view (FOV) of $25 \times 25\,\mathrm{km}^2$ at 18.7 GHz (SSM/I: $69 \times 43\,\mathrm{km}^2$ at 19.4 GHz) and of $15 \times 15\,\mathrm{km}^2$ at 36.5 GHz (SSM/I: $37 \times 29\,\mathrm{km}^2$ at 37 GHz). Furthermore, the corresponding new sea ice concentration algorithm will run more economically since a simple weather correction scheme will be sufficient because of the frequencies used. In addition, the AMSR will provide 89 GHz data with a smaller FOV ($5 \times 5\,\mathrm{km}^2$) than the other AMSR channels. These data can be used to determine higher resolved and thus more realistic sea ice concentrations, at least under clear-sky conditions. In this context, the method proposed in this thesis will be very useful since surface properties can be assumed to be quite similar at 85 and 89 GHz.

Many improvements are neccessary to obtain more precise results with the SEA LION algorithm. Concerning the tie points some ideas have already been stated in Section 7.1. A sufficient weather correction, however, turns out to be the main difficulty. Modeled values of the cloud liquid water content L cannot be expected to become considerably more reliable in polar regions since only few observations are available for validation. Data derived from microwave radiances seem to be more promising. The R-factor method of Miao et al. [2000] (see Section 3.2.4) has already been used to calculate L but, so far, this is validated over open water only. It is planned to improve the performance of the R-factor method over sea ice and to extend this method to the AMSR data set as well. Moreover, the SEA LION algorithm may be improved using maps of the modeled surface wind speed covering both open water and sea ice, particularly in the MIZ and areas covered by large polynyas. Here, the open water fraction might be large enough to cause a significant change of SSM/I brightness temperatures due to scattering at the wind-roughend water surface.

So far it is impossible to use the SEA LION algorithm in an operational mode because the tie points are calculated for each month in advance and the R-factor method used to generate a cloud mask requires also one month of data. However, once L data derived from microwave radiances and/or taken from Numerical Weather Prediction models have improved in quality, particulary over ice-covered regions, a modification towards an operationally running SEA LION algorithm might be feasible. In this case, one would be able to correct the SSM/I (or AMSR) data more efficiently for the influence of L, and the usage of the data-consuming

cloud mask could be avoided. It would be possible to calculate sea ice tie points on a daily or even on an orbital basis using the weather-corrected SSM/I (AMSR) data. This would allow a further improvement of the sea ice concentration obtained, particulary since it might be possible to estimate individual sea ice tie points for different regions. This could be a great advantage dealing with Arctic summer conditions when areas covered by melt-ponds and by dry snow may appear within one swath. Whether becoming operational or not – sea ice concentrations inferred from 85 GHz SSM/I data (or 89 GHz AMSR data) with an enhanced SEA LION algorithm would be very helpful to validate sea ice extents derived from active microwave radiometers such as SAR or QuickSCAT, and to monitor polynyas regularly.

Appendix

Lookup-table for $\epsilon_p(V)$

This section provides the lookup-table of sea surface emissivities (ϵ_v and ϵ_h for vertical and horizontal polarization) as a function of the surface wind speed V for $0\,\mathrm{m\,s^{-1}} \leq V \leq 30\,\mathrm{m\,s^{-1}}$ computed with MWMOD at a frequency of 85 GHz for a SST of 272 K and a surface salinity of 34 ‰.

Table 8.1: *Sea surface emissivities for typical surface wind speeds. The emissivities are rounded to the nearest* $0.5\,\%$.

V [m s^{-1}]	ϵ_h	ϵ_v	V [m s^{-1}]	ϵ_h	ϵ_v
0	0.480	0.840	16	0.630	0.850
1	0.485	0.835	17	0.655	0.855
2	0.490	0.830	18	0.680	0.865
3	0.490	0.830	19	0.705	0.875
4	0.495	0.830	20	0.730	0.885
5	0.500	0.825	21	0.755	0.895
6	0.500	0.825	22	0.780	0.905
7	0.505	0.825	23	0.810	0.915
8	0.515	0.825	24	0.835	0.925
9	0.520	0.825	25	0.855	0.935
10	0.530	0.825	26	0.875	0.940
11	0.545	0.825	27	0.890	0.945
12	0.560	0.830	28	0.900	0.945
13	0.575	0.835	29	0.900	0.940
14	0.595	0.840	30	0.895	0.930
15	0.615	0.845			

Lookup-table for ΔT_{O_2}

This section provides the lookup-table of the contribution of the oxygen absorption to the brightness temperature ΔT_{O_2} that would be measured by the SSM/I at 85 GHz under dry, clear-sky conditions independent of the polarization p. The values listed are computed with MWMOD (Section 2.5.1) at a frequency of 85 GHz for emissivities between 0.5 and 0.95 for a typical polar atmosphere and a surface temperature of 0° C. Values of ΔT_{O_2} decrease with a decreasing surface temperature, however, the change in the values listed is below $2\,\%$ for surface temperatures down to $-30°$ C.

Table 8.2: *Contribution of the oxygen absorption to the brightness temperature at 85 GHz.*

ϵ_p	ΔT_{O_2} [K]	ϵ_p	ΔT_{O_2} [K]
0.50	17.8	0.75	8.3
0.55	15.9	0.80	6.4
0.60	14.0	0.85	4.4
0.65	12.0	0.90	2.5
0.70	10.2	0.95	0.6

The Calculation of C

This section describes in more detail how to derive Equation 5.4. One starts with Equation 5.3

$$\begin{aligned} T_v &= (1-C)\epsilon_{v,w}T_{s,w} + C\epsilon_{v,i}T_i. \\ T_h &= (1-C)\epsilon_{h,w}T_{s,w} + C\epsilon_{h,i}T_i. \end{aligned} \tag{8.1}$$

and Equation 4.2

$$P = \frac{T_v - T_h}{T_v + T_h} \tag{8.2}$$

Here, P is the normalized brightness temperature polarization difference NBTPD at 85 GHz, T_v and T_h are the brightness temperatures at 85 GHz for vertical (v)

and horizontal (h) polarization, C is the total sea ice concentration, $\epsilon_{v,w}$, $\epsilon_{h,w}$ and $\epsilon_{v,i}$, $\epsilon_{h,i}$ are the emissivities of open water and the radiating sea ice and/or snow layer at polarization v or h, respectively, and $T_{s,w}$ and T_i are the physical temperatures of the sea surface and the radiating sea ice and/or snow layer. One gets the open water and sea ice tie points by writing

$$T_{p,w} = \epsilon_{p,w} T_{s,w} \quad \text{and} \quad T_{p,i} = \epsilon_{p,i} T_i. \tag{8.3}$$

We define further

$$\begin{aligned} \Sigma T_w &= T_{v,w} + T_{h,w}, \\ \Delta T_w &= T_{v,w} - T_{h,w}, \\ \Sigma T_i &= T_{v,i} + T_{h,i} \quad \text{and} \\ \Delta T_i &= T_{v,i} - T_{h,i}. \end{aligned} \tag{8.4}$$

By substituting Equation 8.1 into Equation 8.2 and using Equations 8.3 and 8.4 one obtains

$$P = \frac{(1-C)\Delta T_w + C\Delta T_i}{(1-C)\Sigma T_w + C\Sigma T_i}. \tag{8.5}$$

Introduction of

$$P_w = \frac{\Delta T_w}{\Sigma T_w} \quad \text{and} \quad P_i = \frac{\Delta T_i}{\Sigma T_i} \tag{8.6}$$

leads to

$$P = \frac{(1-C)P_w + CP_i \frac{\Sigma T_i}{\Sigma T_w}}{1 - C + C\frac{\Sigma T_i}{\Sigma T_w}}. \tag{8.7}$$

Equation 8.7 can be easily solved for C:

$$C = \frac{P - P_w}{P - P_w + \frac{\Sigma T_i}{\Sigma T_w}(P_i - P)} \tag{8.8}$$

and re-arranged to obtain Equation 5.4

$$C = \left(1 + \frac{T_{v,i} + T_{h,i}}{T_{v,w} + T_{h,w}} \frac{P_i - P}{P - P_w}\right)^{-1}.$$

Bibliography

Aagaard, K., and Carmack, E. C., The Arctic Ocean and Climate: A perspective. In Johannessen, O. M., Muench, R. D., and Overland, J. E., editors, *The Polar Oceans and their role in shaping the Global Environment*, AGU Monograph, 85. Am. Geophys. Union, Washington, D.C., 1994.

Ackley, S. F., and Weeks, W. F., *Sea ice properties and processes: Proc. W.F. Weeks Sea Ice Symposium, San Francisco.* CRREL Monograph, 90-1. Cold Regions Resarch and Engineering Laboratory (CRREL), Hanover, New Hampshire, 1990.

Adolphs, U., Ice thickness variability, isostatic balance and potential for snow ice formation on ice floes in the south polar Pacific Ocean. *J. Geophys. Res.*, **103**(C11), 24,675–24,691, 1998.

Agnew, T. A., Le, H., and Shokr, M., Characteristics of large winter leads over the Arctic Basin from 85.5 GHz DMSP SSM/I and NOAA/AVHRR imagery. *Canadian J. Rem. Sens.*, **25**(1), 12–20, 1999.

Akitaya, E., Studies on depth hoar. *Contr. Inst. Low Temp. Science*, **26A**, 1–67, 1974.

Andreas, E. L., Heat and moisture advection over Antarctic sea ice. *Mon. Wea. Rev.*, **113**, 736–746, 1984.

Andreas, E. L., A theory for the scalar roughness and the scalar transfer coefficients over snow and sea ice. *Bound. Lay. Meteorol.*, **38**, 159–184, 1987.

Antarctic Meteorology Research Center (AMRC), Observations aboard the R.V. Nathaniel B. Palmer: 1994-1998. http://www.ssec.wisc.edu, 1999.

Barber, D. G., Fung, A. K., Grenfell, T. C., Nghiem, S. V., Onstott, R. G., Lytle, V. I., Perovich, D. K., and Gow, A. J., The role of snow on microwave emission and scattering over first-year sea ice. *IEEE Trans. Geosci. Rem. Sens.*, **36**(5), 1750–1763, 1998.

Barber, D. G., and Nghiem, S. V., The role of snow on the thermal dependence of backscatter over sea ice. *J. Geophys. Res.*, **104**(C11), 25,789–25,803, 1999.

Barry, R. G., and Chorley, R. J., *Atmosphere, Weather and Climate*. Routledge, London, U.K., 1989.

Bauer, P., and Schlüssel, P., Rainfall, total water, ice water, and water vapor over sea from polarized microwave simulations and Special Sensor Microwave/Imager data. *J. Geophys. Res.*, **98**(D11), 20,737–20,759, 1993.

Bauer, P., and Grody, N. C., The potential of combining SSM/I and SSM/T2 measurements to improve the identification of snowcover and precipitation. *IEEE Trans. Geosci. Rem. Sens.*, **33**, 251–261, 1995.

Bennartz, R., On the use of SSM/I measurements in coastal regions. *J. Atmos. Ocean. Technol.*, **16**, 417–431, 1999.

Bentamy, A., Queffeulou, P., Quilfen, Y., and Katsaros, K., Ocean surface wind fields estimated with satellite active and passive microwave instruments. *IEEE Trans. Geosci. Rem. Sens.*, **37**(5), 2469–2486, 1999.

Bergeron, T., Problems and methods of rainfall investigation. In *The physics of precipitation*, AGU Monograph, 5, pages 5–30. Am. Geophys. Union, Washington, D.C., 1960.

Burns, B., Comparison of SSM/I ice concentration algorithms for the Weddell Sea. *Ann. Glaciol.*, **17**, 344–350, 1993.

Cavalieri, D. J., Gloersen, P., and Campbell, W. J., Determination of sea ice parameters with the NIMBUS-7 SMMR. *J. Geophys. Res.*, **89**, 5355–5369, 1984.

Cavalieri, D. J., Crawford, J. P., Drinkwater, M. R., Eppler, D. T., Farmer, L. D., Jentz, R. R., and Wackerman, C. C., Aircraft active and passive microwave validation of the sea ice concentration from the Defense Meteorological Satellite Program Special Sensor Microwave Imager. *J. Geophys. Res.*, **96**(C12), 21,998–22,008, 1991.

Cavalieri, D. J., St. Germain, K. M., and Swift, C. T., Reduction of weather effects in the calculation of sea-ice concentration with DMSP SSM/I. *J. Glaciology*, **41**(139), 455–464, 1995.

Cavalieri, D. J., Gloersen, P., Parkinson, L., Comiso, J. C., and Zwally, H. J., Observed hemispheric asymmetriy in global sea ice changes. *Science*, **278**, 1997.

Cavalieri, D. J., and St. Germain, K. M., Arctic sea ice research with satellite passive microwave radiometers. *IEEE Geosci. and Rem. Sens. Soc.*, **97**, 1995.

Cavalieri, D. J., A microwave technique for mapping thin sea ice. *J. Geophys. Res.*, **99**(C6), 12,561–12,572, 1994.

Chang, P. S., and Li, L., Ocean surface wind speed and direction retrievals from the SSM/I. *IEEE Trans. Geosci. Rem. Sens.*, **36**(6), 1866–1871, 1998.

Colbeck, S. C., An overview of seasonal snow metamorphism. *Rev. Geophys.*, **20**(1), 45–61, 1982.

Comiso, J. C., Grenfell, T. C., Bell, D. L., Lange, M. A., and Ackley, S. F., Passive microwave in situ observations of winter Weddell Sea ice. *J. Geophys. Res.*, **94**(C8), 10,891–10,905, 1989.

Comiso, J. C., Grenfell, T. C., Lange, M., Lohanick, A. W., Moore, R. K., and Wadhams, P., Microwave remote sensing of the Southern Ocean ice cover. In Carsey, F. D., editor, *Microwave remote sensing of sea ice*, pages 243–259. Am. Geophys. Union, Washington, D.C., 1992.

Comiso, J. C., Cavalieri, D. J., Parkinson, C. L., and Gloersen, P., Passive microwave algorithms for sea ice concentration – A comparison of two techniques. *Rem. Sens. Environ.*, **12**(60), 357–384, 1997.

Comiso, J. C., and Sullivan, C. W., Satellite microwave and in-situ observations of the Weddell Sea ice cover and its marginal ice zone. *J. Geophys. Res.*, **91**(C1), 9663–9681, 1986.

Comiso, J. C., and Zwally, H. J., Antarctic sea ice concentration inferred from NIMBUS-5 ESMR and LANDSAT imagery. *J. Geophys. Res.*, **87**(C8), 5836–5844, 1982.

Comiso, J. C., Characteristics of Arctic winter sea ice from satellite multispectral microwave observations. *J. Geophys. Res.*, **91**(C1), 975–995, 1986.

Comiso, J. C., Surface temperatures in the polar regions from NIMBUS 7 temperature humidity infrared radiometer. *J. Geophys. Res.*, **99**(C3), 5181–5200, 1994.

Cox, C., and Munk, W., Statistics of the sea surface derived from sun glitter. *J. Marine Res.*, **13**, 198–227, 1954.

Curry, J. A., Ardeel, C. D., and Tian, L., Liquid water content and precipitation characteristics of stratiform clouds as inferred from satellite microwave measurements. *J. Geophys. Res.*, **95**(D10), 16,659–16,671, 1990.

Deirmendjian, D., *Electromagnetic scattering on spherical polydispersions*. Elsevier, New York, N. Y., 1969.

Drinkwater, M. R., and Liu, X., Seasonal to interannual variability in Antarctic sea-ice surface melt. *IEEE Trans. Geosci. Rem. Sens.*, **38**(4), 1827–1842, 2000.

Drinkwater, M. R., and Lytle, V. I., ERS-1 radar and field-observed characteristics of autumn freeze-up in the Weddell Sea. *J. Geophys. Res.*, **102**(C6), 12,593–12,608, 1997.

Drinkwater, M. R., Active microwave remote sensing observations of Weddell Sea ice. In Jeffries, M. O., editor, *Antarctic sea ice: Physical processes, interactions and variability*, Antarctic Research Series, 74, pp. 187–212. Am. Geophys. Union, Washington, D.C., 1998.

Eicken, H., Lange, M. A., and Ackley, S. F., Quantification of sea-ice textures through automated digital image analysis. In Ackley, S. F., and Weeks, W. F., editors, *Sea*

ice properties and processes: Proc. W. F. Weeks Sea Ice Symposium, San Francisco, CRREL Monograph, 90-1, pp. 28–32. Cold Regions Resarch and Engineering Laboratory (CRREL), Hanover, New Hampshire, 1990.

Eicken, H., Lange, M. A., Hubberten, H.-W., and Wadhams, P., Characteristics and distribution patterns of snow and meteoric ice in the Weddell Sea and their contribution to the mass balance of sea ice. *Ann. Geophysicae,* **12**, 80–83, 1994.

Eicken, H., Fischer, H., and Lemke, P., Effects of snow cover on Antarctic sea ice and potential modulation of its response to climate change. *Ann. Glaciol.*, **21**, 369–376, 1995.

Eicken, H., Deriving modes and rates of ice growth in the Weddell Sea from microstructural, salinity and stable-isotope data. In Jeffries, M. O., editor, *Antarctic sea ice: Physical processes, interactions and variability,* Antarctic Research Series, 74, pp. 89–122. Am. Geophys. Union, Washington, D.C., 1998.

Emery, W. J., Fowler, C. W., and Maslanik, J., Satellite-derived maps of Arctic and Antarctic sea ice motion: 1988 to 1994. *Geophys. Res. Lett.*, **24**(8), 897–900, 1997.

Eppler, D., Farmer, L. D., Lohanick, A. W., Anderson, M. R., Cavalieri, D. J., Comiso, J., Gloersen, P., Garrity, C., Grenfell, T. C., Hallikainen, M., Maslanik, J. A., Mätzler, C., Melloh, R. A., Rubinstein, I., and Swift, C. T., Passive Microwave Signatures of Sea Ice. In Carsey, F. D., editor, *Microwave remote sensing of sea ice,* AGU Monograph, 68, pp. 47–71. Am. Geophys. Union, Washington, D.C., 1992.

Fleagle, R., and Businger, J., *An introduction to atmospheric physics.* Academic Press, New York, 1963.

Fuhrhop, R., Heygster, G., Johnsen, K.-P., P. Schlüssel,, Schrader, M., and Simmer, C., Study of passive remote sensing of the atmosphere and surface ice. *ESA-Report,* **Contract No.11198/94/NL/CN**, 1997.

Fuhrhop, R., Grenfell, T. C., Heygster, G., Johnsen, K.-P., Schlüssel, P., Schrader, M., and Simmer, C., A combined radiative transfer model for sea ice, open ocean, and atmosphere. *Radio Sci.*, **33**(2), 303–316, 1998.

Fuhrhop, R., and Simmer, C., SSM/I brightness temperature corrections for incidence angle variations. *J. Atmos. Ocean. Technol.*, **13**(1), 1997.

Fuhrhop, R., and Simmer, C., *MWMOD User Manual, Version 1.12*. Institut für Meereskunde, Kiel, Germany, 1998.

Garrity, C., Characterization of snow on floating ice and case studies of brightness temperature change during the onset of melt. In Carsey, F. D., editor, *Microwave remote sensing of sea ice,* AGU Monograph, 68, pp. 313–328. Am. Geophys. Union, Washington, D.C., 1992.

Gasiewski, A. J., Microwave radiative transfer in hydrometeors. In Janssen, M. A., editor, *Atmospheric remote sensing by microwave radiometry*, John Wiley & sons, inc, New York, 1993.

Künzi, K. F., Patil, S., and Rott, H., Snow-cover parameters retrieved from NIMBUS-7 Scanning Multichannel Microwave Radiometer (SMMR) data. *IEEE Trans. Geosci. Rem. Sens.*, **GE-20**(4), 452–467, 1982.

Schlüter, N., *Satellitenfernerkundung von Wolken mit Infrarot- und passiven Mikrowellensensoren in der Antarktis.* PhD thesis, University of Bremen, Fachbereich 1 (Physik und Elektrotechnik) and Reports from the Institute of Environmental Physics **1**, University of Bremen, 2000.

Gloersen, P., Wilheit, T. T., and Campbell, W. J., Polar sea ice observations by means of microwave radiometry, in: Advanced Study of Snow and Ice, pp. 541–550. *Nat. Acad. Sci.*, 1974.

Gloersen, P., Cavalieri, D. J., Chang, A. T. C., Wilheit, T. T., Campbell, W. J., Johannessen, O. M., Katsaros, K. B., Künzi, K. F., Ross, D. B., Staelin, D., Windsor, E. P. L., Barath, F. T., Gudmandsen, P., Langham, E., and Ramseier, R. O., A summary of results from the first NIMBUS-7 SMMR observations. *J. Geophys. Res.*, **84**(D4), 5335–5344, 1984.

Gloersen, P., Campbell, W. J., Cavalieri, D. J., Comiso, J. C., Parkinson, C. L., and Zwally, H. J., *Arctic and Antarctic sea ice, 1978–1987. Satellite passive–microwave observations and analysis.* Scientific and technical information program. National Aeronautics and Space Administration (NASA), Washington, D.C., 1992.

Gloersen, P., and Barath, F. T., A scanning multichannel microwave radiometer for NIMBUS-G and SeaSat-A. *IEEE J. Ocean. Eng.*, **OE-2**, 172–178, 1977.

Gloersen, P., and Cavalieri, D. J., Reduction of weather effects in the calculation of sea ice concentration from microwave radiances. *J. Geophys. Res.*, **91**(C3), 3913–3919, 1986.

Gohin, F., Some active and passive microwave signatures of Antarctic sea ice from mid-winter to spring 1991. *Int. J. Rem. Sens.*, **16**(11), 2031–2054, 1995.

Goodberlet, M. A., Swift, C. T., and Wilkersen, J. C., Remote sensing of ocean surface winds with the Special Sensor Microwave Imager. *J. Geophys. Res.*, **94**(C10), 14,547–14,555, 1989.

Greenwald, T. J., Stephens, G. L., Vonder Haar, T. H., and Jackson, D. L., A physical retrieval of cloud liquid water over the global oceans using Special Sensor Microwave/Imager (SSM/I) observations. *J. Geophys. Res.*, **98**(D10), 18,471–18,488, 1993.

Greenwald, T. J., Combs, C., Jones, A., Randel, D., and Vonder Haar, T., Further development in estimating cloud liquid water over land using microwave and infrared satellite measurements. *J. Appl. Meteorol.*, **36**, 389–405, 1997.

Grenfell, T. C., Comiso, J. C., Lange, M. A., Eicken, H., and Wensnahan, M. R., Passive microwave observations of the Weddell Sea during austral winter and spring. *J. Geophys. Res.*, **99**(C5), 9995–10,010, 1994.

Grenfell, T. C., Barber, D. G., Fung, A. K., Gow, A. J., Jezek, K. C., Knapp, E. J., Nghiem, S. V., Onstott, R. G., Perovich, D. K., Roesler, C. S., Swift, C. T., and Tanis, F., Evolution of electromagnatic signatures of sea ice from initial formation to the establishment of thick first-year ice. *IEEE Trans. Geosci. Rem. Sens.*, **36**(5), 1642–1654, 1998.

Grenfell, T. C., and Comiso, J. C., Multifrequency passive microwave observations of sea ice in the Bering and Greenland Seas. *IEEE Trans. Geosci. Rem. Sens.*, **GE-24**(6), 826–831, 1986.

Grenfell, T. C., Surface-based passive microwave studies of multiyear sea ice. *J. Geophys. Res.*, **97**(C3), 3485–3502, 1992.

Guissard, A., and Sobieski, P., An approximate model for the microwave brightness temperature of the sea. *Int. J. Rem. Sens.*, **8**(1), 1607–1627, 1987.

Haas, C., The seasonal cycle of ERS scatterometer signatures over perennial Antarctic sea ice and associated surface ice properties and processes. *Ann. Glaciol*, **33**, 2001.

Hallikainen, M., Ulaby, F. T., and Abdelrazik, M., Dielectric properties of snow in the 3 to 37 GHz range. *IEEE Trans. Ann. Propagat.*, **AP-34**, 1329–1340, 1986.

Hallikainen, M., Ulaby, F. T., and Van Deventer, T. E., Extinction behaviour of dry snow in the 18 and 90 GHz range. *IEEE Trans. Geosci. Rem. Sens.*, **GE-25**(6), 737–745, 1987.

Hallikainen, M., and Winebrenner, D. P., The physical basis of sea ice remote sensing. In Carsey, F. D., editor, *Microwave remote sensing of sea ice*, AGU Monograph, 68, pp. 29–46. Am. Geophys. Union, Washington, D.C., 1992.

Harder, M., Lemke, P., and Hilmer, M., Simulation of sea ice transport through Fram Strait: Natural variability and sensitivity to forcing. *J. Geophys. Res.*, **103**(C3), 5595–5606, 1998.

Heygster, G., Toudal, L., Turner, J., Thomas, C., Hunewinkel, T., Schottmüller, H., and Viehoff, T., PELICON: Project for estimation of long-term variability of ice concentration. Tech. Report Contract EV5V–CT93–0268(DG 12 DTEE), European Community (EC), 1996.

Hollinger, J. P., Lo, R., and Poe, G., *Special Sensor Microwave/Imager User's Guide*. Naval Research Laboratory, Washington, D.C., 1987.

Holton, J. R., *An introduction to dynamic meteorology*. International Geophysics Series, 48. Academic Press, San Diego, Ca., 1992.

Hunewinkel, T., Markus, T., and Heygster, G., Improved determination of the sea ice edge with SSM/I data for small-scale analyses. *IEEE Trans. Geosci. Rem. Sens.*, **36**, 1795–1808, 1998.

Jeffries, M. O., Shaw, R. A., Morris, K., Veazey, A. L., and Krouse, H. R., Crystal structure, stable isotopes (δ^{18}O) and development of sea ice in the Ross, Amundsen and Bellingshausen Seas, Antarctica. *J. Geophys. Res.*, **99**(C1), 985–995, 1994.

Jeffries, M. O., and Weeks, W. F., Structural characteristics and development of sea ice in the western Ross Sea. *Antarctic Science*, **5**(1), 63–75, 1992.

Jeffries, M. O., *Antarctic Sea Ice: Physical processes, interactions and variability.* Antarctic Research Series, 74. Am. Geophys. Union, Washington, D.C., 1998.

Johannessen, O. M., Muench, R. D., and Overland, J. E., editors, *The Polar Oceans and their Role in Shaping the Global Environment.* AGU Monograph, 85. Am. Geophys. Union, Washington, D.C., 1994.

Johannessen, O. M., and Miles, M. W., Two decades of microwave satellite observations of Arctic sea ice variability and trends. In *Proc. IGARSS '99, Hamburg, Germany*, pages 311–313. IEEE Catalog No.99CH36293, 1999.

Jones, A. S., and Vonder Haar, T. H., Passive microwave remote sensing of cloud liquid water over land regions. *J. Geophys. Res.*, **95**(D10), 16,673–16,683, 1990.

Karstens, U., Simmer, C., and Ruprecht, E., Remote sensing of cloud liquid water. *Meteorol. and Atmos. Phys.*, **54**, 157–171, 1994.

Key, J., and Haefliger, M., Arctic ice surface temperature retrieval from AVHRR thermal channels. *J. Geophys. Res.*, **97**(D5), 5885–5893, 1992.

King, C. J., and Turner, J., *Antarctic Meteorology and Climatology*. Atmospheric and Space Science Series. Cambridge University Press, Cambridge, U.K., 1997.

Kwok, R., Schweiger, A., Rothrock, D. A., Pang, S., and Kottmeier, C., Sea ice motion from satellite passive microwave imagery assessed with ERS SAR and buoy motions. *J. Geophys. Res.*, **103**(C4), 8191–8214, 1998.

Lachlan-Cope, T. A., and Turner, J., Passive microwave retrievals of precipitation over the Southern Ocean. *Int. J. Rem. Sens.*, **18**(8), 1725–1742, 1997.

Lange, M. A., Ackley, S. F., Wadhams, P., Dieckmann, G. S., and Eicken, H., Development of sea ice in the Weddell Sea. *Ann. Glaciol.*, **12**, 92–96, 1989.

Lange, M. A., and Eicken, H., Textural characteristics of sea ice and major mechanisms of ice growth in the Weddell Sea. *Ann. Glaciol.*, **15**, 210–215, 1991.

Launiainen, J., and Vihma, T., On the surface heat fluxes in the Weddell Sea. In Johannessen, O. M., Muench, R. D., and Overland, J. E., editors, *The Polar Oceans and*

their role in shaping the Global Environment, AGU Monograph, 85, pp. 399–419. Am. Geophys. Union, Washington, D.C., 1994.

Lemke, P., HiblerIII, W. D., Flato, G. M., Harder, M., and Kreyscher, M., On the improvement of sea ice models for climate simulations: The Sea Ice Model Intercomparison Project (SIMIP). *Ann. Glaciol.*, **25**, 183–187, 1997.

Lemke, P., Heygster, G., Toudal, L., and Turner, J., The SEA LION project: SEa ice in the Antarctic LInked with OceaN-atmosphere forcing. In *Proc. EGS2000, Nice, France, April 2000*, 2000.

Liebe, H. J., Hufford, G. A., and Cotton, M. G., Propagation modeling of moist air and suspended water/ice particles at frequencies below 1000 GHz. In *Proc. AGARD 52nd Specialist meeting of the electromagnetic wave propagation panel*, pages 3.1–3.10. Advis. Group for Aerosp. Res. and Dev., Bruessel, Belgium, 1993.

Liu, A. K., and Cavalieri, D. J., On sea ice drift from the wavelet analysis of the Defense Meteorological Satellite Program (DMSP) Special Sensor Microwave Imager (SSM/I) data. *Int. J. Rem. Sens.*, **19**(7), 1415–1423, 1998.

Lo, R. C., A comprehensive description of the emission microwave imager SSMI environmental parameter extraction algorithm. NRL Memo. Rep., 5199, 1983.

Lomax, A. S., Lubin, D., and Whritner, R. H., The potential of interpreting total and multiyear-ice concentration in SSM/I 85.5 GHz imagery. *Rem. Sens. Environ.*, **54**, 13–26, 1995.

Long, D. G., Hardin, P. J., and Whiting, P. T., Resolution enhancement of spaceborne scatterometer data. *IEEE Trans. Geosci. Rem. Sens.*, **31**(3), 700–715, 1993.

Lubin, D., Garrity, C., Ramseier, R., and Whritner, R. H., Total sea ice concentration retrieval from the SSM/I 85.5 GHz channels during the Arctic summer. *Rem. Sens. Environ.*, **62**, 63–76, 1997.

Marbouty, D., An experimental study of temperature gradient metamorphism. *J. Glaciol.*, **26**(94), 303–312, 1980.

Markus, T., Kottmeier, C., and Fahrbach, E., Ice formation in coastal polynyas in the Weddell Sea and their impact on oceanic salinity. In Jeffries, M. O., editor, *Antarctic Sea Ice: Physical processes, interactions and variability*, Antarctic Research Series, 74, pp. 273–292. Am. Geophys. Union, Washington, D.C., 1998.

Markus, T., and Burns, B. A., A method to estimate subpixel-scale coastal polynyas with satellite microwave data. *J. Geophys. Res.*, **100**(C3), 16,707–16,718, 1995.

Markus, T., and Cavalieri, D. J., Snow depth distribution over sea ice in the Southern Ocean from satellite passive microwave data. In Jeffries, M. O., editor, *Antarctic Sea Ice: Physical processes, interactions and variability*, Antarctic Research Series, 74, pp. 19–39. Am. Geophys. Union, Washington, D.C., 1998.

Markus, T., and Cavalieri, D. J., An enhancement of the NASA Team sea ice algorithm. *IEEE Trans. Geosci. Rem. Sens.*, **38**(3), 1387–1398, 2000.

Martin, T., and Augstein, E., Large-scale drift of Arctic sea ice retrieved from passive microwave satellite data. *J. Geophys. Res.*, **105**(C4), 8775–8788, 2000.

Maslanik, J. A., Effects of weather on the retrieval of sea ice concentration and ice type from passive microwave data. *Int. J. Rem. Sens.*, **13**(1), 37–54, 1992.

Mason, B. J., *The physics of cloud.* Oxford University Press, London, U.K., 1972.

Massom, R., Drinkwater, M. R., and Haas, C., Winter snow cover on sea ice in the Weddell Sea. *J. Geophys. Res.*, **102**(C1), 1101–1117, 1997.

Massom, R., Lytle, V. I., Worby, A. P., and Allison, I., Winter snow cover variability on East Antarctic sea ice. *J. Geophys. Res.*, **103**(C11), 24,837–24,855, 1998.

Maykut, G. A., Energy exchange over young sea ice in the central Arctic. *J. Geophys. Res.*, **83**(C7), 3646–3658, 1978.

McPhee, M. G., and Martinson, D. G., Turbulent mixing under drifting pack ice. *Science*, **263**, 218–221, 1994.

Mellor, G. L., and Häkkinen, S., A review of coupled ice-ocean models. In Johannessen, O. M., Muench, R. D., and Overland, J. E., editors, *The Polar Oceans and their role in shaping the Global Environment*, AGU Monograph, 85, pp. 21–31. Am. Geophys. Union, Washington, D.C., 1994.

Miao, J., Johnsen, K.-P., Kern, S., Heygster, G., and Künzi, K., Signature of clouds over Antarctic sea ice detected by the Special Sensor Microwave/Imager. *IEEE Trans. Geosci. Rem. Sens.*, **38**(5), 2333–2345, 2000.

Miao, J., Künzi, K. F., Heygster, G., Lachlan-Cope, T. A., and Turner, J., Atmospheric water vapor over Antarctica derived from SSM/T2 data. *J. Geophys. Res.*, **??**(D?), accepted, 2001.

Miao, J., *Retrieval of atmospheric water vapor content in polar regions using spaceborne microwave radiometry.* PhD thesis, Reports on Polar Research, **289**, Alfred-Wegener-Institut für Polar- und Meeresforschung (AWI), 1998.

Neumann, G., and Pierson, Jr., W. J., *Principles of physical oceanography.* Prentice-Hall, Englewood Cliffs, New Jersey, 1966.

Nordberg, W., Conaway, J., Ross, D. B., and Wilheit, T. T., Measurement of microwave emission from a foam-covered wind driven sea. *J. Atmos. Sci.*, **28**, 429–435, 1971.

NSIDC, DMSP SSM/I Brightness Temperature Grids for the Polar Regions on CD-ROM: User's Guide. Technical report, National Snow and Ice Data Center, Boulder, Colorado, 1990.

NSIDC, DMSP SSM/I Brightness Temperature and Sea Ice Concentration Grids for the Polar Regions: User's Guide – Revised Edition. Technical report, NSIDC Distributed Active Archive Center, University of Colorado, Boulder, Colorado, 1996.

Oelke, C., Atmospheric signatures in sea-ice concentration estimates from passive microwaves: modelled and observed. *Int. J. Rem. Sens.*, **18**, 1113–1136, 1997.

Oke, T. R., *Boundary layer climates.* Methuen & Co Ltd., London, U.K., 1981.

Olbers, D., Gouretski, V., Seiss, G., and Schröter, J., *Hydrographic Atlas of the Southern Ocean.* Alfred Wegener Institute, Bremerhaven, Germany, 1992.

Onstott, R. G., Grenfell, T. C., Mätzler, C., Luther, C. A., and Svendsen, E. A., Evolution of microwave sea ice signatures during early summer and midsummer in the marginal ice zone. *J. Geophys. Res.*, **92**(C7), 6825–6835, 1987.

Onstott, R. G., SAR and scatterometer signatures of Sea Ice. In Carsey, F. D., editor, *Microwave remote sensing of sea ice*, AGU Monograph 68, pp. 73–104. Am. Geophys. Union, Washington, D.C., 1992.

Paltridge, G. W., and Platt, C. M. R., *Radiative processes in meteorology and climatology*, volume 5 of *Developments in Atmospheric Science.* Elsevier, Amsterdam, Netherland, 1984.

Parkinson, C. L., Interannual variability of monthly Southern Ocean sea ice distributions. *J. Geophys. Res.*, **97**(C4), 5349–5363, 1992.

Peake, W. H., Interaction of electromagnetic waves with some natural surfaces. *IEEE Trans. on Antennas and Propagation*, **AP–7**, 324–329, 1959.

Perovich, D. K., Longacre, J., Barber, D. G., Maffione, R. A., Cota, G. F., Mobley, C. D., Gow, A. J., Onstott, R. G., Grenfell, T. C., Pegau, W. S., Landry, M., and Roesler, C. S., Field observations of the electromagnetic properties of first-year sea ice. *IEEE Trans. Geosci. Rem. Sens.*, **36**(5), 1705–1715, 1998.

Persson, A., User Guide to ECMWF forecast products, Version 3.1. Meteorological Bulletin M3.2, European Centre for Medium-Range Weather Forecast (ECMWF), Reading, U.K., 2000.

Poe, G. A., Optimum interpolation of imaging microwave radiometer data. *IEEE Trans. Geosci. Rem. Sens.*, **GRS-28**, 800–810, 1990.

Ramseier, R. O., Garrity, C., Bauernfeind, E., and Peinert, R., Sea-ice impact on long-term particle flux in the Greenland Sea's Is Odden-Nordbukta region: 1985-1996. *J. Geophys. Res.*, **104**(C3), 5329–5343, 1999.

Raney, R. K., Luscombe, A. P., Langham, E. J., and Ahmed, S., RADARSAT. *IEEE Proc.*, **79**(6), 839–849, 1991.

Raschke, E., *Radiation and water in the climate system – remote measurements*. NATO ASI Series, Series I: Global Environmental Change, 45. Springer Verlag, Berlin, Germany, 1996.

Ross, D. B., Cardone, V. J., and Conaway Jr., J. W., Laser and microwave observations of sea-surface conditions for fetch-limited 17- to 25-m s^{-1} winds. *IEEE Trans. Geosci. Electron.*, **GE-8**, 326–336, 1970.

Ross, D. B., and Cardone, V. J., Observations of oceanic whitecaps and their relation to remote measurements of surface wind speed. *J. Geophys. Res.*, **79**(3), 444–452, 1974.

Rossow, W. B., Remote sensing of atmospheric water vapor. In Raschke, E., editor, *Radiation and water in the climate system – remote measurements*, NATO ASI Series, Series I: Global Environmental Change, 45, pp. 175–192. Springer Verlag, Berlin, Germany, 1996.

Sass, B. H., Nielsen, N. W., Jørgensen, J. U., and Amstrup, B., The operational DMI-HIRLAM system: 2nd rev. ed. Tech. Rep. 99-21, Danish Meteorological Institute (DMI), Copenhagen, Danmark, 1999.

Schanda, E., *Physical fundamentals of remote sensing*. Springer Verlag, Berlin, 1986.

Schiffer, R. A., and Rossow, W. B., The International Satellite Cloud Climatology Project (ISCCP). *Bull. Am. Meteorol. Soc.*, **86**, 779–784, 1983.

Simmer, C., *Satellitenfernerkundung hydrologischer Parameter der Atmosphäre mit Mikrowellen*. Verlag Dr. Kovac., 1994.

Simmer, C., Retrieval of precipitation from satellites. In Raschke, E., editor, *Radiation and water in the climate system – remote measurements*, NATO ASI Series, Series I: Global Environmental Change, 45, pp. 249–276. Springer Verlag, Berlin, Germany, 1996.

Sinclair, M. R., An objective cyclone climatology for the Southern Hemisphere. *Mon. Wea. Rev.*, **122**, 2239–2256, 1994.

Smith, S. D., Muench, R. D., and Pease, C. H., Polynyas and Leads: An overview of physical processes and environment. *J. Geophys. Res.*, **95**(C6), 9461–9479, 1990.

Smith, E. K., Centimeter and millimeter wave attenuation and brightness temperature due to atmospheric oxygen and water vapor. *Radio Sci.*, **17**, 1455–1464, 1982.

Smith, D. M., Observation of perennial Arctic sea ice melt and freeze-up using passive microwave data. *J. Geophys. Res.*, **103**(C12), 27,753–27,769, 1998.

Squire, V. A., Wadhams, P., and Moore, S. C., Surface gravity wave processes in the winter Weddell Sea. *EOS Trans. Am. Geophys. Union*, **67**(44), 1005, 1986.

Stammerjohn, S. E., and Smith, R. C., Opposing Southern Ocean climate patterns as revealed by trends in regional sea ice coverage. *Climatic Change*, **37**, 617–639, 1997.

Steffen, K., Key, J., Cavalieri, D. J., Comiso, J., Gloersen, P., St. Germain, K., and Rubinstein, I., The estimation of geophysical parameters using passive microwave algorithms. In Carsey, F. D., editor, *Microwave remote sensing of sea ice*, AGU Monograph, 68, pp. 201–231. Am. Geophys. Union, Washington, D.C., 1992.

St. Germain, K., and Cavalieri, D. J., A microwave technique for mapping ice temperature in the Arctic seasonal sea ice zone. *IEEE Trans. Geosci. Rem. Sens.*, **35**(4), 946–953, 1997.

St. Germain, K., Atmospheric water vapor and cloud liquid water correction for the 85 GHz channels of the SSM/I. *EOS Trans. Am. Geophys. Union*, **74**(43), 324, 1993.

Stogryn, A., and Desargeant, G. J., The dielectric properties of brine in sea ice at microwave frequencies. *IEEE Trans. Ant. Prop.*, **AP-33**(5), 523–532, 1985.

Stogryn, A., The emissivity of sea foam at microwave frequencies. *J. Geophys. Res.*, **77**, 1658–1666, 1972.

Stogryn, A., Estimates of brightness temperatures from scanning radiometer data. *IEEE Trans. on Antennas and Propagation*, **AP-26**, 720–726, 1978.

Sturm, M., Grenfell, T. C., and Perovich, D. K., Passive microwave measurements of tundra and taiga snow covers in Alaska, U.S.A. *Ann. Glaciol.*, **17**, 125–130, 1993.

Sturm, M., Morris, K., and Massom, R., The winter snow cover of the West Antarctic pack ice: its spatial and temporal variability. In Jeffries, M. O., editor, *Antarctic Sea Ice: Physical processes, interactions and variability*, Antarctic Research Series, 74, pp. 1–18. Am. Geophys. Union, Washington, D.C., 1998.

Sturm, M., The role of thermal convection in heat and mass transport in the subarctic snow cover. CRREL Report No. 91-19, U.S.A. Cold Regions Resarch and Engineering Laboratory (CRREL), Hanover, New Hampshire, 1991.

Svendsen, E., Kloster, K., Farrelly, B., Johannessen, O. M., Johannessen, J. A., Campbell, W. J., Gloersen, P., Cavalieri, D., and Mätzler, C., Norwegian remote sensing experiment: evaluation of the NIMBUS 7 Scanning Multichannel Microwave Radiometer for sea ice research. *J. Geophys. Res.*, **88**, 2781–2791, 1983.

Svendsen, E., Mätzler, C., and Grenfell, T. C., A model for retrieving total sea ice concentration from a spaceborne dual-polarized passive microwave instrument operating near 90 GHz. *Int. J. Rem. Sens.*, **8**, 1479–1487, 1987.

Swift, C. T., and Cavalieri, D. J., Passive microwave remote sensing for sea ice research. *EOS, Trans. Am. Geophys. Union*, **66**, 1210–1212, 1985.

Swift, C. T., Passive microwave remote sensing of the ocean – a review. *Bound. Lay. Meteorol.*, **18**, 25–40, 1980.

Szeto, K. K., Stewart, R. E., and Hanesiak, J. M., High-latitude cold season frontal cloud systems and their precipitation efficiency. *Tellus*, **49A**, 439–454, 1997.

The NORSEX Group, Norwegian remote sensing experiment in a marginal ice zone. *Science*, **220**(4599), 781–787, 1983.

Thomas, C. H., *Longtime analysis of Antarctica's sea-ice from passive microwave data*. PhD thesis, University of Bremen, Fachbereich 1 (Physik und Elektrotechnik) and Reports on Polar Research, **284**, Alfred-Wegener-Institut für Polar- und Meeresforschung (AWI), 1998.

Toudal, L., and Saldo, R., A dataset of satellite derived ice motion for the Southern Ocean. In *Proc. EGS2000, Nice, France, April 2000*, 2000.

Tsatsoulis, C., and Kwok, R., *Analysis of SAR data of the polar oceans: Recent advances.* Springer Verlag, Berlin, Germany, 1998.

TuckerIII, W. B., Perovich, D. K., Gow, A. J., Weeks, W. F., and Drinkwater, M. R., Physical properties of sea ice relevant to remote sensing. In Carsey, F. D., editor, *Microwave remote sensing of sea ice*, AGU Monograph, 68, pp. 9–28. Am. Geophys. Union, Washington, D.C., 1992.

Turner, J., Lachlan-Cope, T. A., Thomas, J. P., and Colwell, S. R., The synoptic origins of precipitation over the Antarctic Peninsula. *Antarctic Science*, **7**(3), 327–337, 1995.

Ulaby, F. T., Moore, R. K., and Fung, A. K., *Microwave remote sensing, active and passive. Volume I: Fundamentals and radiometrie.* Addison Wesley Pub., London, U.K., 1981.

Ulaby, F. T., Moore, R. K., and Fung, A. K., *Microwave remote sensing, active and passive. Volume III: From theory to applications.* Addison Wesley Pub., London, U.K., 1986.

Vander Veen, C. J., and Jezek, K. C., Seasonal variation in brightness temperature for central Antarctica. *Ann. Glaciol.*, **17**, 300–306, 1993.

Wadhams, P., Lange, M. A., and Ackley, S. F., The ice thickness distribution across the Atlantic sector of the Antarctic Ocean in midwinter. *J. Geophys. Res.*, **92**(C13), 14,535–14,552, 1987.

Walters, J. M., Ruf, C., and Swift, C. T., A microwave radiometer weather-correction sea ice algorithm. *J. Geophys. Res.*, **92**(C6), 6521–6534, 1987.

Wensnahan, M., Maykut, G. A., and Grenfell, T. C., Passive microwave remote sensing of thin ice using principal component analysis. *J. Geophys. Res.*, **98**(C7), 12,453–12,468, 1993.

White, W. B., and Peterson, R. G., An Antarctic circumpolar wave in surface pressure, wind, temperature and sea-ice extent. *Nature*, **380**, 699–702, 1996.

Winebrenner, D. P., Nelson, E. D., Colony, R., and West, R. D., Observation of melt onset on multiyear Arctic sea ice using ERS 1 synthetic aperture radar. *J. Geophys. Res.*, **99**(C11), 22,425–22,441, 1994.

Worby, A. P., Jeffries, M. O., Weeks, W. F., Morris, K., and Ja na, R., The thickness distribution of sea ice and snow cover during late winter in the Bellingshausen and Amundsen Seas, Antarctica. *J. Geophys. Res.*, **101**(C12), 28,441–28,455, 1996.

Worby, A. P., Massom, R. A., Allison, I., Lytle, V., and Heil, P., East Antarctic sea ice: A review of its structure, properties and drift. In Jeffries, M. O., editor, *Antarctic Sea Ice: Physical processes, interactions and variability*, Antarctic Research Series, 74, pp. 41–68. Am. Geophys. Union, Washington, D.C., 1998.

World Meteorological Organization (WMO), *International Cloud Atlas*. World Meteorological Organization, Geneva, Switzerland, 1956.

World Meteorological Organization (WMO), WMO sea ice nomenclature. Technical Report WMO/OMM/BMO, suppl. 5, WMO, Geneva, Switzerland, 1989.

Yu, Y., and Rothrock, D. A., Thin ice thickness from satellite thermal imagery. *J. Geophys. Res.*, **101**(C10), 25,753–27,766, 1996.

Zwally, H. J., Comiso, J. C., Parkinson, C. L., Campbell, W. J., Carsey, F. D., and Gloersen, P., Antarctic sea-ice, 1973–1976: satellite passive-microwave observations. Technical Report NASA SP-459, National Aereonautics and Space Administration (NASA), Washington, D.C., 1983.

Zwally, H. J., Comiso, J. C., and Gordon, A. L., Antarctic offshore leads and polynyas and oceanographic effects. In Jacobs, S. S., editor, *Oceanology of the Antarctic continental shelf*, Antarctic Research Series, 43, pp. 203–226. Am. Geophys. Union, Washington, D.C., 1985.